Mesoporous film architectures and step gradient formation

TECHNISCHE
UNIVERSITÄT
DARMSTADT

Vom Fachbereich Chemie
der Technischen Universität Darmstadt

zur Erlangung des Grades
Doctor rerum naturalium
(Dr. rer. nat.) genehmigte

Dissertation
von Mathias Stanzel

Erstgutachterin: Prof. Dr. Annette Andrieu-Brunsen
Zweitgutachter: Prof. Dr. Markus Biesalski

Darmstadt 2022

Zusammenfassung

Die Entwicklung neuartiger Geräte zusammen mit dem technologischen Fortschritt unserer Zeit verlangt Miniaturisierung und Kompartmentbildung, und damit Nanotechnologie. So werden beispielsweise dringend innovative Lösungen für ein vom Leben inspiriertes nachhaltiges Wasser- und Energiemanagement angestrebt. Nanoskalige Poren und Kanäle, als ein Bereich innerhalb der Nanotechnologie, bergen ein großes Potential, die herausragende Transportphänomene ihrer biologischen Vorbilder zu imitieren. Solche Transporteigenschaften, wie sie in biologischen Poren und Kanälen zu beobachten sind, beruhen auf einer komplexen Architektur und werden von der Porengeometrie, der Oberflächenladungsverteilung, der chemischen Zusammensetzung und der Benetzbarkeit beeinflusst. Die gewünschten Transporteigenschaften in fortschrittlichen Anwendungen erfordern jedoch eine verbesserte Kontrolle der Oberflächenfunktionalisierung in nanoskaligen Poren und Kanälen zusammen mit dem Design nanoporöser Materialarchitektur.

In dieser Hinsicht stellen mesoporöse Silicadünnfilme geeignete Modellmaterialien für die Entwicklung nanoporöser Materialarchitekturen dar, die geordnete nanoskalige Poren und nanoskalige Filmdicken bieten. In dieser Arbeit wurden mesoporöse Silicadünnfilme untersucht, um mesoporöse Stufengradientenarchitekturen in Bezug auf Porengröße, Oberflächenbenetzbarkeit und Oberflächenladung zu erzeugen. Diese Arbeit gliederte sich in drei Hauptabschnitte: i) Erstellung einer Materialbibliothek, die das Design von Stufengradienten ermöglicht, ii) Herstellung mesoporöser Architekturen und iii) (nano)lokale Platzierung von Polymeren in solchen Mehrschichtarchitekturen.

Um mesoporöse Architekturen zu erzeugen, wurde zunächst eine Materialbibliothek erstellt. Dabei wurde die ionische Porenzugänglichkeit hydrophiler mesoporöser Silicadünnfilme in Abhängigkeit von Präparationsparameter, genauer der Templatentfernung, untersucht. Hydrophobe mesoporöse Silicadünnfilme mit einstellbarer Oberflächenbenetzbarkeit wurden durch Co-Kondensation von Tetraethylorthosilicat und methylierten Silicapräkursoren entwickelt, was zu mesoporösen (Organo)Silicadünnfilmen führte. Dabei wurde bei den hydrophoben Dünnfilmen eine erhöhte chemische Stabilität in basischer Umgebung festgestellt. Um Erdöl-basierte Templatmakromoleküle zu ersetzen, wurde Hydroxypropylcellulose erfolgreich als biobasiertes strukturgebendes Templat für die Herstellung mesoporöser Silicadünnfilme mit permselektiver ionischer Porenzugänglichkeit eingesetzt.

Mesoporöse Stufengradientenarchitekturen wurden durch Verwendung der entwickelten Materialbibliothek und durch Kombination mesoporöser Schichten mit orthogonalen Eigenschaften hergestellt. Beispiele hierfür sind: die Herstellung hydrophiler Porengrößenstufengradienten, und die Kombination von Schichten mit unterschiedlicher

Benetzbarkeit. Interessanterweise zeigte die Untersuchung mesoporöser Benetzbarkeitsstufengradientenfilme in Bezug auf die ionische Porenzugänglichkeit in Abhängigkeit von der Dicke der oberen hydrophoben Schicht eine Überwindung der hydrophoben Schicht durch elektrostatische Anziehung der hydrophilen unteren Schicht im Falle der dünnsten oberen hydrophoben Schicht.

Hinsichtlich der lokalen Polymerplatzierung erwies sich die mehrschichtige Stufengradientenbildung mesoporöser Dünnfilme ebenfalls als vorteilhaft. So wurde beispielsweise die schichtselektive Polymerfunktionalisierung hydrophiler zweischichtiger Silicadünnfilme durch Vorprägung einer einzelnen Schicht und anschließender selektiver Iniferteranbindung erreicht. Die schichtselektive Polymerpfropfung führte zu Stufengradienten mit Ladungsdichtekontrolle. Um die Grenzen der Polymerplatzierung in mesoporösen Filmarchitekturen weiter zu untersuchen, wurden plasmonische Metallnanopartikel in mesoporöse Silicadünnfilme eingebaut. Diese Partikel dienten als nanoskopische plasmonische Lichtquelle und wurden mit Photopolymerisationen kombiniert. Die Untersuchung der hergestellten mesoporösen Kompositmaterialien ermöglichte eine präzise Platzierung der Nanopartikel in mesoporösen Silicadünnfilmen mit einstellbarer Dichte. Das Konzept der nanolokalen Polymerplatzierung unter Verwendung von plasmonischen Metallnanopartikeln in Kombination mit Photopolymerisation wurde für zwei verschiedene Polymerisationsansätze demonstriert. Aufgrund der Sensitivität der Oberflächenplasmonen der Nanopartikel auf den umgebenden Brechungsindex, haben sich solche mesoporösen Kompositmaterialien auch als Sensoreinheit bewährt, die es ermöglichen, lokale Brechungsindexänderungen, z. B. in Folge der nanolokalen Polymerplatzierung, zu detektieren.

Meinem Großvater Gerhard Stanzel

* 21.10.1936 † 02.07.2018

Acknowledgements - Danksagung

The present work was performed at the Ernst-Berl Institut für Makromolekulare und Technische Chemie of the Technical University Darmstadt under the supervision of Mrs. Prof. Dr. Annette Andrieu-Brunsen from October 2016 to November 2020.

Parts of this work are published in scientific journals.

Scientific publications as first author:

1) **<u>Stanzel, M.,</u>** Kunz, U., Andrieu-Brunsen, A., „Layer-selective functionalisation in mesoporous double layer via iniferter initiated polymerization for nanoscale step gradient formation", *Eur. Polym. J.*, **2021**, 156, 110604.

2) **<u>Stanzel, M.,</u>** Zhao, L., Mohammadi, R., Pardehkhorram, R., Kunz, U., Vogel, N., Andrieu-Brunsen, A., „Simultaneous Nanolocal Polymer and In Situ Readout Unit Placement in Mesoporous Separation Layers", *Anal. Chem.*, **2021**, 93, 13, 5394-5402.

3) John, D.*, **<u>Stanzel, M.</u>***, Andrieu-Brunsen, A., „Surface Plasmons and Visible Light Iniferter Initiated Polymerization for Nanolocal Functionalization of Mesoporous Separation Layers", *Adv. Funct. Mater.*, **2021**, 2009732.

   *D.J. and M.S. contributed equally to this work.

Scientific publications as collaborator:

1) Khalil, A., Schäfer, F., Postulka, N., **<u>Stanzel, M.,</u>** Biesalski, M., Andrieu-Brunsen, A., "Wettability-defined droplet imbibition in ceramic mesopores", *Nanoscale*, **2020**, 12, 24228-24236.

2) Herzog, N., Brilmayer, R., **<u>Stanzel, M.,</u>** Kalyta, A., Spiehl, D., Dörsam, E., Hess, C., Andrieu-Brunsen, A., „Gravure printing for mesoporous film preparation", *RSC Adv.*, **2019**, 9, 23570-23578.

Talks:

<u>Stanzel, M.</u>, Andrieu-Brunsen, A., 'Local polymer functionalization in mesoporous multilayer architectures and its influence on mesopore transport', *6th International Conference on Multifunctional, Hybrid and Nanomaterials*, **2019**, Sitges, Spain.

Posters:

1) Despot, L., Förster, C., **<u>Stanzel, M.</u>**, Andrieu-Brunsen, A., '(Visible) light induced RAFT and photoiniferter-mediated polymerization for the functionalization of silica mesopores', *Polymer Brushes: New Developments and Perspectives in Experiment, Theory and Applications,* **2021**, Dresden, Germany, Virtual Meeting.

2) Förster, C., **<u>Stanzel, M.</u>**, Andrieu-Brunsen, A., 'Polymer functionalization and sensing in the nanoconfinement of mesoporous silica thin films', *Minisymposium on Catalysis under Confinement*, **2021**, Stuttgart, Germany, Virtual Meeting.

3) Leskow, F.-H., **Stanzel, M.**, ‚Funktionale nanoporöse Membranen zur selektiven Entfernung von Mikroverunreinigungen in der Wasserwiederverwendung', *91. Darmstädter IWAR Seminar*, **2020**, Darmstadt, Germany.

4) **<u>Stanzel, M.</u>**, Andrieu-Brunsen, A., "Membrane Architecture", *Symposium on Dynamic Sorption*, **2018**, Leipzig, Germany.

Table of content

Abstract

The development of novel devices along with technological progress of our time requires miniaturization and compartmentalization, and with this nanotechnology. For example, future innovative solutions are urgently pursued for life-inspired sustainable water and energy management. Nanoscale pores and channels, as one field within nanotechnology, hold great potential in mimicking the outstanding transport phenomena of their biological paragons. Such transport properties, as observed in biological pores and channels, originate from complex architectures and are influenced by pore geometry, surface charge distribution, chemical composition, and wettability. However, desired transport properties in advanced applications require enhanced control of surface functionalization in nanoscale pores and channels along with nanoporous material architecture design.

In this regard, mesoporous silica thin films represent suitable model materials for nanoporous material architecture design providing ordered nanoscale pores and nanoscale film thicknesses. In this work, mesoporous silica thin films were investigated to create mesoporous step gradient architectures with respect to pore size, surface wettability, and surface charge. This work was divided into three main sections: i) generating a material library allowing step gradient design, ii) the fabrication of mesoporous architectures, and iii) (nano)local polymer placement into such multilayer architectures.

To create mesoporous architectures, a material library was built in the first place. Thereby, the ionic pore accessibility of hydrophilic mesoporous silica thin films was investigated in dependence of preparation parameters, i.e. the template removal. Hydrophobic mesoporous silica thin films with tunable surface wettability were developed using co-condensation of tetraethylorthosilicate and methylated silica precursors resulting in mesoporous (organo)silica thin films. As a side note, an enhanced chemical stability in basic environment was observed for hydrophobic thin films. To replace petro-based templating macromolecules, hydroxypropyl cellulose was successfully applied as bio-based structure directing template for the generation of mesoporous silica thin films with permselective ionic pore accessibility.

Mesoporous step gradient architectures were prepared by applying the developed material library combining mesoporous layers with orthogonal properties. Examples are: the fabrication of hydrophilic pore size step gradients, and the combination of layers with different wettability. Interestingly, investigation of mesoporous wettability step gradient films with respect to the ionic pore accessibility in dependence of the hydrophobic top layer's thickness showed an overcoming of the hydrophobic layer through electrostatic attraction of the hydrophilic bottom layer in case of the thinnest hydrophobic top layer.

Regarding local polymer placement, multilayer step gradient mesoporous film formation turned out to be advantageous, too. For example, the layer-selective polymer functionalization of hydrophilic double layered mesoporous silica thin films was achieved by predisposition of a single layer, followed by selective iniferter binding. Layer-selective polymer grafting was achieved resulting in step gradients with charge density control. To further investigate the limits of polymer placement in mesoporous film architectures, plasmonic metal nanoparticles were incorporated into mesoporous silica thin films. These particles served as nanoscopic plasmonic light source and were combined with photopolymerizations. Investigation of the prepared mesoporous composite materials allowed precise placement of the nanoparticles in mesoporous silica thin films with tunable density. The concept of nanolocal polymer placement using plasmonic metal nanoparticles in combination with photopolymerization was demonstrated for two distinct polymerization approaches. Due to the sensitivity of the nanoparticle's surface plasmons on the surrounding refractive index, such mesoporous composite materials further demonstrated application as sensing unit allowing to detect local refractive index changes, e.g. in consequence of nanolocal polymer placement.

1. Introduction

The unfailing thirst for knowledge of human kind has led to numerous breakthroughs that emerged in today's technological advancement of our present age. In that way, scientists and engineers have ever been inspired by nature and living organisms. For example, water-repellent and self-cleaning surfaces have been inspired by the superhydrophobic properties of the lotus leave which originates from their specific micro- and nanostructured surface,[1] or self-cooling buildings encouraged by the architectural design of termite nests.[2] Miniaturization and compartmentalization are ongoing challenges to meet the ever-growing requirements of novel devices along with the technological progress of our time.[3] Future innovative solutions for life-inspired sustainable water and energy management are urgently pursued.[4] In this context, nanoscience and nanotechnology bear great potential. Interestingly, scientific efforts in the fields of chemistry, physics, and biology have explored quite different material behavior when it comes down to the nanometer scale compared to micrometer and bulk dimensions, as well known as the confinement effect. For example, reaction rates are significantly increased in the nanoconfinement of ~2.3 nm mesopores.[5] Furthermore, simulations and experimental data showed that water is freezing above 100 °C in the confined space close to 1 nm in carbon nanotubes.[6-8] Another example is differences in apparent pH value inside nanopores compared to the pH in the bulk solution determined by experiment and simulations,[9] or local pK_a shifts of polyelectrolytes in the confinement of mesopores demonstrated via an electrochemical study.[10] These endeavors will not only advance the possibility of constructing materials at the nanometer scale, but also provide insights into natural processes to learn from. For example, understanding and mimicking the outstanding performance of biological ion channels, truly natural nanomachines that show adaptive, self-regulated, highly selective, directed and gated transport, which originates from a complex arrangement and interplay of several different areas at nanoscale and lower dimension.[11-13] These areas are either neutral, positively or negatively charged, hydrophilic or hydrophobic. Interestingly, active sites of biological ion channels are often concentrated to a few angstroms indicating the relevance of engineering on the nanometer scale and beyond. The underlying understanding of these complex architectures and resulting transport properties of biological ion channels becomes increasingly important for transport modulation of nanoporous materials which would enable life-inspired sustainable future water, energy and sensing concepts.[14] With this background, synthetic nanopores and channels have been intensively studied with respect to modulation and regulation transport properties in the last decades.[15-16] As a result, for instance, it has been demonstrated that a break in symmetry of nanoscale pores and channels can lead to a preferential transport direction of mass and charge similar to the outstanding performance of biological pores and channels.[17-19] Side-selective

transport or oil-water separation, for example, is obtained by an asymmetric wettability design of porous materials and membranes.[20-23] Furthermore, a preferential transport direction is observed for nanoporous channels with asymmetric pore geometry, which is known as diode-like ionic current rectification (ICR).[24-25] For instance, conical pores show enhanced ICR ratios as compared to cylindrical pores as demonstrated by *Siwy* and co-workers.[26] Regardless of the pore geometry, an asymmetric charge pattern of nanopore surfaces also results in enhanced ICR ratios, which has been demonstrated in comprehensive studies in experiment along with simulations.[27-34] Based on this asymmetric design, bio-inspired artificial ion pumps have been realized by *Jiang* and co-workers by selectively functionalizing the tip ends of an hour-shaped nanochannels with cooperative pH-responsive polyelectrolytes.[35-37] Furthermore, transient capping of the nanopore entrance allows controlled release of guest molecules trapped inside the pores, or gating/switching of ionic transport can be realized by selective functionalization of the outer surface of nanoporous materials.[38-40] Thus, transport properties of nanoporous materials are influenced by pore geometry, surface charge distribution, chemical composition, and wettability, as *Guo* et al. summarized.[41] However, directed transport of mass and charge in advanced applications requires enhanced control of surface functionalization in nanoscale pores and channels along with a detailed understanding of ion transport phenomena in nanoscale confinement.

One prominent class of such nanoporous materials is represented by mesoporous silica thin films (MSTFs), which have been utilized as model materials to manipulate and understand the transport of mass and charge for the last three decades.[42-43] Particularly, the functionalization of such materials by organic matter has led to a variety of hybrid materials allowing to modulate ionic transport providing fundamental insights into the transport properties in nanoscale confinement.[44-45] In general, hybrid MSTFs are prepared either by the manufacturing process through the combination of inorganic precursors together with precursors containing organic functional groups, or by post-modification of the silica surface.[44, 46] The latter is rather versatile and accomplished by physical as well as chemical adsorption. Besides the molecular attachment of functional groups the silica surfaces, various polymerization techniques have been applied for the generation of hybrid MSTFs, i.e. atom transfer radical polymerization (ATRP)[47], reversible addition-fragmentation chain-transfer polymerization (RAFT) along with iniferter initiated polymerizations[48], dye-sensitized polymerization[49], and ring-opening metathesis polymerization (ROMP)[50]. Thereby, modulation of transport of hybrid MSTFs was demonstrated mainly by utilizing polymers with responsiveness to pH, temperature, oxidation or light.[44-45, 51] Above all, tunable functional densities and, thus, tailored transport properties as a consequence of the functionalization of MSTFs have mainly been reported for free radical and

controlled radical polymerization methods such as ATRP and iniferter initiated polymerizations.[47-48, 52-56] In addition, the research group of *Annette Andrieu-Brunsen* recently demonstrated that not only the amount of polymer, thus the functional density is controllable by iniferter initiated polymerization, but further allows the generation of block-co-oligomers, hence control of the polymer chain architecture.[56] In addition, several approaches have been reported for the selective post modification of the inner or outer surface of mesoporous materials, for example by soft template, kinetic or size protection.[57]

Although many different techniques are available for the functionalization of MSTFs, these approaches have only been demonstrated for single layers of mesoporous silica films. However, mesoporous multilayers are well established in the scientific community. Although their preparation mainly focused on optical properties, promising applications in photonics, sensing, and photocatalytic processes have been demonstrated.[58-60] By that, in mesoporous multilayer, mesoporous silica and mesoporous titania are often combined resulting in photonic crystals due to the high difference in optical properties of the individual layers.[61-62] Combining mesoporous films with distinct properties, e.g. surface functionalities, wettability, or pore size, into multilayer would allow the generation of complex mesoporous architectures via sequential deposition. Nonetheless, only a few publications investigating the fabrication and resulting transport properties of mesoporous double layer can be found in literature, and selective post-modification of a single layer had not been demonstrated at the beginning of this work. The latter was expected to allow implementation of functionalities with nanoscale precision in mesoporous multilayer, since the film thickness of mesoporous silica can be tuned from a few tens up to several hundred nanometers by adjusting the deposition parameters.[63]

Further pushing the limit of function placement with nanoscale precision in mesoporous multilayer, would require focusing of light at the nanoscale in combination with photo-sensitive reactions, such as photopolymerization, for example. In the recent past, a new research field evolved investigating the induction of photo-sensitive reactions by the high-energetic electromagnetic near-field of plasmonic metal nanoparticles (NPs), known as localized surface plasmon resonance (LSPR). For instance, photopolymerizations induced by the LSPR of plasmonic metal NPs immobilized on flat surfaces were successfully applied for nanoscale polymer placement in pioneering works of *Bachelot, Soppera* and co-workers.[64-66]

Integration of the concept into porous materials would allow function placement with nanoscale precision independently of the film thickness of individual layers in a multilayer arrangement. The combination of plasmonic metal NPs and mesoporous thin films has just recently been demonstrated in previous studies.[67-69] Thereby, plasmonic metal NPs can be precisely positioned in mesoporous films with spatial control being accessible for further chemical reactions. The

growing and branching of randomly distributed gold NPs in mesoporous films has been demonstrated by *Angelomé* et al.[70]

2. State of research

In this chapter, the current research with respect to nanopore and nanochannel architectures and the resulting properties are discussed. Thereby, asymmetries in pore size, charge distribution, and surface wettability are discussed in detail. In addition, the state of research with respect to plasmonic metal NPs and the utilization of these as nanoscale light sources to trigger chemical reactions are described.

2.1. Asymmetry in nanoscale pores and channels

Asymmetries in geometry and surface properties of nanopores (length comparable with radius) and nanochannels (length much larger than radius) have been identified as key factors to control transport.[15, 71] For example, the transport of ions through nanoscale pores and channels is based on interaction between the surface charge of the pore wall and ions. Attraction of the surface charge and counterions leads to an increase in ion concentration within the pore compared to bulk concentration, while ions carrying the same charge as the pore wall will be depleted, if the pore diameter is sufficiently small, thus the electric double layer is in the same scale as the pore radius.[15, 30, 71]

Recent research has explored a phenomenon known as ICR mostly observed in nanoscale channels, in which the current at a voltage of one polarity is significantly higher or lower than the current at the voltage of opposite polarity indicating preferential transport direction similar to biological ion channels. Such artificial nanochannels that show non-linear current-voltage curves are also described as voltage-gating or voltage-responsive in consequence of their comparable transport properties of electrical semiconductors, diodes and transistors.[30] In most cases, ICR is observed in consequence of a break in symmetry in the electric potential of the pores determining the interaction of ions and the pore wall.[72-73] Similarly, an asymmetric distribution of different components is observed in most biological nanochannels, e.g. areas of different charges and/or different wettability, to implement complex biological functions.[74-76] In 1997, the first example of a synthetic rectifying nanochannel based on a glass nanopipette prepared by conventional micropulling was reported.[77] The nanopipette with an opening diameter of 20 nm (tip) and 200 nm (base), and a tip length of approx. 9 mm showed larger currents at a voltage of negative polarity indicating that cations are moving from the tip towards the wide opening of the nanopipette. Notably, the ICR was strongly dependent on high pH values leading to the formation of deprotonated, negatively charged surface silanolate groups and electrolyte solution lower or equal to 0.1 M KCl. The ICR phenomenon observed in glass nanopipettes was further studied by *Umehara* et al.[78] Interestingly, they demonstrated that the selectivity of the glass nanopipette was inversed from cationic to anionic by modification of the

pipette's surface with positively charged polylysine. In addition, theoretical studies on ICR in glass nanopipettes were conducted by *White* and *Bund*.[79] Furthermore, ICR was observed in conically shaped nanopores in track-etched polymer films.[24, 80-81] Thereby, the track-etching technique relies on irradiating polymer films with single energetic heavy ions, followed by developing the resulting latent tracks by chemical etching into single pores with opening diameters down to several nm.[30, 82] Conical pores are obtained by asymmetric performance of the etching process, i.e. side-selective etching.[30, 83] Compared to glass nanopipettes, the conical pores in thin polyethylene terephthalate (PET) films with a sub-10 nm opening diameter showed strongly non-linear current-voltage curves at much higher salt concentration, but the effect was only observed in presence of surface charges on the pore walls, likewise to glass nanopipettes.[24] Besides in track-etched PET films, ICR was also observed in track-etched films prepared from polyimide[84] and polycarbonate[85]. The same observation of ICR based on ion selectivity and pore asymmetry was discovered in nanoscale channels fabricated in silicon nitride membranes prepared by drilling with a focused ion beam.[86] As result of the fabrication process, the pore diameters on the two sides were different, thus causing ICR.

To explain the ICR phenomena observed in conical pores, two models have been proposed. One model is based on the asymmetry in the electrochemical potential determining the interactions between the transported ions and the immobilized static surface charges on the pore wall.[30] The other model assumes voltage-induced changes in the pore structure: free dangling groups of polymer chains near the small opening, which are generated in the etching process, might move out of the pore inducing an enlarging of the pore opening, thus allowing for higher ionic flux, when a voltage of a given polarity is applied, and/or partially blocking the pore at a voltage of opposite polarity.[30, 84, 87] In addition to conical glass nanopipettes, polymer pores, and porous silicon nitride, ICR was further demonstrated for conical gold nanotubes, which were prepared by covering conical polymer pores with gold by applying electroless plating.[88] The satisfying study nicely demonstrated the requirement of surface charges to obtain ICR in conically shaped nanopores by modification of the gold surface with chloride ions, which are known to adsorb onto gold.[88-89] Contrary, no ICR was observed, when the pores were immersed in a solution of KF, since fluoride anions do not adsorb on gold, thus the conical gold nanotube had no surface charge.[88-89] Since the first observation of ICR in non-biological nanopores in 1997, these early examples of nanochannels with ICR properties depicted above represent the first mode of ICR, ergo a phenomenon indicating preferential ion transport direction through nanochannels, in which an asymmetric potential along the channel axis together with homogenously distributed surface charges on the channel walls are required.[30]

The second mode of ICR, which has gained considerable interest recently, is represented by non-homogenous charge pattern, and does not require an asymmetric pore geometry.[30]

In 2005, the first example of ionic diodes bearing asymmetric surface charge patterns was suggested in a theoretical study by *Daiguji* et al., in which a zone of a nanochannel with positive surface charges is located next to a zone with negative surface charges.[27] Notably, the current in bipolar ionic diodes is carried by both cations and anions, thus the diode is not ion selective.[30] Furthermore, the operation of the nanofluidic diode is analogous to the ICR observed with bipolar membranes, which are composed of anion- and cation-selective membranes brought into physical contact and used for electrochemical splitting along the production of acids and bases.[30, 90-92] The first experimental realization of bipolar diodes was conducted by applying single conically shaped polymer nanopores bearing asymmetric charge pattern, published by *Vlassiouk* et al. in 2007.[93]

To construct the bipolar nanopore, negatively charged carboxyl groups on the surface of conical nanopores in PET films were modified into amine groups at the narrow opening (tip) by covalently attaching ehtylenediamine with the coupling agent 1-ethyl-3-(3-dimethylaminopropyl)carbodiimide hydrochloride (EDC). Thereby, only the tip side of the PET membrane was brought into contact with the reaction solution. In consequence of the conical geometry, the concentration of the reagents was high at the first tens of nanometers of the narrow opening and decayed rapidly along the pore axis. The asymmetric charge patterned conical shaped nanopore showed almost total suppression of the current at negative potentials, and high currents at positive potentials indicating ion flow only in one direction (**Figure 1a**).
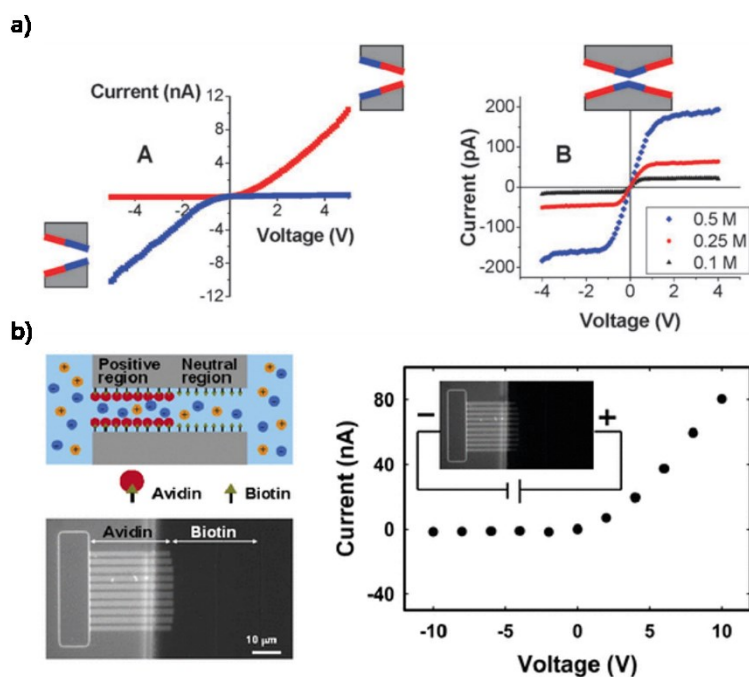
Figure 1: a) Current-voltage curves of bipolar ionic diodes based on polymer nanochannels. Blue and red lines correspond to negative and positive surface charges respectively. Reproduced from Ref. 30 with permission from the Royal Society of Chemistry. b) Schematic representation, epifluorescence image (avidin fluorescently labeled), and current-voltage curve of a unipolar ionic diode based on nanochannels patterned with positively charged avidin in one half of the channels and close to neutral charged biotin in the other half of the channels. Reprinted with permission from Ref. 94. Copyright 2007 American Chemical Society.

By reversing the surface charge pattern, the current-voltage curves flipped and even higher currents at negative potentials were observed. This approach of asymmetric modification of nanochannels, the so-called diffusion limited patterning (DLP), was developed by *Karnik* et al. and firstly introduced in 2006, in which silica nanochannels were firstly modified with the amine bearing silane (3-aminopropyl)trimethoxysilane, subsequently functionalization of the entire channel with biotin, which resulted in a neutral pore surface, followed by diffusion limited grafting of the complementary receptor streptavidin, which carries a positive net charge and has a high affinity to biotin.[95] Implementing this modification strategy, *Karnik* et al. also demonstrated asymmetric rectifying nanochannels in 2007.[94] There, half of the nanochannels were modified with the neutral biotin, the other half modified with positively charged avidin, hence an asymmetric unipolar ionic diode was built (**Figure 1b**). However, diode-like behavior was only observed for low ionic concentration, most likely due to the large dimension of the channels, particularly 30 nm in height.[30] *Vlassiouk* et al. further demonstrated the sensing potential of nanofluidic diodes by selectively immobilizing antibodies on the tip side of conically shaped nanopores, which allows detection of the complementary antigen, when binding to the antibody and thus blocking the tip side of the pore, therefore leading to a change of the

electrochemical signal.[96] Similar observations were obtained by asymmetric immobilization of DNA aptamers via DLP for the detection of lysozyme.[97] Furthermore, dangling DNA strands selectively immobilized at the tip end of conically shaped polymer nanochannels were applied to tune the pore opening diameters in dependence of salt concentration and the voltage applied, thus allowing to regulate transport of neutral and charged species.[17, 98] By increasing the complexity of the pore geometry into a double-conical geometry, in which a narrow negatively charged channel section in the middle of the channel and two positively charged zones at the wider opening on both sides of the membrane are present, two diode-like junctions in series similar to a semiconductor npn junction are observed in the current-voltage curves.[99] Here, the charge pattern was generated by two consecutive amine modifications, in which one side of the PET nanochannel was brought into contact with the reagent solution comprising ethylenediamine and EDC buffered at pH 5.5, and a buffer solution of pH 10 at the other side of the membrane. Since EDC amidation is strongly pH dependent, reactions only occurred at high rate on the side with acidic buffer, but not on the side with basic buffer. Thus, low reaction rates in the narrow region were caused by diffusion of the basic buffer leading to an asymmetric charge pattern.

Accordingly, DLP has been demonstrated for single nanochannels, respectively arrays of nanochannels to generate asymmetric charge patterns resulting in a preferential transport direction of ions through the nanochannels. Hence, the approach has not been validated for multipore materials. Furthermore, the modification approach was demonstrated on channels with nanoscale pore diameters and pore lengths at the microscale, and might not apply to nanoporous materials with pore length of a few or several hundred nanometers, as well as to nanoporous materials deposited on dense substrates. Nevertheless, different approaches for the fabrication and modification of multipore materials with nanoscale pores and asymmetric charge distributions are discussed later in this chapter.

The insights of preferential transport direction observed in nanochannels with a broken symmetry in either geometry or surface charge distribution, or both, have encouraged scientists to develop new strategies with respect to asymmetric fabrication and asymmetric modification of nanochannels and nanopores,[18, 41, 100] which will be introduced and discussed in detail in the following. Before that, interfacial materials with asymmetric surface wettability are introduced, as these interfaces are able to allow directed transport of fluids. Although nanochannels are discussed in this work, porous materials with more than one nanochannel or nanopore are predominantly reviewed, as multipore or multichannel materials, respectively, are favored with respect to applications such as filtration and separation, energy conversion, and catalysis.[18, 100] Differently, single nanochannels and nanopores have been well-established in (bio)sensing applications.[101]

Similar to the preferential transport direction of ions in nanochannels with asymmetric pore geometry and homogenous surface charge distribution, as well as with nanochannels containing asymmetric charge patterns, interfacial materials presenting side-specific opposite wettability, i.e. hydrophilic and hydrophobic surfaces, also show diode-like transport of liquid, and are commonly described as Janus-type materials.[23, 102-104] The name origins from the two-faced Roman god of beginning and ending, doors, and gates in the Roman mythology.[23] Thus, bipolar membranes also represent Janus-type materials, as they consist of negatively charged areas next to positively charged areas along the pore axis. Early fabrication and utilization of Janus materials have been inspired by the desert beetle, which is able to survive by collecting water from humid air by using hydrophilic bumps on a hydrophobic surface.[105] The first example of Janus materials was demonstrated by *Casagrande* et al. in 1989.[106] In this study, Janus particles were obtained by side specific hydrophobization of spherical glass particles with octadecyltrichlorosilane resulting in particles with a hydrophilic hemisphere and a hydrophobic hemisphere that showed different behavior at an oil/water interfaces as compared to polar or apolar particles. Early examples of Janus membranes focused on directional transport of liquid.[102] One of the first example of nanoporous Janus interface materials showing a preferential transport direction of water was demonstrated in 2010 by *Wang* et al.[107] In this study, a polyester fabric was first modified by a superhydrophobic layer containing TiO_2 and hydrophobic silica NPs, followed by UV exposure of only one side of the hydrophobic fabric leading to a hydrophilic side, thus an asymmetric wettability through the fabric thickness was created. Directional water transport through the Janus membrane was observed, when a water drop was placed on the hydrophobic side. Placing a water drop on the hydrophilic side lead to spreading of the drop, but no transport through the membrane occurred. Likewise, Lim et al. generated a Janus membrane by electrospinning of hydrophobic polyacrylonitrile (PAN) fibers mixed with tetraethylorthosilicate (TEOS), followed by a heat treatment to imply superhydrophilicity, and subsequent electrospinning of the identical PAN-TEOS solution.[108] There, water imbibition occurred on the superhydrophilic side, whereas water was repelled on the superhydrophobic side. Furthermore, *Jiang* and co-workers published a theoretical study in 2011, in which molecular dynamics (MD) simulations were utilized to demonstrate preferential water transport direction through carbon nanotubes (CNTs) asymmetrically modified with hydrophilic groups (-COOH) at one tip and hydrophobic groups (-CF$_3$) at the other tip.[109] *Tian* et al. extended the theoretical observation of directed liquid transport by a membrane model composed of spaced microcylinders with a wettability gradient along the thickness and concluded that a critical breakthrough pressure can be improved by reducing the spacing ratio of the cylinder membrane along with increasing the wettability gradient.[110] A highly

sophisticated study was demonstrated by *Jiang* and co-workers in 2012, in which a Janus membrane was formed by sequential deposition of hydrophobic polyurethane (PU) fibers and hydrophilic cross-linked poly(vinyl alcohol) fibers via electrospinning governing water transport from the hydrophobic side to the hydrophilic side.[111]
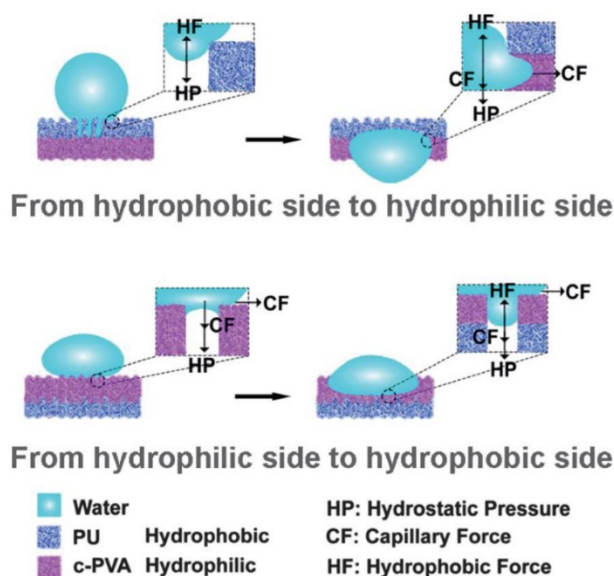
Figure 2: Proposed mechanism of unidirectional water penetration through a Janus-type membrane. Reprinted from Ref. 111 with permission from the Royal Society of Chemistry.

In this study, the hydrostatic pressure in dependence of the layer thickness of the fibrous films, respectively, were investigated and a mechanistic model for the observed preferential water transport direction was postulated (**Figure 2**): a water drop on the hydrophobic side suffers from two opposite forces, the hydrostatic pressure (HP) and hydrophobic force (HF). The HF tends to prevent the waters downward penetration, which is provided by the HP. With increasing HP, i.e. increasing the drop volume, the water drop goes deeper, while the HF is constant. Once the penetration depth reaches the thickness of the hydrophobic layer, water will contact the lower hydrophilic layer, and water penetrates due to the capillary force provided by the hydrophilic layer along with the HP. Contrary, if the water drop is on the hydrophilic side, spreading occurs due to capillary effects, and the HF prohibits water penetration once water reaches the interface.[111]

Since the last decade, many fabrication and modification techniques have been introduced to generate asymmetry in nanoporous materials.[18, 23, 41, 100, 102-104] In most cases, these techniques apply for both ionic diodes with asymmetric surface charge pattern and liquid diodes with asymmetric surface wettability. The latter is related to multipore Janus-type materials, and has, to the best of my knowledge, not been experimentally demonstrated for single nanopores or

single nanochannels. In the following chapter, several techniques for the generation of asymmetric charge pattern and asymmetric surface wettability are summarized and categorized into asymmetric fabrication and asymmetric modification. By that, selected publications will be highlighted.

2.1.1. Asymmetric fabrication

The sequential deposition of materials with opposite wettability, opposite charge or heterogeneous chemical nature is a common way for asymmetric nanoporous material fabrication (**Scheme 1**).
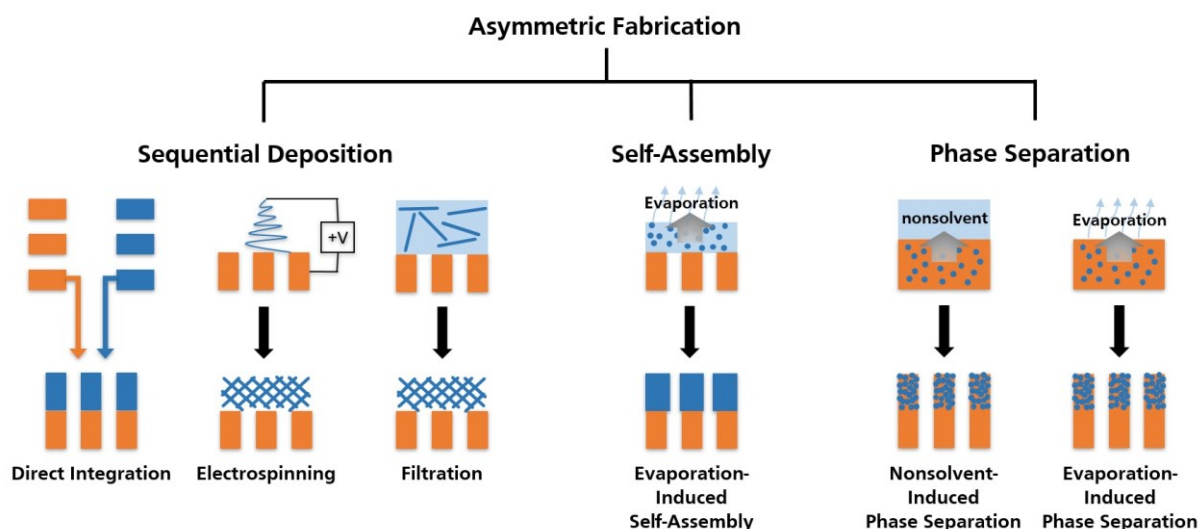
Scheme 1: Schematic illustration of asymmetric fabrication routes for the generation of ionic diodes and Janus-type membranes. Reproduced and adapted with permission from Ref. 104. Copyright 2020 Wiley.

For example, *Cheng* and *Guo* constructed bipolar diodes with positively and negatively charged zones obtained lithographically in inorganic materials by generating a junction between a positively charged Al_2O_3 and negatively charged SiO_2 channel in 2009.[28] Due to the high charge density on the pore walls and small pore height of 20 nm, the highest rectification ratio for ionic diodes of 300 at 1 mM KCl was reported by that time. *Wu* et al. further investigated the combination of Al_2O_3 and SiO_2 with respect to ICR by sequentially depositing amorphous silicon and aluminum by sputtering and evaporation, respectively, followed by applying a pattern transfer of self-organized anodized aluminum oxide (AAO) to generate a Al_2O_3-SiO_2 hetero-structured nanopore membrane, which behaved as a parallel array of ionic diodes with ICR at relatively high salt concentration and low aspect ratios compared to previous approaches.[112] Sequentially electrospinning allows the deposition of hydrophobic fibers onto hydrophilic fibers

and vice versa to generate Janus-type membranes with opposite surface wettability.[111, 113-117] Furthermore, electrospinning can also be applied to deposit a fibrous matt of a certain wettability onto a porous substrate with opposite wettability. For example, *Zhou* et al. very recently generated a Janus membrane by depositing fibrous hydrophobic polyvinylidene fluoride via electrospinning on a hydrophilic cellulose acetate membrane and realized outstanding forward osmosis performance as compared to state-of-the-art thin film composite membranes.[118] Similar to sequential electrospinning, Janus-type membranes with opposite surface wettability can be generated by sequential filtration.[119-120] For example, *Zhang* et al. reported in 2014 the formation of a heterogeneous membrane by sequential filtration of MnO_2 nanowires and $CaWO_4$ nanowires.[121] The heterogeneous nanochannels showed versatile biomimetic properties: Initially, the bilayer was hydrophilic carrying negative surface charges and water was able to penetrate from both directions. At low salt concentration, thus large electric double layer, positively charged ions were attracted and negatively charged ions were depleted from the membrane. When the $CaWO_4$ layer was changed to a hydrophobic state, pH gated ionic transport properties were observed. Moreover, by changing both layers to a hydrophobic state, voltage-gated channels were obtained. Another preparation of ionic diodes is represented by sequential deposition of oppositely charged NPs. In 2010, *Lei* et al. loaded one side of an inverse-pyramid-shaped micro cavity of a silicon substrate with negatively charged hydroxyl carrying silica particles and loaded the cavity on the other side with positively amine bearing silica NPs to realize an ionic diode.[122] Based on polystyrene stabilized gold NPs, *Rao* et al. firstly introduced free-standing asymmetric bilayered NP superlattice nanosheet membranes with diode-like ion transport behavior in 2015.[123] Thereby, the bilayer forms a conically shaped gap between three adjacent NPs, which can be tuned by varying the size of the NPs. Interestingly, it was demonstrated in theory and experiment that the asymmetric ion transport can be regulated by the NP's size.[123] A quite simple and low-cost approach to fabricate asymmetry in geometry, surface wettability or surface charge is the direct integration of heterogeneous materials. For example, *Cao* et al. built a fog collector by simply combining a hydrophobic copper mesh with hydrophilic cotton in 2015.[124] Similarly at the same time, *Meng* et al. combined PET track-etched polymer foils with columnar nanochannel arrays varying in size or in surface charge.[125] Thereby, modification of the PET nanochannel with histidine, which is either negatively or positively charged or neutral depending on the pH, allowed converting the bichannel from a nanofluidic diode to a normal nanochannel or to a reverse diode by changing the pH values, thus changing the surface charge polarity or charge density. By the same time, Zhang et al. demonstrated the combination of PET track-etched conically shaped nanochannels with a porous block co-polymer (BCP) membrane by deposition of a BCP solution

onto the PET film via spin coating, which then formed an asymmetric membrane by microphase separation (**Figure 3a**).[126] Due to the pH dependent negatively charged surface carboxyl groups of the PET membrane and the positively charged poly(4-vinylpyridine) groups inside the BCP membrane's pores, a heterogeneous anion-selective membrane with rectification ratios up to 1075 at 10 mM KCl was built, which was supported by numerical simulations. Furthermore, the dependence of the BCP membrane's thickness on the rectification ratio of the asymmetric membrane had been investigated in simulations, in which a maximum rectification ratio of 1100 was determined for a BCP membrane thickness of 100 nm that rapidly decreased with increasing BCP thickness demonstrating the relevance of implementing ultrathin membranes for the improvement of ion transport properties (**Figure 3b**). In addition, a potential application as concentration-gradient-driven energy harvesting device had been demonstrated.
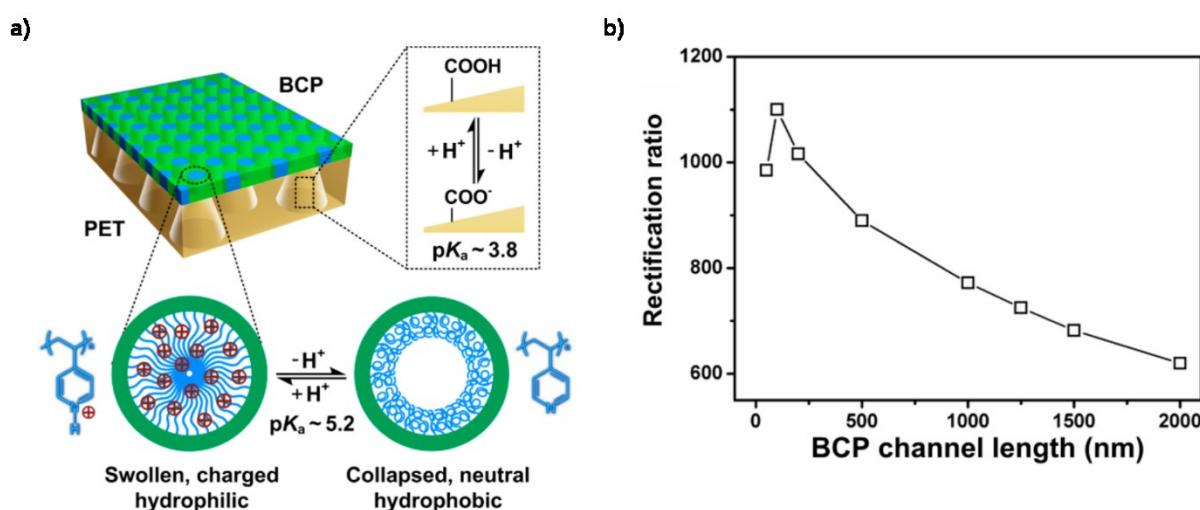
Figure 3: a) Schematic representation of an asymmetric heterogeneous ionic diode membrane composed of a pH-responsive porous BCP membrane and pH-responsive porous PET membrane with conical nanochannels. b) Influence of the BCP nanochannel length on the theoretical rectification ratio. Reprinted with permission from Ref. 126. Copyright 2015 American Chemical Society.

The same group recently supported their findings by building ultrathin bipolar nanofluidic diodes of approximately 500 nm thickness prepared by sequential deposition of two different BCP membranes.[127] BCP membranes have further been combined with inorganic AAO membranes to form ionic diodes for osmotic energy conversion that showed ionic rectification of a broad pH range due to the synergistic effect of carboxyl groups from the BCP and hydroxyl groups of the AAO, which was also supported by numerical simulations.[128] Although these approaches appear simple and low-cost, and clear boundaries between different layers are obtained, one might consider weak interfacial bonding between the heterogeneous building parts due to incompatibility, particularly when hydrophobic and hydrophilic materials are

combined.[104] In terms of Janus materials with opposite surface wettability, interfacial incompatibly could be avoided by applying nonsolvent-induced[129-132] or evaporation-induced phase separation strategies[133, 104]. In terms of ionic diodes, interfacial bonding can be enhanced by deposition of a precursor sol on a porous substrate to form heterogeneous membranes. For example, *Zhang* et al. combined TiO_2 and Al_2O_3 by spin coating a precursor sol of TiO_2 onto AAO membranes, whereby the immobilization of TiO_2 was achieved by oxygen bridge bonds produced by the hydrolysis of the TiO_2 precursors with the surface hydroxyl groups of Al_2O_3.[134] In this study, the surface of the bichannels were functionalized with octadecyltrimethoxysilane (OTS), which lead to hydrophobization of the channel's surface, and subsequently irradiation of the sample with UV light induced a TiO_2 photocatalyzed and irreversible decomposition of OTS leading to a shortening of the OTS molecules and formation of negatively charged carboxyl groups. Thus, the generation a Janus-type unipolar ionic diode membrane was realized in consequence of wettability conversion and asymmetric surface charge distribution through UV irradiation in the TiO_2 regions. Although the charge density and ICR performance could be increased by longer UV irradiation time, the thickness of the hydrophilic and charged layer was determined by the deposited TiO_2 layer. At the same time, *Gao* et al. reported a membrane-scale rectifying ionic diode for energy harvesting from salinity gradient in natural waters by combining ultrathin mesoporous carbon and AAO membranes through spin coating a mesoporous carbon precursor sol onto AAO.[135] Thereby, numerical simulations were applied to investigate the relative length of the negatively charged and positively charged zones in the ionic diode concluding that the highest rectification ratios are observed for a length percentage range of 20-40% of the negatively charged layer (**Figure 4**).
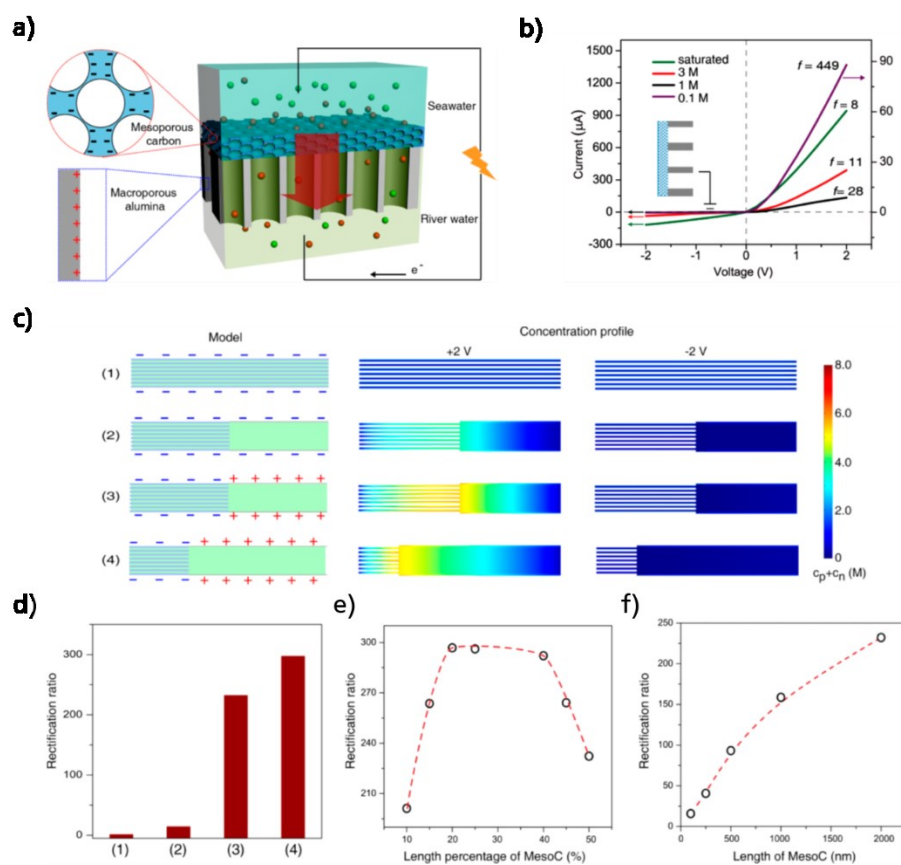
Figure 4: a) Schematic representation of an ionic diode membrane based on mesoporous carbon on top of macroporous alumina. b) Current-voltage curves of the ionic diode membrane at salt concentrations of 0.1 M (magenta), 1 M (black), 3 M (red), and at saturated salt concentration (green). c-d) Numerical simulation of the concentration profile inside the nanochannels and resulting rectification ratios for symmetric nanochannel configuration (2), and after introducing structural (2), electrostatic (3), and length asymmetries (4). e) Calculated rectification ratios of the ionic diode membrane in dependence of the length percentage of mesoporous carbon nanochannels, whereas the total length of the heterogeneous nanochannels is set to be 4000 nm. f) Calculated rectification ratios in dependence of the length of mesoporous carbon nanochannels, whereas the length percentage of the mesoporous carbon channels is set to be 50%. Reprinted with permission from Ref. 135. Copyright 2014 American Chemical Society.

Concluding, several approaches of asymmetric fabrication to generate nanoporous interfaces with asymmetric surface charge or wettability for directional transport of ions or liquids, respectively, have been demonstrated with the advantage of low-cost, fast and simple preparation protocols. However, a significant drawback could be the incompatibility and thus bad interfacial bonding between different layers. To overcome this issue, some alternatives are available for both ionic and liquid diode-like membranes, as discussed above. Furthermore, manifold asymmetric modification approaches of nanoscale pores and channels have been demonstrated in the last decade, which will be discussed in the following.

2.1.2. Asymmetric modification

Most of asymmetric modification techniques of nanoporous interface materials such as membranes are based on single side modification (**Scheme 2**).
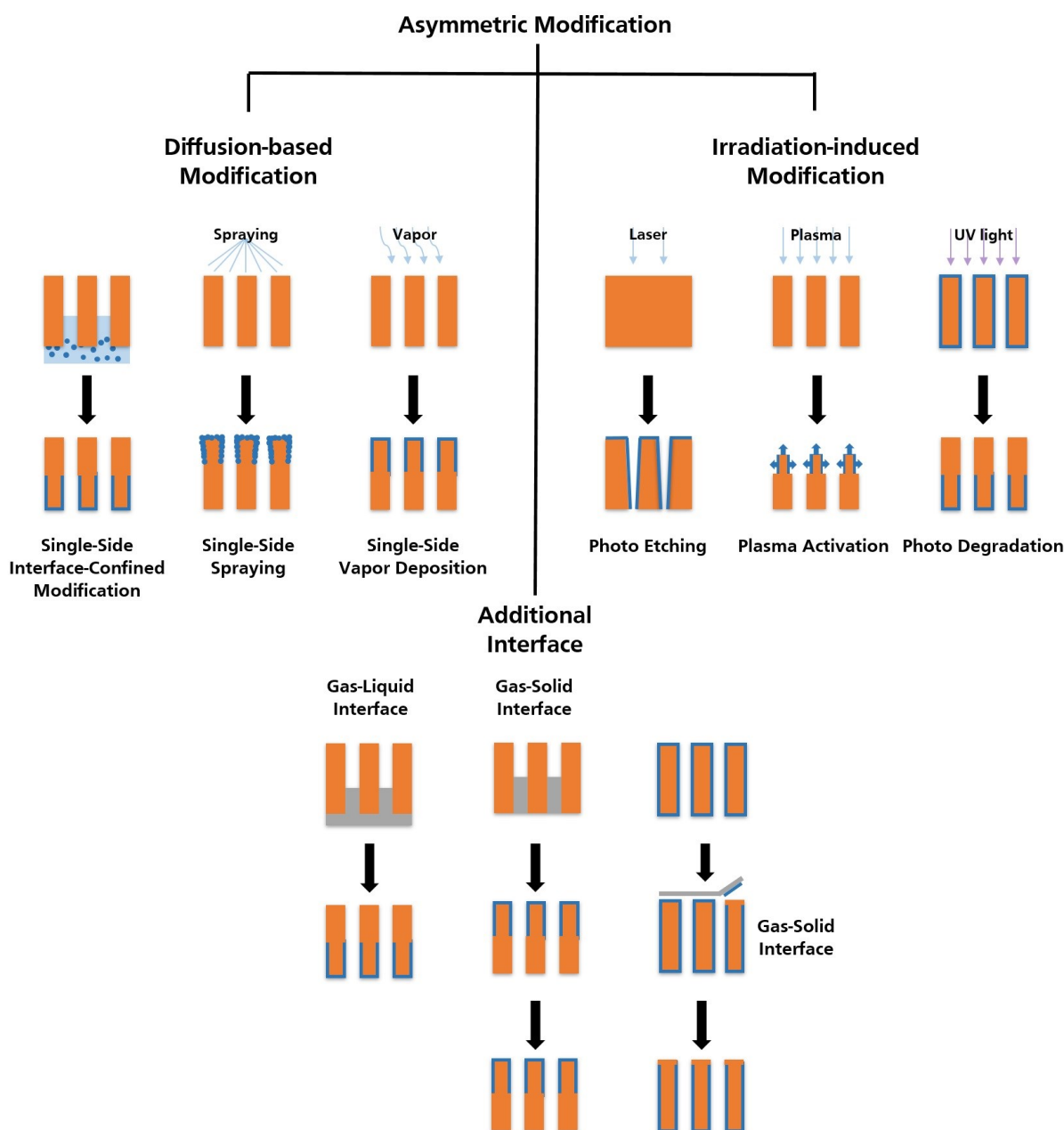
Scheme 2: Schematic illustration of asymmetric modification routes for the generation of ionic diodes and Janus-type membranes. Reproduced and adapted with permission from Ref. 103. Copyright 2018 Wiley. Reproduced and adapted with permission from Ref. 104. Copyright 2020 Wiley.

The earliest example is represented by diffusion limited modification introduced by *Karnik* et al.[95] in 2006 and experimentally applied by the same author to build unipolar ionic diodes with

asymmetric charge distribution[94], as well as by *Vlassiouk* et al.[93] for the generation of bipolar ionic diodes, which has been discussed earlier. *Ma* et al. advanced the single side modification method applying a half-cell-reactor for asymmetric modification of AAO membranes in 2014 by simultaneous chemical polymerization reactions on both sides of the membrane combining ATRP, dopamine self-polymerization (DOP-SP) and ROMP to generate double hydrophilic bipolar, temperature and pH-responsive polymer brush modified asymmetric AAO nanochannels.[136] Parallel processes can also be performed in electrochemical approaches. By placing a hydrophobic membrane parallel to an anode and cathode, *He* et al. developed an electric-field-driven asymmetric deposition of polydopamine (PDA) and various polyelectrolytes on hydrophobic membranes with short deposition times to generate Janus-type membranes with opposite wettability introduced in 2016.[137] Very recently, *Herzog* and *Nau* et al. demonstrated a facile fabrication of Janus-type membranes with opposite wettability by controlling the diffusion and evaporation of a silica precursor sol in paper-based membranes based on controlling the environmental pressure in the drying and curing process of silica, respectively.[22] Other diffusion defined asymmetric functionalization processes of porous materials are represented by single side spray coating techniques, which are dependent on the relative pore size of the membranes and the drop size.[103, 138-139] Similarly, asymmetric modification of membranes can be achieved by single side exposure of the interface to modification reactants applying chemical vapor deposition (CVD)[140-142] as well as atomic layer deposition (ALD)[143-144]. For example, *Tian* et al. generated a Janus-type membrane with opposite surface wettability by side specific exposure of a hydrophilic cotton membrane to the vapor phase of a fluorinated silane allowing the selective transport of water or oil, respectively, thus enabling the application for oil-water separation.[141] Thereby, the modification depths could be controlled by the exposure time of the membrane to the vapor phase. An interesting study has been published by *Yang* et al. in 2017 that implemented the asymmetric modification by side specific CVD to generate a nanoporous Janus-type membrane by depositing a hydrophobic layer of polydimethylsiloxane (PDMS) on a hydrophilic nanoporous silica membrane.[142] By investigating the transport properties of ions through the membrane applying cyclic voltammetry, cation-selective unidirectional transport from the hydrophobic to the hydrophilic side was observed at basic pH and low ion concentration, thus demonstrating that the hydrophobic force of the PDMS layer can be overcome through electrostatic attraction of the negatively charged surface of silica underneath in dependence of pH and salt concentration, which affects the thickness of the electric double layer. Recently, *Tufani* et al. extended the CVD approach to selectively deposit two different polyelectrolytes on different sides of an AAO membrane by sequential and side specific initiated CVD (iCVD), and thereby built a cooperative

pH responsive gating membrane enabling the transport of proteins in one favored direction demonstrating the application as drug delivery device with controlled release of biomolecules (**Figure 5a**).[145]
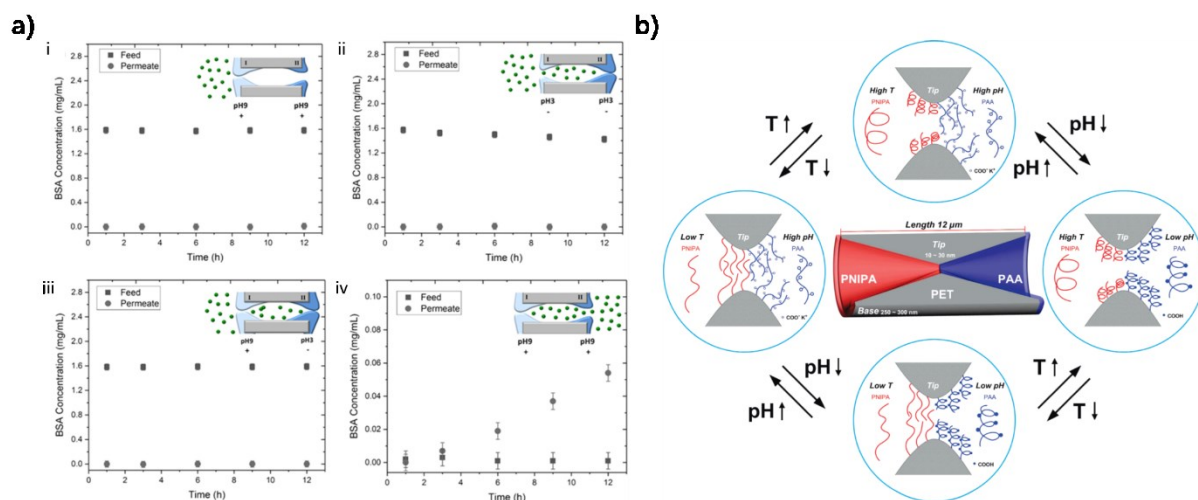
Figure 5: a) Demonstration of directed protein transport through a double pH-responsive membrane showing the concentration of bovine serum albumin (BSA) as a function of time and pH values of feed and permeate. Reproduced and adapted from ref. 145, Copyright 2019, with permission from Elsevier. b) Schematic illustration of open and closed states of a single hourglass-shaped PET nanochannel modified with the temperature-responsive polymer poly(*N*-isopropylacrylamide) (red) and pH-responsive polymer polyacrylic acid (blue) in dependence of temperature and pH. Reprinted with permission from Ref. 74. Copyright 2010 American Chemical Society.

In analogy to the latter strategy, side specific/asymmetric deposition of polymers has been already introduced in the early years of ICR diodes using plasma-induced graft polymerization. In 2010, *Hou* et al. functionalized the two different sides of an hourglass-shaped PET nanochannel with the temperature responsive polymer poly(*N*-isopropylacrylamide) (PNiPAM) and the pH responsive polymer polyacrylic acid (PAA), respectively, using plasma-induced graft polymerization, allowing both temperature and pH control over asymmetric ionic transport properties (**Figure 5b**).[74] Implementing this strategy, *Jiang* and co-workers built a biomimetic ion pump by functionalizing the tip ends of a cigar-shaped PET nanochannel with polyvinylpyridine (PVP) and PAA, respectively, by sequential plasma-induced graft polymerization (**Figure 6**).[35] The cooperative pH responsive double gate nanochannel realized three key ionic transport features of biological ion pumps including alternating gates ion pumping under symmetric pH stimuli, transformation to an ion channel under asymmetric pH stimuli, i.e. disparate pH values at the different sides of the nanochannel, and ion pumping under both symmetric and asymmetric pH stimuli. Based on this architectural principle, the same group reported a biomimetic ion pump with a more complex architecture by combining

direct integration of a BCP membrane bearing pH responsive PVP pores with a PET membrane with conically shaped channels, which tip ends were functionalized with the pH responsive PAA, demonstrating high anion selectivity and unidirectionality.[36]
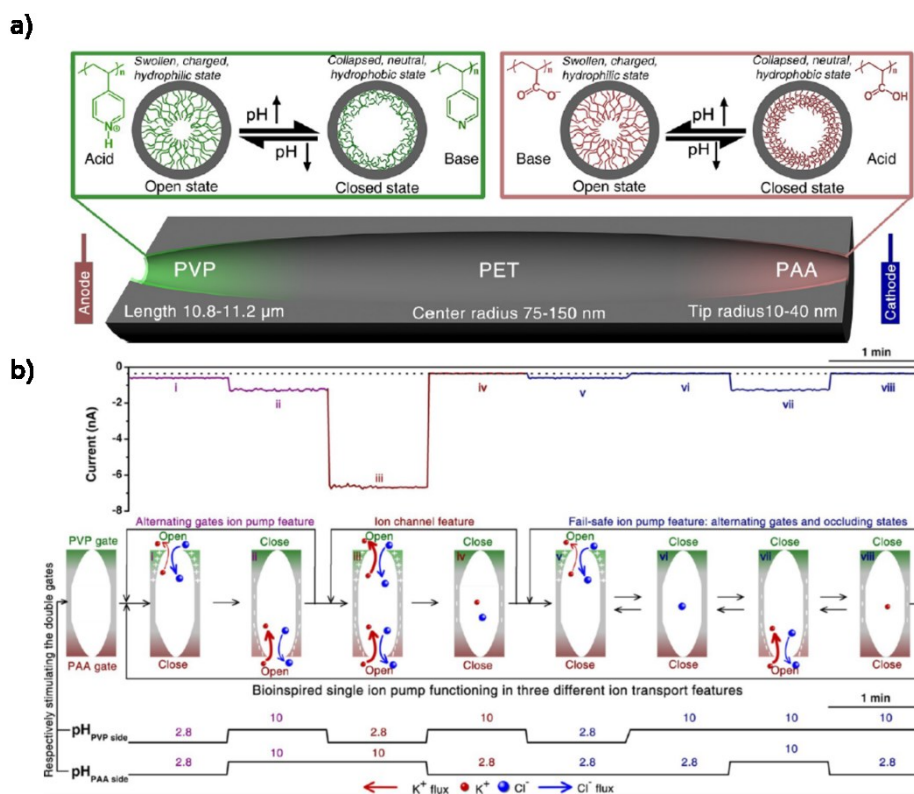
Figure 6: Schematic representation of the cooperative pH responsive double gate PET nanochannel modified with acid-driven PVP gate and base-driven PAA gate respectively immobilized on the tip sides of the nanochannel. b) Ion current states (top) and corresponding schematic representation of ion transport processes (mid) of three ion transport features (alternating gates ion pump feature, ion channel feature, and fail-safe ion pump feature) resulting from switching the pH values of PVP and PAA sides of the nanochannel, respectively (bottom). Reprinted with permission from Ref. 35. Copyright 2013 American Chemical Society.

In addition to diffusion-based asymmetric modification, radiation can also be applied asymmetrically to introduce asymmetry in nanoporous materials, since most of membranes are opaque, thus radiation through the material is limited. Therefore, hydrophobic membranes can easily converted to Janus-type membranes with opposite wettability by single-side photodegradation[20, 146-147] and photoetching[148-149] through energy irradiation.[104] One of the early examples has been introduced by *Lin* and co-workers in 2010, which first modified a hydrophilic membrane with a hydrophobic coating and subsequent degradation of the hydrophobic layer with UV by single-side irradiation to generate opposite wettability, as has been discussed earlier.[107] Generally, hydrophobic surfaces can be in situ converted to hydrophilic amino and hydroxyl bearing surfaces by direct activation using a plasma of nitrogen

and oxygen, respectively.[104, 150-152] Contrary, *Gu* et al. applied UV radiation to functionalize CNT membranes with hydrophilic poly(*N,N*-dimethylaminoethyl methacrylate) and hydrophobic polystyrene on each side, respectively, sequentially applying self-initiated surface photopolymerization and photografting (SIGP).[153] The resulting Janus-type membrane with opposite surface wettability showed side-selective oil/water transport able for selective oil/water separation, even from surfactant stabilized emulsions. Similar results were obtained by *Wang* et al., who applied SIGP on a cotton fabric.[154] Although energy-based irradiation holds the control of modified thickness through radiation time or etching time, mostly energy sources such as lasers and UV are utilized, and a structural damage of the materials from the high-energetic light or plasma have to be considered. In terms of the fabrication of Janus-type membrane with opposite surface wettability by asymmetric modification, an interesting approach based on creating an additional interface evolved recently. For example, *Yang* et al. created asymmetric wettability by a mussel-inspired, controllable, single-side deposition strategy with a gas-liquid interface, particularly air-water interface.[155] Thereby, a hydrophobic polypropylene (PP) membrane was placed on an aqueous solution containing dopamine and polyethyleneimine (PEI) creating a stable air-water interface due to the hydrophobicity of the PP membrane, thus deposition/modification of PDA and PEI only occurred on the wetted surface of the membrane. Based on this strategy, hollow fiber membranes were also modified by circulating the modification solution in the lumen side of the membrane.[156] Thereby, the depth of the hydrophilic layer could be controlled by the deposition time. *Lee* et al. demonstrated asymmetric modification of an AAO membrane by first infiltration of the membrane with a photoresist, followed by air plasma etching and subsequent grafting of fluorinated silanes at the exposed surface, thus utilizing a gas-solid interface.[157] In principle, the depth of removed photoresist, thus the thickness of the hydrophobic layer could be adjusted by the etching time.[103] Vice versa, *Wang* et al. obtained Janus-type membranes with opposite surface wettability by a "peel-off" process.[21] Thereby, a hydrophobic polytetrafluoroethylene membrane was coated with PDA and subsequently removed from one side of the membrane by using an adhesive tape, thus creating a gas-solid interface. However, thickness control of the hydrophilic or hydrophobic layers could not be adjusted by this method. The asymmetric modification methods presented above are versatile and offer several techniques for the fabrication of ionic and liquid diode-like nanoporous interfaces/materials from organic and inorganic substrates, and further allow thickness control of the functional layer in most cases. Concluding, asymmetry in nanoporous interfaces can be generated via asymmetric modification of as-prepared interfaces utilizing several approaches from diffusion-based modification to energy irradiation induced modification based in single-side exposure to modifiers or radiation.

Furthermore, asymmetric modification can also be accomplished by creating an additional interface. Added together, the functionalization strategies presented are mainly combined with stimuli-responsive polymers, as they can provide high function density and responsiveness to common stimuli, such as pH, temperature, light or voltage allowing to gate molecular transport.[158] Nevertheless, most of the nanoporous interfaces presented so far are based on bifunctionality and, as we know, biological paragons are more complex with respect to their architecture and asymmetrically distributed functional patterns. However, bifunctionality cannot be overcome by the approaches of asymmetric modification of nanoporous interfaces presented above in consequence of the synthetic protocols, i.e. single-side modification of as-prepared interfaces. In addition, precise placement of functionalities, e.g. polymers, inside a pore or channel with spatial control along the pore or channel axis and nanoscale precision cannot yet be achieved.

An interesting approach to place more than two functionalities in a nanochannel with spatial control has been introduced by *Voelcker* and co-workers in 2010, which functionalized the pore surface of an AAO membrane by a series of anodization and silanization cycles with hydrophobic pentafluorophenyldimethylpropylchlorosilane, amine group bearing (3-aminopropyl)triethoxysilane (APTES), and polymeric *N*-triethoxysilylpropyl-*O*-polyethyleneoxide urethane, respectively, achieving a range of functionalities and wettabilities.[159] Adapting this approach, *Li* et al. prepared an ionic diode applicable over a broad pH range by modifying half of the AAO channels with the amine group bearing 3-aminoprolytrimethoxysilane concluding that the rectification ratio is mainly determined by the nanochannel size and less sensitive to the patterned length of the amine groups.[31] Applying this functionalization strategy, *Wu* et al. studied the ICR of AAO membranes in theory and experiment in dependence of multiple arrays of bipolar regions, negatively charged Al_2O_3 and positively charged amine groups of covalently bound APTES defined as one tandem unit, along the pore axis, in combination with a multiple number of parallel nanochannels very recently.[34] Thereby, a nonlinear increase with tandem number is observed, while the ICR ratio of parallel bipolar circuits rapidly decreased with the parallel number mainly governed by the interfacial resistance induced by the overlap of ion concentration polarization regions. Nevertheless, the approach of alternating anodization and silanization can be quite time consuming and functionalization after the first couple of layers might be limited due to interactions of modifiers and already modified regions. Furthermore, the thicknesses of functionalized layers are on the microscale and function placement at the nanoscale has, to the best of my knowledge, not yet been reported utilizing this or similar approaches.

To further advance the performance of technological porous materials, precise placement of responsive functionalities along nanoscale pores – ideally together with compartmentalization - is required, but still remains experimentally challenging with respect to nanoscale resolution.[12-13] This has thoroughly been investigated by *Szleifer* and co-workers using molecular theory to understand the behavior of polymers in nanoscale confinement,[160] and to demonstrate the importance of spatial charge distribution for transport direction, which can, for example, be controlled by the polymer chain's architecture.[161] Very recently, *Szleifer* and co-workers applied equilibrium and nonequilibrium molecular theories to investigate the molecular organizations and transport properties of an asymmetric nanopore, which inner wall is coated with an asymmetric weak polyampholyte brush whose main component changes gradually from acidic to basic along the axis of the pore.[162] Thereby, they concluded that the asymmetric charge pattern turns the nanopore into an ionic diode with a rectification factor above 1000 at optimized pH and salt concentration. Furthermore, the nanopore behaves like a double-gate nanofluidic device with pH-triggered opening of the gates, which can serve as an ion pump and pH-responsive molecular filter.

Hence, the key factors for biomimetic transport of mass and charge through synthetic nanopores and nanochannels rely on asymmetries in pore geometry, surface charge pattern as well as surface wettability. Thereby, nanoscale function placement as well as thickness control at the nanoscale are required to enhance the overall performance, which still remains challenging.

Approaches to overcome the thickness limitation of function placement in nanoscale pores might be related to nanoscale layer fabrication in a multilayer architecture and, to further push the limits of function placement, to the utilization of nano-objects that can trigger chemical reactions at the nanoscale, such as gold NPs, which will be discussed in the following.

2.2. Gold nanoparticles as nanoscale source to trigger chemical reactions

Metal NPs, especially gold NPs (Au-NPs) have attracted tremendous attention in research due to their distinct physical and chemical properties making them an attractive platform for the fabrication of novel chemical and biological sensors, as they allow to detect metal ions, small molecules, proteins, nucleic acids, malignant cells, etc. in a rapid and efficient manner.[163-170] In addition, Au-NPs can be synthesized in a straightforward manner with high stability possessing a high surface-to-volume ratio and excellent biocompatibility by application of appropriate ligands.[163] Au-NPs feature surface plasmon resonance (SPR), a result of collective oscillation of the conduction electrons across the NPs due to resonant excitation by interaction with incident light. Upon oscillation, these electrons, which are confined in three dimensions, create an

electromagnetic field near the NPs' surface which energy intensity is enhanced as compared to the incident light.[171] The SPs allow to amplify, concentrate and manipulate light at the nanoscale, overcoming the diffraction limit of traditional optics and increasing the resolution and sensitivity of optical probes.[172] Therefore, Au-NPs can be used in a wide range of applications, such as biomedical[173-175], energy[176-178], environment protection[179-181], and information technology[172, 182]. Consequently, and most important for the here discussed local porous material functionalization, Au-NPs allow to trigger (photo)chemical reactions on the nanoscale, which will be further discussed below.

After plasmon resonance was mainly applied in sensing applications, many photochemical reactions induced by the enhanced electromagnetic field of plasmons have been studied, mainly in the context of surface enhanced Raman scattering (SERS), in which the Raman scattering signal from molecules leaving the surface of metal NPs is enhanced.[183-185] SERS further allows to monitor plasmon enhanced photochemical reactions, for example, *Sun* et al. probed the plasmon enhanced in situ chemical reaction of 4-nitrobenzenethiol dimerization applying vacuum tip-enhanced Raman spectroscopy.[186] The phenomenon of plasmon-enhanced photochemical reaction is accompanied with physical effects, such as optical near-field enhancement, heat generation, and excitation of hot electrons. Therefore, plasmonic NPs can behave as efficient nanosources of heat, light or energetic electrons controllable by light to boost the yield of chemical reactions as well as improving their spatial and temporal control.[187] By that, several mechanisms can be considered: thermal-induced reactions enhanced by temperature increase around plasmonic NPs, light concentration enhancing incident photon rate experienced by nearby reactants, hot electron created by photon absorption and transfer to adjacent reactants, photocatalytic activity enhanced by temperature increase, catalytic activity enhanced by optical field enhancement at the catalytic location, and hot electron transfer from plasmonic NPs to a catalyst (**Figure 7**).[187]
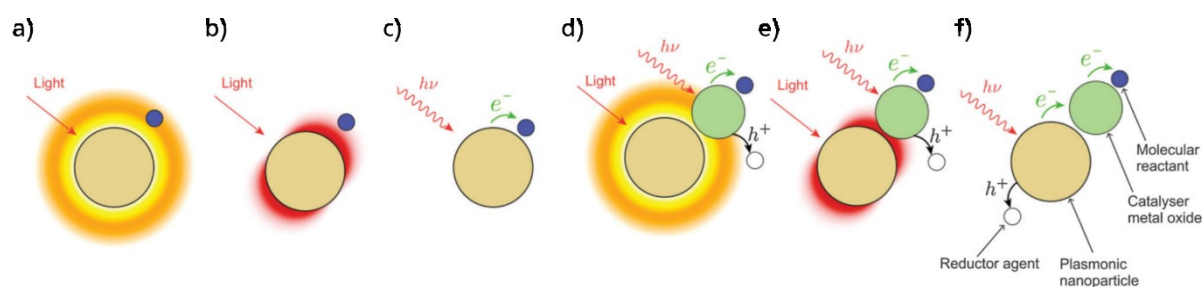
Figure 7: Main physical mechanisms involved in plasmon-assisted chemistry. a) photo-induced temperature increase of the NP provides heat to an adjacent reactant. b) enhancement of the optical near-field at the vicinity of the NP increases the photon rate seen by an adjacent reactant. c) a photo-induced electron is transferred to a nearby reactant. d) the electron-hole generation rate in a photocatalyzer is enhanced by heat generated by the NP. e) the electron-hole generation rate in a photocatalyzer is enhanced by the strong optical near-field of the plasmonic NP. f) the photocatalyst adjacent to the NP is activated by hot electron transfer from the plasmonic NP. Reproduced and adapted from Ref. 187 with permission from the Royal Society of Chemistry.

Photochemical reactions are thus promoted by providing more photons per unit volume, along with control over the reactions down to the nanometer scale. Thereby, an efficient photochemical reaction field can be efficiently build by excitation of SPs induced at the surface of metallic NPs.[188-189] The electromagnetic field enhancement is thought to be a result of localization of electromagnetic field along the incident polarization direction and plasma oscillation, and is 10-100 times larger than the incident electromagnetic field intensity depending on the size and shape of plasmonic nanostructures.[190] A much larger enhancement can be achieved by the interaction between NPs, when two or more plasmonic NPs are in close proximity at a distance of several nanometers, a phenomenon known as dipole coupling.[191] Thereby, the electromagnetic field enhancement increases with decreasing distance of the plasmonic nanostructures due to concentration of the electromagnetic field in the nanogap space leading to theoretical enhancement up to ~10^5-fold.[192-193] Early investigations of plasmon-enhanced photochemical reactions can be assigned to the visualization of the near-field intensity distribution. *Huber* et al. applied surface plasmon-enhanced photochemical reaction of azobenzene-dye polymer, which was investigated theoretically as well as in experiment.[194] This approach has been applied as powerful tool for the visualization of the spatial distribution of near-field intensity of metallic nanostructures.[195-198] Furthermore, the concept can also be applied oppositely to observe the near-field intensity distribution. For example, *Sundaramurthy* et al. visualized the hot site of bowtie gold structures with a nanogap applying two-photon induced photopolymerization of a negative type photoresist.[199] Besides the visualization of the near-field, this approach is conceptually important, as it demonstrates that non-linear chemical reactions induced by two-photon absorption can be initiated even under continuous instead of pulsed illumination due to the localization of photons at the nanometer scale.[200] In addition to

that, it has also been demonstrated that weak incoherent light sources can be applied for photochemical reactions.[195, 201] Another plasmon-enhanced photochemical reaction that has been investigated is assigned to isomerization reaction. The most prominent example is the isomerization of diarylethene (DE). In 2009, *Tsuboi* et al. demonstrated the ring opening of DE molecules in solution assisted by continuous illumination of Au-NPs and investigated the photochromic reaction quantitatively.[202] There, a two-photon absorption mechanism was proposed, as the wavelength of 800 nm did not match the absorption of the molecules. *Nishi* et al. as well investigated the cycloreversion reaction by applying Au-NPs supporting the DE polymer for quantitative analysis of the photochromic reaction influenced by the near-field intensity distribution.[203] Thereby, the quantity of the poly(DE) on NPs could be precisely controlled. Furthermore, it has been demonstrated that reaction efficiency is affected by the distance of the chromophore from the gold surface by varying the chain length of the DE polymer. Quantitative analysis of the localized surface plasmons of metallic NPs has also been investigated applying photopolymerization by *Deeb* et al.[65] As the light is concentrated to the nanoscale in SPs, nanolithography has been proposed based on near-field lithography overcoming the diffraction limit and transferring nanopatterns to a photoresist film.[204-206] Experimental investigation has been performed by *Srituravanich* et al.[207] and was further demonstrated for nanogap-assisted SP nanolithography by *Ueno* et al.[208] Another promising concept is the imprinting of specific chemical functional groups at predefined locations of metallic nanostructures with nanometer accuracy, firstly illustrated in 2012 by *Dostert* et al., who were investigating the cleavage of nitroveratryloxycarbonyl groups of an organosilane upon pulsed near-infrared (NIR) illumination.[209] There, free amine groups are formed at the tips of gold crescent nanostructures, where the plasmonic field is more intense, by absorption of two NIR photons. After illumination, the samples were then incubated in COOH functionalized gold colloids forming an amide bond with the free amine groups of the gold crescent nanostructures. Another example is the light assisted molecular immobilization, in which disulfide bridges of proteins and peptides are disrupted upon absorption of UV photons by the nearby aromatic amino acids and subsequent immobilization of the proteins or peptides with the generated free thiols to a thiol-reactive substrate. *Galloway* et al. demonstrated the immobilization of proteins with nanometer accuracy in the nanogap of two adjacent Au-NPs applying this plasmonic approach.[210] Another approach for selectively functionalizing the tip ends of gold crescent nanostructures has just recently been demonstrated by *Vogel* and co-workers applying a passivation layer covering the central parts of the nanocrescents followed by thiol functionalization of the tip ends, which are selectively uncovered.[211] Recently, plasmon-enhanced local functionalization has also been demonstrated by plasmon-induced reduction of

aryl diazonium salts.[212-213] Thereby, multifunctionalization of Au-NPs has been achieved by consecutive reduction of two different aryl diazonium salts at two different polarizations of the incident light, respectively.[214]

The context of polymer placement at the nanoscale by utilization of plasmonic NPs has been intensively studied and demonstrated in pioneering works of *Soppera*, *Bachelot* and co-workers.[64-66] For example, *Deeb* et al. utilized silver NPs to induce and study dye-sensitized photopolymerization, a free-radical photopolymerization, and thereby postulated the mechanism responsible for the nanoscale polymer placement (**Figure 8**).[66]
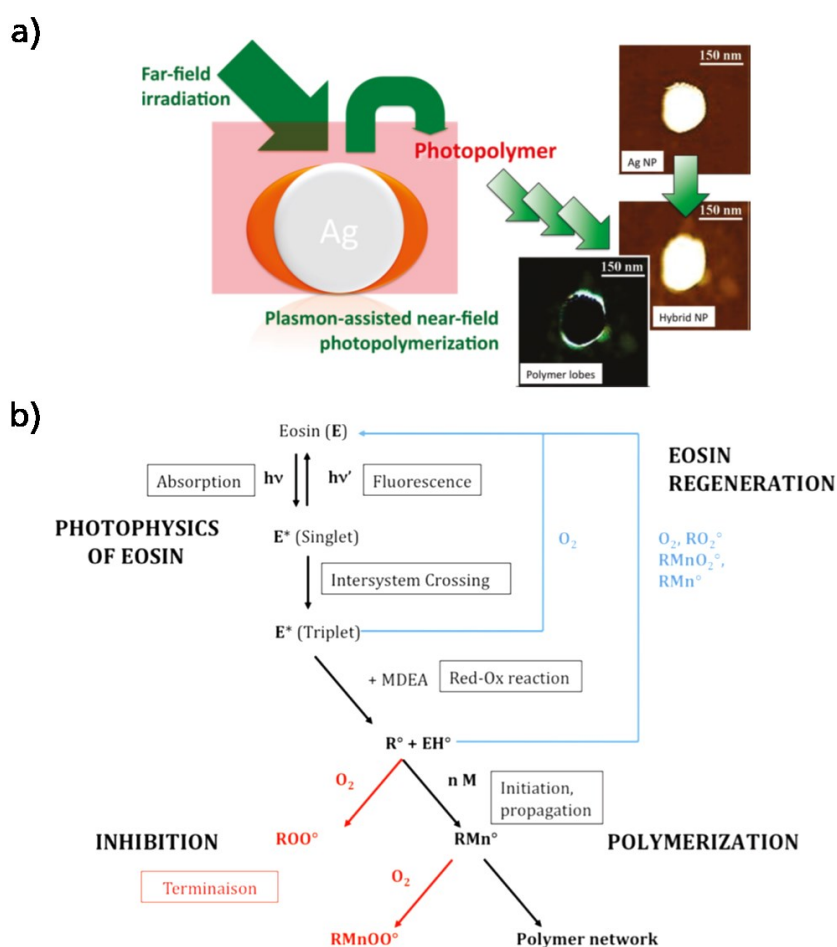
Figure 8: a) Schematic illustration of plasmon induced near field photopolymerization demonstrated by *Deeb* et al. b) Mechanism of plasmon induced dye-sensitized photopolymerization including the polymerization of the methacrylate monomer, the inhibition processes, and the eosin Y regeneration pathways, proposed by *Deeb* et al. Reprinted with permission from Ref. 66. Copyright 2011 American Chemical Society.

Investigation of the dye-sensitized photopolymerization mechanism induced by LSPR has further been studied in depths by *Kameche* et al. very recently.[215] Thereby, a high-resolution characterization method based on transmission electron microscopy (TEM) was developed to

reveal the physicochemical mechanism concluding the photochemical pathway is the main mechanism under the mild irradiation conditions applied. In 2020, *Kameche* et al. extended plasmon induced photopolymerization to living atom transfer radical polymerization demonstrating thickness control at the nanometer scale as well as the possibility to reinitiate the polymerization allowing the architectural design of the polymer shells formed around the NPs.[216] In addition to that, the concept has been further demonstrated for different geometries of plasmonic nano-objects.

Based on the state of the art introduced in this chapter, following research questions have been identified:

- Can MSTFs be combined in multilayer architectures for the generation of nanoporous step gradient architectures with nanoscale dimensions?
- Which method can be used to selectively functionalize a single MSTF with polymer in a multilayer arrangement?
- Which strategies allow precise nanoscopic polymer placement in MSTF architectures?
- How can the nanoscopic polymer placement be verified?

3. Aim and Strategy

In order to advance the performance of technological/artificial nanopores and nanochannels towards the outstanding performance of biological paragons, e.g. a preferred transport direction, complex architectures and advanced modification strategies for the generation of nanopore and nanochannel step gradients are required as indicated in the preceding chapters. To address the research questions concluded from the state of the art, this work is divided into three main sections comprising a material library, mesoporous architecture, and (nano-)local polymer placement as indicated in **Figure 9**.
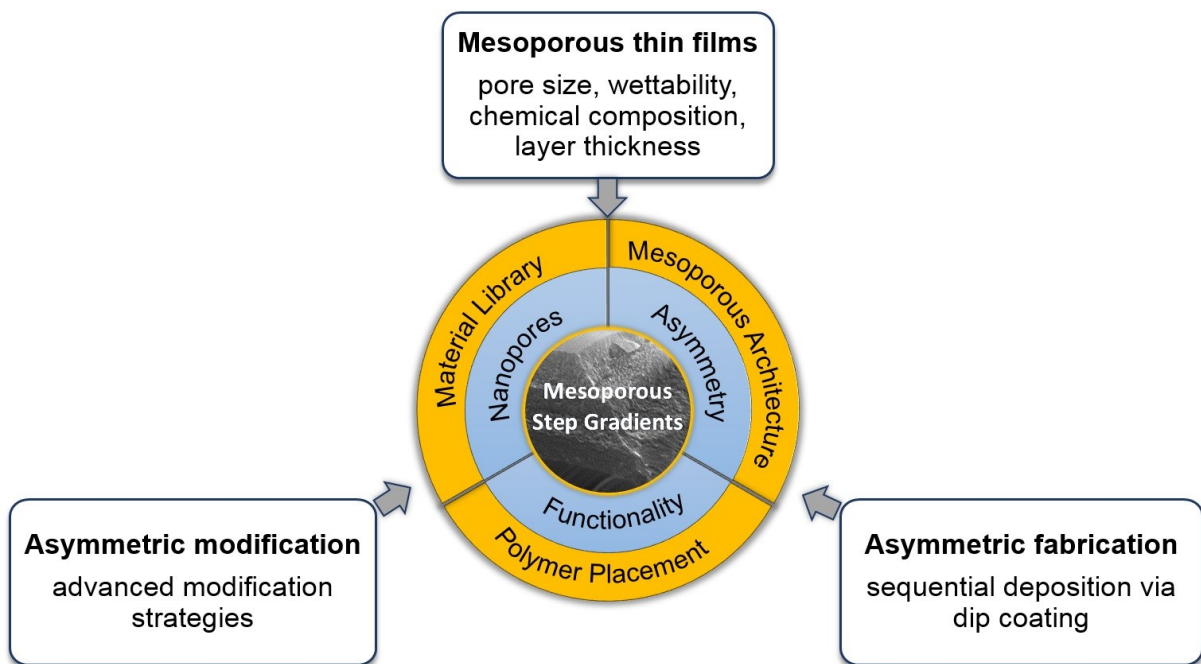
Figure 9: Schematic illustration of the strategic outline of this work.

MSTFs are versatile in pore size and chemical composition, and further allow the combination of such by sequential deposition with adjustable film thicknesses from a few tens up to several hundred nanometers.

The preparation of mesoporous film architectures with step gradients in pore size, surface wettability, and/or charge requires a material library with various MSTFs and a fundamental understanding of physical and chemical properties of multilayered mesoporous thin films. Therefore, hydrophilic MSTFs that exhibit a pore size of 6-8 nm and 8-16 nm according to literature[217-218] respectively were systematically investigated with respect to the ionic pore accessibility in dependence of preparation parameters and the environmental pH of measurement. To realize mesoporous surface wettability step gradients, hydrophilic and hydrophobic MSTFs are needed. For this purpose, MSTFs with tunable surface wettability were

developed by co-condensation of methylated silica precursors with TEOS. In addition, MSTFs with increased chemical stability were developed ensuring the application in harsh conditions, i.e. in basic environment. With respect to sustainable structure directing templates as alternative to petro-based macromolecules, hydroxypropyl cellulose (HPC) was used for the fabrication of MSTFs, which were examined regarding chemical composition, structural properties and ionic pore accessibility.

For the purpose of creating mesoporous architectures with pore size or surface wettability step gradients, MSTFs from the material library were combined by asymmetric fabrication, and the influence of the fabrication in layers was examined. To fabricate a mesoporous pore size step gradient, two hydrophilic MSTFs with different pore sizes were combined. To realize mesoporous surface wettability step gradients, a combination of hydrophilic and hydrophobic MSTFs was chosen.

Mesoporous double layer thin films were then applied to evaluate a suitable functionalization strategy allowing the modification of an individual layer. Thereby, the advantages of well-known functionalization methods of single layer MSTFs were transferred to double layer thin films. In a first step, an asymmetric fabrication of the mesoporous double layer was performed. By that, co-condensation was used to predispose one layer of the double layer architectures with organic groups, which were further selectively modified. Suitable polymerization techniques allowing a layer-selective functionalization of the predisposed layer were then evaluated. For the generation of a mesoporous charge step gradients, photoiniferter initiated polymerization in a layer-selective approach was conducted.

To further investigate the local placement of polymers in mesopores with nanoscale resolution, advanced functionalization strategies are required. For the purpose of nanoscale polymer placement, plasmonic metal NPs were incorporated in MSTFs to serve as nanoscale light source and combined with suitable photopolymerization techniques. Firstly, the preparation of the composite material comprising MSTFs and plasmonic metal NPs was investigated to allow a precise positioning of the plasmonic NPs in MSTFs. Secondly, suitable photopolymerization formulations which could be used in combination with plasmonic metal NPs were then optimized in solution by a colleague within the research group to establish near-field induced polymerizations. The photopolymerization formulations were then applied to functionalize the constructed composite material with polymer at the nanoscale. The results on these approaches are summarized in **Chapter 5**.

4. Methods

In the following chapter, the preparation and functionalization methods of mesoporous silica thin films, which are applied in this thesis are introduced. Furthermore, the versatility of surface modification by polymerization at interfaces are discussed, and photo-induced polymerization techniques that are applied for local placement of functional groups in mesoporous silica thin film architectures are described in detail. Additionally, fundamentals of surface plasmon resonance and the synthesis of plasmonic metal NPs are depicted. As a last point, a theoretic introduction to cyclic voltammetry, which is utilized to investigate the ionic pore accessibility of mesoporous thin films, as well as ellipsometry, which is applied to investigate structural properties of mesoporous thin films, is presented.

4.1. Mesoporous silica thin films and strategies for functionalization

Mesoporous silica materials (MSM) have attracted considerable interest in research due to their high specific surface area, chemical as well as thermal stability,[43] uniform pores in the range of 2-50 nm as classified by IUPAC,[219] and the possibility of functionalization with organic molecules.[42, 220] Naturally occurring porous silica materials are known as zeolites discovered by the Swedish mineralogist *Cronstedt* in 1756 and have been utilized in the 20th century in applications such as molecular sieves, ion exchange for water purification, adsorbents in dishwasher, catalysts, among others.[221-222] However, the pore sizes of zeolites are typically smaller than 1 nm which limits the accessibility of larger molecules, thus reducing the possibility of surface functionalization. The size limitation has been solved by the pioneering work of the *Mobil Group* in 1992 allowing the synthesis of MSM through supramolecular templating.[223] Prominent synthetic materials are MCM-41 (Mobil Composition Matter)[224] and SBA-15 (Santa Barbara Amorphous)[225] with pore sizes of 3-8 nm. MSM can be produced in various forms such as powders, (nano-)particles or thin films, by one of the following major routes: direct precipitation, exo-templating, true liquid crystal templating, or evaporation-induced self-assembly (EISA).[44, 226] In case of MSTFs, these routes require flat and smooth surfaces to obtain homogeneous MSTFs. In 2007, *Walcarius* et al. introduced the electro-assisted self-assembly of MSTFs which allows the homogenous deposition on non-planar or even fibrous supports with uniform structure and vertically aligned mesopores.[227] The EISA process, introduced by *Brinker* et al. in 1999,[228] in combination with dip coating as deposition technique was selected as synthetic route of choice in this work due to its simplicity and high reproducibility.

Liquid crystal templating, in which surfactant liquid crystal structures serve as organic templates for the condensation of the inorganic phase to a stabilized mesophase, and a co-operative self-
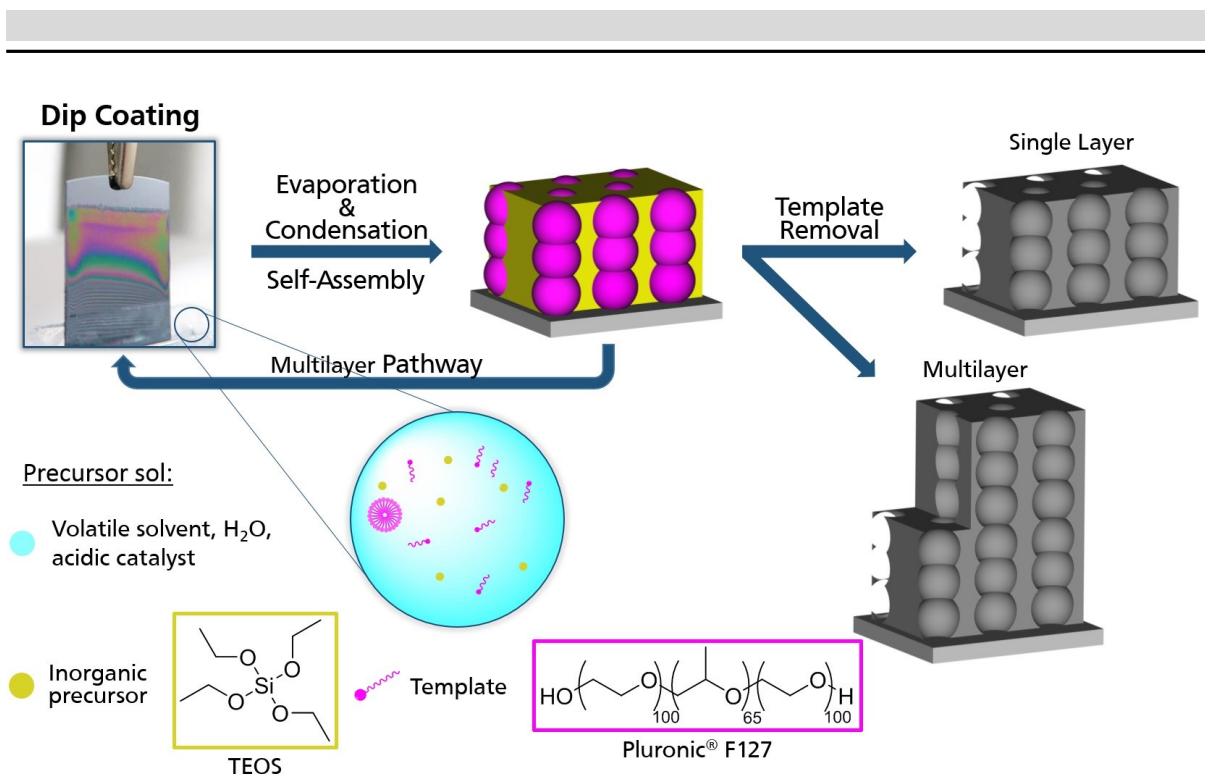
Scheme 3: Schematic representation of MSTF preparation via dip coating and EISA for single and multilayer.

assembly, in which hybrid intermediates are formed by the surfactant and inorganic species as independent blocks of hybrid structures, are the two mechanisms discussed in literature with respect to the nanoscale organization of inorganic mesoporous structures.[223-224, 229]

Based on sol-gel chemistry[230], a precursor solution containing the silica precursor, a template, a condensation promoting catalyst, and a volatile solvent is deposited under controlled conditions (temperature, humidity) on a smooth hydrophilic substrate with defined and constant withdrawing velocity (**Scheme 3**). Typical templates are amphiphilic surfactants such as cetyltrimelhylammonium bromide (CTAB) or triblock-co-polymers of the Pluronic® family like F127, P123 or P103, which determine the pore size of the final material.[231] In a first stage, a mesostructured phase of the inorganic building blocks and an entrapped organized supramolecular template is generated. Thereby, the inorganic precursor, here TEOS, the catalyst and the template molecules enrich in the sol due to solvent evaporation promoting the hydrolysis and condensation of the precursor as well as self-assembly of the template, which forms micelles when the concentration of the critical micellar concentration is reached.[232] Well-ordered mesophases are only obtained, if the process of phase separation/organization of the template is faster than the polycondensation of the inorganic building blocks, which leads to a "freezing" of the inorganic network.[44] The organization of the template molecules to the final equilibrated mesophases, also known as module steady state, has been intensively studied by *Grosso* et al. by combining small angle x-ray scattering and interferometry.[233] Thereby, it has been observed that the template molecules start from a worm-like towards a 2D-hexagonal

structure not only due to the interaction of the template with the inorganic building blocks, but as well due to the interaction of the air/sol and sol/substrate interface from which the micelles start to form, thus determining the orientation of the mesophase. Complete condensation of the inorganic network is achieved by further promoting the hydrolysis and condensation using elevated temperatures between 60 °C and 130 °C. Sequential deposition of MSTFs via dip coating, after one mesostructured film has been stabilized upon temperature treatment, allows the formation of double or even multilayered films.[59, 234] The final mesoporous film is obtained after template removal, which can be either performed by calcination or chemical extraction using suitable solvents.[231, 235]

Functionalization of MSTFs

The variety of possible applications of MSM is broadened by the functionalization with organic molecules.[42, 44, 46] Thereby, synergetic or even new material properties arise from the
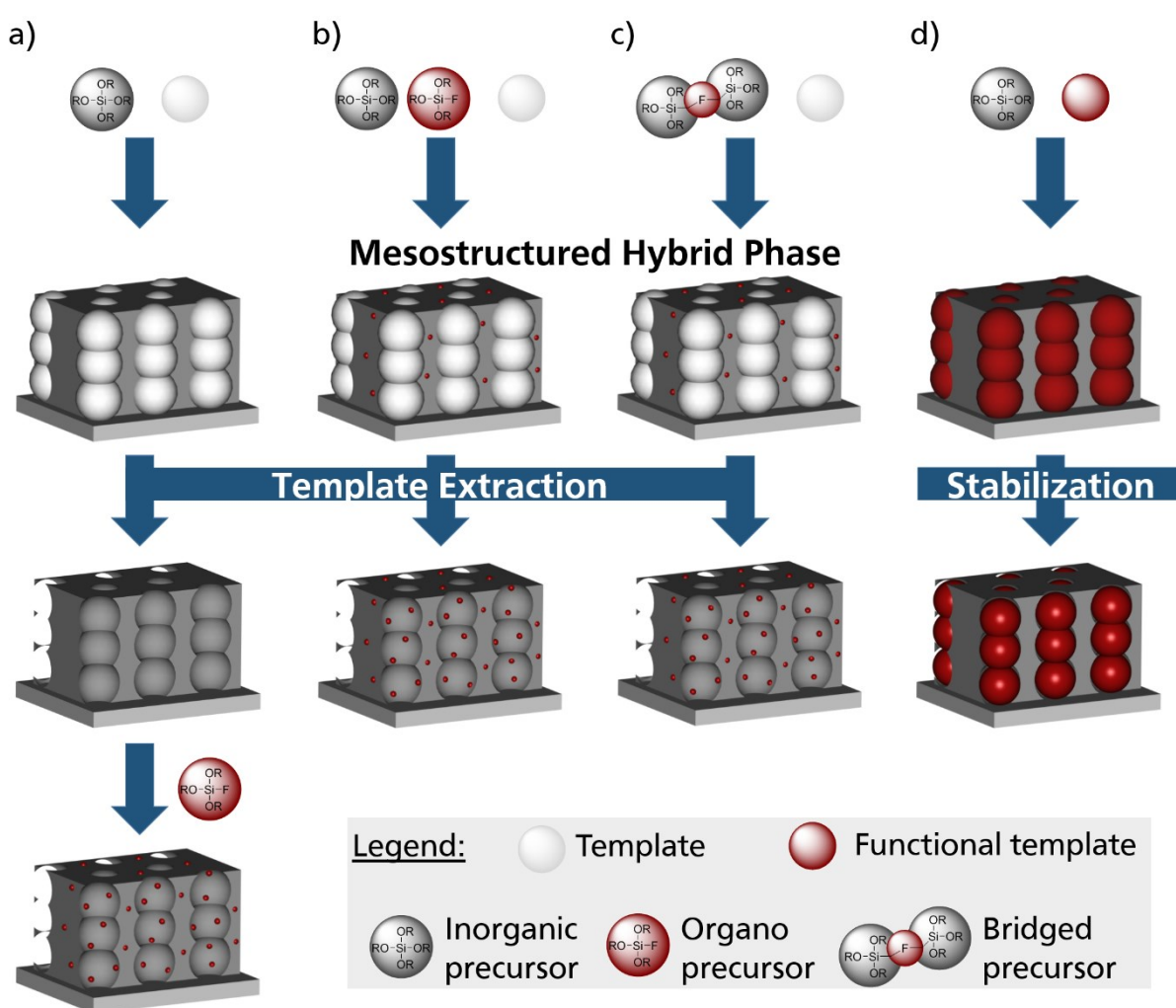
Scheme 4: Schematic representation of various synthetic routes towards hybrid mesoporous silica thin films. a) Post modification with organosilanes, b) co-condensation of inorganic and organosilane precursors, c) bridged precursor for the generation of periodic mesoporous organosilicas, and d) application of functional templates.

combination of the inorganic framework having a high specific surface area and organic molecules providing a plethora of functionalities that can be incorporated in the hybrid material. In principle, two main synthetic routes can be followed: 1) incorporating the organic function whilst synthesis of the mesostructured phase or 2) subsequent modification of the inorganic surface.[236] The latter contains a two-step synthetic approach and is described as **post-grafting** (**Scheme 4a**) allowing the functionalization of the surface not only in solution, but as well via the gaseous phase.[237-238] One-step synthetic routes towards the formation of hybrid mesoporous materials (HMM) are **co-condensation** of the inorganic precursor with organosilanes bearing the desired organic functionality (**Scheme 4b**) or the application of **bridged organosilane** hybrid precursors (**Scheme 4c**). A novel one-step approach for the formation of HMMs has been intensively explored by *Gérardin* and co-workers for silica powders by utilizing functional templates that also serve as structure directing molecules,[239-244] and has further been demonstrated for MSTFs by *Tom* et al. and *Herzog* et al. of the research group of *Annette Andrieu-Brunsen* allowing the in situ functionalization of MSTFs (**Scheme 4d**).[245-246] The choice of functionalization route is determined by the desired degree of functionalization, localization of functionality, limitation of the strategies respectively, and are further discussed below with respect to hybrid mesoporous silica thin films (HMSTF).

Post-Grafting

MSTF have a high surface area with good pore accessibility and are rich on chemically active surface silanol groups ($-Si-OH \sim 1-2$ nm^{-2}),[247-248] which allows simple surface modification by applying bifunctional organic molecules bearing suitable anchor groups and the desired organic functional group. Such anchor groups are typically alkoxy, silazane or halogenous nature, which undergo nucleophilic substitution reactions with surface silanol groups forming covalent bonds.[44, 220, 249] Thereby, the synthetic procedure is determined by the different reactivity of the anchor group. Whereas anchor groups of halogenous nature show the highest reactivity and can be applied at room temperature or even in the gaseous phase, the reactivity of ethoxy groups, for instance, is decreased compared to methoxy groups, thus elevated temperatures are required.[230] For homogeneous modification of the surface of MSTF, several aspects have to be considered. While the hydrophilicity/hydrophobicity of the inorganic surface and the organosilane needs to be tuned to prevent local condensation of the latter, competing reactions of the anchor group and other nucleophilic components in the reaction solution, such as water, need to be avoided.[44] Furthermore, the presence of more than one anchor group can lead to self-condensation of the organosilane inducing the formation of multilayer on the surface and even pore blockage, as the surface reaction is favored on pore openings and interpore

connections.[250] Nevertheless, post modification of MSTF also holds the great potential to locally functionalize either the outer surface, which can result in transient capping of the mesopores allowing controlled release of cargo molecules trapped inside the pores,[38-39] or gating/switching of ionic transport[40, 47, 56], or functionalization of the inner surface area allowing asymmetric design of functional placement.[48, 50, 57] On the one hand, the outer silica surface can selectively be modified, when the functionalization is carried out on a mesostructured surface still bearing the structure directing template.[251] Subsequent template removal reveals the inner silica surface, which is then accessible for further modification. On the other hand, selective functionalization of the inner silica surface is achieved by destroying the organic functionalities, for example by CO_2-plasma treatment.[252] The approaches for the selective functionalization of the inner or outer surface of mesoporous materials have been summarized by *Tiemann* and *Weinberger*.[57]

Co-Condensation

For the preparation of HMSTF via co-condensation, an organosilane bearing the functional organic group is present in the precursor solution containing the inorganic precursor, for example TEOS. Thereby, the different precursors co-condensate in the precursor solution as well as in the process of EISA forming the mesostructured hybrid phase. Although this approach represents the simplest way to incorporate organic functionalities in MSTF, again several aspects need to be considered. Template removal of the mesostructured hybrid phase needs to be performed under mild conditions, e.g. by selective extraction, to avoid damage of the organic functionality upon high temperature treatment (calcination).[44, 220] As result of different kinetics and thermodynamics of organosilanes compared to the inorganic precursor, differences in the co-assembly have to be considered.[230] Therefore, the kinetics of hydrolysis and condensation of the precursors have to be adjusted to prevent clustering of the organosilane and thus formation of a patchy functional density.[249] Furthermore, increasing the concentration of organosilanes in the precursor solution results in a decreased mesophase separation in the EISA process leading to a loss of homogeneity and order of the mesostructure. Thus, the amount of organosilane is typically kept to a minimum.[44, 220] Several studies demonstrated that a co-condensate concentration above 20% with respect to the total amount of precursors can lead to significant loss of the mesoporous ordering.[253-255] In consequence of the precursor solution's composition containing the inorganic precursor as well as the organosilane, the organic functionality is not only present at the surface, but also incorporated in the silica network, thus the resulting materials exhibit different chemical and mechanical properties compared to pure inorganic silica materials.[44] For example, *Calvo* et al. demonstrated that only 16% of the co-condensed

amino groups of APTES are chemically available after co-condensation compared to 37% when the material is functionalized via post-grafting.[256] Similar observations have been concluded by *Kobayashi* et al. comparing the spatial distribution of organic functional groups on mesoporous silica NPs incorporated via post-grafting and co-condensation respectively utilizing dynamic polarization (DNP)-enhanced ^{29}Si solid-state nuclear magnetic resonance (ssNMR).[257] Thereby, the co-condensation route lead to less homogenous distributions compared to post-grafting and also produced clustered organic moieties which were partly embedded into the silica walls.

The formation of HMSTF by applying bridged precursors is a 'one-pot' approach analogue to the strategy of co-condensation, in which bis- or polysilylated –trialkoxysilyl-organosilane precursors are utilized. Compared to co-condensation, one advantage is that the organic part is integrated in the framework walls and remains accessible, it has neither influence on the pore formation nor the pore size.[44, 220] Combination of different bridged precursors among each other and also the combination with terminal trialkoxysilyl-organosilanes allows the preparation of bi- or multifunctional HMSTF. However, hydrothermal treatment and extreme pH values are required synthesis conditions,[44, 258] which might lead to Si-C bond cleavage.

Functional Templates

In regard of the preparation route of mesoporous thin films, the EISA process involves organic template molecules directing the mesophase structure. The route of employing functional templates to form HMSTF (**Scheme 4d**) strongly differs from the approaches discussed above with respect to **Scheme 4a-c**, as the functionality originates from the structure directing template rather than by application of organosilanes. It is noteworthy that many structure directing templates have been proposed to prepare mesoporous materials. Common templates for utilization of the latter are: poly(ethylene glycol)-*block*-poly(propylene glycol)-*block*-poly(ethylene glycol) (Pluronic® P123), poly(ethylene oxide)-poly(propylene oxide)-poly(ethylene oxide) (Pluronic® F127) as nonionic surfactants, CTAB and cetyltriethylammonium bromide as cationic surfactants, sodium dodecyl benzenesulfonate SDBS and sodium dodecyl sulfate as anionic surfactants, as well as ionic liquids.[259] However, these templates are typically removed to obtain mesoporous materials throughout various techniques, such as calcination and solvent extraction.[259] The synthesis of functional templates for the preparation of in situ functionalized mesoporous materials, which are not designated to be removed from the hybrid materials is a completely new research field, which has been intensively studied by *Gérardin* and co-workers,[239-244] and further represents current research in the group of *Annette Andrieu-Brunsen*.[245-246]

Although an in situ functionalization with high functional density is achieved after deposition and stabilization of the mesostructured hybrid phase, functional templates have to be carefully designed and synthesized upfront guaranteeing an amphiphilic nature, which results in micelle and thus pore formation without hindering the co-assembly process and the development of the inorganic framework.[245-246] However, this strategy has just recently evolved and in situ functionalized mesoporous materials with responsive properties to stimuli such as temperature, redox, and pH have been reported lately, it further could open the opportunity of simple and automated material deposition, e.g. through additive manufacturing of HMSTF in a single step. As discussed above, the formation of HMSTF can be performed by application of various approaches, but has to be chosen thoughtfully with respect to the desired hybrid material. Whereas co-condensation leads to a homogenous distribution of the organic function and a minimum of synthetic steps are required, the application of functional templates and the post-grafting approach lead to a higher degree of function placement. The latter has extensively been studied and reported with respect to surface-initiated polymerization in the last two decades, due to a wide range of applicable monomers and different polymerization techniques available, which is further reviewed in the section below.

4.2. Polymerization at the surface

Polymer functionalization of surfaces, particularly flat surfaces and surfaces of porous materials, has attracted tremendous attention in the recent past, as it easily allows tailoring of chemical and physical properties of surfaces.[260-261] For example, antifouling properties of surfaces can be implemented by polymer functionalization applying zwitter-ionic monomers.[262] Furthermore, polymer functionalization of porous materials with stimuli-responsive polymers allows transport modulation, often combined with gating properties granting the opportunity of transporting and controlled release of cargo molecules trapped inside the pores.[158] In principle, polymer functionalization of surfaces can be either performed by physisorption via van-der-Waals, hydrogen-bond, or electrostatic interactions of the surface and the polymer, or by chemisorption implying the covalent attachment of the polymer at the surface. The latter can be performed by utilization of following main strategies: grafting-(on-)to, grafting-from and grafting-through. The former implies a covalent grafting of a pre-synthesized polymer chain bearing an anchor group, which binds to a suitable binding group on the surface. The advantage of this route is the possibility to design and characterize the as-synthesized polymer chain upfront. However, the generation of high grafting densities and thus formation of polymer brushes at the surface is restricted due to the radius of gyration together with entropic penalty resulting in limited chain density at the surface.[260] Furthermore, access of the polymer chain to

porous materials can also be limited due to the small pore entrance of nanoporous materials, for instance.[82] In the grafting-through approach, a growing polymer chain can covalently anchor to a surface, if a monomer functionality is present on the surface.[263] This strategy requires surface functionalities that can be involved in the polymerization growth reaction. Therefore, the attachment of a polymer chain through this approach consists of both grafting-to and grafting from steps.[264] The grafting-from approach allows high functional density, thus the generation of polymer brushes at the surfaces.[265] However, one drawback of the approach is that controlled architectural design of the polymer chain as well as characterization of the same is challenging, due to low material amounts. Nevertheless, in terms of polymer functionalization of nanoporous materials, the grafting-from approach has mostly been applied, in which the polymer chain is polymerized from the surface.[158] With respect to different polymerization techniques that can be performed at surfaces, especially controlled radical polymerizations have attracted reasonable interest as they are well-established and very convenient for surface polymerizations.[260] Key technologies in this regard are ATRP, RAFT polymerization and the analog photoiniferter-mediated polymerization (PIMP). The latter is mechanistically related to RAFT polymerization, but does not require an external radical source compared to RAFT polymerization as the iniferter is able to <u>ini</u>tiate, trans<u>fer</u>, and <u>ter</u>minate the polymer chain. In the recent past, ATRP has become the most extensively utilized technique for surface modification.[266-269] Here, the polymerization control is obtained via an activation/deactivation equilibrium of a transition metal complex and a dormant alkyl halide-terminated polymer chain-end propagating in the presence of monomers. In case of RAFT polymerization, control is achieved based on a reversible chain transfer and combines a chain transfer agent (CTA) such as dithiocarbamates, dithioesters, and dithiocarbonates, and an external radical initiator, azobisisobutyronitrile for instance. RAFT polymerization at the surface can be performed either by surface immobilization of the CTA or the free radical initiator. In SI-PIMP, polymerization control is accomplished by the intensity of applied irradiation, and therefore allows spatial as well as temporal control.

In the following, SI-PIMP and dye-sensitized (radical) polymerization are further discussed in detail with respect to the functionalization of mesoporous thin films, as these represent the main polymerization techniques used in this work. At this point, a detailed review article on SI-polymerizations of surfaces published the group of *Harm-Anton Klok*[260] as well as a review on recent trends in polymer functionalization of nanopores published by the group of *Annette Andrieu-Brunsen*[158] are recommended for further reading. In addition, detailed articles on ATRP published by its inventor *Krzystof Matyjaszewski*[270], as well as an article on RAFT polymerization published by the group of *Michael Whittaker*[271] are recommended for further reading. For this

work, Si-PIMP polymerization has been chosen due to its simplicity and good applicability in terms of functionalization of porous materials, and dye-sensitized polymerization due to the possibility of initiation via visible light irradiation.

4.3. Photopolymerization

Polymerization reactions, in which many monomer units are added to each other to create a macromolecule, are often thermally initiated by decomposition of a molecule. Instead of thermal activation, other stimuli such as electron beam, x-rays, plasma, microwaves, or light can also be used for polymer initiation.[272] Applying light of a suitable wavelength represents a convenient way to initiate polymerization (photopolymerization), which has firstly been demonstrated in pioneering works from more than half a century ago allowing the performance of polymerization under mild conditions with spatial as well as temporal control.[273] It is noteworthy that photopolymerizations differ from classical photochemical transformations, as the initiation process typically becomes photo-induced, but chain growth polymerizations are thermally driven chain reactions, hence following *Arrhenius* law.[274] Thus, increasing light intensities does not necessarily lead to faster or better polymerizations, since a too high radical concentration can be counterproductive.[274]

In photopolymerization, the initiators can be either unimolecular or multimolecular.[275-276] Unimolecular initiators comprise one component that forms active free radicals initiating the polymerization upon absorption of a photon and subsequent homolytic bond cleavage. Multimolecular initiators require at least two species: an initiator/photosensitizer that forms an excited state upon photon absorption and further reacts by red-ox, hydrogen abstraction or an electron transfer mechanism with a so-called co-initiator that quenches the excited molecule creating radicals to initiate the polymerization reaction. Typical unimolecular photoinitiators are represented by benzoin ethers or benzyl ketals, whereas bimolecular techniques often consist of benzophenones or thioxanthones as photosensitizer in combination with alcohols, amines and thiols as hydrogen donors.[277] However, a plethora of photoinitiators and photoinitiating molecules are available and have been summarized in a book by *Fouassier* and *Lalevée*.[278]

4.3.1. PIMP in mesopores

Iniferter initiated polymerizations are one of the oldest controlled polymerization techniques.[279-280] Thereby, initiation is conducted either thermally or by irradiation with light. The latter is also known as PIMP and holds several advantages: Using light for initiation allows

performing the polymerization under mild conditions granting the utilization of thermally instable compounds such as pharmaceuticals, peptides, and enzymes.[281-282] In addition, photoinitiation offers a temporal and spatial control by controlling the light intensity or concentration of the photosensitive compounds unlike to thermal initiation.[283]

Furthermore, SI-PIMP of mesoporous thin films has already been successfully demonstrated allowing not only to adjust the function and thus charge density in case charged monomers are applied,[48] but also the re-initiation for the synthesis of block-co-oligomers enabling architectural design of the polymer chains.[56]

Upon irradiation with light of a suitable wavelength, mostly UV, the photoiniferter undergoes a homolytic C-S bond cleavage (**eq. 4.1**), followed by polymerization and end-capping of the polymer chains. The structure of the iniferter determines the polymerization control by the properties of the free radical leaving group R· and the Z-group that can either activate or deactivate the thiocarbonyl bond of the iniferter modifying the stability of intermediate radicals.[284] Thereby, the iniferter cleaves either in two identical radicals (cc-type) or two different radicals (ab-type). Is the Z-group represented by a suitable anchor group that can bind to a surface, SI-PIMP can be carried out.[285]

The mechanism of PIMP is exemplarily depicted in the following:

Initiation
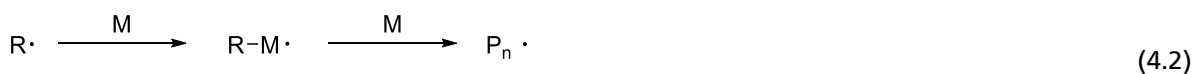
$$(4.1)$$

$$(4.2)$$

Reversible chain transfer

$$(4.3)$$

Re-initiation

$$(4.4)$$

Chain equilibrium and propagation

$$P_m{}^\bullet \;+\; \underset{Z}{\overset{S}{\bigvee}}\!\!S\!-\!P_n \;\rightleftharpoons\; P_m\!-\!S\underset{Z}{\overset{\bullet}{\bigvee}}S\!-\!P_n \;\rightleftharpoons\; P_m\!-\!S\underset{Z}{\overset{S}{\bigvee}} \;+\; P_n{}^\bullet$$

(M) $\qquad\qquad\qquad\qquad\qquad\qquad\qquad\qquad\qquad\qquad (M)$ (4.5)

Termination

$$P_m{}^\bullet \;+\; P_n{}^\bullet \;\longrightarrow\; \text{dead polymer}$$

(4.6)
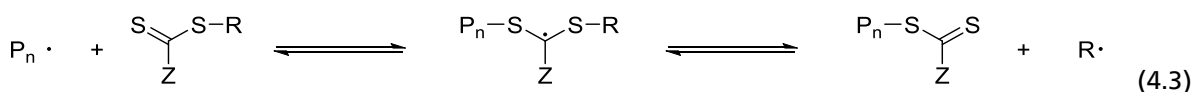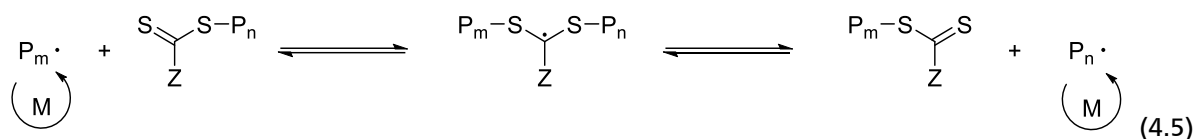
Initiated through irradiation, the photoiniferter splits into the dithiocarbamate radical and the free radical leaving group R· (**eq. 4.1**). The latter is not stabilized and most likely to react with present monomer forming the propagating chain $P_n{}^\bullet$ (**eq. 4.2**). By addition of the latter to another iniferter, the first equilibrium is accomplished generating the centered radical in **eq. 4.3**. This radical can fragment in both directions either reverting to the original structure releasing $P_n{}^\bullet$ or generating the macro-iniferter by releasing the new radical R·. In the second case, the radical R· forms another propagating radical $P_m{}^\bullet$ by reaction with monomer. The second equilibrium is achieved (**eq. 4.5**, chain equilibrium and propagation) by addition of the propagating radical $P_m{}^\bullet$ to the macro-iniferter. There, an equal probability for all chains to grow is provided by a rapid equilibrium between the active propagating radicals $P_n{}^\bullet$ and $P_m{}^\bullet$ and the dormant macro-iniferter allowing the synthesis of low dispersive polymers. Termination reactions by recombination or disproportion are present, but significantly suppressed and, in case of SI-polymerization, even less likely compared to polymerization in solution, as only two adjacent chains can undergo termination reactions. As highlighted before, no radicals are formed after irradiation and the polymerizations stops allowing re-initiation of the dormant species.

4.3.2. Dye-sensitized polymerization in mesopores

Although not representing controlled polymerizations, dye-sensitized polymerizations offer the application of a broad wavelength range in the visible light spectrum, thus possible degradation by using high-energetic light, e.g. ultraviolet, could be limited. The application of light to induce the polymerization further allows to control the introduced energy, and the polymerization can be carried out in aqueous solutions. On top of these advantages, dye-sensitized polymerizations

have been successfully combined with surface plasmons to functionalize plasmonic metal NPs,[65-66, 215] and also mesoporous silica thin films deposited on thin metal layers.[49, 286]

In this work, a bimolecular initiating approach comprised of a photosensitizing dye in combination with a tertiary amine has been applied. The mechanism postulated by *Kim* et al. is further discussed below (**eq. 4.7**).[287]

By irradiation with light of a suitable wavelength, the dye is excited to a singlet state ($^1D^*$) by absorption of a photon. The excited dye can either relax to its ground state (D) by emitting electromagnetic radiation or undergoes a non-radiative transition to a triplet state ($^3D^*$) by intersystem crossing. Excited in the triplet state, the dye is photoreduced by a tertiary amine leading to a semi-oxidized form of the amine and a semi-reduced protonated form of the dye. The latter is colorless and also known as leuco form of the dye, which can either proportionate to its primary form or to its double-protonated form. By hydrogen abstraction of a neighboring methylene group with respect to nitrogen of the amine, the polymerization initiating form of the amine (Am·) is generated.

$$D \underset{h\nu'}{\overset{h\nu}{\rightleftharpoons}} {}^1D^* \xrightarrow{\substack{\text{intersystem} \\ \text{crossing}}} {}^3D^* + Am \longrightarrow D^{\bullet-} + Am^{\bullet+} \xrightarrow{\text{Red-Ox}} DH^{\bullet} + Am^{\bullet} \xrightarrow{n\,M} \text{Polymer}$$

$$(4.7)$$
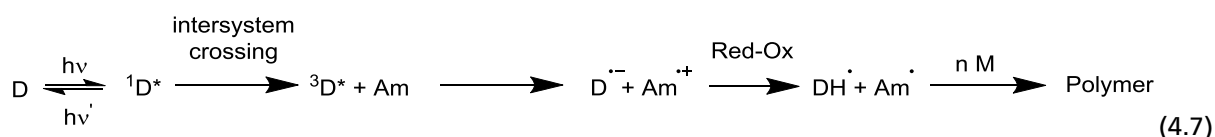
Although oxygen should be avoided in radical polymerizations, as peroxo compounds unable to promote the chain growth are formed, oxygen can react with the protonated and double-protonated form of the dye regenerating its primary form according to **equation 4.8** and **4.9**.[288]

$$DH^{\bullet} + O_2 \longrightarrow D + HO_2^{\bullet} \tag{4.8}$$

$$DH_2 + O_2 \longrightarrow D + H_2O_2 \tag{4.9}$$

In this regard, the acidity of the reaction medium is crucial, since the protonated form of the dye can as well be a result of the acid-base equilibrium of the semi-reduced dye and a proton.[278] In this work, dibromofluorescein absorbing at 530 nm as photosensitizing dye and N-methyl diethanolamine as co-initiator have been used for photopolymerization, since preliminary work showed successfully the application in mesoporous silica thin films by application of visible light irradiation.[49] Thereby, the enhanced electromagnetic field of the evanescent wave of surface plasmons of a nanometer thin gold layer underneath the MSTF has been applied to induce the polymerization inside the mesopores. Furthermore, *Soppera* and *Bachelot* have thoroughly investigated such photopolymerization formulations in combination

with metal NPs allowing nanolocal polymer formation by taking advantage of the high energetic field of localized surface plasmons of metal NP.[64-66, 216]

4.4. Surface plasmon resonance and synthesis of plasmonic metal NPs

The phenomenon of surface plasmons (SPs) has been used for a long time, particularly in coloring of glass. For example, glasses from the Bronze Age (1000-1200 BC) found in northern Italy exhibit coloration by presence of copper NPs.[289] The *Lycurgus* cup (400 AC) is one of the most prominent example showing different coloration when observed upon illumination inside or outside the cup.[290-291] Furthermore, the Mayan civilization used metallic NPs to develop blue paints.[292] Likewise, there is evidence of metallic NPs in glass and pottery of Egyptian dynasties[293], Celtic enamels[294], Japanese[295] and Chinese glasses[296].

The SPR is influenced not only by the size of plasmonic nanostructures, but as well by solvent, i.e. the refractive index /dielectric of the surrounding medium, ligands, interparticle distance, and temperature.[171, 297] Compared to symmetric spherical Au-NPs, unsymmetrical NPs, such as rods, wires, cubes, nanocages, triangular prism and other structures have also received significant attention to research, as their unique and fine-tuned properties strongly differ.[298]

A simplified classical picture can help to understand SPs: Metallic NPs can be described as a lattice of ionic cores with conduction electrons moving almost freely inside the NP, also known as *Fermi* sea.[171] Upon illumination, the electromagnetic field of the incident light exerts a force on the conduction electrons moving them towards the NP surface. Since the electrons are confined in the NP, negative charge will be accumulated on one side and positive charge will be accumulated on the opposite side creating an electric dipole (**Figure 10**). The electrons are then forced to return to the equilibrium position, as the dipole generates an electric field inside the NP opposite to that of light. Here, the electric dipole is larger, the more intense the electron displacement is, similar to a linear oscillator with restoring force proportional to the displacement from the equilibrium position.
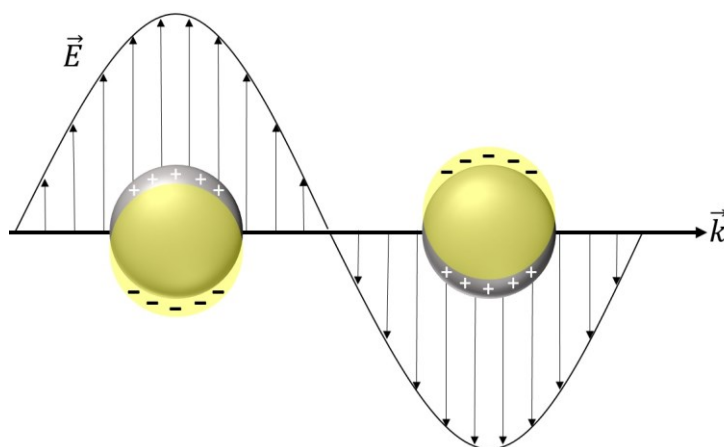
Figure 10: Schematic illustration of the LSPR of metal NPs upon irradiation.

If the electrons are displaced from the equilibrium position and the field is removed later, they will oscillate with a certain frequency, which is called plasmon resonant frequency.[171, 299] The wave motion of charge density by the collective oscillation of conduction electrons can also be described as plasma oscillation.[200] The resonant conditions are mainly reached in the visible wavelength range for which the NPs possess a distinct coloration like blue, red, green or brown depending on the nanostructure size, shape, composition, or environment of the NPs caused by the interaction of electrons in the metal NPs with incident light.[298, 300-303] For instance, the resonant conditions undergo a redshift with increasing size of spherical Au-NPs.[302, 304] Furthermore, the resonant wavelength of alloy NPs can be tuned by variation of the composition. For example, alloy gold/silver-NPs (Au/Ag-NPs) show a blue shift with increasing amount of Ag.[305] The optical extinction of SP can simply be measured by optical absorption spectroscopy[306-307], but as well directly probed by far-field extinction microscopy[308-309], electron energy loss spectroscopy[310-311], or cathodoluminescence[312-313].

The synthesis of Au-NPs can be performed either by a top down (physical manipulation) or bottom up (chemical transformation) approach,[163] and can be retraced to *Faraday's* work in 1857, in which gold hydrosols were prepared by reduction of an aqueous solution of chloroaurate with phosphorous dissolved in carbon sulfide.[314] In 1951, *Turkevich* developed one of the most popular approach using citrate reduction of chloroauric acid in water.[315] In addition, *Frens* reported the control over size by feed ration of gold salt to sodium citrate.[316] Finally, the kinetics to the *Turkevich* approach were provided by *Chow* and *Zukoski*.[317] Since these first developments, a plethora of synthetic protocols, especially with respect to different NP shapes, but also with respect to the compatibility with various media have been published.[163, 318-323]

In this work, the synthetic protocols of spherical plasmonic metal NPs based on the *Turkevich* method were extracted from the doctoral thesis of *Meike Roskamp*[324]. Thereby, the type of metal

and the size of the NP's were chosen according to the wavelength of the LSPR that matches the necessary wavelength of the selected photopolymerizations. Furthermore, metal NPs synthesized via the *Turkevich* method exhibit citrate ligands which shall allow the immobilization of the NPs on the surface of amine functionalized silica films.

4.5. Cyclic Voltammetry for investigation of ionic pore accessibility

Cyclic voltammetry (CV) is a potentiodynamic electrochemical method allowing the investigation of electrochemical reaction mechanisms, redox potentials of molecules, as well as kinetics of electron transfer processes.[325-326] In this work, CV is used to investigate the pore accessibility of mesoporous thin films in dependence of pH by applying positively or negatively charged redox-active probe molecules. Thereby, the charged probe molecules can either pass the mesoporous structure generating an electrochemical signal due to an electron transfer reaction at the electrode located underneath the mesoporous thin film, or be rejected due to, for example, electrostatic repulsion of the surface charge. In addition, the influence of mesopore functionalization can be studied via CV, as the pore size along with additional intrinsic reactivity of integrated functional groups might affect the mesopore accessibility.[327] For further reading on electrochemical characterization methods of mesoporous materials, the fabrication of such materials by electro-assisted deposition, as well as applications of mesoporous materials for electrochemical purposes, a review article of *Walcarius*[327] is recommended. Additionally, *Steinberg* et al. very recently published an article correlating experimental voltammograms of mesoporous titania with a previously developed model of partially covered electrodes.[328]

Generally, the measurement setup consists of three electrodes, namely a working electrode, a counter electrode, and a reference electrode (**Figure 11**). By that, electrochemical reactions of interest occur on the working electrode. The reference electrode measures the true potential and the counter electrode compensates differences between the measured and applied potential. In a cyclic voltammetric measurement, the initial potential (U_1) is linearly increased until a desired potential is reached (U_2). Subsequently, the potential decreases linearly until the initial potential is reached again, as schematically illustrated in **Figure 11b**. This potential change proceeds in a controlled way by applying a potentiostat.
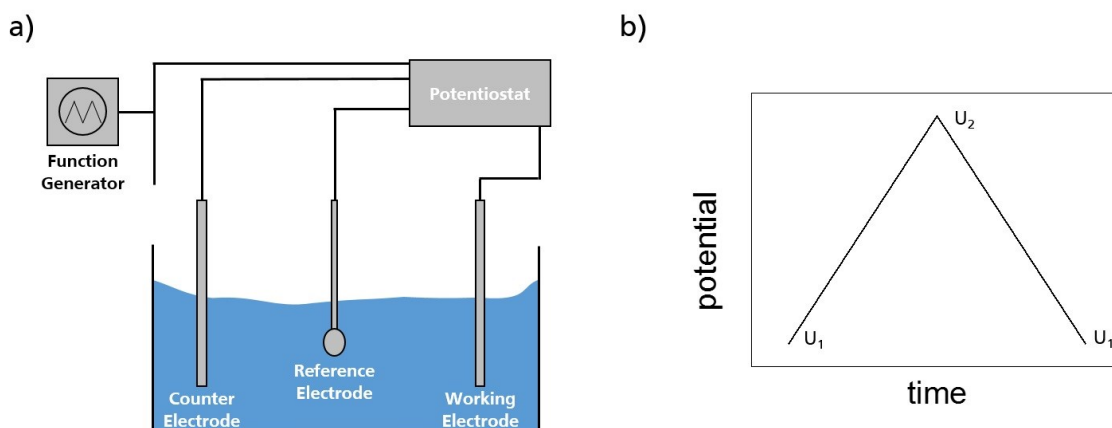
Figure 11: a) Schematic representation of the measurement setup of CV. b) Illustration of potential variation in cyclic voltammetric measurements.

In this work, CV is used to investigate the ionic pore accessibility of mesoporous thin films utilizing the charged and redox-active probe molecules ferricyanide $[Fe(CN)_6]^{3-/4-}$ and ruthenium hexamine $[Ru(NH_3)_6]^{2+/3+}$. Therefore, mesoporous thin films were deposited on indium-tin oxide (ITO) covered glass substrates. In this case, ITO represents the working electrode and electrochemical reactions can only be monitored, if the probe molecules can pass the mesoporous structure reaching the working electrode below (**Figure 12**).
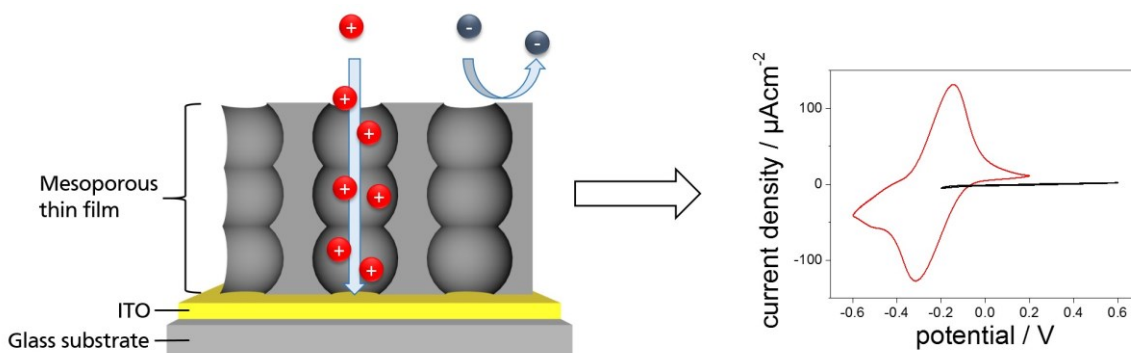
Figure 12: Schematic representation of mesoporous thin films deposited on ITO covered glass substrates to perform cyclic voltammetric measurements to investigate the ionic pore accessibility. The current density refers to the measured electrode area without considering the covered surface area below silica.

Fundamentally, mass transport is determined by diffusion, migration and convection. To increase the conductivity of the probe molecule solution, a background electrolyte is added that also suppresses mass transport as result of migration. In presence of a redox-active probe molecule, the electrochemical signal increases until the oxidation or reduction potential of the probe molecule is reached, and decreases once the concentration of the probe molecule

becomes depleted at the working electrode surface. For reversible reactions, the same electrochemical signal with a negative current is observed, when the potential is decreased to the initial potential. In case of redox reactions, the electrode potential (*E*) correlates with the concentration of the oxidized and reduced form of the probe molecules, which can be described by the *Nernst* equation (**eq. 4.10**)

$$E = E^0 + \frac{RT}{zF} log \frac{[ox]}{[red]} \tag{4.10}$$

with the standard electrode potential *E⁰*, the ideal gas constant *R* (8.31446 J/mol), the temperature *T* in Kelvin, the number of transferred electrons *z*, the *Faraday* constant *F* (96.48534 kJ/Vmol), and the concentration of the oxidized *[ox]* and reduced *[red]* form of the probe molecule.

The detected peak current (i_p) correlates with the temporal change of the potential, which is known as the scan rate (*v*), and is further dependent on the concentration of analyte c_i, the electrode area *A*, and the diffusion coefficient *D* according to the *Randles-Sevcik* equation (**eq. 4.11**). Hence, diffusion processes can be investigated by observing the peak current in dependence of different scan rates, as the scan rate determines the time for the probe molecules to diffuse to the working electrode. A diffusion controlled mass transport is governed, when a linear correlation of the peak current versus the square route of the scan rate is present.

$$i_p = (2.69 \cdot 10^5) \cdot n^{\frac{3}{2}} \cdot A \cdot D^{\frac{1}{2}} \cdot c_i \cdot v^{\frac{1}{2}} \tag{4.11}$$

However, *Steinberg* et al. just recently investigated the application of the *Randles-Sevcik* equation for mesoporous insulating materials, and thereby concluded that this model is insufficient, since mesoporous insulating materials, including mesoporous silica, behave as planar electrodes under certain conditions, although a great fraction of the electrode is covered, thus the electrode area *A* should not be applied.[328] They further propose the application of the model for partially covered electrodes previously developed by *Matsuda* and co-workers[329], which could be successfully applied to interpret experimental results.[328]

CV not only provides the investigation of ionic pore accessibility of mesoporous thin films, but also allows to determine various properties. For example, only a homogeneous and crack-free mesoporous thin film shows a suppressed electrochemical signal in case the template has not been removed. Hence, the presence of well-defined electrochemical signals after template removal gives information on the quality of template removal. Furthermore, it has been shown that CV can be used to identify the structure (type, pore size, orientation)[227, 330-331] of

mesoporous thin films as well allows the investigation of the applied probe molecules (concentration, size, charge)[332]. In addition, it has been demonstrated by utilizing CV that enhanced transport rates can be induced by periodically hierarchical pore structures.[333-334] Besides that, ionic pore accessibility is mainly governed by the charge of the probe molecules and the charge of the pore wall, as the Debye-Screening length plays an important role in such nanoscale pores. For example, MSTFs exhibit a naturally negative charge in basic environment in consequence of deprotonated silanol groups on the surface. Therefore, positively charged probe molecules are more likely to pass the porous structure reaching the electrode below, and are often pre-concentrated in the porous network due to electrostatic attraction. Contrary to this, negatively charged probe molecules are rejected due to electrostatic repulsion of the negatively charged mesopore. However, by modification of the surface functionality of mesoporous thin films, the ionic pore accessibility can be modulated. Thus, CV allows to evaluate functionalization of the pore walls, not only for single mesoporous thin films, but also for double-layered mesoporous thin films.[245-246] Moreover, it has been demonstrated that the nature of transport of charged probe molecules through mesopores can be investigated in dependence of the wetting state of the pores.[238] In this regard, *Khalil* et al. were able to distinguish between transport across the mesopores and transport along the mesopore walls. In another context, *Brilmayer* et al. demonstrated the possibility of determining pK_a values of functional groups on the mesopore walls from cyclic voltammetric measurements in dependence of pH (titration).[10] Thereby, a shift of the pK_a values was observed in consequence of the confinement effect in such nanoscale pores.

4.6. Ellipsometry

Ellipsometry is a non-destructive and very sensitive optical method, which determines the polarization change of light that is reflected at a surface. If a thin film is deposited on a reflecting surface, the optical system comprised of a thin film and the substrate will influence the polarization of light, thus optical/dielectric properties of the thin film, such as thickness and refractive index, can be determined.

Light can be described as an electromagnetic wave, which electric field E undergoes higher interaction with matter as compared to the magnetic field.[335] Further, the electric field can be allocated into two components: the p component running parallel to the propagating plane of incidence of the light wave, and the s component running perpendicular to the plane of incidence. Since these p and s components undergo different phase shifts as well as different reflectivities through the interaction with the sample, a change of polarization of the reflected light is induced.

In this work, nulling-ellipsometry is applied to determine the refractive indices and film thicknesses of MSTFs. Fundamentally, the setup consists of a light source, a polarizer (P), a compensator (C), an analyzer (A), and a photosensitive detector as schematically depicted in **Figure 13**.
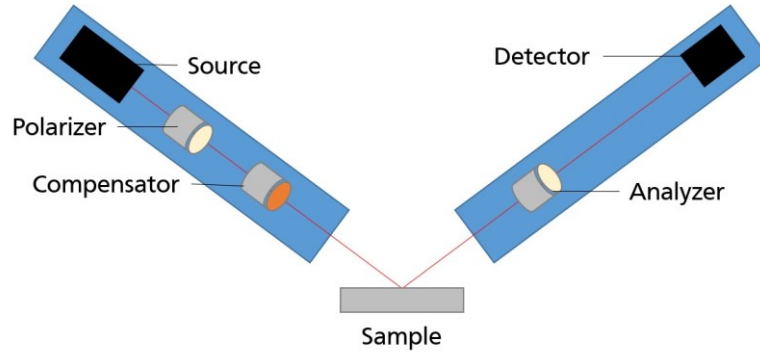
Figure 13: Schematic PCSA setup of nulling-ellipsometry.

Firstly, a laser light beam is linearly polarized by the P and becomes elliptic after passing the C (quaterwave plate), which has a designated position with respect to the P capable to shift the phase of one component of E along the axis of the P. The elliptic light beam impinges on the sample (S) interacting with matter and is then reflected on the substrate, where the sample is deposited. By a suitable angle of P, the reflected light is linearly polarized and passes the A, which is in principle a polarizer as well that is able to measure the ratio of the p and s components of E. If the A is in a 90° position with respect to the axis of the reflected and linearly polarized light, the light intensity passing the polarizer will be zero and the light beam is "extinguished". The polarization changes throughout the setup of nulling-ellipsometry is schematically depicted in following **Figure 14**:
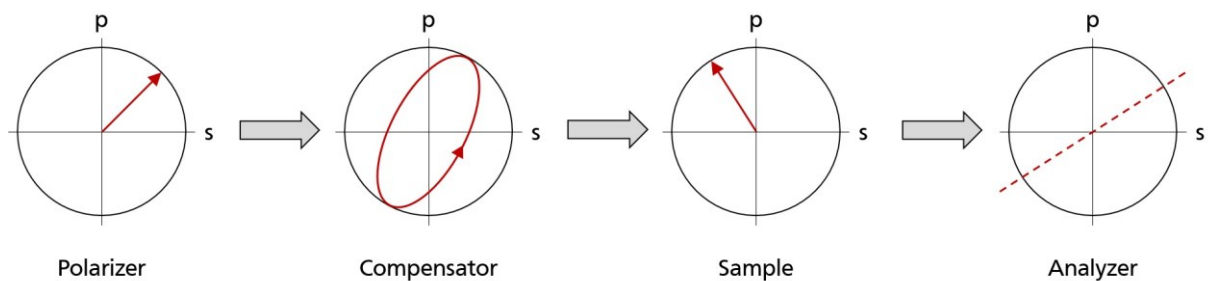
Figure 14: Schematic representation of the polarization of light in the PCSA configuration of nulling-ellipsometry.

The detector, which is generally a photosensitive charge-coupled device, measures the intensity of light. In case of nulling-ellipsometry, the angles of P and A are varied until the detector quantifies a minimum of light intensity. Thus, a set of angles for P, C, A and the angle of incidence (AOI) is the result of an ellipsometric measurement, and correlates with the ellipsometric angles Δ and Ψ as follows:

$$\Psi = A, \Delta = 2P + \frac{\pi}{2} \qquad (4.12)$$

for A ≥ 0.

The ellipsometric angle Δ describes the difference in phase of the p and s component of light before (δ_i) and after reflection (δ_r):

$$\Delta = \delta_i - \delta_r. \qquad (4.13)$$

The second ellipsometric angle Ψ describes the ratio of the amplitudes of the p and s components of light and can be deduced from the Fresnel equation:

$$\tan \Psi = \frac{|R_{pp}|}{|R_{ss}|} \qquad (4.14)$$

with the reflectivity of the p component R_{pp} and the reflectivity of the s component R_{ss} of the incident light.
The reflectivities of the p and s components can be expressed by **equation 4.14** applying the reflection coefficients of the p (r_p) and s component (r_s) according to Snell's law (**eq. 4.15**):

$$R_{pp} = \frac{r_{01p} - r_{12p} e^{-i2\Delta}}{1 + r_{01p} r_{12p} e^{-i2\Delta}} \text{ and } R_{ss} = \frac{r_{01s} - r_{12s} e^{-i2\Delta}}{1 + r_{01s} r_{12s} e^{-i2\Delta}} \qquad (4.15)$$

for a single-layer model with two boundary layers between air and the porous layer, and between the porous layer and substrate. Exemplary, the boundary layers between air and porous layer (r_{01p}/r_{01s}) are given by:

$$r_{01p} = \frac{n_1 \cos \alpha - n_0 \cos \beta}{n_1 \cos \alpha + n_0 \cos \beta} \text{ and } r_{01s} = \frac{n_0 \cos \alpha - n_1 \cos \beta}{n_0 \cos \alpha + n_1 \cos \beta}. \qquad (4.16)$$

Consequently, the fundamental equation of ellipsometry that implies both ellipsometric angles is obtained:

$$e^{i\Delta} \tan \Psi = \frac{R_{pp}}{R_{ss}}. \tag{4.17}$$

In case the wavelength of the light is known, as well as the AOI, and the refractive index of the surrounding medium along with the substrate, the thickness of the thin film together with the refractive index is obtained with a periodical result according to:

$$d = \frac{\lambda}{2\sqrt{n_{D2}^2 - n_{D1}^2 sin^2\theta}}. \tag{4.18}$$

Plotting the ellipsometric angles Δ and Ψ versus a set of AOIs allows the calculation of the refractive index and the film thickness by applying a suitable layer model and a graphical fit. Thereby, the root mean square error (RMSE) determines the quality of the graphical fit. According to the manufacturer, a RMSE=1 indicates an optimal fit taking into account the experimental errors provided with the data, whereas a RMSE<1 represents a fit better than may be expected from the data errors and a RMSE>1 indicates a sub-optimal match. With respect to the latter, RMSE values below 2-3 may usually still be regarded as a good fit, depending on the sample's complexity.

Since P, C and A can be rotated in a range of 360°, four zones of linear polarized light can be detected, thus fourfold zeroing can be performed in the measurement. Thereby, four-zone measurements take four times longer than a zero-zone measurements. In this work, one-zone measurements are performed.

In addition to the determination of film thickness and the refractive index of MSTFs, the porosity can be determined by applying the *Bruggeman*[336] effective medium approximation (BEMA, **eq. 4.19**) and the refractive index obtained by following equation

$$\left(p - V_p\right)\left[\frac{\varepsilon_{air} - \varepsilon_s}{\varepsilon_{air} + 2\varepsilon_s}\right] + \left(V_p\right)\left[\frac{\varepsilon_p - \varepsilon_s}{\varepsilon_p + 2\varepsilon_s}\right] + (1 - p)\left[\frac{\varepsilon_{Si} - \varepsilon_s}{\varepsilon_{Si} + 2\varepsilon_s}\right] = 0 \tag{4.19}$$

with the porosity of the layer p, the volume fraction of polymer V_p, the dielectric constants of air ε_{air} , silica ε_{Si}, the measured sample ε_S, and of polymer ε_p respectively, assuming $\varepsilon = n^2$ ($n_{air} = 1$ and $n_{silica} = 1.46$[337]).[338] Furthermore, by determining the refractive index of MSTFs before and after functionalization, one can calculate the pore volume fraction of organic molecules, e.g. polymer, by applying the BEMA.[339]

5. Results and Discussion

The scientific results obtained in this work are presented and discussed in this chapter. The results of this work, which have partially been published as scientific articles, are introduced and discussed by following outline:

I. Material library for mesoporous architecture (**Chapter 5.1**)

II. Mesoporous thin films with asymmetries in pore size and surface wettability prepared by asymmetric fabrication (**Chapter 5.2.1** and **5.2.2**)

III. Asymmetric modification of mesoporous film architectures by layer-selective polymer functionalization of mesoporous double-layer thin films (**Chapter 5.2.3**)

IV. Asymmetric modification of mesoporous film architectures by nanolocal functionalization of mesoporous thin film architectures (**Chapter 5.2.4**).

In **Chapter 5.1**, the preparation of mesoporous single thin films is presented. Thereby, two hydrophilic MSTFs with different pore sizes, respectively, that are mainly used in this work are intensively studied with respect to the ionic pore accessibility in dependence of the environmental pH. Furthermore, MSTFs with adjustable surface wettability are introduced, which allow asymmetric fabrication of mesoporous architectures to generate mesoporous wettability step gradients by sequential deposition of hydrophilic and hydrophobic MSTFs, respectively, using dip coating. In addition, mesoporous thin films prepared with a bridged silica precursor that result in increased chemical stability in basic environment are introduced and discussed. Moreover, MSTFs templated with bio-based and sustainable macromolecules are proposed as alternative to petro-based block-co-polymers used as structure directing templates. Based on the introduced material library, prepared mesoporous film architectures with respect to the fabrication of MSTFs with asymmetries in pore size, surface wettability, and charge distribution are discussed in **Chapter 5.2**. Thereby, hydrophilic MSTFs with different mesopore sizes are combined in order to prepare MSTFs with pore size step gradients. Further, hydrophilic and hydrophobic MSTFs are merged to generate MSTFs with wettability step gradients. The selective polymer functionalization of an individual MSTF layer in double layer arrangements is represented. By that, well-established functionalization strategies of single layer MSTFs are transferred to double layer MSTFs to generate mesoporous charge step gradients by asymmetric modification. The ionic mesopore accessibility of the resulting step gradient architecture is investigated. Finally, nano-local functionalization strategies by applying plasmonic metal NPs as nanoscale light source to induce photosensitive polymerizations in the confinement of MSTFs are illustrated. The concept is demonstrated for two mesoporous film architectures and two different polymerization techniques.

5.1. Material library for mesoporous architecture

In terms of the generation of mesoporous architectures with step gradients in pore size, wettability, or charge, a mesoporous film library was built, which is represented in this chapter. Firstly, two distinct MSTFs with different pores sizes[217-218], which were used to fabricate MSTFs with pore size step gradients, are systematically investigated with respect to chemical and structural properties, as well as ionic pore accessibility in dependence of preparation parameters. Secondly, MSTFs with tunable wettability are introduced. With respect to the fabrication of MSTFs with defined surface wettability – from a hydrophilic to hydrophobic nature – by co-condensation of different silica precursors represents a facile route for asymmetric fabrication of Janus-type materials with wettability step gradients. Recently, *Nakanishi* and co-workers introduced marshmallow-like gels and aerogels from di- and trifunctional alkoxysilanes as co-precursors through sol-gel reaction.[340] By applying the methylated precursors methyltrimethoxysilane (MTMS) and dimethyldimethoxysilane (DMDMS), a porous material was obtained that shows superhydrophobicity and high mechanical stability over a wide temperature range.[341] Inspired by this work, MTMS and DMDMS were used for co-condensation with TEOS to develop MSTFs with tunable surface wettability.

Besides mechanical stability of MSTFs, several researches have recently investigated the stability of mesoporous materials in aqueous solutions in dependence of the environmental pH and concluded a lack of stability especially in basic environment, whereas silica dissolves in acidic environment slowly.[342-344] Thereby, one relevant aspect affecting the chemical stability is the high specific surface area due to the mesoporosity, while other aspects such as ionic strength, attractive interaction between probe molecules and silica walls, as well as multiple cycles, e.g. in electrochemical investigation via cyclic voltammetry, further affect the chemical stability.[343-344] Hence, the time scale in applications such as permselective sensors, drug delivery devices, and separation membranes have to be considered.[344] Recently, *ten Elshof* and co-workers studied the hydrothermal stability of organosilicas, i.e. organically bridged silsesquioxanes compared to pure silica derived from the precursor TEOS, for example.[345] Thereby, significant improvement of the chemical stability, not only in acidic, but as well in basic environment was observed for bridged precursor molecules with two or more CH_2 bridging units.[345] Mesoporous materials generated by applying silica precursors with two CH_2 bridging units, and the surfactant assisted approach were firstly demonstrated by *Inagaki* and co-workers in 1999 that used octadecyltrimethylammonium chloride as structure directing template.[346] Further studies have also applied the common surfactants CTAB[347-349] and Pluronic® P123[350]. By that, *Melde* et al. observed an improved hydrothermal stability of

mesoporous organosilicas compared to pure silica MCM-41 analogously prepared.[347] However, in this study no explicit pH value was mentioned nor adjusted, thus the effect on the chemical stability at basic conditions was not explicitly investigated. To address an improvement of chemical stability, also in basic environment, MSTFs prepared by applying a bridged silica precursor and the structure directing template Pluronic® F127 are discussed in the third subchapter. The last subchapter of the mesoporous film material library focuses on structure directing templates used in the preparation process of MSTFs, since research nowadays focuses on the development of porosity and ordered mesoporous materials derived from sustainable biomass raw materials or biomolecules.[42] By that, cellulose derivates have gained tremendous attraction, since these are cheap, easily available, and hold a whole range of structural motifs.[351-352] For example, *MacLachlan* and co-workers generated free-standing micro-scale thick mesoporous silica and titania films templated with cellulose nanocrystals.[353-354] The resulting helical pore structure of the mesopores showed tunable chiral reflectance across the entire visible spectrum and into the near-infrared towards possible applications in optical filters or reflectors, for example.[353-354] *Thomas* and *Antonietti* used the cellulose derivate HPC as a template to generate macroscopic mesoporous silica, as HPC is known to form nematic structures in water with very well defined cholesteric superstructures.[351] Investigations of the porous silica through polarization microscopy, circular dichroism, along with TEM and sorption measurements indicated that the complex hierarchical superstructure is essentially kept in the solid hybrid materials and also replicated as a pore structure into the calcined silica.[351] Encouraged by the scientific works discussed above, MSTFs were prepared by using hydroxypropyl cellulose as structure directing template, and were investigated with respect to their chemical composition, structural properties, as well as ionic pore accessibility.

5.1.1. Ionic pore accessibility of hydrophilic MSTFs

In this paragraph, the MSTFs mainly used in this work that result in MSTFs with different pore sizes, respectively, are discussed with respect to the thin film properties in dependence of preparation parameters, along with the determination of ionic pore accessibility.

In the context of mesoporous thin film architectures and the functionalization of the pore wall, MSTFs with different pore sizes have been applied in this work ensuring the functionalization agents can enter the porous structure. For the preparation and investigation of hierarchical mesoporous architectures, along with the investigation of a local and controlled functionalization strategy thereof, MSTFs with high homogeneity together with uniform pore size and structure (pore orientation perpendicular to the substrate) are required. Further, the preparation of mesoporous multilayer thin films with respect to the formation of step gradients

requires pore connections between the individual layers to study the pore accessibility, if mass transport through the porous material shall be provided. The EISA process in combination with dip coating is a well-established method for the deposition of mesoporous thin films on flat substrates. Together with *Robert Brilmayer*, investigation of the ionic pore accessibility by comparing two methods for template removal – either by calcination or acidic ethanol extraction – was performed, which resulted in temperature treatment dependent permselective behavior. Thin films that have been treated up to 200 °C show more intense the pre-concentration of the positively probe molecule at basic conditions due to electrostatic attraction of an increased number of deprotonated, thus negatively charged surface silanolate groups as compared to thin films that have been calcined at 350 °C. This is consistent to the observation of a higher silanol vibration at ~950 cm^{-1} in the attenuated total reflection fourier transform infrared (ATR-IR) spectrum for MSTFs that were treated up to 200 °C as compared to MSTFs that were treated up to 350 °C indicating a lower degree of silica condensation at lower temperatures.[355]

The deposition of multilayer films using dip-coating can be quite time-consuming, as each layer has to be thermally stabilized to avoid dissolution before deposition of the following layer. Furthermore, thin films deposited via dip coating exhibit substrate rim effects that result in inhomogeneities of the film thickness on the edges of the substrate. *Nicole Rath* (born *Herzog*) *Anastasia Kalyta*, and *Dieter Spiehl* demonstrated that film thickness of MSTFs can be adjusted in a controlled manner, from a few tens up to several hundred nanometers, by variation of process parameters such as the withdrawing speed in the dip coating process, and by variation of the cylinder cell depth along with the contact force in the process of gravure printing for two different formulations resulting in MSTFs with a pore size of 3-8 nm and 8-16 nm respectively. Thereby, the thin films deposited via gravure printing show higher homogeneity, since no substrate rim effects are present. Furthermore, the deposition of thin films is much faster applying gravure printing and does not require thermal stabilization of individual layers in case of the preparation of multilayer thin films. In addition, less precursor solution is necessary by using gravure printing as compared to dip coating.

Contribution to the publication in RSC Advances, 2019, 9, 23570: Together with Robert Brilmayer, who developed mesoporous silica thin films with enlarged pore size, investigation and data curation of cyclic voltammetry measurements of single layer mesoporous silica thin films prepared via dip coating in dependence of the template removal were performed. This allowed the correlation of template removal on the concentration of surface silanol groups. Furthermore, I contributed to the data discussion with respect to the chemical composition and structural properties in dependence of withdrawing speeds in the dip coating process, especially with respect to IR characterization. Nicole Rath (born Herzog), Dieter Spiehl (Institute of Printing Science and Technology, TU Darmstadt) and Anastasia Kalyta developed the preparation of mesoporous silica thin films via gravure printing. Structural characterization using ellipsometry and scanning electron microscopy, characterization of chemical composition using ATR-IR spectroscopy, and investigation of ionic pore accessibility using cyclic voltammetry of gravure printed mesoporous silica thin films were performed by Nicole Rath. Furthermore Nicole Rath prepared double layered mesoporous silica thin films using gravure printing as well as performed functionalization thereof together with the characterization using ellipsometry, ATR-IR spectroscopy, and cyclic voltammetry. Edgar Dörsam (Institute of Printing Science and Technology, TU Darmstadt) was intensively involved in discussions with respect to gravure printing as preparation method for mesoporous silica thin films. Christian Hess (Eduard-Zintl-Institut für Anorganische und Physikalische Chemie, TU Darmstadt) provided access to XPS measurements and was involved in data curation of such. Annette Andrieu-Brunsen acquired funding, supervised the project and supported in manuscript writing.

The results of this paragraph are published in *RSC Advances*:

Nicole Herzog, Robert Brilmayer, Mathias Stanzel, Anastasia Kalyta, Dieter Spiehl, Edgar Dörsam, Christian Hess, Annette Andrieu-Brunsen, **Gravure printing for mesoporous film preparation**, *RSC Advances*, **2019**, 9, 23570.

The Supporting Information is not replicated here, but can be found in the electronic version of the article (DOI: 10.1039/c9ra04266k).

Check for updates

Gravure printing for mesoporous film preparation†

Nicole Herzog,[a] Robert Brilmayer,[a] Mathias Stanzel,[a] Anastasia Kalyta,[a] Dieter Spiehl, [b] Edgar Dörsam, [b] Christian Hess [c] and Annette Andrieu-Brunsen [*a]

This study presents gravure printing as a new strategy for rapid printing of ceramic mesoporous films and highlights its advantages over conventional mesoporous film preparation using evaporation induced self-assembly together with dip-coating. By varying the printing process parameters, the mesoporous coating thicknesses can be adjusted between 20 and 200 nm while maintaining a very high film homogeneity allowing the printing of ultrathin mesoporous films. Step gradients in film composition are accessible by consecutively printing two different "inks". Thereby, gravure printing is a much faster process than mesoporous single- and multilayer preparation using conventional dip-coating because lower amounts of solution are transferred and dissolution of previously deposited layers is avoided. The effect of printing process parameters on resulting film characteristics as well as the resulting mesoporous film's ionic accessibility is systematically investigated.

Introduction

Printing is a powerful tool for manufacturing thin films and coatings. Mesoporous ceramic coatings or thin films are of special interest because they provide an ordered porous framework able to include a variety of functional molecules, resulting in hybrid materials with organized and specific features such as a large surface area and functionalized mesopore walls. These features enable tuning of material characteristics such as ionic permselectivity or optical properties.[1–3] Therefore, functional mesoporous materials and coatings play a key role in many technological applications such as nanoscale reaction vessels, sensors, optics, separation, catalysis or lab on chip devices.[4–12] Commonly, mesoporous ceramic coatings are prepared by Evaporation-Induced Self-Assembly (EISA) and sol–gel chemistry using a dip- or spin-coating process.[13] Within this process mesoporous film characteristics, especially the film thickness, can be easily adjusted by varying the solvent or withdrawal speed and by varying the geometry of the solution level within the solution reservoir.[14,15] Despite this versatility, the fabrication of structured or patterned films as well as the automated fabrication of complex coating architectures or ultrathin films of interest e.g. in electronic applications, is not

easily possible and film homogeneity, especially with respect to film thickness, varies significantly within the coating. For example, composition control along the film thickness by dip-coating requires multiple dip-coating steps with intermediate temperature-stabilization, to avoid dissolution of previous layers. Aside from being very time consuming, this procedure affects film homogeneity along the film thickness. In addition, substrate rims induce film inhomogeneities, limiting the fabrication of small patterns, for example those desired in microelectronic devices. As another example ultrathin mesoporous films with film thicknesses down to 10 nm, of interest e.g. in electronic devices, have been recently prepared by wet-etching previously deposited films.[16] Printing such films would be much faster and allow much more precise local control. Interestingly, only a few examples of ink-jet printed, structured mesoporous coatings are reported. A technology allowing the construction of highly defined multiple layer and step gradient coatings with the potential for scale up is still missing.[17–19] Nevertheless, porous structures with well controlled compositions along the film thickness are of special interest in advanced molecular transport control and porous material compartmentalization, and thus in technologies such as sensors, separation or energy conversion. Consequently, a technology allowing homogeneous large area coatings as well as structured deposition while being scalable to an industrial scale that is fast and allows well defined multilayer generation at the nanoscale is required.

These criteria are fulfilled by printing technologies. With respect to mesoporous materials, printing is mainly based on paste printing usually to fabricate net-like macroscopic architectures of mesoporous silica, mostly intended to be used for cell growth.[20,21] Thereby ordered mesoporous structures such as

[a]Ernst-Berl Institut für Technische und Makromolekulare Chemie, Technische Universität Darmstadt, Alarich-Weiss-Str. 4, D-64287 Darmstadt, Germany. E-mail: andrieu-brunsen@smartmem.tu-darmstadt.de

[b]Institute of Printing Science and Technology, Technische Universität Darmstadt, Magdalenenstr. 2, D-64289 Darmstadt, Germany

[c]Eduard-Zintl-Institut für Anorganische und Physikalische Chemie, Technische Universität Darmstadt, Alarich-Weiss-Str. 8, D-64287 Darmstadt, Germany

† Electronic supplementary information (ESI) available. See DOI: 10.1039/c9ra04266k

hexagonally arranged mesopores have been demonstrated.[20] Only a few studies focus on printing with higher local resolution. For example, Kotz *et al.* show the possibility to print fused silica 3D structures by using stereolithography.[22] Instead of a sol used for EISA-based dip-coating, SiO_2 particles within a UV-curable polymer are applied. Thereby, the polymer matrix stabilizes the 3D structure upon hardening with UV-light followed by sintering resulting in a silica structure. This approach allows the design of transparent 3D silica structures but does not directly allow printing of ordered mesoporous 3D materials. Other experiments to create a 3D ceramic structure are based on ink-jet printing using a layer-by-layer approach, depositing ceramic suspension micro droplets ejected *via* nozzles.[23–25] Additionally, the group of Brinker demonstrated silica nanostructures prepared by micro-pen lithography and ink-jet printing. Printing is performed with functional organosilanes on patterned self-assembly monolayers, which leads to functional, hierarchically organized structures.[17] Unfortunately, ink-jet printing of microdot arrays of mesoporous silica is limited by the homogeneity of the dots. For optimal results this technique is limited to hydrophobic organosilanes as co-condensates.[26] The hydrophobic organosilanes are required to avoid clogging of the nozzle aperture.[27]

Currently, gravure printing is explored as an alternative fabrication process to be combined with sol–gel chemistry. A recent study published in 2018 demonstrates gravure printing of silica nanoparticles for metal oxide thin film formation.[28] Gravure printing has not yet been used to generate ordered mesoporous silica coatings. Thereby, gravure printing of mesoporous architectures bares a strong potential for automated thin film production with highly defined composition. As a roll to roll process it allows relatively high manufacturing speed of up to 15 ms^{-1} at up to 4 m width.[29] For example, literature describes gravure printing as a good candidate for thin film production in electronics as it allows high throughput, high control of film characteristics and provides the opportunity to print well-defined multiple layers.[30] With respect to production of complex mesoporous film architectures, gravure printing bares the potential to generate more homogeneous films in much shorter production time as compared to established EISA using dip- or spin-coating and ink-jet printing. In addition, standardization and automation of the film preparation process as well as complex film architecture fabrication should be relatively easy. Combining structuring by gravure printing with different sol inks and co-condensation approaches, known from conventional sol–gel chemistry, and using subsequent post-functionalization strategies further supports complex film architecture design. In general, gravure printing allows nanoscale adjustment of film thickness and film homogeneity based on the substrate, ink viscosity, cell volume, printing speed and printing force. Consequently, smart process design is expected to not only allow the deposition of nanometer thick, homogeneous, and structured mesoporous film architecture in an automated fashion but also layer selective functional placement.

Here, we establish gravure printing as a rapid and scalable process to prepare homogeneous mesoporous thin film architectures with nanoscale thickness resolution, including multilayer and thus step gradient design, using layer-selective *in situ* functionalization exemplified for co-condensation of amine functional groups. The gravure printed mesoporous silica film properties, especially ionic mesopore accessibility, are compared to films prepared *via* conventional dip-coating based evaporation induced self-assembly. The gravure printing process has been optimized by exploring different curing processes and their influence on functional film properties. Regarding functional film properties mesopore ionic permselectivity and the apparent pK_a values of silanol groups in the confinement of printed mesopores have been explored.

Results and discussion

The mesoporous silica film preparation process combining evaporation induced self-assembly (EISA) and gravure printing is schematically shown in Fig. 1 and compared to conventionally used dip-coating. The working principle of the gravure printing process starts with filling the cells of the rotating gravure cylinder in an inking unit. A doctor blade removes excess ink so that a defined amount of ink remains within the cells. The layout of the cells determines the printed layout. After further rotation of the cylinder, the cells come into contact with the substrate and most of the ink is transferred onto it. On the substrate, these transferred dots of ink start to merge into a homogeneous layer and the solvent evaporates. Thereby the influence of process parameters such as the cell volume, printing force, withdrawal speed and co-condensate solution composition are systematically controlled and the effect on film characteristics such as film thickness, porosity, and morphology is investigated. In general, gravure printing produces very homogeneous mesoporous silica films on large areas (here 6 × 20 cm^2) in an automated fashion. Micrometerscale patches are accessible printing individual spots (Fig. S1b†).

Gravure printed *versus* dip-coated mesoporous film characterization

Structural characterization by transmission electron microscopy (TEM) reveals similar mesoporous structures with pores 6–8 nm in diameter (Fig. 2a and b) for dip-coated and gravure printed mesoporous films. Furthermore, SEM images (ESI Fig. S2†) do not show any microscale cracks or structural defects. Gravure printed films appear to be very homogeneous microscopically as well as macroscopically as deduced from very homogeneous optical interference colors (Fig. 2d). Notably, substrate rim effects resulting in thicker films close to the substrate rims are absent when using gravure printing, as observed in electron microscopy and based on the reflected interference color visible for mesoporous films printed onto silicon wafer substrates (Fig. 2e and f). This makes gravure printing a versatile technique to print homogeneous microscopically small area mesoporous film architectures. In contrast to dip-coating, gravure printing easily allows for film thickness and film composition patterns and gradients by adjusting
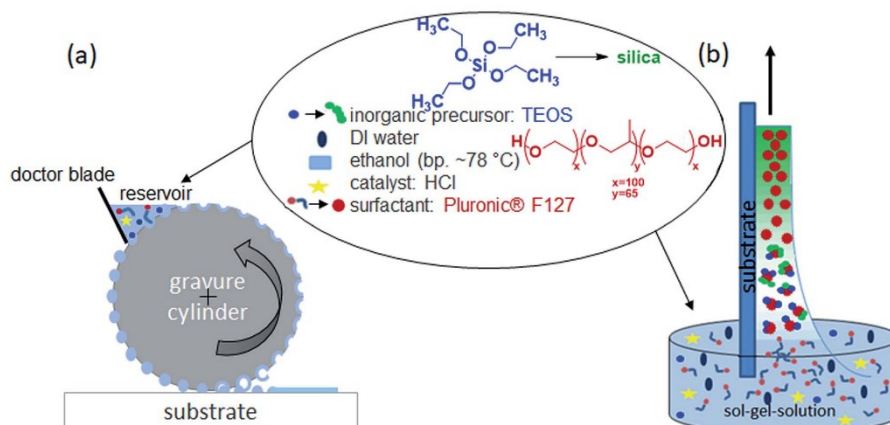
Fig. 1 Comparison of the two mesoporous film preparation strategies, evaporation-induced self-assembly (EISA) by dip-coating or gravure printing. (a) Gravure printing using a metal cylinder transferring the "ink" (sol–gel-solution) to the substrate. The ink is filled out of a reservoir into the cells of the gravure cylinder and directly transferred to the substrate. Excess ink is scraped off by a doctor blade. The cells are not completely emptied, as it comes to a film splitting. The settled fluid spots on the substrate extend to a surface at appropriate ratios of the surface tension of fluid and substrate. The arrangement of the cells specifies the layout to be printed film. The layout repeats after one cylinder revolution. (b) Conventional dip-coating process based on withdrawing a substrate with a defined speed from the sol–gel-solution. The film thickness and quality mainly depends on the used withdrawal speed, solution viscosity and substrate wetting.
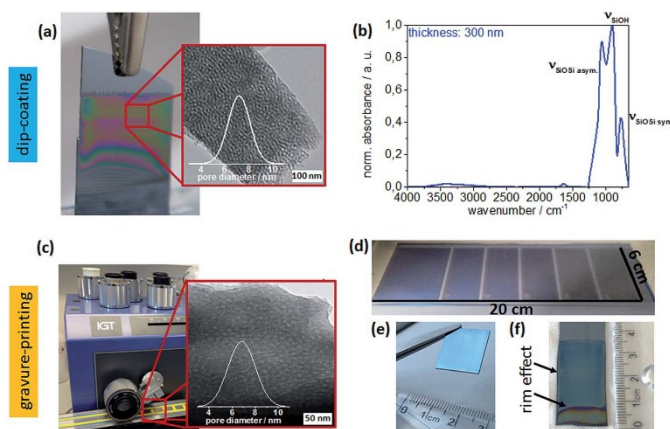
Fig. 2 Comparison of dip-coating (a, b and f) and gravure printing (c–e) as a mesoporous thin film preparation process. (a) Photograph of the dip-coating process as well as TEM image of a mesoporous silica film prepared by dip-coating with a withdrawal speed of 2 mm s^{-1} and template calcination at 350 °C showing a statistic pore distribution (7.2 ± 0.8 nm). (b) Infrared spectra of the mesoporous film after template calcination at 350 °C measured directly on a glass substrate. (c) Photograph of gravure printed mesoporous silica films and a TEM image of mesoporous silica prepared by gravure printing and calcination at 350 °C using a cylinder with a cell volume of 8.5 mL m^{-2} with a statistic pore distribution (6.8 ± 1.2 nm). (d) Photograph showing the homogeneity of gravure printed mesoporous silica films with different cylinder cell volume field (9.19 mL m^{-2}, 8.3 mL m^{-2}, 5.98 mL m^{-2}, 4.71 mL m^{-2}, 2.72 mL m^{-2} and 1.67 mL m^{-2} from left to right). By using gravure printing, it is possible to print mm-scale patterns. Substrate size is demonstrated with 6 cm × 20 cm. The different film thickness is visible by the different interference colors. (e) Image of a printed homogeneous mesoporous silica film prepared with a cell volume of 8.5 mL m^{-2}. (f) Image of a dip-coated mesoporous silica film prepared with 2 mm s^{-1} withdrawal speed. Inhomogeneity's because of edge effects are indicated by the black arrow and are visible by a colour change at the end of the substrate indicating a different film thickness originating from drop formation during dip-coating (rim effects).

62

gravure cylinder cell volume and sol composition (ink), respectively. Without special optimization, our experiments allow resolution down to 10–20 nm for film thickness while maintaining film homogeneity (Fig. 3) allowing to homogeneously print ultrathin mesoporous films. In accordance with literature, film thicknesses between 60 nm and 400 nm are achieved by dip-coating upon varying the withdrawal speed between 0.05 and 30 mm s^{-1} as shown in Fig. 2b.[31] In gravure printing, the film thicknesses and homogeneity is mainly determined by the cell volume of the grounded cylinders (we used a range from 1.6 to 24 mL cm^{-2}) resulting in film thickness variation between 20–240 nm (Fig. 3b) for a contact force of 500 N. In addition, film thickness can be tuned by varying the contact force between gravure cylinder and substrate. Increasing contact force from 500 N to 700 N leads to increasing film thickness of 10–20 nm (ESI, Fig. S3†). Consequently, gravure printing yields thinner homogeneous films compared to dip-coating. Porosity (pore volume) of 40–45 vol% as calculated from ellipsometry data (refractive index) using Brügge-mann effective medium approximation (please refer to the ESI, Tables S1–S3†) is detected for dip-coated as well as gravure printed films. High refractive indices resulting in low porosities of below 20 vol% are observed only when very small cell volumes of less than 1.67 mL cm^{-2} are used. This can be attributed to insufficient ink transfer resulting in inhomogeneous film

formation (ESI, Fig. S1†), which is supported by SEM and microscopy results. Using a critical cell volume (above 2 mL cm^{-2}) seems to be crucial for obtaining homogeneous mesoporous silica films by gravure printing with a comparable pore volume to dip-coated mesoporous silica films.

Changing the ink composition can introduce functional groups into the mesopore wall (co-condensation) and produce films with varying pore diameters. Here, we demonstrate pore diameters of about 16 nm instead of about 8 nm. These films show higher film thickness under identical gravure printing or dip-coating conditions and the calculated pore volume is slightly larger reaching up to 70 vol% (ESI, Tables S4 and S5†). Interestingly, film thickness variation for these films is more sensitive to withdrawal speed and cylinder volume (ESI, Fig. S2†) allowing a thickness variation range of 750 nm between film thickness of 250–1000 nm.

Functional integrity is characterized by using ATR-IR of 350 °C calcinated mesoporous silica films deposited on glass substrates. Three different silica stretching vibrational bands are observed (Fig. 2b):[32] the asymmetric stretching vibration of bridged Si–O–Si at 1260–1000 cm^{-1} and the symmetric stretching vibration of Si–O–Si ring structure at around 800 cm^{-1}, both originating from the silica network Si–O–Si as well as the stretching vibrational band of free silanol (Si–OH) groups in the range of 900–980 cm^{-1}. Based on these ATR-IR results no significant difference within the chemical structures, such as degree of silica condensation, can be observed for mesoporous silica films prepared under different process conditions or location on the supporting substrate (compare as well Fig. S4†).

Gravure printed mesoporous film performance

With respect to technological applications, such as separation, sensing, or catalysis, performance-limiting mesoporous film characteristics are mesopore accessibility and ionic permselectivity. Mesoporous silica ionic permselectivity and mesoporous silica film ionic uptake capability is mainly determined by structural characteristics such as pore size and porosity, together with pore wall functionalisation depending interface characteristics such as charge but might as well be affected by mesoporous film thickness. Walcarius and co-workers for example demonstrate an increasing peak current in cyclic voltammetry, representing, according to Nernst equation, an increasing molecule concentration, with increasing number of mesoporous silica layers produced by dip-coating.[33] As gravure printing allows very precise adjustment of homogeneous mesoporous layer thickness the correlation of film thickness and ionic permselectivity is shown in Fig. 4 as detected by the maximum peak current density deduced from cyclic voltammetry. Ionic mesopore accessibility of gravure printed and dip-coated mesoporous silica thin films with increasing film thickness using anionic and cationic probe molecules $[Fe(CN)_6]^{3-/4-}$ and $[Ru(NH_3)_6]^{2+/3+}$ at acidic and basic pH are compared. Thereby film stability has to be considered as recently demonstrated by Alberti et al.[34] Within the discussed experiments, cycling time has always been kept below 6
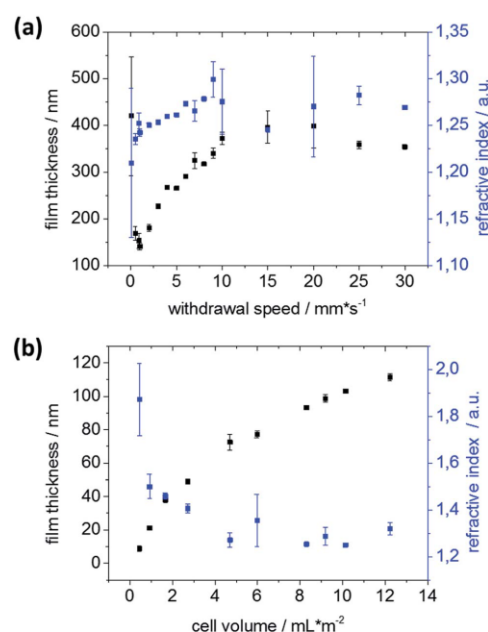

Fig. 3 (a) Film thickness (black) and refractive index (blue) determined by ellipsometry in dependence of the dip-coating withdrawal speed. (b) Film thickness (black) and refractive index (blue) determined by ellipsometry in dependence of the cell volume of the used gravure printing cylinder.
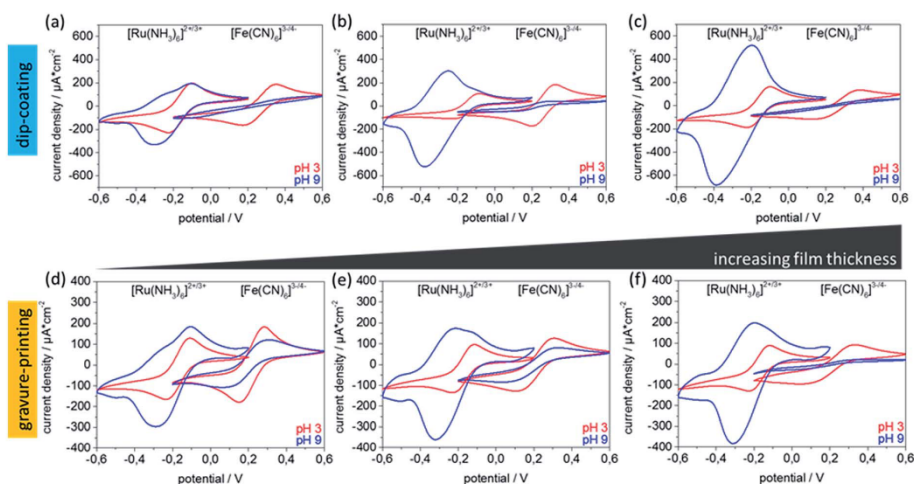
Fig. 4 Cyclic voltammograms of mesoporous silica thin films using $[Ru(NH_3)_6]^{2+/3+}$ (-0.6 to $+0.2$ V) and $[Fe(CN)_6]^{3-/4-}$ (-0.2 to $+0.6$ V) as an ionic redox probes at pH 3 (red) and 9 (blue). The dip-coated mesoporous silica films are prepared with different withdrawal speeds (a) 0.5 mm s^{-1} (b) 2 mm s^{-1} and (c) 10 mm s^{-1} resulting in film thicknesses of (a) 140 nm (47 vol% porosity), (b) 180 nm (44 vol% porosity), (c) 300 nm (39 vol% porosity). Mesoporous silica films prepared by gravure printing are prepared using different cell volumes of (d) 8.5 mL m^{-2} (e) 16.3 mL m^{-2} and (f) 24 mL m^{-2} resulting in film thicknesses of (d) 100 nm (48 vol% porosity), (e) 162 nm (40 vol% porosity), (f) 250 nm (48 vol% porosity).

minutes and a strict data quality control has been applied ensuring stable and reproducible cyclic voltammograms as described in Experimental section and Fig. S13.† At basic pH values (Fig. 4a–c blue) the silica mesopore wall is negatively charged due to deprotonated silanol groups. Under these conditions an exclusion of $[Fe(CN_6)]^{3-/4-}$ due to overlapping Debye screening layers reflected by zero maximum peak current density (j_p) as well as a preconcentration of positively charged $[Ru(NH_3)_6]^{2+/3+}$ in the silica mesopores reflected by increased maximum peak-current densities and peak broadening is expected. At acidic pH, and thus neutral pore wall charge, no ion discrimination in pore accessibility and thus similar j_p is expected. In accordance with this expectation both probe molecules show similar, and thickness independent, maximum peak currents at acidic pH (Fig. 4, red). As well in accordance with expectation, electrostatic exclusion of $[Fe(CN_6)]^{3-/4-}$ at basic pH is observed indicating a defect-free film structure. Except for very thin films with a film thickness of below 100 nm a thickness dependent peak current reduction is observed (Fig. 4d–f). Interestingly, the preconcentration of $[Ru(NH_3)_6]^{2+/3+}$ at basic pH and the simultaneously observed broadening of the cyclic voltammograms seems to be film thickness and thus preparation process dependent, although no direct correlation can be drawn due to the dependence on multiple parameters especially on the free electrode area which is not directly accessible. Reference measurements of unmodified ITO electrodes are shown in Fig. S5.† These are not showing any peak broadening or preconcentration at basic or acidic pH values. In addition, the ATR-IR spectra (Fig. S4†) do not show differences in the Si–O–

Si to Si–OH ratio in dependence of film thickness or preparation process, and ellipsometry indicates comparable pore volumes for all investigated films. Together, this indicates that the variation of Si–O–Si$_{asym./sym.}$ to Si–OH band intensity with varying cylinder volume is probably caused by the mesoporous film thickness but not by a difference in Si–OH concentration and thus charge density at the mesopore wall. In addition, data evaluation using Randles–Sevcik's equation (Fig. S6†) indicates that non-diffusional transport becomes significant for mesoporous films thicker than 250 nm for basic pH values and positively charged probe molecule and thus with existing attractive electrostatic interaction between pore wall and diffusing ions. This is reflected by a non-linear correlation of peak currents to the square root of scan rates. All these results indicate good accessibility and a comparable behavior for gravure printed to dip-coated mesoporous silica films.

Gravure printing of complex mesoporous film architectures

Besides the opportunity of printing different inks and thus creating gradient architectures, an advantage of mesoporous film gravure printing is the rapidity of the printing process itself. The very short contact time between supporting substrate and the sol–gel solution leads to fast drying, avoiding penetration of sol into a pre-printed layer and thus facilitating complex but homogeneous, defect-free multilayer fabrication. This allows printing of multiple mesoporous silica layers directly on top of one another without using stabilizing temperature treatments between layer deposition steps, which may negatively affect film homogeneity. Specifically, two-layer
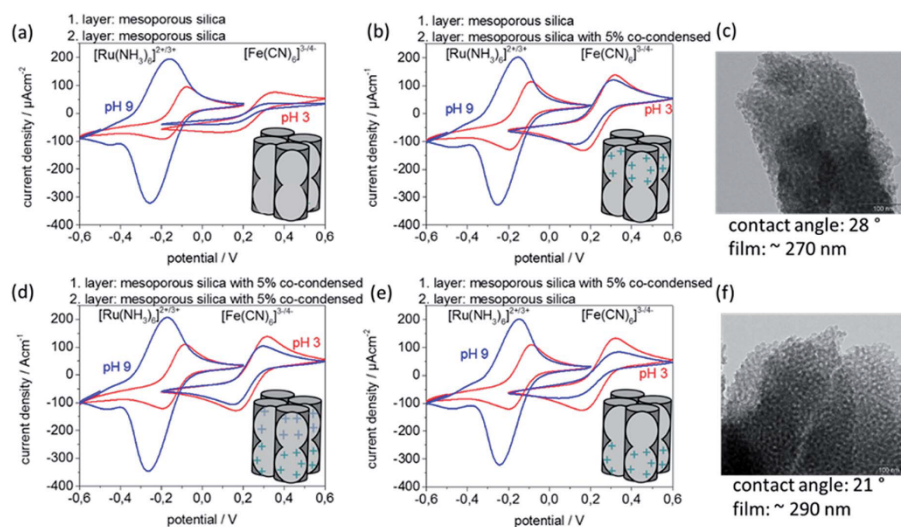
Fig. 5 Cyclic voltammograms of mesoporous silica thin films using $[Ru(NH_3)_6]^{2+/3+}$ and $[Fe(CN)_6]^{3-/4-}$ as ionic redox probes at pH 3 (red) and 9 (blue). Mesoporous silica films prepared by gravure printing are prepared using the cell volumes 8.5 mL m^{-2} resulting in film thicknesses 150 nm for one layer and 300 nm for two layers. (a) Two gravure printed layers of unfunctionalized mesoporous silica. (b) Two gravure printed layers consisting of a first mesoporous silica layer and a second mesoporous silica layer containing 5 mol% co-condensed (bis(2-hydroxyethyl)-3-aminopropyl-triethoxysilane) (c) TEM image of a two-layer mesoporous silica film prepared by gravure printing with two different inks corresponding to (b). (d) Two gravure printed layers of 5 mol% co-condensed mesoporous silica. (e) Two gravure printed layers consisting of a first mesoporous silica layer containing 5 mol% co-condensed (bis(2-hydroxyethyl)-3-aminopropyl-triethoxysilane) and a second mesoporous silica layer, (f) TEM image of a two-layer mesoporous silica film prepared by gravure printing with two different inks. The first layer consists of mesoporous silica with 5 mol% co-condensed (bis(2-hydroxyethyl)-3-aminopropyl-triethoxysilane) and a second layer of unfunctionalized mesoporous silica. The mesoporous films are thermally treated up to 200 °C and template extracted with acidic ethanol.

gravure printed mesoporous silica films using two different inks resulting in two different functional layers are prepared (Fig. 5). The corresponding characterization concerning porosity, contact angles, temperature treatment dependent ionic permselectivity, and morphology are summarized within the ESI (Fig. S9–S11 and Table S6†). Thereby it must be considered that layer functionalization by co-condensation of organic functional groups limits the maximum applicable temperatures, here to 200 °C. Successful multilayer step gradient preparation is as well supported by XPS measurements (ESI, Fig. S12 and Table S7†). XPS results show one nitrogen atom per seven Si-atoms after printing two layers of 5 mol% co-condensed mesoporous silica. When printing one layer of 5 mol% mesoporous co-condensed silica followed by a second top layer of mesoporous silica only one nitrogen atom per 32 Si-atoms is detected by XPS. Printing 5 mol% mesoporous co-condensed silica on top of mesoporous silica leads to one nitrogen atom per 17 Si-atoms. The reference sample of two printed mesoporous silica layers shows no nitrogen within the XPS. The discussed double layer gravure printed films (Fig. 5) have a film thickness around 280 nm. According to this estimation XPS detects around 10 nm of the entire film.[35]

In Fig. 5 cyclic voltammetry measurements of double layer gravure printed films consisting of one mesoporous silica layer

and one mesoporous silica containing 5 mol% of co-condensed (bis(2-hydroxyethyl)-3-aminopropyl-triethoxysilane) are depicted. The cyclic voltammograms for two layer films consisting of two identical layers of mesoporous silica, measured as reference, are comparable to those shown above for one layer with a comparable film thickness (Fig. 5a and 4d) co-condensation of (bis(2-hydroxyethyl)-3-aminopropyl-triethoxysilane) results into inclusion of amino groups with a pK_a value around 8 inducing a change of the mesopore wall charge. This results in a reduced exclusion of the negatively charged probe molecule $[Fe(CN)_6]^{3-/4-}$ at pH 9 visible by a detected j_p of 100 μA cm^{-2} instead of 30 μA cm^{-2} for unmodified mesoporous silica (Fig. 5d). When printing two layers as a step gradient with different functional composition and individual film thicknesses of 140 nm, here mesoporous silica and 5% co-condensed mesoporous silica (Fig. 5b and c), the top layer which is in contact with the probe molecule solution seems to determine the overall transport characteristics. When the 5 mol% co-condensed mesoporous silica film is located on top (Fig. 5b) the observed pore accessibility is very similar to the pure 5 mol% co-condensed mesoporous silica layers (Fig. 5d) showing no exclusion of $[Fe(CN)_6]^{3-/4-}$ at pH 9. But when the unmodified mesoporous silica layer is located on top of a 5 mol% co-condensed mesoporous film the exclusion of negatively charged $[Fe(CN)_6]^{3-/4-}$ at pH 9 is again observed (Fig. 5e).

65
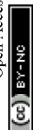
Experimental section

Mesoporous silica film preparation

Mesoporous silica films are synthesized *via* sol–gel-chemistry using tetraethyl orthosilicate (TEOS) in the presence of the template Pluronic® F127. The precursor solutions (1TEOS : 0.0075F127 : 40EtOH : 10H$_2$O : 0.2HCl) resulting in 8 nm mesopores or (1TEOS : 0.02F127 : 40EtOH : 34.5H$_2$O : 0.08HCl)[36] resulting in 16 nm mesopores or ((1 − *x*)TEOS : *x*(bis(2-hydroxyethyl)-3-aminopropyl-triethoxysilane) : 0.0075F127 : 40EtOH : 10H$_2$O : 0.2HCl) with *x* being between 0 and 25 mol% are stirred for 24 h at room temperature before being used to produce mesoporous silica films by evaporation induced self-assembly (EISA)[13] on silicon wafer, glass, or indium tin oxide coated glass substrates at 40–50% relative humidity and 298 K.

Dip-coating

The mesoporous silica films are dip-coated using varying withdrawal speeds between 0.1 and 30 mm s^{-1}. After deposition the films were kept at 50% relative humidity for 1 h followed by a stabilizing thermal treatment and extraction like for films treated to 200 °C. After successful film deposition a stabilizing thermal treatment is carried out in two successive 1 h steps at 60 and 130 °C. Consecutively, the temperature is increased to 350 °C, or to 200 °C, with a gradient of 1 °C min^{-1}. This final film stabilization temperature is applied for 2 h. Finally, the films treated up to 350 °C are rinsed with ethanol and stored under ambient conditions. Template extraction of the films, treated only up to 200 °C, are treated with acidic ethanol (0.01 M HCl in abs. ethanol) for 3 days to remove the mesopore template.

Gravure printing

The mesoporous silica films are gravure printed using a laboratory scale gravure printing machine G1-5 (IGT Testing Systems) with different gravure cylinder cell volumes between 0.2 and 24 mL m^{-2}. A printing speed of 0.6 m s^{-1} and a printing force of 700 N are used. Freshly deposited films are stored at 50% relative humidity for 1 h. In case of printing two layers the cylinder with 8.5 mL m^{-2} cell volume was used. Between the first and the second layer an aging time of 10 min is used. After deposition of the second layer films were kept at 50% relative humidity for 1 h followed by an identical stabilizing thermal treatment and chemical template extraction used for dip-coated films treated up to 200 °C: after successful film deposition a stabilizing thermal treatment is carried out in two successive 1 h steps at 60 and 130 °C. Consecutively, the temperature is increased to 350 °C, or to 200 °C in case of co-condensed mesoporous silica films, with a gradient of 1 °C min^{-1}. This final film stabilization temperature is applied for 2 h. Finally, the films treated up to 350 °C are rinsed with ethanol and stored under ambient conditions. Template extraction of the films with co-condensed organic groups, treated only up to 200 °C, are treated with acidic ethanol (0.01 M HCl in abs. ethanol) for 3 days to remove the mesopore template.

Infrared spectroscopy (IR)

IR is performed using a Spectrum One (PerkinElmer) instrument in attenuated total reflection mode. The measured spectra are automatically background corrected, measured at glass surface and normalized to the Si–OH vibrational band at 912 cm^{-1}.

Ellipsometry

Film thicknesses and refractive indices are determined on silicon wafer substrates using a Nanofilm EP3 imaging ellipsometer. One zone angle of incidence (AOI) variation measurements are captured between AOIs of 38 and 68° using a 658 nm laser. The relative humidity is constantly adjusted to 15% using a humidity control (ACEflow, Solgelway). The apparent film thickness and refractive indices are calculated from the measured angles Ψ and Δ using the EP4 analysis software supplied with the instrument. The fitting parameters for the silicon oxide layer thickness on the wafer substrate ($d(\text{SiO}_x) =$ 2.8 nm) are measured separately. The measured data is fitted with a one-layer box model. The fitting program is allowed to vary film thickness of the mesoporous silica thin films between 100 and 500 nm and the refractive index between 1.1 and 1.7. All films are measured at three defined positions before and after each functionalization step. Changes in film thickness and refractive index are calculated for each specific position. Error bars result from the changes in *n* and *d* at these three different positions. To determine the porosity from refractive indices the Brüggemann effective medium approximation was used as discussed elsewhere.[37,38]

Transmission electron microscopy (TEM)

TEM measurements are recorded using a FEI CM20 TEM microscope with a maximum resolution of 2.3 Å, equipped with a LAB-6 cathode and a charge coupled device camera (Olympus), using an acceleration voltage of 200 kV. Samples are scratched from substrate, dispersed in ethanol and sonicated. Subsequently, the suspension is placed onto a TEM grid.

Scanning electron microscopy (SEM)

Scanning electron microscopy (SEM) micrographs were acquired using a Philips XL30 FEG scanning electron microscope operated at an acceleration voltage of 30 kV. Samples are sputtered prior to analysis with a platinum/palladium layer of 3 nm using a Sputter Coater 208 HR comprising a thickness controller MTM-20 (both Cressington).

Cyclic voltammetry (CV)

Quantitative variations of ionic mesopore permselectivity are studied by following the changes of voltammetric peak currents associated with cationic $[\text{Ru(NH}_3)_6]^{2+/3+}$ and anionic $[\text{Fe(CN)}_6]^{3-/4-}$ redox probes. Cyclic voltammograms and thus maximum peak currents, are recorded using an Autolab PGSTAT302N (Metrohm). All probe molecule solutions are prepared with a concentration of 1 mM in 100 mM KCl as supporting electrolyte resulting in a pH 5–6 solution besides

measurements shown in ESI (Fig. S7†) which are measured in 150 mmol PBS solution as supporting electrolyte. Acidic or basic conditions (pH 3 and pH 9) are adjusted by adding a drop of a concentrated HCl or NaOH solution directly before starting the measurement. Mesoporous silica films are prepared on indium tin oxide (ITO) coated glass substrates being used as working electrode. An Ag/AgCl electrode (BASi RE-6) serves as reference electrode, and a carbon electrode as counter electrode. Various scan rates between 25 and 1000 mV s^{-1} are measured. The electrode area is 0.21 cm^2. Cyclic voltammetry data are strongly quality controlled by measuring the scanrate of 200 mV s^{-1} at the beginning and at the end of each scanrate variation. Only if both scans are comparable the data are further evaluated. In addition each scanrate is measured three times and the data is only further evaluated if these scans are comparable. Finally, the first pH-value is re-measured for all scanrates after screening all pH-values in between and the data are only further evaluated if the first and the last measurement of one pH series are comparable. For an example please refer as well to Fig. S13 (ESI†).

Contact angle

Macroscopic static contact angle measurements are performed using model TBU90E from company Dataphysics Instruments GmbH with the Program SCA-Software. The static contact angles are measured using a 1 μL s^{-1} rate with a final DI water drop volume of 2 μL.

X-ray photoelectron spectroscopy (XPS)

XP spectra were recorded on a SSX 100 ESCA spectrometer (Surface Science Laboratories Inc.) equipped with a monochromatic Al Kα X-ray source (100 W). XPS analysis reveals peaks at around 103 eV, 154 eV, 200 eV, 285 eV, 400 eV, 533 eV, and 1073 eV, which are attributed to Si2p, Si2s, Cl2p, C1s, N1s, O1s, and Na1s photoemissions, respectively.[39] The observed Si2p, Si2s and O1s peaks are consistent with the presence of silica, whereas the N1s peak originates from the nitrogen in the co-initiator. The presence of small amounts of K, Na, indium and Cl may result from indium-thin-oxide coated glass support substrate.

Conclusions

In summary, this study demonstrates the versatility of gravure printing for preparation of homogeneous, large area and complex architecture mesoporous coatings in comparison to conventionally used dip-coating. The resulting printed mesoporous silica films are more homogeneous and show no substrate rim effects even on very large areas. The fabrication of ultrathin homogeneous films down to a film thickness of 20 nm is possible and film thickness can be tuned by adjusting process parameters such as the printing cylinder cell depth and the contact force. Fast and homogeneous multilayer fabrication with nanoscale thickness resolution has been demonstrated relying on preventing sol incubation into bottom, pre-printed layers due to the controlled, low solution volume applied to

the substrate. Thereby, the achieved film properties, such as high porosity and pH-dependent ionic permselectivity, are comparable to dip-coated films. Using co-condensation and different sol compositions for gravure printing enables the fabrication of homogeneous multi-layer films with nanoscale step gradient in porosity, pore size, or layer functionalization and thus charge density. For such multilayer films the ionic permselectivity is influenced by the condensation degree of the mesoporous silica (due to temperature treatment), film thickness, and in case of double layer films with pore sizes below the Debye screening length and layer thicknesses of about 280 nm, seems to be determined by the second layer which is in contact with the probe molecule solution. Based on the advantages of gravure printing for mesoporous film preparation and its potential for automation and complex film architecture design we expect these results to impact scale up and application potential of mesoporous films.

Conflicts of interest

There are no conflicts to declare.

Acknowledgements

Notes and references

1 A. Walcarius, *Chem. Soc. Rev.*, 2013, **42**, 4098–4140.
2 P. Innocenzi and L. Malfatti, *Chem. Soc. Rev.*, 2013, **42**, 4198–4216.
3 G. J. Soler-Illia and O. Azzaroni, *Chem. Soc. Rev.*, 2011, **40**, 1107–1150.
4 M. E. Davis, *Nature*, 2002, **417**, 813–821.
5 G. M. Whitesides, *Small*, 2005, **1**, 172–179.

6 C. Burda, X. Chen, R. Narayanan and M. A. El-Sayed, *Chem. Rev.*, 2005, **105**, 1025–1102.

7 Y. Piao, A. Burns, J. Kim, U. Wiesner and T. Hyeon, *Adv. Funct. Mater.*, 2008, **18**, 3745–3758.

8 D. Grosso, F. Cagnol, G. J. A. A. Soler-Illia, E. L. Crepaldi, H. Amenitsch, A. Brunet Bruneau, A. Bourgeois and C. Sanchez, *Adv. Funct. Mater.*, 2004, **14**, 309–322.

9 J. Hwang, N. Shoji, A. Endo and H. Daiguji, *Langmuir*, 2014, **30**, 15550–15559.

10 A. Brunsen, A. Calvo, F. J. Williams, G. J. Soler-Illia and O. Azzaroni, *Langmuir*, 2011, **27**, 4328–4333.

11 A. Brunsen, J. Cui, M. Ceolin, A. del Campo, G. J. Soler-Illia and O. Azzaroni, *Chem. Commun.*, 2012, **48**, 1422–1424.

12 C. Sanchez, P. Belleville, M. Popall and L. Nicole, *Chem. Soc. Rev.*, 2011, **40**, 696–753.

13 C. J. Brinker, Y. Lu, A. Sellinger and H. Fan, *Adv. Mater.*, 1999, **11**, 579–585.

14 M. Faustini, C. Boissière, L. Nicole and D. Grosso, *Chem. Mater.*, 2013, **26**, 709–723.

15 E. Bindini, G. Naudin, M. Faustini, D. Grosso and C. Boissière, *J. Phys. Chem. C*, 2017, **121**, 14572–14580.

16 M. Kobayashi, K. Susuki, T. Otani, S. Enomoto, H. Otsuji, Y. Kuroda, H. Wada, A. Shimojima, T. Homma and K. Kuroda, *Nanoscale*, 2017, **9**, 8321–8329.

17 H. Fan, Y. Lu, A. Stump, S. T. Reed, T. Baer, R. Schunk, V. Perez-Luna, G. P. López and C. J. Brinker, *Nature*, 2000, **405**, 56–60.

18 T. Homola, M. Shekargoftar, P. Dzik, R. Krumpolec, Z. Ďurašová, M. Veselý and M. Černák, *Flexible Printed Electron.*, 2017, **2**, 035010.

19 T. T. Baby, R. Rommel, F. von Seggern, P. Friederich, C. Reitz, S. Dehm, C. Kubel, W. Wenzel, H. Hahn and S. Dasgupta, *Adv. Mater.*, 2017, **29**, 1603858.

20 F. Putz, S. Scherer, M. Ober, R. Morak, O. Paris and N. Hüsing, *Adv. Mater. Technol.*, 2018, 1800060, DOI: 10.1002/admt.201800060.

21 E. B. Duoss, M. Twardowski and J. A. Lewis, *Adv. Mater.*, 2007, **19**, 3485–3489.

22 F. Kotz, K. Arnold, W. Bauer, D. Schild, N. Keller, K. Sachsenheimer, T. M. Nargang, C. Richter, D. Helmer and B. E. Rapp, *Nature*, 2017, **544**, 337–339.

23 G. Senlis, M. Dubarry, M. Lejeune and T. Chartier, *Ferroelectrics*, 2002, **273**, 279–284.

24 R. Noguera, C. Dossou-Yovo, M. Lejeune and T. Chartier, *J. Eur. Ceram. Soc.*, 2005, **126**, 133–137.

25 R. Noguera, M. Lejeune and T. Chartier, *J. Eur. Ceram. Soc.*, 2005, **25**, 2055–2059.

26 M. Mougenot, M. Lejeune, J. F. Baumard, C. Boissiere, F. Ribot, D. Grosso, C. Sanchez and R. Noguera, *J. Am. Ceram. Soc.*, 2006, **89**, 1876–1882.

27 B. Fousseret, M. Mougenot, F. Rossignol, J.-F. o. Baumard, B. Soulestin, C. d. Boissière, F. o. Ribot, D. Jalabert, C. Carrion, C. m. Sanchez and M. Lejeune, *Chem. Mater.*, 2010, **22**, 3875–3883.

28 G. Sico, M. Montanino, C. T. Prontera, A. De Girolamo Del Mauro and C. Minarini, *Ceram. Int.*, 2018, **44**, 19526–19534.

29 R. Wilken, I. Pollex, S. Stahl, E. Dörsam, R. Klein and M. Miletić, *Handbook of Paper and Board*, Wiley-VCH Verlag GmbH & Co. KGaA, Weinheim, Germany, 2nd edn, 2013.

30 D. Spiehl, M. Haming, H. M. Sauer, K. Bonrad and E. Dorsam, *IEEE Trans. Electron Devices*, 2015, **62**, 2871–2877.

31 M. Faustini, D. R. Ceratti, B. Louis, M. Boudot, P. A. Albouy, C. Boissiere and D. Grosso, *ACS Appl. Mater. Interfaces*, 2014, **6**, 17102–17110.

32 R. F. S. Lenza and M. L. Vasconcelos, *Mater. Res.*, 2001, **4**, 189–194.

33 G. Giordano, N. Vilà, E. Aubert, J. Ghanbaja and A. Walcarius, *Electrochim. Acta*, 2017, **237**, 227–236.

34 S. Alberti, P. Y. Steinberg, G. Giménez, H. Amenitsch, G. Ybarra, O. Azzaroni, P. C. Angelomé and G. J. A. A. Soler-Illia, *Langmuir*, 2019, **35**, 6279–6287.

35 A. Calvo, P. C. Angelomé, C. Sanchez, D. A. Scherlis, F. J. Williams and G. J. A. A. Soler-Illia, *Chem. Mater.*, 2008, **20**, 4661–4668.

36 D. R. Dunphy, P. H. Sheth, F. L. Garcia and C. J. Brinker, *Chem. Mater.*, 2015, **27**, 75–84.

37 C. Boissiere, D. Grosso, S. Lepoutre, L. Nicole, A. Brunet Bruneau and C. Sanchez, *Langmuir*, 2005, **21**, 12362–12371.

38 J. E. Spanier and I. P. Herman, *Phys. Rev. B: Condens. Matter Mater. Phys.*, 2000, **61**, 10437–10450.

39 J. F. Moulder, W. F. Stickle, P. E. Sobol and K. D. Bomben, *Handbook of X-ray Photoelectron Spectroscopy*, Physical Electronics Inc., USA, 1995.

68

5.1.2. MSTFs with tunable surface wettability for asymmetric fabrication of mesoporous wettability step gradient architectures

MSTFs can be sequentially deposited on a substrate using, for example, dip coating to realize mesoporous step gradient architectures by consecutive deposition of different types of MSTFs. In order to fabricate MSTFs with wettability step gradients, thin films with tunable wettability were developed. Therefore, MTMS and DMDMS were used as co-precursors in combination with TEOS and Pluronic® F127 as templating agent. The chemical structures of these precursors are depicted in **Figure 15a**. In order to obtain MSTFs with adjustable surface wettability, the mole fraction of TEOS was varied, whereas the methylated precursors MTMS and DMDMS maintained in a fixed molar ratio of 3:2 according to following molar ratios of the dip coating sol:

x **TEOS/(1-x)·0.6 MTMS/(1-x)·0.4 DMDMS/40 EtOH/0.0075 F127/10 H$_2$O/0.028 HCl**
with x=0, 0.2, 0.5, and 0.8.

It is assumed that MSTFs with hydrophobic surface wettability are observed for low molar fractions of TEOS and hydrophilic MSTFs for high molar fractions of TEOS. Furthermore, an increase of the refractive indices of MSTFs with higher molar fractions of the MTMS and DMDMS are expected. To investigate the chemical compositions, MSTFs with various molar fractions of TEOS have been characterized via ATR-IR spectroscopy and compared to a MSTF without methylated precursors (**Figure 15b**).
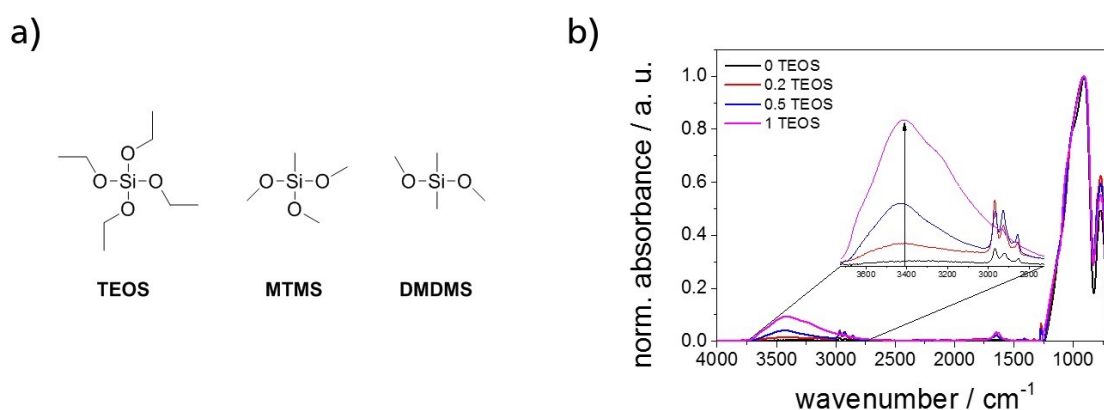
Figure 15: a) Chemical structures of the silica precursors TEOS, MTMS and DMDMS. b) ATR-IR spectra of MSTFs co-condensed with TEOS, MTMS and DMDMS with different mole fractions of TEOS, x=0 (black curve), 0.2 (red curve), 0.5 (blue curve), and a MSTFs without the methylated precursors (magenta curve). All spectra were normalized to the stretching vibration of free silanol groups at ~ 905 cm^{-1}.

Comparing the ATR-IR spectra of MSTFs produced with different mole fractions of TEOS depicted in **Figure 15b**, all spectra show typical bands for MSTFs in the range of 650 and 1280 cm^{-1} implying the presence of Si-OH ($\sim$ 905 cm^{-1}) and Si-O-Si ($\sim$ 1050 cm^{-1} and $\sim$ 770 cm^{-1}). MSTFs co-condensed with MTMS and DMDMS display additional bands in the range of 2800-3000 cm^{-1} that can be assigned to CH$_2$/CH$_3$ vibrational bands. It can further be noticed that the broad band in the range of 2700-3700 cm^{-1}, which can be assigned to O-H stretching vibration of adsorbed water, increases with higher mole fractions of TEOS indicating increasing hydrophilicity.

The structural characterization was carried out by ellipsometry to determine the film thickness and refractive indices (see Appendix, **Table A1**). The obtained values are depicted in dependence of the mole fraction of TEOS in **Figure 16a**.

a)
b)
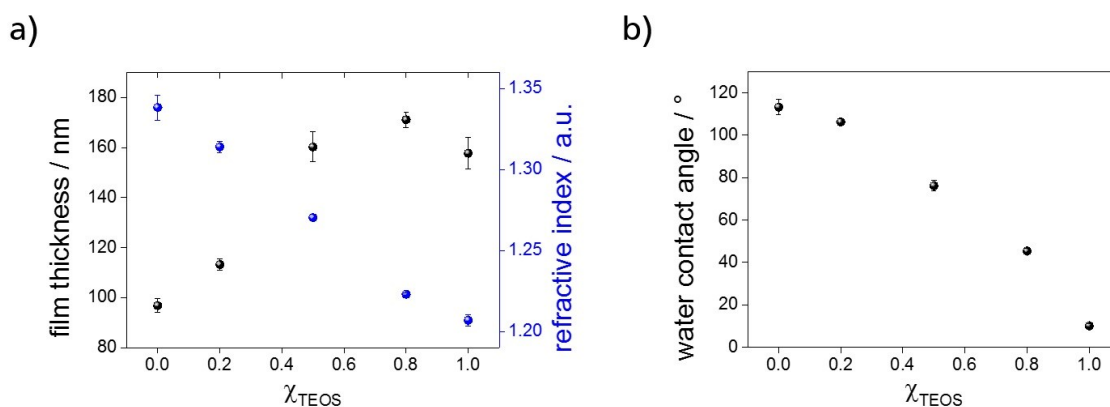
Figure 16: a) Film thickness and refractive indices of MSTFs co-condensed with TEOS, MTMS and DMDMS with different mole fractions of TEOS, *x*=0, 0.2, 0.5, 0.8, and a MSTFs without the methylated precursors obtained from ellipsometric measurements at 15 rH%. b) Apparent water contact angle of a 2 µL water drop on MSTFs co-condensed with TEOS, MTMS and DMDMS with different mole fractions of TEOS, *x*=0, 0.2, 0.5, 0.8, and a MSTFs without the methylated precursors determined at 23 °C and 50 rH%.

Comparing the film thicknesses obtained from ellipsometric measurements, an increasing film thickness with higher mole fraction of TEOS can be observed. Simultaneously, the refractive indices decrease with higher mole fraction of TEOS. The latter was expected, since higher amount of MTMS and DMDMS results in higher amount of incorporated organic groups, i.e. methyl groups, and the refractive index of organic materials is assumed to be 1.5, whereas silica has a refractive index of 1.46[356]. Furthermore, increasing the concentration of co-condensates, here the methylated precursors, results in a decreased mesophase, thus lower porosity, as mentioned in **Chapter 4.1**.

The surface wettability was investigated by determining the apparent water contact angle of a $2\,\mu L$ water drop on top of the MSTFs (see Appendix, **Table A2**). Comparing the apparent water contact angles obtained from MSTFs with different mole fractions of TEOS, apparent water contact angles decrease with increasing mole fraction of TEOS (**Figure 16b**). The MSTF without TEOS shows the highest value of 113° and the MSTF without MTMS and DMDMS shows the lowest contact angle of 10°. Thus, MSTFs with defined water wettability can be generated in situ by co-condensation of TEOS and the methylated precursors MTMS and DMDMS - from hydrophobic to hydrophilic - in dependence of the mole fraction of TEOS.

5.1.3. MSTFs with improved chemical stability

In terms of enhancing the chemical stability of MSTFs, especially in basic environment, mesoporous (organo)silica thin films (MOSTFs) were prepared by using the bridged silica precursor 1,2-bis(triethoxysilyl)ethane (BTESE), which chemical structure is depicted in **Figure 17a**, and the structure directing template Pluronic® F127. Thereby, a precursor sol recipe of a mesoporous silica thin film templated with Pluronic® F127 that is common in the working group of *Annette Andrieu-Brunsen* was applied and the amount of substance of the silica source bisected resulting in following molar ratios of the components in the precursor sol:

1 BTESE / 80 EtOH / 0.015 F127 / 20 H_2O / 0.56 HCl.
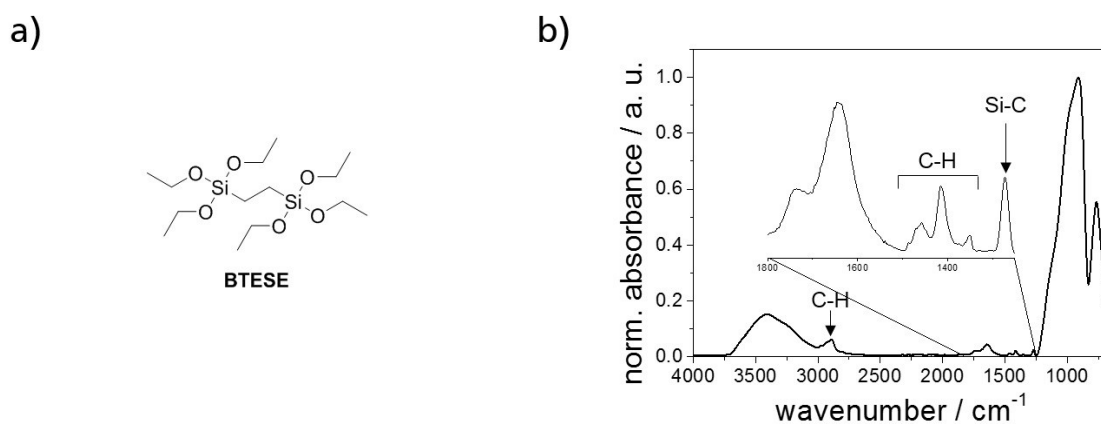
Figure 17: a) Chemical structure of the bridged (organo)silica precursor BTESE. b) ATR-IR spectrum of the MOSTF obtained with the bridged precursor BTESE normalized to the stretching vibration of free silanol groups at ~ 905 cm-1.

It is assumed that the MOSTF results in comparable film thickness to pure mesoporous silica thin films prepared with the silica precursor TEOS based on the precursor sol recipe that was used. Due to the incorporation of organic groups, i.e. CH_2 bridging units, organic groups are

expected in the chemical composition resulting in a higher macroscopic contact angle compared to pure MSTFs (~ 10°). Furthermore, an improved chemical stability in basic environment is pursued in consequence of higher hydrophobicity and chemically more stable Si-C and CH_2-CH_2 bonds.

To investigate the chemical compositions, the MOSTF has been characterized via ATR-IR spectroscopy (**Figure 17b**). The ATR-IR spectrum of the MOSTF displays typical bands of MSTFs in the range of 650 and 1280 cm^{-1} implying the presence of Si-OH (~ 905 cm^{-1}) and Si-O-Si (~ 1050 cm^{-1} and ~ 770 cm^{-1}). MOSTFs further show additional bands as compared to pure MSTFs in the range of 2800-3000 cm^{-1} that can be assigned to C-H vibrational bands. Again, a broad band in the range of 2700-3700 cm^{-1}, which can be assigned to O-H stretching vibration of adsorbed water, can be observed. Additional bands can be found in the region of 2750-3000 cm^{-1} and 1330-1500 cm^{-1} that can be assigned to C-H stretching vibration, and another band at 1272 cm^{-1} that is assigned to the Si-C bond.[349] Another additional band can be observed at 1735 cm^{-1}, which is in a typical range of C=O vibrations and might be assigned to either residues of the template or oxidation products of the bridging groups upon heat treatment of the MOSTF.

The structural characterization through ellipsometry (see Appendix, **Table A3**) revealed a film thickness 219 ± 5 nm, which is in good agreement to the film thickness of pure MSTF withdrawn with a speed of 2 mm/s in the dip coating process[357]. The MOSTF has a refractive index of 1.313 ± 0.006 (RMSE=0.62 ± 0.09), which results in a porosity of 31 vol% calculated by applying the BEMA. Compared to pure MSTFs, the refractive index of the MOSTF is slightly higher, thus the porosity decreased. Contact angle measurements were conducted on three spots on the film surface to determine the surface wettability. Thereby, an apparent water contact angle of 40 ± 1° (see Appendix, **Table A4**) was determined which is in agreement with the before mentioned expectation due to the incorporation of the organic bridging units.

Investigating the structural properties via scanning electron microscopy (SEM) (**Figure 18**), a smooth and crack-free surface of the MOSTF and a film thickness of 191 ± 9 nm derived from cross sectional measurement are observed, which is in good agreement to the film thickness determined via ellipsometry.
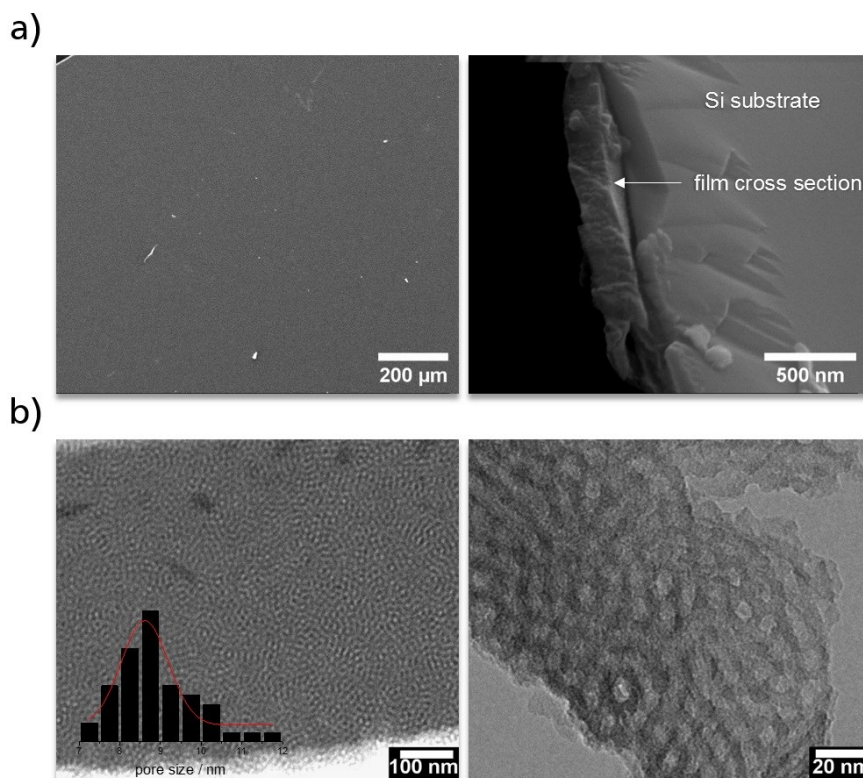
Figure 18: a) SEM micrographs of the top view of the mesoporous (organo)silica thin film (right) and the film cross section (right). Scale bar: 200 µm left, 500 nm right. b) TEM micrographs of the mesoporous (organo)silica thin film. Scale bar: 100 nm left, 20 nm right. The inset on the left displays the pore size distribution obtained from TEM analysis, N=50. TEM measurements were conducted by Ulrike Kunz.

Further structural analysis of the MOSTF using TEM reveals a mesoporous structure with a mean pore size of 8.6 nm as derived from the micrographs shown in **Figure 18**.

To investigate the chemical stability various mesoporous thin films, i.e. pure MSTFs prepared with the precursor TEOS, MSTFs co-condensed with MTMS and DMDMS, as well as MOSTFs prepared with the bridged precursor BTESE, were immersed in buffered solution at pH 10. Thereby, the film thickness of individual pieces of the thin films were determined on three spots via ellipsometry before immersion in the basic solution and after immersion in the basic solution every 30 minutes over a total immersion time of 240 minutes (four hours). It is expected that the chemical stability is increased for mesoporous thin films with lower porosity, i.e. higher refractive indices, and for higher organic composition of the thin films resulting in higher hydrophobicity. The change in film thickness in dependence of immersion time in buffered pH 10 solution is depicted in following **Figure 19**.
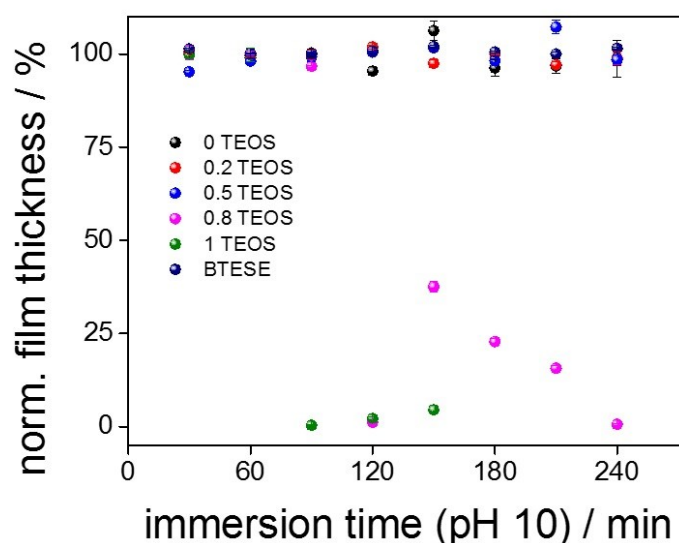
Figure 19: Illustration of the film thickness in dependence of immersion time in buffered pH 10 solution for MSTFs co-condensed with TEOS, MTMS and DMDMS with different mole fractions of TEOS, x=0 (black), 0.2 (red), 0.5 (blue), 0.8 (magenta), a MSTFs without the methylated precursors (green), and the MOSTF prepared with the bridged precursor BTESE (marine).

Comparing the film thicknesses of various mesoporous thin films in dependence of the immersion time in basic solution, it is clearly observable that the pure MSTF prepared with the precursor TEOS shows almost total degradation after an immersion time of 90 minutes in a pH 10 solution. The MSTF that has been prepared via co-condensation of TEOS, MTMS and DMDMs with a high mole fraction of TEOS of 0.8 displays a degradation between 120 and 240 minutes, whereas less than 50% of the initial film thickness is observed after an immersion time of 150 minutes. MSTF that has been prepared via co-condensation of TEOS, MTMS and DMDMs having lower mole fraction of TEOS, i.e. 0.5-0, are stable throughout the total investigated immersion time of 240 minutes, as well as the MOSTF prepared with the bridged precursor BTESE. This can be explained due to lower porosity (higher refractive index), which determines the specific surface area for potential chemical etching, and lower surface wettability (higher values for apparent water contact angles) in consequence of the incorporation of organic moieties. As expected from literature[345], improved chemical stability in basic environment, i.e. pH 10 has been successfully demonstrated for the MOSTF prepared with the bridged precursor BTESE, and as well for MSTFs prepared by co-condensation of TEOS, MTMS, and DMDMS with TEOS mole fractions lower than 0.8.

5.1.4. MSTFs templated with sustainable cellulose-derived macromolecules with possible chiral pore structure

In order to investigate the possibility of using bio-based and sustainable macromolecules as templates for the preparation of MSTFs, MSTFs with a thickness at the nanometer-scale were developed using HPC (**Figure 20a**) as structure directing template. Thereby, the precursor solution with following molar ratios:

1 TEOS / 40 EtOH / 0.001 HPC / 10 H_2O / 0.28 HCl

was used to deposit MSTFs onto various flat substrates via dip coating.
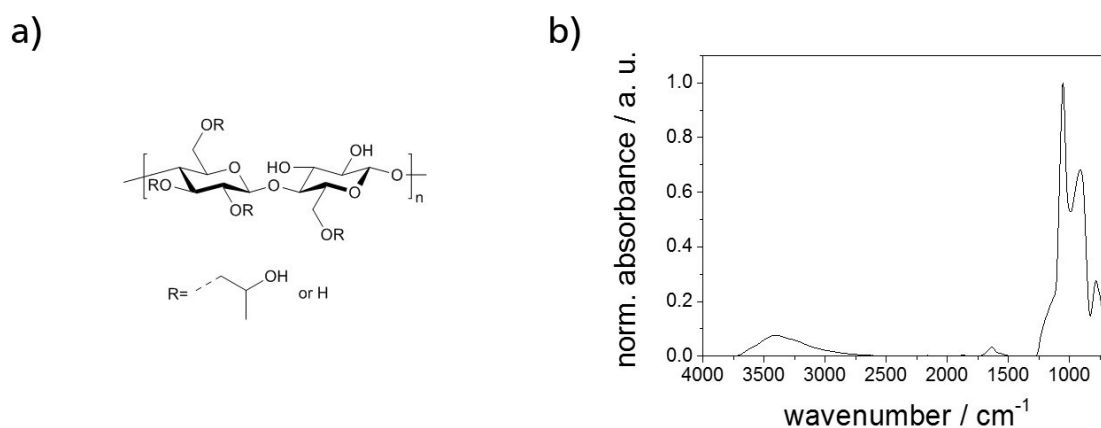
Figure 20: a) Chemical structure of HPC. b) ATR-IR spectrum of a MSTF templated with HPC normalized to the stretching vibration of Si-O-Si at ~ 1054 cm-1.

Investigation of the chemical composition of the MSTF templated with HPC was performed using ATR-IR spectroscopy. In the ATR-IR spectrum (**Figure 20b**) of the MSTF typical bands of MSTFs in the range of 650 and 1280 cm^{-1} implying the presence of Si-OH (~ 905 cm^{-1}) and Si-O-Si (~ 1050 cm^{-1} and ~ 770 cm^{-1}), as well as a broad band in the range of 2700-3700 cm^{-1} that are assigned to O-H stretching vibration of physisorbed and chemisorbed water, can be observed. Thereby, a sharp and strong band is observed for the asymmetric stretching vibration at ~ 1050 cm^{-1} compared to the band of free silanol groups at ~ 905 cm^{-1}. This can be explained due to the high temperature treatment up to 540 °C that was used to remove the template HPC by calcination compared to 350 °C for Pluronic® F127 templated MSTFs, which results in reduction of chemisorbed water, thus reduction of surface silanol groups.[355]

Structural characterization was performed using ellipsometry to determine the film thickness and refractive index. Thereby, a mean value of the film thickness of 382 ± 54 nm and a mean

value of the refractive index of 1.169 ± 0.084 were determined (see Appendix, **Table A5**). From the latter, a mean value of the porosity can be calculated by applying the BEMA, which results in a mean value of the porosity of 61 ± 2 vol%, hence MSTFs templated with HPC result in silica films with high porosity comparable to MSTFs templated with Pluronic® F127[357]. However, the ellipsometry measurements, respectively the fitting of the determined ellipsometric angles to obtain the values for film thickness and refractive index were obtained with quite high RMSE values of 6.1 ± 0.3 indicating a sub-optimal match, which could be the result of an inapplicable model. Likewise, one can imagine that the elliptic polarized light, which penetrates the MSTF while measurement, might interfere with a potential helical structure of the pores.[354]

Further structural characterization via electron microscopy reveals a smooth and crack-free film obtained from SEM (**Figure 21a**). A mesoporous structure with a mean pore size of 2.9 nm is captured by TEM analysis (**Figure 21b**).
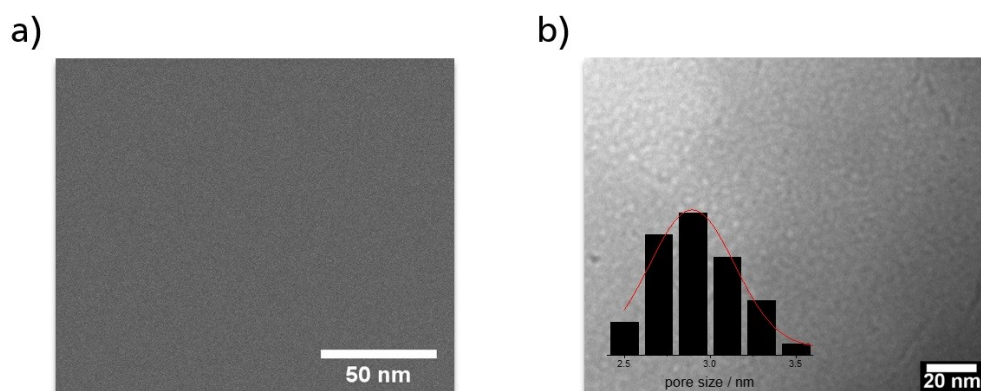
Figure 21: a) SEM micrograph of the top view of the MSTF prepared by using HPC as template. Scale bar: 50 nm. b) TEM micrograph of the MSTF prepared by using HPC as template. Scale bar: 20 nm. The inset shows the pore size distribution obtained from TEM analysis, N=25. TEM measurements were conducted by Ulrike Kunz.

From the mesoporous structure of the MSTF prepared with HPC as template as obtained from TEM analysis, permselective ionic pore accessibility is expected, so that negatively charged probe molecules can only enter at pH 2 and are repelled in consequence of the repulsive electrostatic interaction with the negatively charged pore walls in basic environment, whereas positively charged probe molecules can enter the pore at pH 2, and are pre-concentrated in basic environment due to the attractive electrostatic interaction with the negatively charged pore walls. To investigate the ionic pore accessibility, CV was performed at pH 2-3 and pH 9 (**Figure 22**).
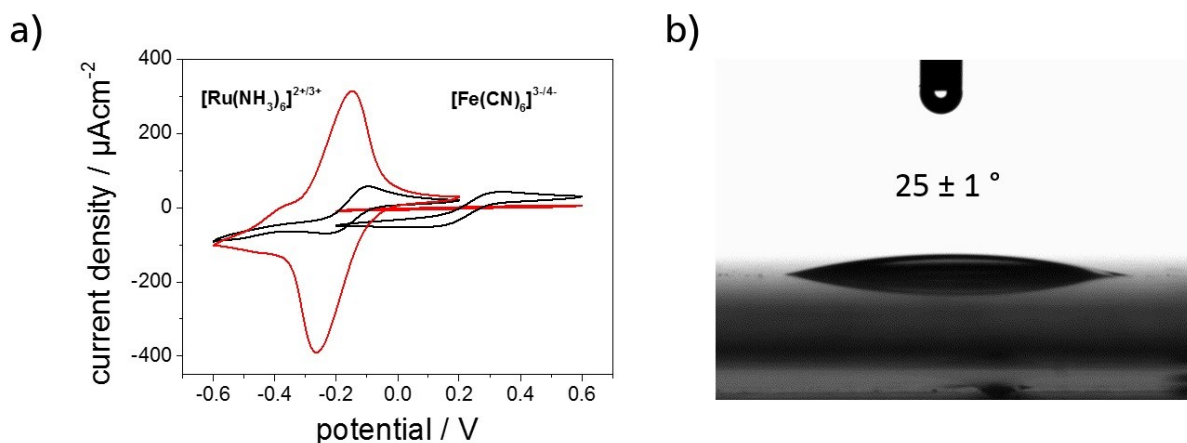
Figure 22: a) Cyclic voltammogram of the MSTF prepared with HPC as template using the redox active probe molecules $[Ru(NH_3)_6]^{2+/3+}$ and $[Fe(CN)_6]^{3-/4-}$ at a concentration of 1 mM, respectively, in 100 mM KCl supporting electrolyte solution at pH 2-3 (black curves) and pH 9 (red curves). Scan rate: 100 mV s^{-1}. The current density refers to the measured electrode area without considering the covered surface area below silica. b) Illustration of the apparent water contact angle measurement by capturing a 2 µL water droplet on top of the MSTF prepared by using HPC as a template. The inset displays the mean value of the determined apparent water contact angles.

Comparing the cyclic voltammograms obtained from CV measurements with the redox active and counter-charged probe molecules $[Ru(NH_3)_6]^{2+/3+}$ and $[Fe(CN)_6]^{3-/4-}$, a permselective behavior of the MSTF prepared with HPC as template is observed as expected. At pH 2-3 (**Figure 22a**, black curves), low current densities are detected for both, positively and negatively charged probe molecules. Contrary at basic pH value of 9, no current density is observed for the negatively charged probe molecule due to the electrostatic repulsion with the negatively charged silica pore walls, whereas high current densities are present for the positively charged probe molecule in consequence of the attractive electrostatic interaction of the positively charged probe molecule with the negatively charged silica pore walls leading to a pre-concentration of the probe molecules in the negatively charged silica.

In addition, the surface wettability of MSTF prepared with HPC as template was investigated by determining the apparent water contact angle of a water droplet on the surface of the MSTF (see Appendix, **Table A6**). From three measurements on top of the MSTF, a hydrophilic surface with a mean water contact angle of 25 ± 1 ° is obtained (**Figure 22b**).

Investigation of the pore structure with respect to a possible helical structure due to the intrinsic nature of HPC to form chiral nematic structures did not lead to a clear conclusion due to the low amount of material that is deposited on substrates, and as well due to a lack of complementary characterization methods. However, hydrophilic MSTFs were successfully prepared with HPC as template that show typical mesopore ionic pore accessibility.

5.2. Mesoporous architecture and step gradient formation

The following chapter illustrates the mesoporous film architectures that have been prepared based on the material library introduced above. Thereby, approaches for the fabrication of mesoporous films with pore size step gradients, and surface wettability step gradients are described. Following, two strategies for an asymmetric modification of mesoporous films after film fabrication are presented. Thereby, the first strategy is based on a layer-selective functionalization of a double layered MSTFs. The second strategy outlines the possibility of utilizing plasmonic metal NPs as nanoscopic light source to induce photopolymerizations in the confinement of mesoporous thin films with nanoscale precision.

5.2.1. Preparation of MSTFs with pore size step gradients by asymmetric fabrication

In order to fabricate MSTFs with pore size step gradients, MSTFs with two different pore sizes are combined by asymmetric fabrication via sequential dip coating. Therefore, MSTFs templated with the surfactant CTAB that result in mesopores with a size of 1-3 nm,[48, 224, 232, 249] and MSTFs templated with Pluronic® F127 that result in mesopores with a size of 6-8 nm have been chosen.[357] Double layered MSTFs are combined in both sequential arrangements, so that the CTAB templated MSTF serves as bottom layer in one arrangement and as top layer in the other arrangement. To verify the pore connection between the two different MSTFs, which is mandatory, if transport of mass and charge through the mesopores is required, double layered MSTFs have been investigated with respect to their ionic pore accessibility by utilization of CV. By that, an electrochemical signal can only be observed, if an interpore connection between the two layers is granted. Thus, in case of an interpore connection between the two different MSTFs, an ionic pore accessibility is expected.

Initially, structural characterization of the single layer MSTFs templated with Pluronic® F127 and CTAB, respectively, has been performed via ellipsometry to determine the film thicknesses and refractive indices (see Appendix, **Table A7**). For MSTFs templated with Pluronic® F127, a film thickness of 176 ± 4 nm and a refractive index of 1.212 ± 0.001 are obtained. From the latter, a porosity of 52 vol% can be calculated applying the BEMA. MSTFs templated with CTAB show a film thickness of 224 ± 3 nm and a refractive index of 1.203 ± 0.002, which results in a porosity of 54 vol% calculated by applying the BEMA.

Structural characterization was then conducted for the double layered MSTFs by using ellipsometry (see Appendix, **Table A8**). For the double layer film bearing a MSTFs templated with CTAB as bottom layer, a bottom layer thickness of 208 ± 1 nm with a refractive index of 1.22 ± 0.001, and a total thickness of the double layer of 282 ± 3 nm with a refractive index of

1.357 ± 0.009 are obtained. From the latter, a film thickness of the top layer of 74 nm can be calculated by subtracting the bottom layer thickness from the double layer thickness. For the double layer film bearing a MSTFs templated with Pluronic® F127 as bottom layer, a bottom layer thickness of 161 nm with a refractive index of 1.237 ± 0.001, and a total film thickness of the double layer of 239 ± 1 nm with a refractive index of 1.374 ± 0.002 are obtained. The film thickness of the top layer can be calculated to 78 nm. The film thicknesses and refractive indices obtained for the bottom layers are in very good agreement to the values obtained for single layer MSTFs discusses above. Contrary, the film thickness calculated for the top layers are much smaller compared to single layers, which could be explained due to lower adhesive forces on the mesostructured hybrid bottom layer still bearing the template. The template of the first deposited layer was not removed to prevent infiltration of the precursor sol of the second layer during deposition. Furthermore, the refractive indices of the double layered MSTFs show higher values compared to the single layers, which cannot be explained at this stage. At this point, it is noteworthy to mention that ellipsometry measurements of the bottom and double layered films have been performed only at one spot on the films. However, the film thicknesses have further been determined three times by using a profilometer (see Appendix, **Table A9**). Profilometer measurements revealed a film thickness of the CTAB templated bottom layer of 176 ± 1 nm and a film thickness of the Pluronic® F127 templated top layer of 64 ± 1 nm. For the Pluronic® F127 templated bottom layer, a film thickness of 168 ± 39 nm, and a film thickness of the CTAB templated top layer of 77 ± 2 nm. Hence, the film thicknesses determined by using a profilometer are in very good agreement to the values obtained from ellipsometry measurements. Additional structural characterization was performed by SEM (**Figure 23**).
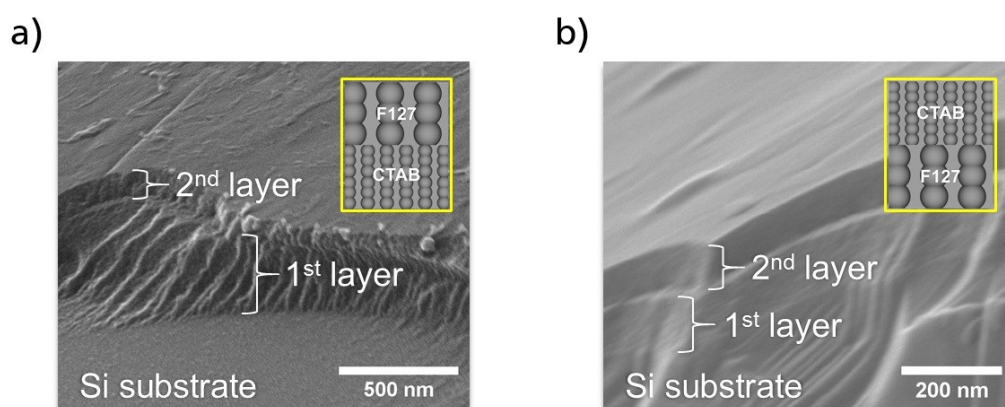
Figure 23: a) SEM micrograph of the double layered MSTF with the CTAB templated film as bottom layer and Pluronic® F127 templated film as top layer. Scale bar: 500 nm. b) SEM micrograph of the double layered MSTF with the Pluronic® F127 templated film as bottom layer and the CTAB templated film as top layer. Scale bar: 200 nm.

The SEM micrographs of the double layered MSTFs in **Figure 23** display the successful fabrication of double layered MSTFs. Furthermore, a thinner top layer compared to the bottom layer can be observed in both sequential arrangements, which confirm the structural observation from ellipsometry as well as profilometer measurements. Due to the transversely perspective of the SEM micrographs, no film thickness determination was conducted.

In order to proof an interpore connection of the double layered MSTFs, the ionic pore accessibility has been investigated using CV with the redox active and charged probe molecule $[Ru(NH_3)_6]^{2+/3+}$ (**Figure 24**).
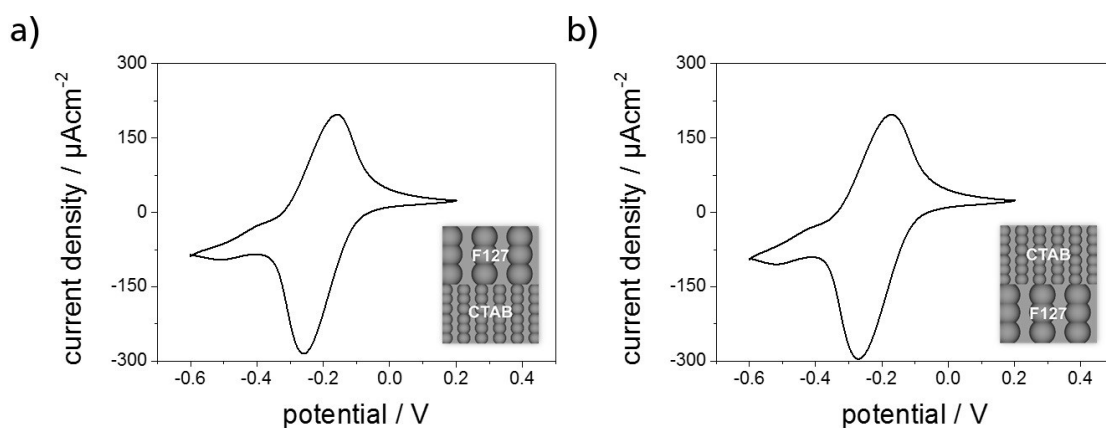
Figure 24: Cyclic voltammogram of the double layered MSTFs with the CTAB templated film as bottom layer in a) and as top layer in b) using the redox active probe molecule $[Ru(NH_3)_6]^{2+/3+}$ at a concentration of 1 mM in 100 mM KCl supporting electrolyte solution at pH 10. Scan rate: 100 mV s^{-1}. The current density refers to the measured electrode area without considering the covered surface area below silica.

From the cyclic voltammograms of the double layered MSTFs depicted in **Figure 24**, peak current densities can be observed indicating an interpore connection of the bottom and top layers. Thus, ionic transport through both double layered MSTF arrangements indicate successful preparation of MSTFs with pore size step gradients via asymmetric fabrication.

5.2.2. Preparation of MSTFs with wettability step gradients by asymmetric fabrication

In order to prepare MSTFs with asymmetric surface wettability, more precisely wettability step gradients, hydrophilic and hydrophobic MSTFs were combined by sequential deposition via dip coating. Therefore, the hydrophilic MSTF templated with Pluronic® F127 (pore size 6-8 nm) was deposited on substrates first, followed by deposition of the hydrophobic MSTFs prepared by co-condensation of the precursors TEOS, MTMS, and DMDMS with a mole fraction of TEOS of 0.2 (**Chapter 5.1.2.**) By deposition of the hydrophobic MSTF on top of the hydrophilic

bottom layer via dip coating, withdrawal speeds of 1, 2, and 3 mm s^{-1} were used to vary the thickness of the hydrophobic layer. It is assumed that the film thickness increases with higher withdrawal speeds according to literature[62-63]. Various thicknesses of the hydrophobic layer were intended in order to investigate a possible overcoming of the hydrophobic layer of positively charged ions due to attractive electrostatic interaction with the negatively charged pore walls of the hydrophilic bottom layer (**Figure 25a**). This has been observed by *Yang* et al. for a nanoporous membrane covered with a thin (~ 1.6 nm) PDMS layer that shows unidirectional transport of positively charged ions at basic pH and low ion concentration.[142]

In terms of structural characterization, film thicknesses of the hydrophilic bottom layer as well as from the hydrophobic top layers deposited with different withdrawal speeds in the dip coating process were determined via ellipsometry (see Appendix, **Table A10**). The hydrophilic bottom layer shows a film thickness of 171 ± 1 nm, whereas the hydrophobic top layers deposited with withdrawal speeds of 1, 2, and 3 mm s^{-1} show film thicknesses of 62 ± 2, 86 ± 3, and 114 ± 7 nm, respectively (**Figure 25b**), hence increasing film thicknesses of the hydrophobic top layer are obtained with faster withdrawal speeds in the dip coating process as expected from literature[62-63].
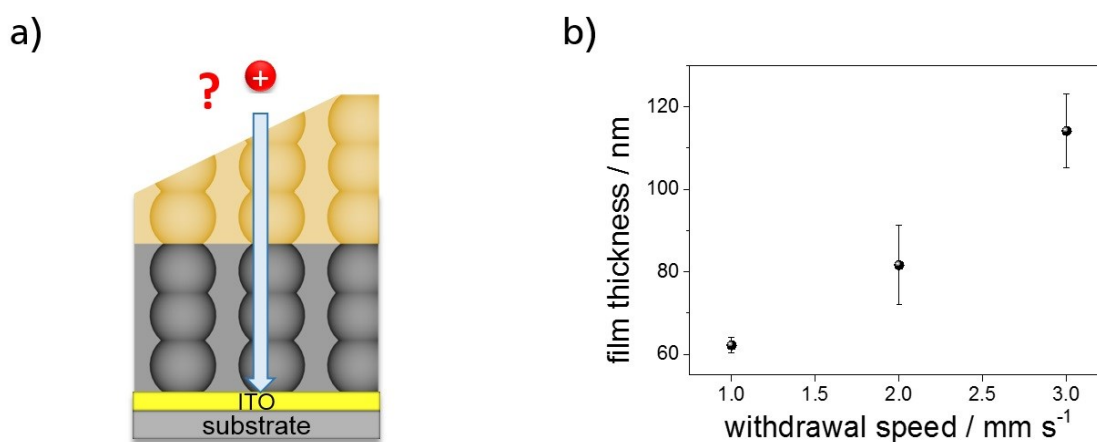
Figure 25: a) Schematic illustration for the investigation of charge-wetting effects on ionic pore accessibility of MSTFs with wettability step gradients and different film thicknesses of the hydrophobic top layer. b) Film thicknesses obtained from ellipsometry measurements of a hydrophobic MSTF prepared by co-condensation of the precursors TEOS, MTMS, and DMDMS with a mole fraction of TEOS of *x*=0.2 on top of a hydrophilic MSTF prepared with the template Pluronic® F127 (pore size: 6-8 nm).

The surface wettability of both deposited layers was investigated by determining water contact angles of water drops casted on the surfaces (see Appendix, **Table A11**). For the mesoporous bottom layer that has not been covered with a hydrophobic layer, a mean value of three apparent water contact angles of $28 \pm 0.5°$ was obtained. The hydrophobic top layers that were

deposited via dip coating with withdrawal speeds of 1, 2, and 3 mm s⁻¹ result in mean values of apparent water contact angles of $108.3 \pm 0.3°$, $108.0 \pm 0.1°$, and $106.7 \pm 0.3°$, respectively. Hence, double layered MSTFs with wettability step gradients have been constructed.

The ionic pore accessibility of the MSTFs with wettability step gradients and different hydrophobic top layer thicknesses was investigated using CV. Thereby, only the positively charged probe molecule $[Ru(NH_3)_6]^{2+/3+}$ was used at pH 2 and pH 11.5, as no pore accessibility is assumed for negatively charged ions due to the hydrophobic barrier of the top layer. Peak current densities are only expected for the positively charged probe molecule at basic pH in consequence of electrostatic attraction of the negatively charged pore walls and overcoming of the hydrophobic barrier. Cyclic voltammograms of the MSTFs with wettability step gradients recorded at pH 2 and pH 11.5 are depicted in **Figure 26**.
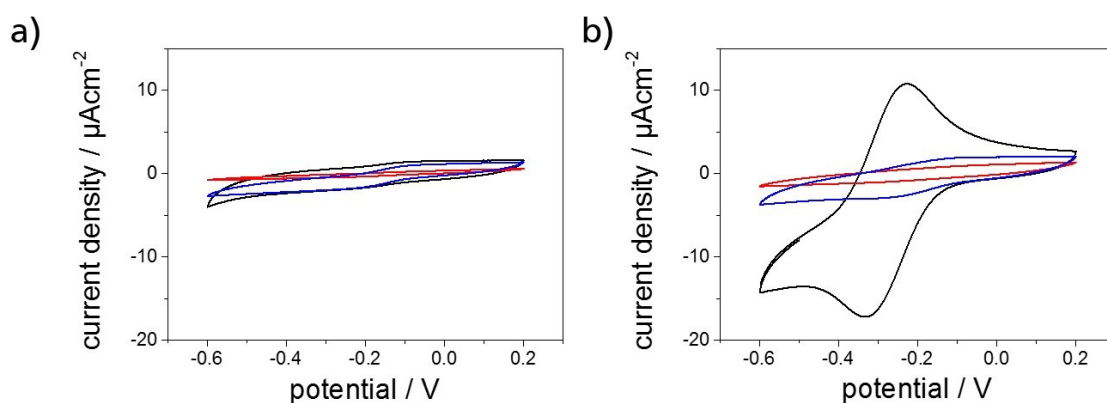
Figure 26: Cyclic voltammograms of the double layered MSTFs with wettability step gradients and different film thicknesses of the hydrophobic top layer deposited via dip coating with a withdrawal speed of 1 (black curves), 2 (red curves), and 3 mm s⁻¹ (blue curves) using the redox active probe molecule $[Ru(NH_3)_6]^{2+/3+}$ at a concentration of 1 mM in 100 mM KCl supporting electrolyte solution at pH 2 in a) and pH 11.5 in b). Scan rate: 100 mV s⁻¹. The current density refers to the measured electrode area without considering the covered surface area below silica.

Comparing the cyclic voltammograms obtained from CV measurements with the MSTFs with wettability step gradients using the positively charged probe molecule $[Ru(NH_3)_6]^{2+/3+}$, no peak current densities, hence no ionic pore accessibility is observed at pH 2 for all three MSTFs with different thicknesses of the hydrophobic top layer (**Figure 26a**). In contrast at pH 11.5, peak current densities are only obtained for the MSTFs with wettability step gradients and the thinnest hydrophobic top layer deposited with a withdrawal speed of 1 mms⁻¹ in the dip coating process (**Figure 25b**). MSTFs with wettability step gradients and thicker film thicknesses of the hydrophobic top layer show no peak current densities, thus no ionic pore accessibility is achieved. Consequently, MSTFs with wettability step gradients were successfully prepared by asymmetric fabrication that show ionic pore accessibility for positively charged ions in case of

a thin hydrophobic top layer of $62 \pm 2\,\text{nm}$ (black cyclic voltammogram in **Figure 26b**) and strong basic conditions, which results in a negatively charged bottom layer, thus electrostatic attraction leading to an overcome of the hydrophobic barrier (**Figure 27**). Although a dependence of the ionic pore accessibility on the hydrophobic film thickness is observed, no quantitative statement with respect to a limiting film thickness is made due to a lack of film thicknesses between 60 and 80 nm and further investigations. Nevertheless, a basis for the observed effect was built and further investigation will be conducted in continuing work in the research group of *Annette Andrieu-Brunsen*. Furthermore, an interpore connection of the hydrophilic bottom and hydrophobic top layer is indicated due to the detected peak current density of $10\,\mu\text{Acm}^2$ for the MSTFs with the thinnest hydrophobic top layer at basic conditions.
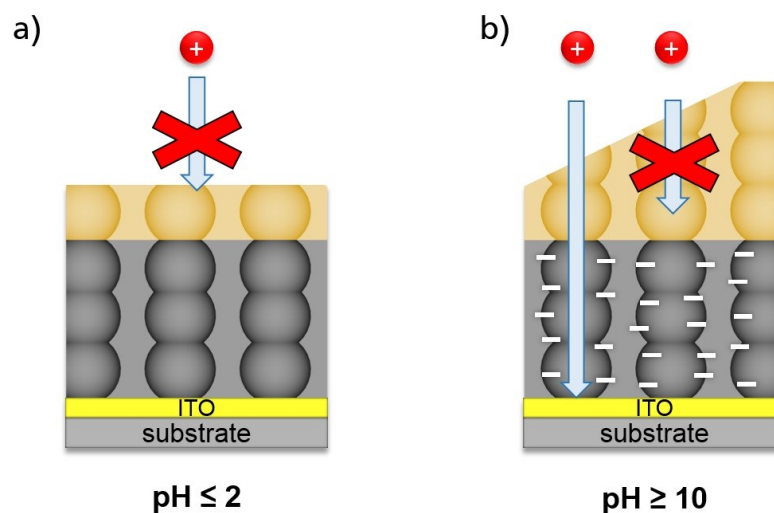
Figure 27: Schematic illustration of the charge-wetting effect on ionic pore accessibility through MSTFs with wettability step gradients bearing a hydrophobic top layer. a) In acidic environment (pH ≤ 2), no transport of positively charged ions is expected due to the hydrophobic barrier of the hydrophobic top layer. b) Transport of positively charged ions through the porous network of MSTFs with wettability step gradients overcoming the hydrophobic barrier with the lowest applied thickness due to electrostatic attraction of the negatively charged pore walls of the bottom layer in basic environment (pH ≥ 10).

5.2.3. Layer selective functionalization of mesoporous double layered thin films for step gradient formation by asymmetric modification

This paragraph describes the asymmetric modification of MSTFs in order to prepare MSTFs with asymmetric surface charge distribution, more precisely a charge step gradient, at the nanometer scale. In a double layer architecture, polymer functionalization is performed in only one designated single layer. To achieve the layer-selective polymer functionalization in a double layer arrangement, one layer is predisposed with amino groups applying co-condensation of

APTES and TEOS resulting in an aminosilica film. The amino groups are then selectively addressed to immobilize a polymerization initiator for further layer-selective placement of poly(2-(methacryloyloxy)ethyltrimethylammonium chloride (PMETAC). Thus, advantages of co-condensation and post modification techniques from single MSTFs are combined to incorporate a permanent positively charged molecule to the mesopore wall resulting in a charge step gradient architecture by layer-selective polymer functionalization. In addition, the ionic pore accessibility of the asymmetric MSTFs is investigated.

For the preparation of mesoporous double layer thin films allowing surface-initiated polymerization (grafting from) exclusively in one layer, MSTFs with a pore size of 6-8 nm that have been introduced in **Chapter 5.1** were applied, along with a co-condensed mesoporous aminosilica thin films containing 20 mol% of an amine group bearing precursor, namely APTES, in one layer of the double layer films. The thin films were deposited via sol-gel chemistry and dip coating such that a double layer film was present in the middle of the substrate and each individual thin film, the bottom and top layer, were present as single layer next to the double layer that allowed characterization and direct comparison of each individual layer (see Fig. 1 in following publication). Furthermore, double layers were prepared in both sequential arrangements, so that the aminosilica thin films was present as bottom layer in one arrangement, and present as top layer in the other arrangement. Aminosilica thin films produced by co-condensation applying the precursor APTES are well-investigated and have further been chosen to integrate a certain predisposition to one mesoporous layer allowing further modification. To increase the function density in the aminosilica layer, an iniferter initiated polymerization was selected, as these polymerization methods are well-established for the functionalization of MSTFs allowing to tune the function density as well as to design the polymer chain architecture.[10, 48, 56] A carboxylic acid bearing iniferter 4-(N,N-Diethyldithiocarbamoylmethyl)benzoic acid (BDC) was synthesized and selectively bound to the amino groups of the aminosilica thin films utilizing the amide forming coupling agent 1-[Bis(dimethylamino)methylene]-1H-1,2,3-triazolo[4,5-b]pyridinium-3-oxide hexafluorophosphate (HATU), which is a common reagent in peptide synthesis. After careful extraction of unbound BDC, polymerization of the permanent positively charged monomer [2-(methacryloyloxy)ethyl]trimethylammonium chloride (METAC) was performed by applying UV light at a wavelength of 365 nm. The double layer as well as single layer mesoporous films were then characterized regarding the chemical composition using ATR-IR spectroscopy. Thereby, a selective functionalization of the aminosilica layer was observed, which was further confirmed by EDX mapping of the top view of single and double layer thin films. By investigation of the optical properties using ellipsometry, a pore filling fraction of up to 84% in the aminosilica layer was calculated applying the BEMA. To further confirm the successful layer-

selective functionalization, the single as well as double layer thin films were immersed in dye solutions containing the positively charged dye rhodamine B and the negatively charged dye fluorescein respectively. Thereby, rhodamine B was only detected in unfunctionalized silica layers due to the electrostatic attraction of negatively charged silanolate groups on the mesopore wall, and fluorescein was only present in the positively charged aminosilica layer due to electrostatic attraction of the positively charged polymer PMETAC. At the last, the ionic pore accessibility of the functionalized double layer thin films was studied utilizing CV and compared to the double layer thin films before functionalization. By that, a significant change of the ionic pore accessibility was observed further confirming the successful functionalization of an individual layer. Interestingly, it was found that the bottom layer has a dominant role on the pore accessibility and is able to induce an overcoming of local electrostatic repulsion of the top layer, although it is not directly in contact with the probe molecule solution. This has implications on data interpretation in hierarchical and complex porous materials, e.g. applied in separation.

Contribution to the publication in European Polymer Journal, 2021, 156, 110604: My contribution involves the conceptualization, investigation, data curation, visualization, as well as writing the original draft. Ulrike Kunz (Department of Materials and Earth Sciences, Physical Metallurgy Group, TU Darmstadt) supported this study with TEM measurements including sample preparation by ultrathin sectioning, as well as SEM/EDX measurements. Annette Andrieu-Brunsen acquired funding, supervised the project and supported in manuscript writing.

Layer-selective functionalisation in mesoporous double layer via iniferter initiated polymerisation for nanoscale step gradient formation

Mathias Stanzel [a], Ulrike Kunz [b], Annette Andrieu-Brunsen [a],[*]

[a] Ernst-Berl Institut für Technische und Makromolekulare Chemie, Technische Universität Darmstadt, Alarich-Weiss-Strasse 8, D-64287 Darmstadt, Germany
[b] Department of Materials and Earth Sciences, Physical Metallurgy Group, Technische Universität Darmstadt, Alarich-Weiss-Straße 2, 64287 Darmstadt, Germany

ARTICLE INFO

ABSTRACT

Functionalisation of technological nanopores and investigation of their transport properties have attracted considerable interest from scientific as from technological point of view, among others due to their potential regarding molecular transport design. Asymmetric design of nanopore structure and functionalisation is expected to trigger increased and directed transport of ionic species. Based on this motivation, we demonstrate a layer-selective polymer functionalisation in a mesoporous double layer thin film to generate nanoscale step gradient architectures with asymmetric charge distribution by taking advantage of co-condensation and polymer modi-fication techniques. Thereby, mesoporous silica and co-condensed mesoporous amino silica thin films are combined to double layered films with a film thickness of 300 – 400 nm in both sequential arrangements, respectively. Iniferter initiated polymerisation is used to selectively functionalise only the amino silica layer with polymers such as poly(2-(methacryloyloxy)ethyltrimethylammonium chloride) (PMETAC) in a grafting from approach. Investigation of the ionic pore accessibility of the mesoporous double layered films before and after layer-selective polymer functionalisation shows that the ionic pore accessibility is dominated by the bottom layer when overcoming the electrostatic repulsion of the top layer.

1. Introduction

Modulation and understanding the transport of mass and charge in nanoscale pores and channels has attracted reasonable interest in the field of biology, chemistry, and physics, based on the transport phenomena that arise in such nanoconfined environment, which can be quite different to larger microscale dimension [1–4]. Particular interest of such porous materials can be assigned to the field of nanofluidics, as artificial nanoscale pores and channels have made major progress in the last two decades emerging applications in the field of biosensing, molecular transport, separation, drug delivery, and catalysis [5–8]. Thereby, recent results show that a break in symmetry of nanoscale pores and channels can lead to directional or gated transport of mass and charge similar to the outstanding performance of biological pores and channels [9–11]. For example, side-selective transport or oil–water separation is obtained by asymmetric wettability design of porous materials and membranes [12–16]. Preferential transport direction in nanochannels is also observed as diode-like ionic current rectification (ICR) phenomena by applying asymmetric pore geometry [17,18]. For example, Siwy et al. demonstrated enhanced ICR ratios in the case of a conical pore compared to cylindrical pores [19]. Likewise, regardless of the pore geometry, enhanced ICR ratios have been observed, when the pore surface exhibits an asymmetric surface charge pattern, which has been comprehensively studied in experiment along with simulations [20–27]. Implementing this asymmetric design, bio-inspired artificial single ion pumps have been realized [28–30]. For example, Jiang and co-workers achieved pH regulated ion pumping by selectively functionalising the tip ends of an hour shaped nanochannel with cooperative pH-responsive polyelectrolytes [31]. Furthermore, selectively functionalising the outer surface of nanoporous materials can result in transient capping of the nanopore entrance allowing controlled release of guest molecules trapped inside the pores [32–34] or gating/switching of ionic transport [35–39]. Thus, influential factors for asymmetric ion transport behaviour that can be built in nanoscale structures are: nanopore geometry, surface charge distribution, chemical composition, and wettability on the channel wall, as has been summarised by Guo et al. [40]. However, to meet the requirements for selectively regulating ion transport for advanced applications would require enhanced control over surface functionalisation in such nanoscale pores and channels, as well as detailed understanding of ion transport behaviour in nanoscale

---

confinement.

In this context, mesoporous silica thin films (MSTF) representing solid-state nanopores have been utilised as model systems to manipulate ionic transport upon functionalisation providing fundamental insights of transport properties at the nanoscale.

In general, organic functionalities can be placed in MSTF by either co-condensation of inorganic precursors containing organic functional groups, or by post modification of the silica surface. Different polymerisation techniques, such as dye sensitised polymerization [41], ring opening metathesis polymerisation (ROMP) [42], reversible addition-fragmentation chain-transfer polymerisation (RAFT) as well as iniferter initiated polymerisation [43], and atom transfer radical polymerisation (ATRP) [35] have been applied to generate hybrid MSTF. Thereby, regulation of transport has been demonstrated using stimuli, such as pH, temperature or light [44,45].

In particular, tuneable functional densities and thus tailored transport properties arising from hybrid MSTF have been reported for the living radical polymerisation methods RAFT and iniferter initiated polymerisations [46]. Recently, our research group demonstrated that iniferter initiated polymerisations do not only offer the ability of controlled polymer amount and thus controlled functional density in mesopores, but also allow to control polymer chain's architecture by generation of block-cooligomers [47]. Nonetheless, in terms of MSTF, scientific reports on polymerisation methods for preparation of hybrid materials are limited to single layer system. Multilayered MSTF have been mainly focusing on optical properties and have been demonstrated as promising materials in photonics, sensing, and photocatalytic processes [48–50]. Thereby, in mesoporous multilayer, MSTF are often combined with mesoporous titania to form photonic crystals [51,52]. In previous works, our group investigated transport properties of mesoporous and mesostructured double layer silica thin films by applying functional structure determining templates to form step gradient architectures [53,54]. Yet, only a few examples investigating transport properties of multilayered mesoporous system can be found in literature.

Here, we demonstrate a strategy for layer-selective polymer functionalisation in mesoporous silica double layer films using iniferter initiated polymerisation in a grafting from approach for the formation of nanoscale step gradient architectures with asymmetric charge distribution on the nanoscale. We take advantage of the well-known co-condensation and post modification techniques of MSTF by integration of an amino group comprising precursor into one layer of a double layer MSTF, followed by selective binding of the iniferter to polymerise the positively charged monomer [2-(methacryloyloxy)ethyl]trimethylammonium chloride (METAC) layer-selectively. Thereby, we evaluate the functionalisation with respect to layer selectivity using IR spectroscopy, charged dye adsorption, as well as ellipsometry. Ionic pore accessibility of the functionalised double layer is investigated by applying cyclic voltammetry and discussed with respect to the layer arrangement. Thereby, we demonstrate that the ionic pore accessibility is dominated by the bottom layer that can overcome local electrostatic repulsion.

2. Experimental

2.1. Chemicals

All materials and solvents were purchased from Sigma-Aldrich, Acros Organics, and VWR and used as received unless stated otherwise. Microscope slides (VWR, glass, cut edges) were cleaned with ethanol and dried under ambient conditions. Silicon wafers (Si–Mat, Kaufering, Germany, 100 mm diameter, 525 ± 25 μm thickness, type P/Bor, ⟨1 0 0⟩ orientation, CZ growth method, 2–5 W resistivity, polished on 1 side) and indium tin oxide (ITO, Delta Technologies, Ltd., Loveland, CO, USA, polished float glass, $150 \times 150 \times 1.1$ mm, SiO_2 passivated/Indium Tin Oxide coated one surface, RS = 4–8 Ω, cut edges) were cut to desired size using a diamond cutter, cleaned using technical grade ethanol, and dried

under ambient conditions prior to dip coating of mesoporous films.

2.2. Preparation of mesoporous double layer

Mesoporous thin films were prepared as previously described [55] via sol–gel chemistry using tetraethoxysilane (TEOS) and (3-aminopropyl)triethoxysilane (APTES) as inorganic precursors and an amphiphilic triblock copolymer, Pluronic® F127, as structure directing template that undergoes micellisation upon solvent evaporation resulting in formation of a porous inorganic network. The molar ratios of the compounds in the precursor solution used for dip coating were 1-x TEOS / x APTES / 0.0075 F127 / 40 EtOH / 10 H_2O / 0.28 HCl with $\times = 0$ for silica thin films and $\times = 0.2$ for amino silica thin films resulting in 6–10 nm mesopores. The precursor solutions were prepared at room temperature and stirred overnight prior the deposition on glass, silicon wafers and ITO covered glass applying the evaporation induced self-assembly (EISA) [56]. The films were dip coated at a withdrawal speed of 2 mm s^{-1} at 23 °C and 50% relative humidity. After deposition, the films were kept at 23 °C and 50% relative humidity for 1 h. The first film was then stabilised by a temperature treatment at 60 °C and 130 °C for 1 h respectively. The mesostructured bottom layer was then covered with a second silica film via dip coating using the above mentioned conditions and stored at 23 °C and 50% relative humidity for 1 h. Finally, the mesoporous double layer was obtained, after template removal that was performed by extracting the mesoporous double layer in acidic ethanol (0.01 M HCl) for 3 days after consecutive temperature treatments at 60 °C, 130 °C for 1 h respectively and at 200 °C for 2 h.

2.3. Surface grafting of 4–(N,N–Diethyldithiocarbamoylmethyl)benzoic acid (BDC)

Surface grafting of BDC was performed under inert conditions and water was removed from all glass ware by heating under high vaccum. A solution of 60 mg BDC (212 μmol, 1 eq) in 60 mL anhydrous DMF was prepared. Then, 46.7 μL *N,N*-Diisopropylethylamine (DIPEA, 275 μmol, 1.3 eq) and 104.6 mg 1–[Bis(dimethylamino)methylene]–1H–1,2,3–triazolo[4,5–b]pyridinium 3-oxide hexafluorophosphate (HATU, 275 μmol, 1.3 eq) were added and the solution stirred at room temperature for 15 min. The mesoporous double layer were immersed in the solution at room temperature overnight. Afterwards, the samples were intensively rinsed with DMF and ethanol to wash unbound BDC.

2.4. Iniferter initiated polymerisation of METAC

Polymer functionalisation was performed with BDC functionalised samples. Therefore, an aqueous 1 M solution of METAC was prepared and purged with nitrogen for 15 min. Then, the mesoporous double layer films were placed in the monomer solution and irradiated with UV light at a wavelength of 365 nm for 1 h. After polymerisation, the samples were extracted in deionised water for 1 h to remove unreacted monomer.

2.5. Attenuated total reflection fourier transform Infrared spectroscopy (ATR-FTIR)

Infrared spectra of the prepared mesoporous films on glass substrates were recorded using a Perkin Elmer Instrument Spectrum One FT-IR Spectrometer equipped with a Universal ATR Polarisation Accessory (Waltham, MA, USA). All spectra were normalised to the stretching vibration of free silanol groups at ~ 905 cm^{-1}. The spectra were recorded using the Spectrum Software (Version 10.5.4.738, PerkinElmer, Inc. Waltham, MA, USA, 2016) between 4000 and 650 cm^{-1} with a resolution of 4 cm^{-1}. A background and a baseline correction was automatically performed. Additional bands of the glass substrate are visible in the FTIR spectra: Mesoporous film signals are partially superimposed by signals originating from the glass substrate in the region of 830 – 1250

2

cm^{-1} depending on the penetration depth of the ATR-IR evanescent waves. Nevertheless, due to the comparable film thickness, IR-spectra of different films can be compared. All further data processing was performed in OriginPro9 (ADDITIVE Soft- und Hardware für Technik und Wissenschaft GmbH, Friedrichsdorf, Germany, 2012).

2.6. Scanning electron microscopy (SEM)

SEM micrographs were obtained using a Philips XL30 FEG scanning electron microscope equipped with a tungsten cathode and a back scattered electron yttrium aluminium garnet (BSE YAG) detector with an accelerating voltage of 15–25 kV, a 30 μm aperture, and a spot size of 3–4. The samples were sputter-coated with a 7 nm coating of Pt/Pd. The digital micrographs were recorded over a range of magnifications at a working distance of 11 mm using an SE2 detector.

2.7. Transmission electron microscopy (TEM)

TEM micrographs were recorded using a Philips FEI CM-20 transmission electron microscope (Philips, Netherlands) equipped with a LaB_6 cathode and Olympus CCD camera, and with a maximum resolution of 2.3 Å operating at an accelerating voltage of 200 kV. Samples were prepared by scratching off the mesoporous films from the substrate and dispersion in filtered ethanol. After 5 min of sonication, scratched mesoporous films were drop cast onto 3.05 mm Cu grids (mesh size 200) with a Lacey carbon film (Plano GmbH, article number S166–2). The samples were dried under ambient conditions. For ultrathin sectioning, mesoporous double layer films were transferred on PET membrane discs (OxyDisc®, 13 mm diameter, Oxyphen, Germany) following the procedure of Lin et al. [57], embedded in Araldit© (polymerisation at 60 °C for 10 h) and cut in 70 nm sections using an ultramicrotome (Ultracut E, Reichert-Jung, Micro Star diamond knife).

2.8. Fluorescence imaging

Fluorescence images were recorded using a Fusion FX7 Edge imaging system (Vilber Lourmat, Germany).

2.9. Ellipsometry

The film thicknesses and refractive indices of mesoporous single- and double layer films deposited on silicon wafer substrates are determined using a Nanofilm EP3 imaging ellipsometer. By keeping the relative humidity constant at 15% relative humidity (humidity control: ACE-flow, Solgelway), the one-zone angle of incidence (AOI) variation measurements are performed between AOIs of 38° and 68° in 2° steps using a laser wavelength of 658 nm. Film thicknesses and refractive indices are calculated using the measured ellipsometric angles Δ and Ψ with the software EP4 Model supplied with the instrument. The silicon oxide thickness of the substrate is kept constant at 4 nm. Layer thicknesses are fitted allowing an iteration between 100 and 200 nm for silica layers and iteration between 150 and 250 nm for amino silica layers respectively. The refractive indices are simultaneously fitted by iteration between the values 1.0 and 1.5. All films are measured on three spots along the direction of dip coating. Applying the Bruggeman effective medium approximation (BEMA), porosities and pore filling fractions are calculated with the refractive indices determined.

2.10. Cyclic voltammetry

The ionic pore accessibility of the mesoporous materials was investigated via cyclic voltammetry (CV) using $[Fe(CN)_6]^{3-/4-}$ and $[Ru(NH_3)_6]^{2+/3+}$ as charged, redox-active probe molecules. Measurements were recorded using a Metrohm Autolab PGSTAT302N potentiostat. Mesoporous films prepared on ITO coated glass substrates (Delta Technologies, Ltd., Loveland, CO, USA, polished float glass, 150 × 150 × 1.1

mm, SiO_2 passivated/Indium Tin Oxide coated one surface, RS = 4–8 Ω, cut edges) were characterised using a 1 mM solution of either the positively- or negatively charged probe molecule in a 100 mM KCl electrolyte solution. The pH-dependent pore accessibility was investigated by adjusting the solution pH between 2 and 10 by the addition of either concentrated aqueous NaOH or HCl to the probe molecule containing buffer solutions. The pH was determined using a pH–meter (pH110, VWR). An Ag/AgCl reference electrode (BASi RE–6) and graphite counter electrode was used in the sample cell. The measured working electrode area was 0.21 cm^2. Pore accessibility for each pH was measured using a scan rate sequence of 200, 100, 25, 300, 1000, and 200 mV s^{-1}, with each scan rate being cycled three times. Quality control of the cyclic voltammograms was performed by ensuring comparability of the first and last scan rate, as well as between each scan of one rate. In addition, the first pH applied is re-measured for all scan rates ensuring reversible switching of charge and thus ionic pore accessibility.

3. Results and discussion

3.1. Structural characterisation of mesoporous thin films

The mesoporous films were prepared via well-established sol–gel chemistry and EISA [56] using TEOS and APTES as precursors and the amphiphilic triblock copolymer, Pluronic® F127, as structure directing template, as described in previous studies [55]. Thin multilayer layer films were deposited on glass, ITO coated glass, and silicon wafers via dip coating such that both individual layers, the bottom one as well as the top one are accessible for characterisation as depicted in Fig. 1. MSTF with 160–190 nm thickness, ~40 vol% porosity, and mesoporous amino silica thin films with 230–240 nm film thickness and ~ 25–30 vol % porosity are obtained as determined from ellipsometry measurements (Table S1-S2). Both layers present ordered mesopore arrays with mesopore diameters in a range of 6–10 nm as expected from manifold previous studies [43,47,58,59] and as analysed by TEM micrographs shown in Fig. 1c, d. The resulting double layered mesoporous film architecture is well observed in SEM cross sectional measurement depicted in Fig. 1e.

3.2. Layer-selective polymer functionalisation

Layer-selective polymer functionalisation was achieved following a controlled iniferter initiated polymerisation approach which is schematically presented in Fig. 1a. The photoiniferter BDC was synthesised according to a published protocol [60] and covalently bound to the surface amino groups of the amino silica layer via HATU coupling under formation of an amide (Figure S2 and S3). Investigation of chemical functionality of the mesoporous layers using ATR-IR spectroscopy shows layer-selective functionalisation with BDC exclusively on mesoporous amino silica. As the selective binding of BDC to amine groups determines subsequent local functionalisation, a careful extraction of unbound BDC has to be performed before polymerisation. Polymerisation of the monomer METAC was carried out in aqueous solution by applying UV light at a wavelength of 365 nm.

In order to investigate the chemical functionality of each individual layer as well as the double layer films through polymerisation of METAC, ATR-IR spectroscopy measurements have been performed before and after modification. Ideally, chemical modification as the result of iniferter-initiated METAC polymerisation is limited to the amino silica layer, as only these contain the covalently grafted initiator BDC. Comparing the ATR-IR spectra shown in Fig. 2, all spectra display typical bands for mesoporous silica in the range of 650 and 1280 cm^{-1} indicating the presence of Si-O-Si (~1050 cm^{-1}) as well as Si-OH (~905 cm^{-1}) bands as discussed in previous studies [55,61,62]. The successful METAC polymerisation is validated based on the C = O vibrational band at 1725 cm^{-1} corresponding to the acrylate group of PMETAC. This C = O vibrational band originating from PMETAC functionalisation is
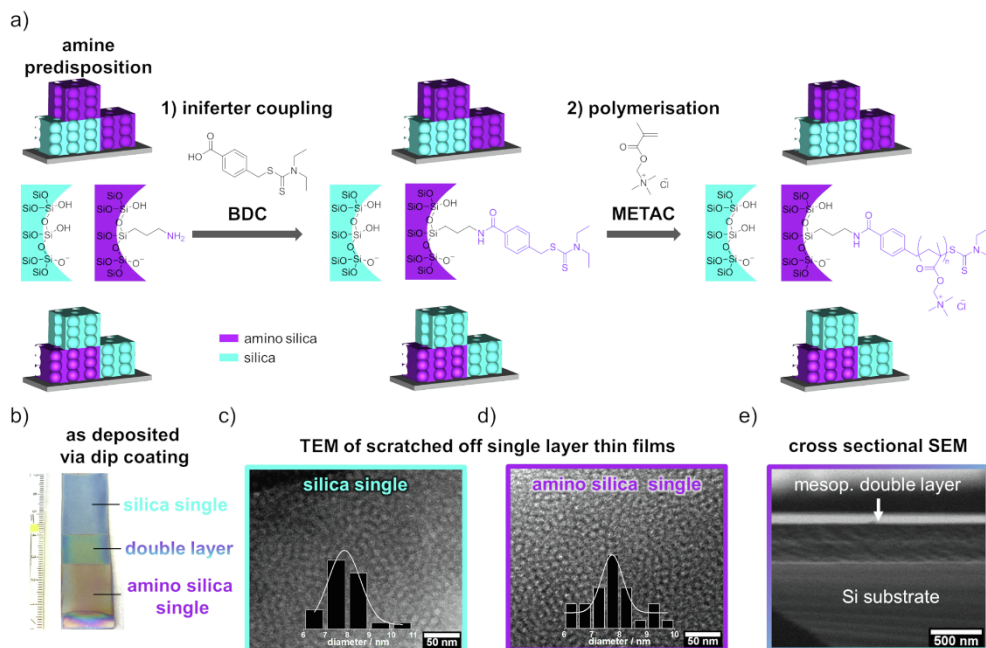
Fig. 1. Schematic representation of layer-selective functionalisation of mesoporous double layer architectures following an UV induced iniferter initiated polymerisation approach (a). Representative image of MSTF deposited on silicon wafer whereas both single layers and the double layer are present (b). TEM micrographs of MSTF (c) and mesoporous amino silica thin film (d), scale bar: 50 nm. SEM micrograph of a mesoporous double layer film cross section after polymerisation (e), scale bar: 500 nm.
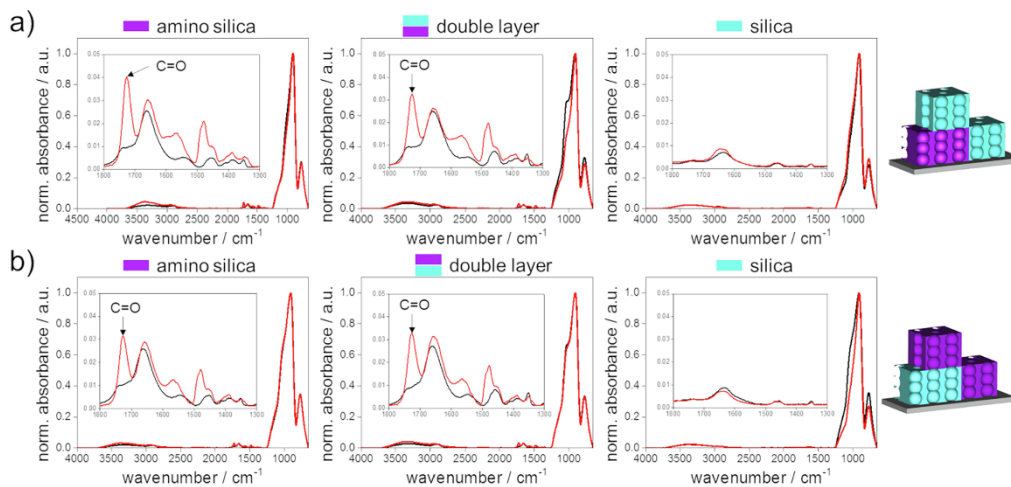
Fig. 2. ATR-IR spectra before (black curves) and after polymer modification (red curves) for single layer films and the double layer film with following sequence: silica layer at bottom - amino silica layer at top (a). ATR-IR spectra before (black curves) and after polymer modification (red curves) for single layer films and the double layer film with following sequence: amino silica layer at bottom - silica layer at top (b). For comparison, all spectra are normalised to the stretching vibration of free silanol groups at ~ 905 cm^{-1}.

observed for BDC functionalised amino silica single layers as well as in the double layer films after polymerisation (Fig. 2, red curves) independently of the layer arrangement (BDC containing amino silica layer on top or at the bottom of a double layer film). This PMETAC C = O band at 1725 cm^{-1} is not observed in the ATR-IR spectra of the silica single layer indicating that these have not been functionalised with BDC and consequently do not contain grafted PMETAC as well as no physically adsorbed polymer. As mentioned above, layer-selective polymer functionalisation using grafting from requires a selective and locally confined binding of the iniferter for layer-selective polymer placement in mesoporous double layer films. The successful layer-selective functionalisation is achieved due to low unspecific adsorption of BDC, suitable MW of METAC allowing successful extraction of non-covalently bound species.

As the presence of the PMETAC C = O band in the ATR-IR spectra indicates a successful layer-selective polymerisation of METAC in the amino silica layers and thus nanoscale step gradient formation, further characterisation on layer selectivity has been conducted. Independently of pH, the PMETAC functionalised layer exhibit positively charged mesopores in consequence of the permanent positive charge of PMETAC. On the contrary, the mesoporous silica layers can be negatively or neutrally charged depending on the protonation state of surface silanol groups and thus depending on pH. For visualisation, mesoporous single layers as well as double layer, which were deposited on glass substrates, as demonstrated in Fig. 1b, were immersed in aqueous fluorescein and rhodamine B solution at pH ~ 5, followed by analysis via fluorescence imaging. Charge-dependent dye adsorption is expected, as fluorescein carries a negative charge and the PMETAC functionalised amino silica layers exhibit a permanent positive charge, while rhodamine B carries a

positive charge and the unmodified silica layers exhibit a negative charge. As shown in Fig. 3a, the functionalised and thus positively charged PMETAC functionalised amino silica layers are coloured in magenta due to the physisorption of negatively charged fluorescein. The unmodified mesoporous layers are represented by the cyan coloured regions due to physisorption of positively charged rhodamine B into the negatively charged mesoporous silica. Note that the colour code matches rather the cartoons than the natural emission colour of the dyes. This charge selective dye adsorption further supports the successful layer-selective PMETAC functionalisation and thus step gradient formation, but as well indicates the potential relevance for transport control.

Following a published protocol from Lin et al. [57], double layer films were transferred from ITO coated glass substrates to PET membrane discs (OxyDisc®) allowing ultrathin sectioning of the samples and further analysis by TEM. Depicted in Fig. 3b, the TEM micrograph shows the cross section of the mesoporous double layer film with the amino silica layer at the bottom and silica layer on top. A layer thickness of 206 ± 2 nm for the amino silica bottom layer, and a thickness of 137 ± 1 nm for the silica top layer is obtained, which is in very good agreement to the thicknesses derived from ellipsometry measurements (Table S3-S4). Furthermore, the mesopore structure of the layers is very well observed indicating that no damage occurred upon the transfer from the solid substrate. Additional TEM micrographs can be found in Figure S4. Furthermore, EDX spectroscopy of the top-view of amino silica single layer as well as double layer films using SEM shows the presence of sulphur and nitrogen confirming successful iniferter coupling along with successful functionalization via polymerization (Figure S6).

Comparing the refractive indices obtained from ellipsometry measurements before and after applying the polymerisation conditions (Fig. 3c-d, Table S1-S4), layer-selective functionalisation is further investigated. Thereby, an increase of the refractive index is expected in consequence of successful polymerisation, since PMETAC (assumption: n_{PMETAC} = 1.5 for organic molecules) replaces the volume of air (n_{air} = 1.0) in the porous material. Considering the single layers, MSTF show a slight decrease in refractive index indicating no functionalisation, whereas the mesoporous amino silica show an increased refractive index due to successful polymerisation of METAC. Pore filling of mesoporous amino silica single layer of 35–56 vol% is calculated by applying the BEMA and refractive indices before and after functionalisation. These observations are in agreement with the respective layers of the mesoporous double layer film, where the mesoporous silica layer is present as bottom layer and mesoporous amino silica layer on top (Fig. 3d), and a pore filling of 84 vol% of the amino silica layer is calculated. Comparing the respective layers of the mesoporous double layer film, where the mesoporous amino silica layer is present as bottom layer and mesoporous silica layer on top (Fig. 3c), again, an increased refractive index of the amino silica layer with a pore filling of 59 vol% is observed upon polymer functionalisation. Although the mesoporous silica bottom layer as well shows an increase in refractive index with a theoretical pore filling of 27 vol%, the initial refractive index (before functionalisation), as well as the film thickness (Table S2), seem to be an artefact of the complex model and undervalued from the fit, when compared to the mesoporous silica single layer, which had been exposed to the same experimental conditions (same substrate) showing no increase in refractive index. In an additional dataset of refractive index changes with lower polymer amount (pore filling 25 – 34 vol%) provided in the Supporting Information (Figure S1), this artefact is not observed, but again an increase of refractive index of mesoporous amino silica layers after polymerisation is observed in single and double layer arrangements. Thus, layer-selective functionalisation is further confirmed by ellipsometry measurements and high pore filling seems to result in difficulties fitting the obtained two layer films with strong refractive index step gradient.
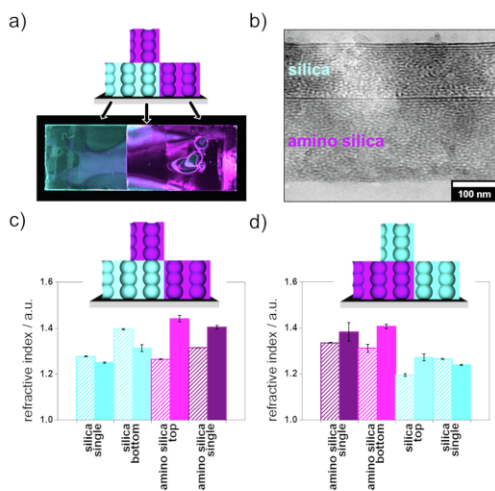
Fig. 3. Fluorescence image of single layers and double layer after subsequent incubation in aqueous fluorescein and rhodamine B solutions marking positively charged layers in magenta which can be attributed to PMETAC functionalised layers and negatively charged layers in cyan corresponding to the unmodified silica layers. Substrate size: 76 × 26 mm (a). Note, that the colour code does not represent the natural emission colour of the dyes used, but rather match the colour code of the cartoons. TEM micrograph of the mesoporous double layer film cross section after applying the polymerisation conditions, scale bar: 100 nm (b). Refractive indices obtained from ellipsometric measurements before (dashed columns) and after applying the polymerisation conditions (filled columns) for mesoporous single layer films and double layer films of the sequence: silica layer at bottom - amino silica layer at top (c) and for the sequence: amino silica layer at bottom - silica layer at top (d).

5

3.3. Correlation to ionic permselectivity of mesoporous thin films

The ionic pore accessibility of the differently and pH-responsively charged mesoporous double layers deposited on conductive ITO coated glass substrates is characterised by cyclic voltammetry using the redox-active probe molecules $[Ru(NH_3)_6]^{2+/3+}$ and $[Fe(CN)_6]^{3-/4-}$, which result in a detected current at their redox potential after diffusing through the mesoporous film reaching the ITO electrode below. Measurements were performed at pH 2 and pH 10 for investigation of pH dependent negative charge of silica, which results from the deprotonation of silanol groups present on the pore wall surface at basic conditions. For the initial and hence unmodified double layers shown in Fig. 4a, the expected pH-dependent ionic permselectivity is observed. At pH 2, $[Fe(CN)_6]^{3-/4-}$ is able to pass through the mesoporous film generating a current at the electrode upon oxidation and reduction. Thereby, no current density is detected for $[Ru(NH_3)_6]^{2+/3+}$, which can be ascribed to electrostatic repulsion and thus $[Ru(NH_3)_6]^{2+/3+}$ exclusion by the positively charged amine groups present in the amino silica layer. At pH 10, the negative charge of deprotonated silanol groups in both layers dominate the ionic mesopore accessibility. At this basic pH, $[Fe(CN)_6]^{3-/4-}$ is electrostatically excluded from the mesopores and no relevant current density is detected at the corresponding oxidation and reduction potential. Contrary to this, $[Ru(NH_3)_6]^{2+/3+}$ shows higher peak current densities as compared to an unmodified ITO electrode for both double layers, along with a peak broadening indicating a pre-concentration of the probe molecule in the mesoporous film. Here, the peak current densities are 1.7–1.8 times higher as compared to an unmodified ITO electrodes (Figure S5). Considering the ionic pore accessibility of the double layer films after modification of the amino silica layer with PMETAC (Fig. 4b), significant influence of the PMETAC functionalisation, but as well of the layer arrangement are observed, especially for the positively charged probe molecule $[Ru(NH_3)_6]^{2+/3+}$ (Fig. 4b). At pH 2 (Fig. 4b-c, black), where the silica layer is neutral in consequence of protonated silanol groups and the PMETAC functionalised amino silica layer positively charged, similar transport properties with respect to $[Fe(CN)_6]^{3-/4-}$ compared to before functionalisation are observed for both layer arrangements into a double layer film. Only a slightly reduced peak current density is detected compared to before functionalisation, which might arise due to steric hindrance upon functionalisation with PMETAC for both double layer arrangements.
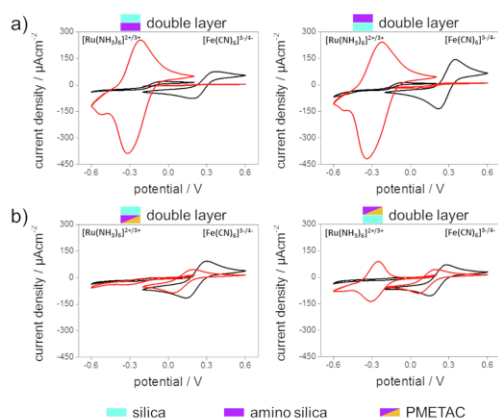
Under the same conditions, $[Ru(NH_3)_6]^{2+/3+}$ is not able to reach the ITO electrode underneath the mesoporous double layer film independently of the layer arrangement induced by the electrostatic repulsion of the PMETAC functionalised and thus positively charged layer. Differently to the unmodified double layers (Fig. 4a) at basic conditions, an increase of peak current density is detected for $[Fe(CN)_6]^{3-/4-}$ at pH 10 after functionalisation with PMETAC for both layer arrangements indicating a weakening of the electrostatic repulsion of the negatively charged silanoate groups of the silica layer as result of incorporation of PMETAC in the amino silica layer, and thus positive charges. Interestingly, $[Fe(CN)_6]^{3-/4-}$ is even able to pass the negatively charged silica top layer (Fig. 4b, left). In case the PMETAC functionalised layer is present as bottom layer, thus a step gradient from negatively charged top layer to positively charged bottom layer, no current density for $[Ru(NH_3)_6]^{2+/3+}$ is observed due to electrostatic repulsion of the positive charge induced by PMETAC functionalised amino silica bottom layer. A different result is obtained for the double layer with inverted layer arrangement containing the PMETAC functionalised, and thus positively charged amino silica as top layer, hence a step gradient from positively charged top layer to negatively charged bottom layer. For this layer arrangement, a peak current density is detected at pH 10, as $[Ru(NH_3)_6]^{2+/3+}$ is able to overcome the positively charged top layer probably by electrostatic attraction of the negatively charged bottom layer. This is a very interesting observation: a reduced peak current density is detected as compared to the unmodified double layer, although the present film thicknesses are much higher than the Debye Screening length (DBL) in these films (DBL here around ~ 1 nm). This indicates that the electrostatic repulsion in such systems can be locally overcome and ionic pore accessibility is dominated by the bottom layer, which is not in direct contact with the solution. The mesoporous double layers and layer-selective functionalisation presented serve as model systems for future mesoporous architectures, whose complexity can be further enhanced by, for example, increasing the number of the incorporated layers, which can be precisely adjusted in film thickness and pore dimensions, or compartmentalisation with other functional units like metal nanoparticles, along with further polymer functionalisation.

4. Conclusions

In summary, we described a layer-selective functionalisation strategy of mesoporous double layered films resulting in charge step gradient formation at the nanoscale. Key elements to this achievement are consecutive layer deposition of mesoporous silica films and co-condensed mesoporous amino silica films, thus predisposition of one layer, followed by layer-selective and controlled iniferter initiated polymerisation. The way of depositing the respective layers allows investigation of single as well as double layered films upon functionalisation granting indirect proof of layer-selective functionalisation by concluding the collective results obtained from IR spectroscopy, ellipsometry, charged dye immobilisation experiment, and cyclic voltammetry. Furthermore, the pH dependent ionic pore accessibility of the mesoporous double layered films before and after PMETAC functionalisation is investigated using cyclic voltammetry. Thereby, the bottom layer revealed a dominant role overcoming local electrostatic repulsion, even it is not in direct contact with the solution. We consider these results will broaden the possibility of creating complex mesoporous multilayer architectures toward multifunctional interfaces for nanofluidics and separation.

Fig. 4. Cyclic voltammograms of the mesoporous double layers using the redox active probe molecules $[Ru(NH_3)_6]^{2+/3+}$ and $[Fe(CN)_6]^{3-/4-}$ at concentration of 1 mM respectively in 100 mM KCl supporting electrolyte solution at pH 2 (black curves) and pH 10 (red curves) before (a) and after PMETAC functionalisation (b). Scan rate: 100 mV s^{-1}.

Credit authorship contribution statement

Mathias Stanzel: Conceptualisation, Investigation, Data curation, Visualisation, Writing - original draft. **Ulrike Kunz:** Investigation, Resources, Data curation. **Annette Andrieu-Brunsen:** Conceptualisation, Supervision, Validation, Writing - review & editing, Funding acquisition.

Declaration of Competing Interest

The authors declare that they have no known competing financial interests or personal relationships that could have appeared to influence the work reported in this paper.

Data availability

The raw/processed data required to reproduce these findings cannot be shared at this time due to technical or time limitations.

Appendix A. Supplementary material

Supplementary data to this article can be found online at https://doi.org/10.1016/j.eurpolymj.2021.110604.

References

[1] C. Dekker, Solid-state nanopores, Nat. Nanotechnol. 2 (2007) 209–215, https://doi.org/10.1038/nnano.2007.27.

[2] R.B. Schoch, J. Han, P. Renaud, Transport phenomena in nanofluidics, Rev. Mod. Phys. 80 (2008) 839–883, https://doi.org/10.1103/RevModPhys.80.839.

[3] S.W. Kowalczyk, T.R. Blosser, C. Dekker, Biomimetic nanopores: learning from and about nature, Trends Biotechnol. 29 (2011) 607–614, https://doi.org/10.1016/j.tibtech.2011.07.006.

[4] S. Zhang, T. Hedtke, X. Zhou, M. Elimelech, J.-H. Kim, Environmental applications of engineered materials with nanoconfinement, ACS ES&T Eng. (2021), https://doi.org/10.1021/acsestengg.1c00007.

[5] L. Bocquet, E. Charlaix, Nanofluidics, from bulk to interfaces, Chem. Soc. Rev. 39 (2010) 1073–1095, https://doi.org/10.1039/b909366b.

[6] H. Daiguji, Ion transport in nanofluidic channels, Chem. Soc. Rev. 39 (2010) 901–911, https://doi.org/10.1039/b820556f.

[7] D.G. Haywood, A. Saha-Shah, L.A. Baker, S.C. Jacobson, Fundamental studies of nanofluidics: nanopores, nanochannels, and nanopipets, Anal. Chem. 87 (2015) 172–187, https://doi.org/10.1021/ac504180h.

[8] L. Bocquet, Nanofluidics coming of age, Nat. Mater. 19 (2020) 254–256, https://doi.org/10.1038/s41563-020-0625-8.

[9] S.F. Buchsbaum, G. Nguyen, S. Howorka, Z.S. Siwy, DNA-modified polymer pores allow pH- and voltage-gated control of channel flux, J. Am. Chem. Soc. 136 (2014) 9902–9905, https://doi.org/10.1021/ja505302q.

[10] Z. Zhang, L. Wen, L. Jiang, Bioinspired smart asymmetric nanochannel membranes, Chem. Soc. Rev. 47 (2018) 322–356, https://doi.org/10.1039/c7cs00688h.

[11] Y.A. Perez Sirkin, M. Tagliazucchi, I. Szleifer, Transport in nanopores and nanochannels: some fundamental challenges and nature-inspired solutions, Mater. Today Adv. 5 (2020), 100047, https://doi.org/10.1016/j.mtadv.2019.100047.

[12] H. Zhou, H. Wang, H. Niu, T. Lin, Superphobicity/philicity Janus fabrics with switchable, spontaneous, directional transport ability to water and oil fluids, Sci. Rep. 3 (2013) 2964, https://doi.org/10.1038/srep02964.

[13] Z. Wang, X. Yang, Z. Cheng, Y. Liu, L. Shao, L. Jiang, Simply realizing "water diode" Janus membranes for multifunctional smart applications, Mater. Horiz. 4 (2017) 701–708, https://doi.org/10.1039/c7mh00216e.

[14] M.B. Wu, H.C. Yang, J.J. Wang, G.P. Wu, Z.K. Xu, Janus membranes with opposing surface wettability enabling oil-to-water and water-to-oil emulsification, ACS Appl. Mater. Interf. 9 (2017) 5062–5066, https://doi.org/10.1021/acsami.7b00017.

[15] M. Nau, N. Herzog, J. Schmidt, T. Meckel, A. Andrieu-Brunsen, M. Biesalski, Janus-type hybrid paper membranes, Adv. Mater. Interf. 6 (2019) 1900892, https://doi.org/10.1002/admi.201900892.

[16] Ç.K. Söz, S. Trosien, M. Biesalski, Janus interface materials: a critical review and comparative study, ACS Mater. Lett. 2 (2020) 336–357, https://doi.org/10.1021/acsmaterialslett.9b00489.

[17] Z. Siwy, A. Fulinski, Fabrication of a synthetic nanopore ion pump, Phys. Rev. Lett. 89 (2002), 198103, https://doi.org/10.1103/PhysRevLett.89.198103.

[18] Z.S. Siwy, Ion-Current Rectification in Nanopores and Nanotubes with Broken Symmetry, Adv. Funct. Mater. 16 (2006) 735–746, https://doi.org/10.1002/adfm.200500471.

[19] Z. Siwy, Y. Gu, H.A. Spohr, D. Baur, A. Wolf-Reber, R. Spohr, P. Apel, Y.E. Korchev, Rectification and voltage gating of ion currents in a nanofabricated pore, Europhys. Lett. 60 (2002) 349–355, https://doi.org/10.1209/epl/i2002-00271-3.

[20] H. Daiguji, Y. Oka, K. Shirono, Nanofluidic diode and bipolar transistor, Nano Lett. 5 (2005) 2274–2280, https://doi.org/10.1021/nl051646y.

[21] L.J. Cheng, L.J. Guo, Ionic current rectification, breakdown, and switching in heterogeneous oxide nanofluidic devices, ACS Nano 3 (2009) 575–584, https://doi.org/10.1021/nn8007542.

[22] R. Yan, W. Liang, R. Fan, P. Yang, Nanofluidic diodes based on nanotube heterojunctions, Nano Lett. 9 (2009) 3820–3825, https://doi.org/10.1021/nl9020123.

[23] Z.S. Siwy, S. Howorka, Engineered voltage-responsive nanopores, Chem. Soc. Rev. 39 (2010) 1115–1132, https://doi.org/10.1039/b909105j.

[24] C.-Y. Li, F.-X. Ma, Z.-Q. Wu, H.-L. Gao, W.-T. Shao, K. Wang, X.-H. Xia, Solution-pH-Modulated Rectification of Ionic Current in Highly Ordered Nanochannel Arrays Patterned with Chemical Functional Groups at Designed Positions, Adv. Funct. Mater. 23 (2013) 3836–3844, https://doi.org/10.1002/adfm.201300315.

[25] C.-Y. Lin, J.-P. Hsu, L.-H. Yeh, Rectification of ionic current in nanopores functionalized with bipolar polyelectrolyte brushes, Sens. Actuators, B 258 (2018) 1223–1229, https://doi.org/10.1016/j.snb.2017.11.172.

[26] E. Madai, M. Valisko, D. Boda, Application of a bipolar nanopore as a sensor: rectification as an additional device function, Phys Chem Chem Phys 21 (2019) 19772–19784, https://doi.org/10.1039/c9cp03821c.

[27] Z.Q. Wu, Z.Q. Li, Y. Wang, X.H. Xia, Regulating ion transport in a nanochannel with tandem and parallel structures via concentration polarization, J. Phys. Chem. Lett. 11 (2020) 524–529, https://doi.org/10.1021/acs.jpclett.9b03016.

[28] X. Wu, P. Ramiah Rajasekaran, C.R. Martin, An alternating current electroosmotic pump based on conical nanopore membranes, ACS Nano 10 (2016) 4637–4643, https://doi.org/10.1021/acsnano.6b00939.

[29] Z. Zhang, P. Li, X.Y. Kong, G. Xie, Y. Qian, Z. Wang, Y. Tian, L. Wen, L. Jiang, Bioinspired heterogeneous ion pump membranes: unidirectional selective pumping and controllable gating properties stemming from asymmetric ionic group distribution, J. Am. Chem. Soc. 140 (2018) 1083–1090, https://doi.org/10.1021/jacs.7b11472.

[30] K. Xiao, L. Chen, R. Chen, T. Heil, S.D.C. Lemus, F. Fan, L. Wen, L. Jiang, M. Antonietti, Artificial light-driven ion pump for photoelectric energy conversion, Nat. Commun. 10 (2019) 74, https://doi.org/10.1038/s41467-018-08029-5.

[31] H. Zhang, X. Hou, L. Zeng, F. Yang, L. Li, D. Yan, Y. Tian, L. Jiang, Bioinspired artificial single ion pump, J. Am. Chem. Soc. 135 (2013) 16102–16110, https://doi.org/10.1021/ja4037669.

[32] A. Bernardos, E. Aznar, M.D. Marcos, R. Martinez-Manez, F. Sancenon, J. Soto, J. M. Barat, P. Amoros, Enzyme-responsive controlled release using mesoporous silica supports capped with lactose, Angew. Chem. Int. Ed. Engl. 48 (2009) 5884–5887, https://doi.org/10.1002/anie.200900880.

[33] C. Coll, L. Mondragon, R. Martinez-Manez, F. Sancenon, M.D. Marcos, J. Soto, P. Amoros, E. Perez-Paya, Enzyme-mediated controlled release systems by anchoring peptide sequences on mesoporous silica supports, Angew. Chem. Int. Ed. Engl. 50 (2011) 2138–2140, https://doi.org/10.1002/anie.201004133.

[34] D.X. Zhang, C. Yoshikawa, N.G. Welch, P. Pasic, H. Thissen, N.H. Voelcker, Spatially controlled surface modification of porous silicon for sustained drug delivery applications, Sci. Rep. 9 (2019) 1367, https://doi.org/10.1038/s41598-018-37750-w.

[35] A. Brunsen, J. Cui, M. Ceolin, A. del Campo, G.J. Soler-Illia, O. Azzaroni, Light-activated gating and permselectivity in interfacial architectures combining "caged" polymer brushes and mesoporous thin films, Chem. Commun. (Camb) 48 (2012) 1422–1424, https://doi.org/10.1039/c1cc14443j.

[36] J. Elbert, F. Krohm, C. Rüttiger, S. Kienle, H. Didzoleit, B.N. Balzer, T. Hugel, B. Stühn, M. Gallei, A. Brunsen, Polymer-modified mesoporous silica thin films for redox-mediated selective membrane gating, Adv. Funct. Mater. 24 (2014) 1591–1601, https://doi.org/10.1002/adfm.201302304.

[37] X. Lin, Q. Yang, F. Yan, B. Zhang, B. Su, Gated molecular transport in highly ordered heterogeneous nanochannel array electrode, ACS Appl. Mater. Interf. 8 (2016) 33343–33349, https://doi.org/10.1021/acsami.6b13772.

[38] S. Schmidt, S. Alberti, P. Vana, G. Soler-Illia, O. Azzaroni, Thermosensitive cation-selective mesochannels: PNIPAM-capped mesoporous thin films as bioinspired interfacial architectures with concerted functions, Chemistry 23 (2017) 14500–14506, https://doi.org/10.1002/chem.201702368.

[39] Q. Yang, X. Lin, Y. Wang, B. Su, Nanochannels as molecular check valves, Nanoscale 9 (2017) 18523–18528, https://doi.org/10.1039/c7nr05924h.

[40] W. Guo, Y. Tian, L. Jiang, Asymmetric ion transport through ion-channel-mimetic solid-state nanopores, Acc. Chem. Res. 46 (2013) 2834–2846, https://doi.org/10.1021/ar400024p.

[41] N. Herzog, J. Kind, C. Hess, A. Andrieu-Brunsen, Surface plasmon & visible light for polymer functionalization of mesopores and manipulation of ionic permselectivity, Chem. Commun. (Camb) 51 (2015) 11697–11700, https://doi.org/10.1039/c5cc03507d.

[42] F. Krohm, J. Kind, R. Savka, M. Alcaraz Janßen, D. Herold, H. Plenio, C.M. Thiele, A. Andrieu-Brunsen, Photochromic spiropyran- and spirooxazine-homopolymers in mesoporous thin films by surface initiated ROMP, J. Mater. Chem. C 4 (2016) 4067–4076, https://doi.org/10.1039/c5tc04054j.

[43] L. Silies, H. Didzoleit, C. Hess, B. Stühn, A. Andrieu-Brunsen, Mesoporous thin films, zwitterionic monomers, and iniferter-initiated polymerization: polymerization in a confined space, Chem. Mater. 27 (2015) 1971–1981, https://doi.org/10.1021/cm503748d.

[44] S. Alberti, G.J. Soler-Illia, O. Azzaroni, Gated supramolecular chemistry in hybrid mesoporous silica nanoarchitectures: controlled delivery and molecular transport

in response to chemical, physical and biological stimuli, Chem. Commun. (Camb) 51 (2015) 6050–6075, https://doi.org/10.1039/c4cc10414e.

[45] G.J. Soler-Illia, O. Azzaroni, Multifunctional hybrids by combining ordered mesoporous materials and macromolecular building blocks, Chem. Soc. Rev. 40 (2011) 1107–1150, https://doi.org/10.1039/c0cs00208a.

[46] A. Brunsen, A. Calvo, F.J. Williams, G.J. Soler-Illia, O. Azzaroni, Manipulation of molecular transport into mesoporous silica thin films by the infiltration of polyelectrolytes, Langmuir 27 (2011) 4328–4333, https://doi.org/10.1021/la200501h.

[47] J.C. Tom, R. Brilmayer, J. Schmidt, A. Andrieu-Brunsen, Optimisation of surface-initiated photoiniferter-mediated polymerisation under confinement, and the formation of block copolymers in mesoporous films, Polymers (Basel) 9 (2017), https://doi.org/10.3390/polym9100539.

[48] L.A. Villaescusa, A. Mihi, I. Rodriguez, A.E. Garcia-Bennett, H. Miguez, Growth of mesoporous materials within colloidal crystal films by spin-coating, J. Phys. Chem. B 109 (2005) 19643–19649, https://doi.org/10.1021/jp053511m.

[49] P.C. Angelomé, M.C. Fuertes, G.J.A.A. Soler-Illia, Multifunctional, multilayer, multiscale: integrative synthesis of complex macroporous and mesoporous thin films with spatial separation of porosity and function, Adv. Mater. 18 (2006) 2397–2402, https://doi.org/10.1002/adma.200600439.

[50] T. Brezesinski, M. Antonietti, B.M. Smarsly, Self-assembled metal oxide bilayer films with "single-crystalline" overlayer mesopore structure, Adv. Mater. 19 (2007) 1074–1078, https://doi.org/10.1002/adma.200602867.

[51] M. Faustini, D.R. Ceratti, B. Louis, M. Boudot, P.A. Albouy, C. Boissiere, D. Grosso, Engineering functionality gradients by dip coating process in acceleration mode, ACS Appl. Mater. Interf. 6 (2014) 17102–17110, https://doi.org/10.1021/am504770x.

[52] M. Faustini, L. Nicole, C.D. Boissière, P. Innocenzi, C.M. Sanchez, D. Grosso, Hydrophobic, antireflective, self-cleaning, and antifogging sol–gel coatings: an example of multifunctional nanostructured materials for photovoltaic cells, Chem. Mater. 22 (2010) 4406–4413, https://doi.org/10.1021/cm100937e.

[53] N. Herzog, H. Hübner, C. Rüttiger, M. Gallei, A. Andrieu-Brunsen, Functional metalloblock copolymers for the preparation and in situ functionalization of porous silica films, Langmuir 36 (2020) 4015–4024, https://doi.org/10.1021/acs.langmuir.0c00245.

[54] J.C. Tom, C. Appel, A. Andrieu-Brunsen, Fabrication and in situ functionalisation of mesoporous silica films by the physical entrapment of functional and responsive block copolymer structuring agents, Soft Matter 15 (2019) 8077–8083, https://doi.org/10.1039/c9sm00872a.

[55] N. Herzog, R. Brilmayer, M. Stanzel, A. Kalyta, D. Spiehl, E. Dörsam, C. Hess, A. Andrieu-Brunsen, Gravure printing for mesoporous film preparation, RSC Adv. 9 (2019) 23570–23578, https://doi.org/10.1039/c9ra04266k.

[56] C.J. Brinker, Y. Lu, A. Sellinger, H. Fan, Evaporation-induced self-assembly: nanostructures made easy, Adv. Mater 11 (1999) 579–585, https://doi.org/10.1002/(SICI)1521-4095(199905)11:7<579::AID-ADMA579>3.0.CO;2-R.

[57] X. Lin, Q. Yang, L. Ding, B. Su, Ultrathin silica membranes with highly ordered and perpendicular nanochannels for precise and fast molecular separation, ACS Nano 9 (2015) 11266–11277, https://doi.org/10.1021/acsnano.5b04887.

[58] A. Calvo, M. Joselevich, G.J.A.A. Soler-Illia, F.J. Williams, Chemical reactivity of amino-functionalized mesoporous silica thin films obtained by co-condensation and post-grafting routes, Microporous Mesoporous Mater. 121 (2009) 67–72, https://doi.org/10.1016/j.micromeso.2009.01.005.

[59] M.G. Bellino, S. Municoy, G.J.A.A. Soler-Illia, Enzymatic tandem systems engineered from mesoporous thin films: synergy leading to efficient starch-electricity conversion, Mater. Today Commun. 7 (2016) 67–72, https://doi.org/10.1016/j.mtcomm.2016.04.002.

[60] T. Magoshi, H. Ziani-Cherif, S. Ohya, Y. Nakayama, T. Matsuda, Thermoresponsive heparin coating: heparin conjugated with poly(N-isopropylacrylamide) at one terminus, Langmuir 18 (2002) 4862–4872, https://doi.org/10.1021/La011408s.

[61] P. Innocenzi, Infrared spectroscopy of sol–gel derived silica-based films: a spectra-microstructure overview, J. Non-Cryst. Solids 316 (2003) 309–319, https://doi.org/10.1016/S0022-3093(02)01637-X.

[62] A. Calvo, P.C. Angelomé, V.M. Sánchez, D.A. Scherlis, F.J. Williams, G.J.A.A. Soler-Illia, Mesoporous aminopropyl-functionalized hybrid thin films with modulable surface and environment-responsive behavior, Chem. Mater. 20 (2008) 4661–4668, https://doi.org/10.1021/cm800597k.

8

5.2.4. Nanolocal functionalization of mesoporous thin films for step gradient formation by asymmetric modification

An alternative asymmetric modification strategy of MSTFs for the incorporation of polymer step gradients with nanoscale spatial control inside a mesoporous multilayer film is introduced in this chapter. Thereby, plasmonic metal NPs are utilized as nanoscale light source to initiate photopolymerizations inside MSTFs. By that, the plasmonic metal NPs additionally serve as nanoscopic sensing unit due to the high sensitivity of LSPR to the dielectric of the NP's surrounding resulting in a nanoporous composite material offering the possibility to detect nanolocal polymer functionalization.

Further pushing the local placement of organic molecules to the nanoscale would require, e.g. nanoscale focusing of light by utilizing surface plasmons offering a highly confined electromagnetic near-field in combination with photopolymerization. The plasmon induced polymer functionalization of MSTFs that were deposited on planar gold or silver surfaces has been successfully demonstrated by our group in previous works.[49, 286] Thereby, the mesopores can be fully functionalized by utilizing transversal modes or partially functionalized utilizing the SPR of the planar metal surfaces. The polymer functionalization of plasmonic metal NPs has been demonstrated in pioneering works of *Soppera*, *Bachelot* and co-workers,[64-66] as discussed in **Chapter 4.3.2**. The combination of plasmonic metal NPs with mesoporous oxide films has been demonstrated in many publications in the last 15 years, envisioning applications in catalysis, optics, and sensing based on the synergy of the properties of the individual materials and new properties arising from their composite materials.[358-364] Thereby, chemical accessibility of Au-NPs inside mesoporous thin films has been demonstrated by *Angelomé* et al. showing the growth and branching of Au-NPs inside mesopores.[70] In addition, plasmonic metal nanostructures offer great potential to be utilized as sensors as summarized in a review article of *Knoll* and co-workers on photonic and plasmonic optical refractive index sensors.[365]

Utilizing plasmonic metal NPs as nanoscale light source to induce photopolymerization with spatial nanoscale resolution in MSTFs, required the precise positioning of the NPs inside the mesoporous material. Therefore, Au-NPs were located between two individual MSTF layers of a double layer film. Firstly, the mesoporous silica bottom layer was deposited using EISA and dip coating, and was thermally stabilized so that the template remains in the porous structure allowing to selectively functionalize the outer silica surface with amino groups for subsequent immobilization of citrate stabilized Au-NPs (see Figure 1 in first following publication). After immersion of the amine functionalized bottom layer in an aqueous Au-NP dispersion, the second silica thin film was deposited as top layer. As the thickness of each individual MSTF can

be adjusted by varying the process parameters of dip coating, the spatial location of the Au-NPs along the mesoporous film cross section can be tuned. Furthermore, it was demonstrated that the particle loading can be tuned by varying the immersion time of the amine functionalized bottom layer in the Au-NP dispersion. A homogeneous distribution of the NPs was demonstrated by TEM, and could be as well deduced from the absorption spectrum of the composite material as no change of the absorption spectrum compared to the absorption spectrum of Au-NP dispersion was observed. Utilizing UV/Vis spectroscopy to observe the LSPR band and varying the refractive index of the composite material's environment by changing the solvent from air (refractive index $n=1.0$) to water ($n=1.33$) and DMSO ($n=1.48$) allowed the determination of the sensitivity of the composite material for detection. A sensing sensitivity of 51 nm/RIU of the composite material was obtained, which is in very good agreement to FEM simulations that resulted in a sensing sensitivity of 55 nm/RIU and also in very good agreement with reported sensing sensitivity for spherical Au-NPs in dispersion solutions[366]. Locally resolved sensing close to the NP surrounding inside the mesoporous material was proven by covering the composite material with a hydrophobic polysiloxane layer showing no change in of the LSPR band by changing the solvent, thus increasing the refractive index, as no liquid entered the mesoporous composite thin film.

To utilize the Au-NPs as nanoscale light source to induce a photopolymerization on the nanoscale, a suitable photopolymerization formulation was developed and optimized for near-field induced polymerization. As the Au-NPs absorbed visible light at a wavelength of 530 nm, a dye-sensitized polymerization with dibromofluorescein absorbing at 525 nm was selected. The threshold energy of the polymerization reaction was investigated and determined to 5.7 mJ/cm^2 under the applied conditions. To ensure that only near-field induced polymerization occurs in the composite material, only an energy dosage of 3.8 mJ/cm^2, two-third of the determined threshold energy, was applied. Successful nanoscale polymer functionalization was then confirmed by ATR-IR spectroscopy compared to a reference material without Au-NPs, as well by a 3 nm red shift of the LSPR band in consequence of an increase of refractive index of the Au-NP's surrounding determined by UV/Vis spectroscopy. Further proof for nanoscale polymerization close to the NPs was obtained by TEM that revealed polymer shells of 5 nm around the Au-NPs, and EDX spectroscopy that proofed the presence of phosphorus originating from the incorporated polymer poly(2-methacryloyloxy)ethyl phosphate (PMEP). As the polymer functionalization could be monitored by a red shift in the UV/Vis, the Au-NPs served as in situ readout unit of successful polymer functionalization. After polymerization, a slight decrease of sensing sensitivity was observed from experiment (44 nm/RIU) as well from FEM simulations (31 nm/RIU) for refractive index sensing after polymer functionalization which was

attributed to the polymer fraction in the sensing area of the LSPR resulting in a higher initial refractive index.

The concept of utilizing plasmonic metal NPs as nanoscale light source inducing photopolymerization inside MSTFs with spatial nanoscale resolution was subsequently transferred to controlled radical polymerization. Thereby, suitable controlled radical and light initiated polymerization reactions were developed and evaluated in grafting from and grafting through approaches by *Daniel John* of the research group of *Annette Andrieu-Brunsen* investigating iniferter initiated polymerizations of two iniferters, namely s-p-trimethoxysilylbenzyl-S'-dodecyltrithiocarbonate (SBDTTC) and 4-cyano-4-((dodecylsulfanylthiocarbonyl)sulfanyl)pentanoic acid (CDTPA). SBDTTC bearing siloxane anchors for covalent attachment on the mesopore wall was used to perform polymer functionalization in a grafting from approach. CDTPA was used in a grafting through approach in presence of polymerizable allyl groups attached to the mesopore wall. As demonstrated by *Daniel John*, the latter allowed polymer functionalization limited to the laser spot, and was further utilized to demonstrate 3D nanoscale resolution of plasmon induced iniferter initiated polymerization.

The photopolymerization with the iniferter CDTPA developed by *Daniel John* was then transferred to mesoporous composite architectures bearing Au/Ag-NPs, which plasmon resonance conditions apply to the irradiation wavelength to induce the polymerization. To demonstrate nanolocal polymer placement by utilization of the LSPR of Au/Ag-NPs, the applied energy dosage was gradually reduced and the composite material bearing alloy Au/Ag-NPs was compared to a reference material without plasmonic metal NPs. Applying an energy dosage of 0.6 J/cm^2, only polymer formation was observed in the composite material containing Au-NPs but not in the absence of Au-NPs, which was again confirmed by UV/Vis spectroscopy, TEM and ATR-IR spectroscopy. The potentially controlled polymerization in combination with nanolocal polymer deposition by utilizing plasmonic metal NPs as nanoscale light source for the functionalization of mesoporous thin films is expected to open up new pathways for nanoporous hybrid materials and device design.

Contribution to the publication in Analytical Chemistry, 2021, 2009732: My contribution to the publication involves the development and performance of mesoporous composite material preparation as well as polymer modification thereof, plasmon-induced polymer modification of mesoporous composite materials, SEM measurements, investigation of particle loading in the composite material using UV/Vis spectroscopy, investigation and determination of the sensing sensitivity of unmodified and polymer modified composite materials in experiment using UV/vis

spectroscopy. Furthermore, I performed the structural characterization by ellipsometry, chemical characterization using ATR-IR spectroscopy, and ionic pore accessibility using cyclic voltammetry of unmodified and polymer modified composite materials. Furthermore I contributed to the conceptualization, visualization and writing the original draft. Lucy Zhao developed and optimized the polymerization formulation based on dye-sensitized polymerization in solution. Thereby, Lucy Zhao determined the threshold energy using ATR-IR spectroscopy. Additionally, Lucy Zhao performed reference experiments with respect to the applied photopolymerization conditions on mesoporous double layer films without gold nanoparticles, as well as on the influence of the base on the polymerization that was used to adjust the solution pH for polymerization. Reza Mohammadi (Institute of Particle Technology, Friedrich-Alexander University Erlangen-Nürnberg) contributed to the publication by conducting FEM simulations and data curation of unmodified and polymer modified mesoporous composite materials, supporting in manuscript writing and visualization. Raheleh Pardehkhorram supported this study by synthesizing CTAB capped gold nanorods as well as by preparation of SH-PEG12-COOH modified gold nanorods and immobilization of such on amine functionalized mesostructured silica thin films. Furthermore, Raheleh Pardehkhorram performed UV/Vis measurements of gold nanorod modified mesostructured silica thin films in dependence of the surrounding media to determine the sensing sensitivity, and supported in manuscript writing. Ulrike Kunz (Department of Materials and Earth Sciences, Physical Metallurgy Group, TU Darmstadt) supported this study with TEM measurements as well as SEM/EDX measurements. Nicolas Vogel (Institute of Particle Technology, Friedrich-Alexander University Erlangen-Nürnberg) supported in conceptualization of FEM simulations as well as in data interpretation, and manuscript writing. Annette Andrieu-Brunsen acquired funding, supervised the project and supported in manuscript writing.

Contribution to the publication in Advanced Functional Materials, 2021, 93, 5394-5402: My contribution to the publication involves the development and performance of mesoporous composite material preparation as well as polymer modification thereof by near-field-induced iniferter initiated polymerization, SEM measurements and investigation of ionic pore accessibility of mesoporous composite materials, and investigation of polymer modified composite materials using UV/vis spectroscopy and ATR-IR spectroscopy. Furthermore, I conducted cyclic voltammetry measurements on allyl silica as well as silica double layer and composite materials to investigate the ionic pore accessibility using redox active and charged probe molecules. Together with Daniel John, I contributed to the conceptualization and visualization, as well as writing the original draft. Daniel John developed and synthesized the visible light sensitive iniferter SBDTTC, and further developed as well as optimized the polymerization formulations using SBDTTC and CDTPA for

visible light iniferter initiated polymerizations respectively. Daniel John further prepared single layer mesoporous silica thin films and modification of such using far-field polymerization, and conducted the characterization of such using ATR-IR spectroscopy, thermogravimetric analysis, ^{1}H-NMR, SEM and ellipsometry. Thereby he demonstrated polymer modification of mesoporous silica thin films locally limited to the laser spot of the applied light source. Annette Andrieu-Brunsen acquired funding, supervised the project and supported in manuscript writing.

Simultaneous Nanolocal Polymer and *In Situ* Readout Unit Placement in Mesoporous Separation Layers

Mathias Stanzel, Lucy Zhao, Reza Mohammadi, Raheleh Pardehkhorram, Ulrike Kunz, Nicolas Vogel, and Annette Andrieu-Brunsen*

ABSTRACT: Bioinspired solid-state nanopores and nanochannels have attracted interest in the last two decades, as they are envisioned to advance future sensing, energy conversion, and separation concepts. Although much effort has been made regarding functionalization of these materials, multifunctionality and accurate positioning of functionalities with nanoscale precision still remain challenging. However, this precision is necessary to meet transport performance and complexity of natural pores in living systems, which are often based on nonequilibrium states and compartmentalization. In this work, a nanolocal functionalization and simultaneous localized sensing strategy inside a filtering mesoporous film using precisely placed plasmonic metal nanoparticles inside mesoporous films with pore accessibility control is

demonstrated. A single layer of gold nanoparticles is incorporated into mesoporous thin films with precise spatial control along the nanoscale layer thickness. The local surface plasmon resonance is applied to induce a photopolymerization leading to a nanoscopic polymer shell around the particles and thus nanolocal polymer placement inside the mesoporous material. As near-field modes are sensitive to the dielectric properties of their surrounding, the *in situ* sensing capability is demonstrated using UV−vis spectroscopy. It is demonstrated that the sensing sensitivity only slightly decreases upon functionalization. The presented nanolocal placement of responsive functional polymers into nanopores offers a simultaneous filtering and nanoscopic readout function. Such a nanoscale local control is envisioned to have a strong impact onto the development of new transport and sensor concepts, especially as the system can be developed into higher complexity using different metal nanoparticles and additional design of mesoporous film filtering properties.
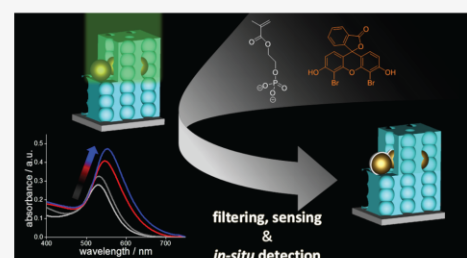
■ INTRODUCTION

Nanoscience and nanotechnology have ever since been inspired by nature, and a variety of bioinspired materials mimicking nature have been successfully introduced.[1−6] One important research goal in this context is related to compartmentalization, miniaturization, and local control of structure formation and functional placement. Therefore, a toolbox of approaches has been developed mainly using top-down and bottom-up approaches. This knowledge becomes increasingly important in the context of nanopore transport modulation to enable nature and life-inspired sustainable future water, energy, and sensing concepts.[7−9] While state-of-the-art approaches in top-down nanofabrication reach a resolution of 10 nm and such devices are approaching mass production, bottom-up approaches attempting to produce nanoscale devices have gained limited success.[10,11] Especially polymer functionalization of pores with nanoscale resolution is still a challenge, but represents an important step toward bioinspired and dynamic transport control in technological pores. This has been demonstrated by natural channels, such as

the potassium-ion channel.[12] In biological channels, the arrangement of several different domains—different charges and hydrophobic side chains—leads to a dynamic, directional, and highly selective transport with high tuning rates. Interestingly, active sides of such biological ion channels are mostly concentrated to a few angstroms, which again indicates the relevance of engineering on the nanometer scale and beyond. Precise placement of responsive functionalities along nanoscale pores together with compartmentalization has to be experimentally implemented by overcoming the passive responsiveness of technological porous materials advancing toward dynamic, self-regulating, adaptive, and active materials directing flow of mass, energy, and information.[11,13] These

5394
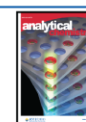
findings have been theoretically demonstrated by Szleifer and co-workers for nanopores and by Bocquet and co-workers regarding responsive membranes.[7,8]

In this context, polymers and especially responsive polymers are well-established functional components that enable the precise functionalization of nanoscale pores with controlled surface coverage or charge density.[14] For example, polymer-functionalized hybrid mesoporous silica thin films show transport properties gradually tunable by controlling the polymer amount and thus controlling the functional density.[15] Furthermore, applying controlled radical polymerizations allows the generation of block-co-oligomers.[16] Selective functionalization of the inner or outer surface of mesoporous materials has been demonstrated by applying several approaches, for example, soft template protection, kinetic protection, or size protection as, for example, recently summarized in a review article of Tiemann and Weinberger.[17] Functionalization of the outer surface of mesoporous materials allows capping of the mesopores enabling gating/switching of ionic transport[18] or controlled release of guest molecules entrapped inside the mesopores,[19] for instance. Such porous architectures can result in Janus-type multilayer porous materials and membranes, and several studies have been published, showing side-selective transport or oil−water separation.[20−23] Local functionalization of artificial nano-channels has been demonstrated by Jiang and co-workers using plasma-induced graft polymerization in an hourglass-shaped nanochannel to generate side-specific double respon-siveness.[24] Applying this asymmetric modification method and cooperative pH-responsive polyelectrolytes, namely, polyvinyl-pyridine and poly(acrylic acid), bioinspired artificial single-ion pumps have been realized.[25] Voelcker and co-workers demonstrated multilayered surface functionalization of alumi-nium oxide membranes by means of multiple anodization and silanization cycles.[26] Furthermore, Liu et al. demonstrated local pore wall functionalization of a single nanopore using contactless electrofunctionalization.[27] Likewise, we demon-strated a strategy to introduce three functional components with precise local control into the pores of an inverse colloidal monolayer as a model system by combining orthogonal surface chemistry and control of the local wetting state of the pores very recently.[28] However, these techniques allow local functionalization of small pores, but precise spatial control perpendicular to the substrate along a porous system and implementation of multiple functionalities inside nanopores still remain challenging. Pushing further local placement of polymers in small pores, nanoscale resolution would require nanoscale focusing of light in combination with photo-polymerizations. This can be achieved using two photon processes, for instance.[29] Alternatively, near-field modes, such as surface plasmons, offer a highly confined electromagnetic near field which is known to initiate polymerization, if compatible initiators are used.[30−33] For example, successful polymer functionalization of mesoporous films deposited on planar gold or silver metal surfaces applying surface plasmons and dye-sensitized photopolymerization systems have been demonstrated in previous studies.[34,35]

Bachelot, Soppera and co-workers pioneered the photo-polymerization induced by the high-energetic near field of silver nanoparticles, thus demonstrating nanoscale functional-ization of plasmonic metal particles.[36] Based on these findings, the same groups investigated not only the plasmonic optical near field of single silver nanoparticles but also the underlying mechanism of the dye-sensitized photopolymerization induced by the plasmonic nanoparticles.[31,37] Furthermore, gold nano-particles (Au-NPs) represent attractive sensing properties, as the spectral position of the localized surface plasmon resonance (LSPR) is highly sensitive to the dielectric environment.[38,39] Previous studies on composite materials using Au-NPs and inorganic mesoporous thin films demon-strated that Au-NPs can be precisely positioned with spatial control and remain accessible for chemical reactions.[40−42] For instance, Angelomé et al. showed growing and branching of Au-NPs embedded in mesoporous films[43] and very recently extended this concept to reaction monitoring.[44]

Herein, we demonstrate for the first time nanolocally limited polymer functionalization with spatial control in mesoporous silica films by taking advantage of the LSPR of Au-NPs to induce a dye-sensitized photopolymerization. Thereby, we present the preparation of a composite material consisting of mesoporous thin films and Au-NPs positioned with spatial control between the mesoporous layers and the consecutive local polymer modification. We investigate the particle loading and refractive index-based sensing sensitivity of the composite material. By that, the sensitivity of LSPR toward environmental changes in the vicinity of the particles allows *in situ* detection of the polymer functionalization. Moreover, the sensing sensitivity of the embedded Au-NPs only slightly decreases upon functionalization in the presented system. As the nanoparticles are synthesized before thin film deposition, the size and shape of the colloids can be easily tuned and engineered to desired properties by applying well-known synthetic protocols. Also, a variety of monomers can be applied with dye-sensitized photopolymerizations, which allows incorporation of a plethora of functionalities and thus rational design of multifunctional porous nanomaterials.

■ EXPERIMENTAL SECTION

Chemicals. All materials and solvents were purchased from Sigma-Aldrich, Acros Organics, and VWR and used as received unless stated otherwise. The precursor solutions for dip coating mesoporous films were prepared using the inorganic precursor tetraethoxysilane (TEOS, Acros Organics, 98%, Geel, Belgium) in absolute ethanol (EtOH, Merck, ≥99.5%), with hydrochloric acid as a catalyst (HCl, 37%) and water. Pluronic F127 (F127, BioReagent, Sigma-Aldrich, 12,600 g mol⁻¹) was used as structure directing agent. Microscope slides (VWR, glass, cut edges), silicon wafers (Si-Mat, Kaufering, Germany, 100 mm diameter, 525 ± 25 μm thickness, type P/Bor, ⟨100⟩ orientation, CZ growth method, 2−5 W resistivity, polished on 1 side), and indium tin oxide (ITO, Delta Technologies, Ltd., Lovel and, CO, USA, polished float glass, $150 \times 150 \times 1.1$ mm, SiO2-passivated/indium tin oxide-coated one surface, RS = 4−8 Ω, cut edges) were cut to the desired size using a diamond cutter, cleaned using technical grade ethanol, and dried under ambient conditions prior to dip coating of mesoporous films.

Synthesis of Au-NPs. According to a procedure from Panigrahi et al.,[45] a solution of 34 mg (0.09 mmol, 1 equiv) of HAuCl₄·3 H₂O in 360 mL of water was refluxed for 10 min. Under vigorous stirring, a solution of 45 mg of sodium citrate (0.126 mmol, 1.4 equiv) in 4.5 mL of water (Milli-Q) was added quickly, and the solution is stirred for another 30 min at reflux. Then, the mixture was cooled to 0 °C and filtered (0.4 μm).

Synthesis of the Mesoporous Composite Material. Mesoporous silica thin films were prepared as previously described[46] *via* sol−gel chemistry using TEOS as an inorganic precursor and an amphiphilic triblock copolymer, Pluronic F127, as a structure-directing template that undergoes micellization upon solvent evaporation, resulting in the formation of a porous inorganic network. The molar ratio of the compounds in the precursor solution used for dip coating was 1 TEOS/0.01 F127/19 EtOH/16.4 H_2O/0.015 HCl. The precursor solution was prepared at room temperature and stirred for 20 min before deposition on glass, silicon wafer, or indium tin oxide coated glass. The films were dip coated at a withdrawal speed of 2 mm/s at 25 °C and 50% relative humidity. After deposition, the films were kept at 25 °C and 50% relative humidity for 1 h. The first film is stabilized by a temperature treatment at 60 and 130 °C for 1 h, respectively. For immobilization of Au-NPs, the mesostructured silica films were functionalized with 3-aminopropyldimethylmethoxysilane using a 0.01 wt % solution in anhydrous toluene. The reaction mixture and the functionalization itself have to be prepared under inert conditions. The reaction mixture was added to the mesostructured film and heated at 80 °C for 1 h. Then, the films were rinsed with toluene and ethanol to remove unbound silane. After drying, the amine-functionalized mesostructured films were incubated in the Au-NP dispersion overnight. The Au-NP functionalized mesostructured films were then covered with a second silica film *via* dip coating using the above-mentioned conditions and stored at 25 °C and 50% relative humidity for 1 h. Finally, the mesoporous composite material was obtained, after a consecutive temperature treatment at 60 and 130 °C for 1 h, followed by a calcination step up to 350 °C with a heating rate of 1 °C/min and holding the temperature for 2 h.

Photopolymerization. The photopolymerization in solution and in the mesoporous composite material was performed with a formulation composed of 1.22×10^{-6} mol· L^{-1} dibromofluorescein as a sensitizer dye, 6.71×10^{-6} mol· L^{-1} N,N-diethylmethylamine (DEMA) as a coinitiator, and 2 mmol· L^{-1} 2-(methacryloyloxy)ethyl phosphate (MEP) as a monomer dissolved in dimethylformamide (DMF). The photopolymerizable formulation was adjusted to pH 7 with triethylamine (Et_3N) and purged with nitrogen for 20 min. Irradiation was performed with a green LED emitting at 530 nm (Metrohm AG, max. 487 lumen) with a distance of 14 cm with respect to the reaction vessel. The light intensity in dependency of the applied current can be found in the Supporting Information (Figure S7).

Attenuated Total Reflection−Fourier Transform Infrared Spectroscopy (ATR-FTIR). Infrared spectra of the prepared mesoporous films on glass substrates were recorded using a PerkinElmer Instrument Spectrum One FT-IR spectrometer equipped with a Universal ATR Polarization Accessory (Waltham, MA, USA). All spectra were normalized to the stretching vibration of free silanol groups at ∼905 cm⁻¹. The spectra were recorded using Spectrum software (Version 10.5.4.738, PerkinElmer, Inc. Waltham, MA, USA, 2016) between 4000 and 650 cm⁻¹ with a resolution of 4 cm⁻¹. A background and a baseline correction were automatically performed. Additional bands of the glass substrate are visible in the FTIR spectra: mesoporous film signals are partially superimposed by signals originating from the glass substrate in the region of 830−1250 cm⁻¹ depending on the penetration depth of the ATR-IR evanescent waves. Nevertheless, due to

the comparable film thickness, IR spectra of different films can be compared. All further data processing was performed in OriginPro9 (ADDITIVE Soft-und Hardware für Technik und Wissenschaft GmbH, Friedrichsdorf, Germany, 2012).

Transmission Electron Microscopy (TEM). TEM micrographs were recorded using a Philips FEI CM-20 transmission electron microscope (Philips, Amsterdam, Netherlands) equipped with an LAB-6 cathode and Olympus CCD camera and with a maximum resolution of 2.3 Å operating at an accelerating voltage of 200 kV. Samples were prepared by scratching off the mesoporous films from the substrate and dispersion in filtered ethanol. After 5 min of sonication, scratched mesoporous films were drop-cast onto 3.05 mm Cu grids (mesh size 200) with a Lacey carbon film (Plano GmbH, article number S166-2). The samples were dried under ambient conditions.

Scanning Electron Microscopy (SEM). SEM micrographs were obtained using a Philips XL30 FEG scanning electron microscope equipped with a tungsten cathode and a back-scattered electron yttrium aluminum garnet (BSE YAG) detector with an accelerating voltage of 15−25 kV, a 30 μm aperture, and a spot size of 3−4. The samples were sputter-coated with a 7 nm coating of Pt/Pd. The digital micrographs were recorded over a range of magnifications at a working distance of approximately 10 mm using an SE2 detector.

Ultraviolet−Visible Spectroscopy (UV−vis). UV−vis spectra were recorded using an Agilent Technologies Cary 60 UV−vis spectrophotometer equipped with a full-spectrum Xenon pulse lamp single source. The spectra were background-corrected using the corresponding solvent. Each spectrum was recorded between 750 and 400 nm at a scan speed of 600 nm min⁻¹. A square aperture PMMA cell with a 1.0 cm path length was used for all measurements.

FEM Simulations. To calculate the absorption spectra of mesoporous composite materials, COMSOL Multiphysics software was used. A cuboid unit cell with periodic boundary conditions in the *xy* plane and port boundary conditions in the *z* direction was chosen. The optical constants of gold were taken from experimental data of Johnson and Christy.[47] The porous matrix was simulated as an effective medium with a homogeneous refractive index calculated by the approximated volume fraction of air and the silica matrix. The refractive index of different surrounding medium was chosen according to the experimental values without dispersion for the whole spectrum range. The illumination was a monochromatic plane wave with linear polarization in the *x* direction and traveling in the *z* direction. Simulations were carried out between 400 and 800 nm in 5 nm steps. The simulations qualitatively reproduce all features of the experiments, including change in intensity and—most importantly—shift in resonance. Quantitative differences between experiments and simulations result from the idealized structure of the model, which assumes identical spherical particles within an identical local environment. In experiments, size distribution, deviations from spherical symmetry, surface inhomogeneities, variations in local environment, and possible deviations in the dielectric function of the synthesized particles all contribute to differences in the plasmon resonances.

■ RESULTS AND DISCUSSION

Composite Fabrication and Characterization. Precise polymer placement inside a nanoporous material was demonstrated by applying LSPR of Au-NPs and a dye-
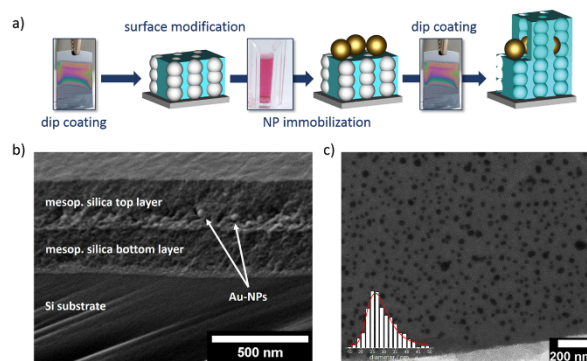
Figure 1. (a) Schematic representation of the mesoporous composite material fabrication procedure: After deposition of the first mesostructured silica thin film, Au-NPs are immobilized on the outer film surface followed by deposition of the second layer and calcination to the final porous architecture. Note that the photographs with respect to dip coating are both the same and only serve for representative purpose of the process itself showing an interference color observable on silicon wafers when the substrate had just been withdrawn from the precursor solution. (b) SEM micrograph of the composite film cross section. Scale bar: 500 nm. (c) TEM micrograph of the composite material showing the Au-NPs with an average particle size of 26 nm embedded between two mesoporous silica thin films. Scale bar: 200 nm. The Au-NP size distribution extracted from the TEM micrograph is shown as the inset.
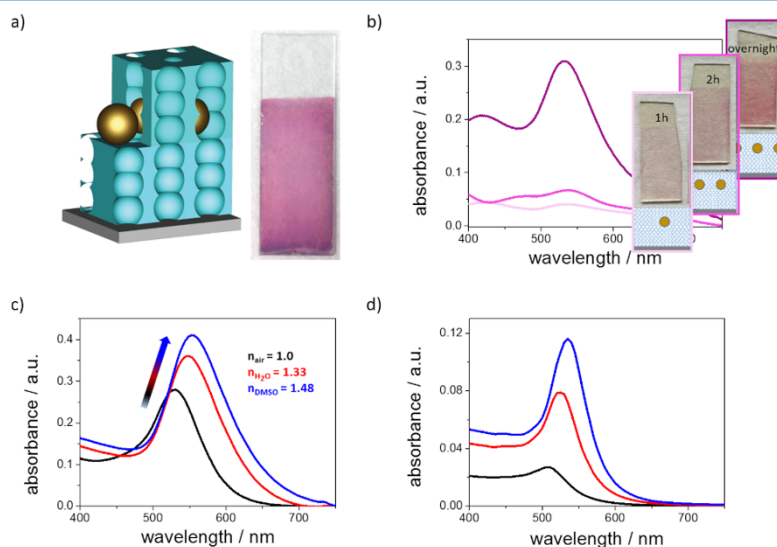
Figure 2. (a) Schematic representation of the mesoporous composite architecture and photograph of the material deposited on a glass slide. (b) Absorption spectra of composite materials in dependence of Au-NP loading. (c) Absorption spectra of the composite material in dependence of the solvents air (black curve), water (red curve), and DMSO (blue curve) obtained experimentally and (d) by FEM simulation.

sensitized photopolymerization. The Au-NP loading of the composite material and the functionalization thereof were investigated with respect to the sensing properties of the composite in experiment and simulation.

The porous composite material was composed of a mesoporous silica double layer with Au-NPs that can be precisely positioned between the two mesoporous layers and thus along the mesoporous film cross section (Figure 1a). First,

a mesostructured thin film is deposited on a substrate *via* dip coating using evaporation-induced self-assembly (EISA).[48]

For further Au-NP sensing unit deposition, amine modification of the outer silica surface allows immobilization of Au-NPs. The immobilized Au-NPs on top of the first crack-free mesostructured thin film distribute homogeneously without aggregate formation (Figures 1 and S1). To complete the mesoporous architecture, we deposit a second mesostruc-

tured silica layer. Calcination finally resulted in the desired mesoporous composite material depicted in Figure 1. Both layers can be adjusted in film thickness allowing to precisely position the metal nanoparticle sensor and thus the nanoscale polymerization light source along the pore dimension.[46]

TEM and SEM micrographs (Figure 1b,c) reveal no influence of Au-NPs on the formation and structural integrity of the second mesoporous thin film, which is in accordance with similar architectures reported in the literature.[49,50] Also from SEM, it can be deduced that the top layer has a smooth surface without appreciable defects. Particle size analysis of the TEM micrograph shows a narrow size distribution with a mean particle size of 26 ($\pm$0.5) nm. Furthermore, an average pore size of the mesoporous silica film of 11 ($\pm$1) nm is obtained from TEM (Figure S13).

The Au-NP loading was investigated regarding the incubation time of the first layer in the Au-NP suspension. The coloration of the final material is visible by the eye, as depicted in Figure 2a, and characterization by UV−vis spectroscopy shows an absorption maximum at 530 nm. Based on UV−vis spectroscopy, control of the immobilized Au-NP amount by varying the immersing time in Au-NP solution was confirmed (Figure 2b). Here, coloration occurs due to localized surface plasmons of the Au-NPs. Taking into account a Au-NP concentration of 0.246 nM in the aqueous suspension resulting in an absorbance of 0.85 at a wavelength of 530 nm, a maximum Au-NP loading of 540 Au-NP/μm^2 on the silica surface of the first thin film can be assumed, which is in good agreement with the TEM micrograph representing an Au-NP loading of around 300 Au-NP/μm^2, shown in Figure 1c. It is worth mentioning that the TEM samples were prepared by scratching off the films from their supporting substrates, thus a loss of Au-NP cannot be excluded.

Comparing the UV−vis spectrum of the Au-NP suspension (Figure S2) with the spectra observed from the mesoporous composite, it is clear that the shape of the LSPR absorption does not change upon integration into mesoporous films, indicating that the nanoparticles were stable and no aggregation occurred. This again confirms a controlled and homogenous immobilization of the particles between two mesoporous silica thin films.

The resonance conditions of surface plasmons are highly dependent on the refractive index of the Au-NP vicinity, which makes them attractive sensors in such constructions, as demonstrated in the UV−vis spectra in Figure 2c. Due to this sensitivity to the local environment, an increase in the refractive index of the surrounding medium (*e.g.*, solvent) leads to a redshift of the LSPR absorption maximum. By varying the surrounding media of the composite material from air (n = 1.00) to water (n = 1.33) or DMSO (n = 1.48) and thus increasing the refractive indices, the sensing sensitivity is investigated. Typically, the sensing sensitivity S of an LSPR sensor is described as the ratio of the sensor output to the change in quantity measured. Here, the refractive index is considered and the sensitivity is reported in nanometers of peak shift per refractive index unit (nm/RIU)

$$S = \Delta\lambda/\Delta n \qquad (1)$$

Plotting the resonance wavelength against the refractive index and proceeding a linear fit allows calculation of the sensing sensitivity, which is represented by the slope of the linear fit. Although the plasmon resonance wavelength is not strictly linear with the refractive index, it is linear to a good

approximation over small ranges of n.[51] As a result of linear fitting the resonance wavelength in dependency of the refractive index obtained from experiment, a sensitivity of 51 nm/RIU with a Pearson correlation coefficient R^2 of 0.99082 is determined for the composite material (Figure S9). Furthermore, with increasing refractive index, an increase in the absorption of the LSPR can be found, which can be attributed to the index matching of the surrounding media and silica.

The simulated spectra in dependence of the material's surrounding shown in Figure 2d qualitatively agree with the experimental results. With increasing refractive index, the absorption of the LSPR shows a redshift, and a sensitivity of 55 nm/RIU with a Pearson correlation coefficient R^2 of 0.97732 is obtained. Additionally, an increase in the absorption is also observed for the simulated spectra. Furthermore, we proved local sensing inside the porous material by covering the composite material with a hydrophobic polysiloxane thin film (Figure S10) and observing no change in the LSPR band upon change in media and thus change in refractive index (Figure S11), as the liquid did not enter the mesoporous film.

Polymer functionalization of such complex systems with nanoscale resolution is possible by combining the plasmonic features of the composite material and dye-sensitized polymerization. This should enable future multifunctional and precisely defined hierarchical nanoporous system design. Here, the absorption spectrum of the composite material overlaps well with the absorption of the dye dibromofluorescein (DBF), and a photopolymerizable formulation thereof has been investigated.

For a locally controlled polymerization induced by the LSPR of the particles, a photopolymerizable formulation containing DBF as sensitizing dye, *N,N*-diethylmethylamine (DEMA) as a coinitiator, and 2-(methacryloyloxy)ethyl phosphate (MEP) as monomer has been systematically studied to determine the energy threshold at which the polymerization is initiated. Such polymerization systems are very flexible, because the components can be modified independently to adjust the physical and chemical properties of the formulation with respect to viscosity, spectral sensitivity, and polymerization threshold.[31]

LSPR-Induced Photopolymerization and Characterization. First of all, the polymerization has been investigated and optimized in solution to establish suitable polymerization conditions for near-field induced polymerization. To excite the sensitizing dye DBF at its absorption maximum at 525 nm, a green LED emitting at 530 nm was used and the pH of the polymerizable solution was adjusted to pH 7 by the addition of Et$_3$N. The latter is crucial, since the polymerization solution becomes acidic when adding the monomer MEP, and DBF shows no absorption in an acidic environment (Figure S3). As a tertiary amine serves as a coinitiator, the influence of Et$_3$N, which is used to adjust pH, is investigated by polymerization without the presence of the coinitiator, and no significant influence of Et$_3$N was observed (Figure S4).

In order to locally limit the polymerization to the presence of the surface plasmon, the irradiation energy has to be kept below the threshold energy of the polymerization initiation. The threshold energy dosage was carried out by investigation of the photopolymerization in solution, keeping the light intensity and the irradiating distance constant. Thereby, the irradiation time is varied and the C= C monomer stretching band of MEP in the FTIR spectrum is observed. The threshold energy corresponds to a significant
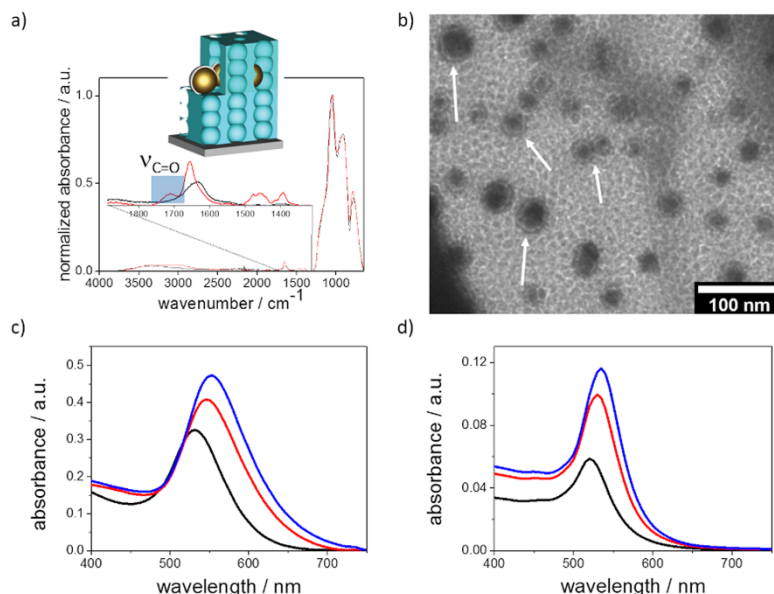
Figure 3. (a) Schematic representation of the polymer-functionalized mesoporous composite material, and FTIR spectra before (black) and after polymer functionalization (red). (b) TEM micrograph of the polymer-functionalized mesoporous composite material. Representative polymer halos of the Au-NPs are indicated by white arrows. Scale bar: 100 nm. (c) Absorption spectra of the composite material before (black) and after polymer functionalization (red) in air and dependence of the solvents water and DMSO obtained experimentally and (d) by FEM simulation.

decrease in the absorption of the C=C stretching band of the monomer at 1635 cm^{-1} in the FTIR (Figure S5) and is of significant importance to determine the energy dosage necessary for near-field polymerization. From this investigation, a threshold energy dosage of 5.7 mJ/cm^2 was determined under the applied conditions.

The LSPR-induced photopolymerization was thus carried out in the presence of the mesoporous composite material by applying an energy dosage of 3.8 mJ/cm^2, which corresponds to two-thirds of the threshold energy dosage needed to initiate the polymerization, in order to avoid free polymerization.

Characterization of functional groups using ATR-FTIR spectroscopy reveals the typical bands for mesoporous silica materials at lower wavenumbers in the range of 650 and 1280 cm^{-1}, indicating the presence of Si−O−Si and Si−OH bands, as discussed intensively in previous studies.[46,52] After polymerization, the appearance of a carbonyl C=O vibrational band at 1700 cm^{-1} can be assigned to the polymer's C=O band (Figure 3a), which does not vanish after careful extraction overnight using DMF as a solvent, indicating covalent grafting (Figure S8). The carbonyl band is not observed, when these polymerization conditions are applied to a reference material without Au-NPs (Figure S14). Furthermore, the TEM micrograph shown in Figure 3b reveals the formation of nanoscopic shells around the plasmonic Au-NPs with a thickness of approximately 5 nm ascribed to polymer formation after polymerization, confirming, together with ATR-IR data, the nanolocal placement of the polymer around the Au-NPs. Additionally, a three nm redshift of the LSPR in the UV−vis is observed after polymerization, indicating an

increase in the refractive index in the vicinity of the Au-NPs (Figure S8). This demonstrates *in situ* detection of the Au-NP's functionalization upon polymerization. Assuming total replacement of air with the polymer in the sensing range of the Au-NPs, a change in refractive index of 0.5 and a redshift of 24 nm were expected based on the sensitivity calculated from experimental results before functionalization. Thus, a redshift of three nm indicates a refractive index change of 0.059 in the sensitive vicinity of the Au-NPs, which corresponds to 12% of the maximum change expected in case of complete pore filling. Moreover, element-specific analysis using EDX spectroscopy proves the presence of phosphorus which can be attributed to the presence of PMEP (Figure S6).

Investigation of the refractive index sensitivity for additional molecules after polymer functionalization of the Au-NPs (Figure 3c,d) reveals a slight reduction of the sensing sensitivity as compared to before polymer functionalization (Figure 2) obtained from experimental and for simulated results. After polymer functionalization, a sensitivity of 44 nm/RIU with an R^2 of 0.99828 is observed from experimental data (Figure 3c and Figure S9), whereas a sensitivity of 31 nm/RIU with an R^2 of 0.99893 is obtained from the simulated data. Due to functionalization, the sensing sensitivity dropped by 14%, which is in good accordance to the calculated polymer amount of 12 vol % in the sensing range of the Au-NPs. However, an increase in the LSPR's absorption with higher refractive indices is also observed after polymer functionalization from both experimental and simulated spectra, which again can be attributed to the index matching of the surrounding media and silica.

Concluding the sensitivity obtained from experiment before (51 nm/RIU) and after functionalization (44 nm/RIU), which is in very good agreement with the sensing sensitivity reported for spherical Au-NPs in dispersion solutions,[53] the detection limit for aqueous protein solutions, as one sensing example, can be calculated[54] (T = 298.15 K) as 8.6 wt % before and 9.5 wt % after functionalization of the Au-NPs inside the porous material, taking a signal output change of $\Delta\lambda = 1$ nm into account. Translating into values of concentration and taking bovine serum albumin as an analyte, 1.3 mM aqueous solutions before and 1.4 mM aqueous solutions after polymer functionalization would be detectable. Although the obtained sensitivity is lower compared to optimized commercial systems,[55] this material represents a promising starting point as an application of different colloidal metals[56−58] and as well different shapes[53,59,60] (Figure S14), together with ultra-sensitive analytical methods, such as surface-enhanced Raman scattering (SERS),[42,44,61] will improve the sensitivity significantly. In addition, the mesoporous film provides a prefilter function (Figure S12) to increase selectivity and the local placement of responsive, ligand-binding polymers enables compartmentalization, allowing new sensing concepts for future applications, as the transport properties can be easily designed upon functionalization.[62−66]

CONCLUSIONS

In summary, nanolocal polymer placement with precise positioning into nanoscale porous thin films and simultaneous readout of functionalization and sensing option have been demonstrated. This has been achieved by placing plasmonic gold nanoparticles as a nanolocal light source for polymerizations between two layers of mesoporous silica thin films. The position can be precisely adjusted by regulating the individual layer thickness. The nanoparticle loading can be tuned by variation of the immersion time of the chemically modified bottom layer in the aqueous nanoparticle solution. Applying dye-sensitized photopolymerization and irradiation dosage below the threshold energy, covalent polymer grafting exclusively in the nanoscopic surrounding and thus within the near-field of gold nanoparticles has been achieved. A redshift of the nanoparticle absorbance has been observed after polymerization, due to the refractive index change in the nanoparticle surrounding, which allows *in situ* detection of functionalization inside the nanoscale porous films. In addition, the sensing ability of the gold nanoparticles has been evaluated regarding the refractive index change, showing a sensitivity of 51 nm/ RIU for the unmodified Au-NPs in the porous system. After nanolocal functionalization, the sensitivity decreases slightly to 44 nm/RIU, which can be attributed to the polymer shell of Au-NPs. FEM simulations of the absorption properties of the plasmonic properties are in good agreement to the experimental results obtained before and after polymer placement. This approach to functionalize nanopores and nanochannels with precise nanoscale spatial control is a key step toward the design of complex multifunctional and multiresponsive porous architectures and thus for the implementation of future water, energy management, and sensing concepts. A general classification of composite materials bearing colloidal metal and mesoporous materials into possible applications is described in detail in ref 49. The presented material design concept allows us to direct the sensing sensitivity toward highly sensitive detection playing with different colloidal metals in different shapes, together with

ultrasensitive analytical methods, for example, SERS. In addition, the selectivity can be tuned using the well-known filtration, selective preconcentration, and, in general, transport and condensation control of mesopores. Furthermore, the presented material and nanoscopic sensing abilities are envisioned to open new insights into the functionalization and transport of nanopores and nanochannels themselves, providing nanoscopic local information of the confinement of nanoporous materials.

ASSOCIATED CONTENT

ⓈⒾ Supporting Information

The Supporting Information is available free of charge at https://pubs.acs.org/doi/10.1021/acs.analchem.0c04446.

Procedure of cyclic voltammetry measurements, synthesis of the hydrophobic polysiloxane thin film, synthesis of gold nanorods, surface modification of gold nanorods, immobilization of gold nanorods on the mesostructured silica surface, additional SEM image of Au-NPs immobilized on the first mesostructured layer, comparison of UV−vis spectra of aqueous Au-NP dispersion solution and the composite material, additional data on the photopolymerization system, EDX data of polymer-functionalized Au-NPs, light intensity and photocurrent of the light source, additional data on polymer functionalization of the composite material, determination of sensing sensitivity, contact angle and data obtained from ellipsometry measurements of the hydrophobic polysiloxane thin film, UV−vis of the composite material covered with a hydrophobic layer in dependence of media, demonstration of permselectivity *via* cyclic voltammetry, pore size distribution of the mesoporous separation layer, reference experiment on nanolocal polymer placement, TEM of gold nanorods, and absorption spectra of gold nanorods immobilized on the first mesostructured silica film (PDF)

AUTHOR INFORMATION

Corresponding Author

Annette Andrieu-Brunsen − *Ernst-Berl Institut für Technische und Makromolekulare Chemie, Technische Universität Darmstadt, 64287 Darmstadt, Germany;* ⓞ orcid.org/ 0000-0002-3850-3047; Email: andrieu-brunsen@ smartmem.tu-darmstadt.de

Authors

Mathias Stanzel − *Ernst-Berl Institut für Technische und Makromolekulare Chemie, Technische Universität Darmstadt, 64287 Darmstadt, Germany*

Lucy Zhao − *Ernst-Berl Institut für Technische und Makromolekulare Chemie, Technische Universität Darmstadt, 64287 Darmstadt, Germany*

Reza Mohammadi − *Institute of Particle Technology, Friedrich-Alexander University Erlangen-Nürnberg, 91058 Erlangen, Germany*

Raheleh Pardehkhorram − *Ernst-Berl Institut für Technische und Makromolekulare Chemie, Technische Universität Darmstadt, 64287 Darmstadt, Germany*

Ulrike Kunz − *Department of Materials and Earth Sciences, Physical Metallurgy Group, Technische Universität Darmstadt, 64287 Darmstadt, Germany*

Nicolas Vogel − *Institute of Particle Technology, Friedrich-Alexander University Erlangen-Nürnberg, 91058 Erlangen, Germany;* ● orcid.org/0000-0002-9831-6905

■ REFERENCES

(1) Bayda, S.; Adeel, M.; Tuccinardi, T.; Cordani, M.; Rizzolio, F. *Molecules* **2019**, *25*, 112.
(2) Benezra, M.; Penate-Medina, O.; Zanzonico, P. B.; Schaer, D.; Ow, H.; Burns, A.; DeStanchina, E.; Longo, V.; Herz, E.; Iyer, S.; Wolchok, J.; Larson, S. M.; Wiesner, U.; Bradbury, M. S. *J. Clin. Invest.* **2011**, *121*, 2768−2780.
(3) Kim, S. E.; Zhang, L.; Ma, K.; Riegman, M.; Chen, F.; Ingold, I.; Conrad, M.; Turker, M. Z.; Gao, M.; Jiang, X.; Monette, S.; Pauliah, M.; Gonen, M.; Zanzonico, P.; Quinn, T.; Wiesner, U.; Bradbury, M. S.; Overholtzer, M. *Nat. Nanotechnol.* **2016**, *11*, 977−985.
(4) Vanag, V. K.; Epstein, I. R. *PNAS* **2003**, *100*, 14635−14638.
(5) Gimenéz, C.; Climent, E.; Aznar, E.; Martínez-Máñez, R.; Sancenón, F.; Marcos, M. D.; Amoros, P.; Rurack, K. *Angew. Chem., Int. Ed. Engl.* **2014**, *53*, 12629−12633.
(6) Tonga, G. Y.; Jeong, Y.; Duncan, B.; Mizuhara, T.; Mout, R.; Das, R.; Kim, S. T.; Yeh, Y.-C.; Yan, B.; Hou, S.; Rotello, V. M. *Nat. Chem.* **2015**, *7*, 597−603.
(7) Huang, K.; Szleifer, I. *J. Am. Chem. Soc.* **2017**, *139*, 6422−6430.
(8) Marbach, S.; Kavokine, N.; Bocquet, L. *J. Chem. Phys.* **2020**, *152*, 054704.
(9) Püttmann, W.; Keil, F.; Oehlmann, J.; Schulte-Oehlmann, U. *Environ. Sci. Eur.* **2008**, *20*, 209−226.
(10) Nasrollahzadeh, M.; Sajadi, S. M.; Sajjadi, M.; Issaabadi, Z. *Interface Sci.* **2019**, *28*, 113−143.
(11) Grzybowski, B. A.; Huck, W. T. S. *Nat. Nanotechnol.* **2016**, *11*, 585−592.
(12) Doyle, D. A.; Morais Cabral, J.; Pfuetzner, R. A.; Kuo, A.; Gulbis, J. M.; Cohen, S. L.; Chait, B. T.; MacKinnon, R. *Science* **1998**, *280*, 69−77.
(13) Merindol, R.; Walther, A. *Chem. Soc. Rev.* **2017**, *46*, 5588−5619.
(14) Brilmayer, R.; Förster, C.; Zhao, L.; Andrieu-Brunsen, A. *Curr. Opin. Biotechnol.* **2020**, *63*, 200−209.
(15) Brunsen, A.; Calvo, A.; Williams, F. J.; Soler-Illia, G. J. A. A.; Azzaroni, O. *Langmuir* **2011**, *27*, 4328−4333.
(16) Brilmayer, R.; Hess, C.; Andrieu-Brunsen, A. *Small* **2019**, *15*, 1902710.
(17) Tiemann, M.; Weinberger, C. *Adv. Mater. Interfaces* **2020**, *8*, 2001153.
(18) Brunsen, A.; Cui, J.; Ceolín, M.; Campo, A. d.; Soler-Illia, G. J. A. A.; Azzaroni, O. *Chem. Commun.* **2012**, *48*, 1422−1424.
(19) Bernardos, A.; Aznar, E.; Marcos, M. D.; Martínez-Máñez, R.; Sancenón, F.; Soto, J.; Barat, J. M.; Amorós, P. *Angew. Chem., Int. Ed. Engl.* **2009**, *48*, 5884−5887.

(20) Lin, X.; Yang, Q.; Yan, F.; Zhang, B.; Su, B. *ACS Appl. Mater. Interfaces* **2016**, *8*, 33343−33349.
(21) Zhang, Z.; Li, P.; Kong, X.-Y.; Xie, G.; Qian, Y.; Wang, Z.; Tian, Y.; Wen, L.; Jiang, L. *J. Am. Chem. Soc.* **2018**, *140*, 1083−1090.
(22) Wang, Z.; Yang, X.; Cheng, Z.; Liu, Y.; Shao, L.; Jiang, L. *Mater. Horiz.* **2017**, *4*, 701−708.
(23) Söz, Ç. K.; Trosien, S.; Biesalski, M. *ACS Mater. Lett.* **2020**, *2*, 336−357.
(24) Hou, X.; Yang, F.; Li, L.; Song, Y.; Jiang, L.; Zhu, D. *J. Am. Chem. Soc.* **2010**, *132*, 11736−11742.
(25) Zhang, H.; Hou, X.; Zeng, L.; Yang, F.; Li, L.; Yan, D.; Tian, Y.; Jiang, L. *J. Am. Chem. Soc.* **2013**, *135*, 16102−16110.
(26) Jani, A. M. M.; Kempson, I. M.; Losic, D.; Voelcker, N. H. *Angew. Chem., Int. Ed. Engl.* **2010**, *49*, 7933−7937.
(27) Liu, J.; Pham, P.; Haguet, V.; Sauter-Starace, F.; Leroy, L.; Roget, A.; Descamps, E.; Bouchet, A.; Buhot, A.; Mailley, P.; Livache, T. *Anal. Chem.* **2012**, *84*, 3254−3261.
(28) Ochs, M.; Mohammadi, R.; Vogel, N.; Andrieu-Brunsen, A. *Small* **2020**, *16*, 1906463.
(29) Rühe, J. *ACS Nano* **2017**, *11*, 8537−8541.
(30) Nguyen, M.; Lamouri, A.; Salameh, C.; Lévi, G.; Grand, J.; Boubekeur-Lecaque, L.; Mangeney, C.; Félidj, N. *Nanoscale* **2016**, *8*, 8633−8640.
(31) Deeb, C.; Ecoffet, C.; Bachelot, R.; Plain, J.; Bouhelier, A.; Soppera, O. *J. Am. Chem. Soc.* **2011**, *133*, 10535−10542.
(32) Haggui, M.; Dridi, M.; Plain, J.; Marguet, S.; Perez, H.; Schatz, G. C.; Wiederrecht, G. P.; Gray, S. K.; Bachelot, R. *ACS Nano* **2012**, *6*, 1299−1307.
(33) Zhou, X.; Deeb, C.; Kostcheev, S.; Wiederrecht, G. P.; Adam, P.-M.; Béal, J.; Plain, J.; Gosztola, D. J.; Grand, J.; Félidj, N.; Wang, H.; Vial, A.; Bachelot, R. *ACS Photonics* **2014**, *2*, 121−129.
(34) Herzog, N.; Kind, J.; Hess, C.; Andrieu-Brunsen, A. *Chem. Commun.* **2015**, *51*, 11697−11700.
(35) John, D.; Mohammadi, R.; Vogel, N.; Andrieu-Brunsen, A. *Langmuir* **2020**, *36*, 1671−1679.
(36) El Ahrach, H. I.; Bachelot, R.; Vial, A.; Lérondel, G.; Plain, J.; Royer, P.; Soppera, O. *Phys. Rev. Lett.* **2007**, *98*, 107402.
(37) Deeb, C.; Bachelot, R.; Plain, J.; Baudrion, A.-L.; Jradi, S.; Bouhelier, A.; Soppera, O.; Jain, P. K.; Huang, L.; Ecoffet, C.; Balan, L.; Royer, P. *ACS Nano* **2010**, *4*, 4579−4586.
(38) Alvarez-Puebla, R.; Liz-Marzán, L. M.; García de Abajo, F. J. *J. Phys. Chem. Lett.* **2010**, *1*, 2428−2434.
(39) Dai, Y.; Wang, Y.; Liu, B.; Yang, Y. *Small* **2015**, *11*, 268−289.
(40) Innocenzi, P.; Malfatti, L. *J. Nanoparticle Res.* **2018**, *20*, 167.
(41) Martínez, E. D.; Boissière, C.; Grosso, D.; Sanchez, C.; Troiani, H.; Soler-Illia, G. J. A. A. *J. Phys. Chem. C* **2014**, *118*, 13137−13151.
(42) López-Puente, V.; Abalde-Cela, S.; Angelomé, P. C.; Alvarez-Puebla, R. A.; Liz-Marzán, L. M. *J. Phys. Chem. Lett.* **2013**, *4*, 2715−2720.
(43) Angelomé, P. C.; Pastoriza-Santos, I.; Pérez-Juste, J.; Rodríguez-González, B.; Zelcer, A.; Soler-Illia, G. J. A. A.; Liz-Marzán, L. M. *Nanoscale* **2012**, *4*, 931−939.
(44) Zalduendo, M. M.; Oestreicher, V.; Langer, J.; Liz-Marzán, L. M.; Angelomé, P. C. *Anal. Chem.* **2020**, *92*, 13656−13660.
(45) Panigrahi, S.; Basu, S.; Praharaj, S.; Pande, S.; Jana, S.; Pal, A.; Ghosh, S. K.; Pal, T. *J. Phys. Chem. C* **2007**, *111*, 4596−4605.
(46) Herzog, N.; Brilmayer, R.; Stanzel, M.; Kalyta, A.; Spiehl, D.; Dörsam, E.; Hess, C.; Andrieu-Brunsen, A. *RSC Adv.* **2019**, *9*, 23570−23578.
(47) Johnson, P. B.; Christy, R. W. *Phys. Rev. B: Condens. Matter Mater. Phys.* **1972**, *6*, 4370−4379.
(48) Brinker, C. J.; Lu, Y.; Sellinger, A.; Fan, H. *Adv. Mater.* **1999**, *11*, 579−585.
(49) Angelomé, P. C.; Liz-Marzán, L. M. *J. Sol-Gel Sci. Technol.* **2014**, *70*, 180−190.
(50) Rodríguez-Fernández, D.; Angelomé, P. C.; Soler-Illia, G. J. A. A.; Liz-Marzán, L. M. *Part. Part. Syst. Char.* **2017**, *34*, 1600428.
(51) Mayer, K. M.; Hafner, J. H. *Chem. Rev.* **2011**, *111*, 3828−3857.

(52) Stanzel, M.; Brilmayer, R.; Langhans, M.; Meckel, T.; Andrieu-Brunsen, A. *Microporous Mesoporous Mater.* **2019**, *282*, 29−37.

(53) Chen, H.; Kou, X.; Yang, Z.; Ni, W.; Wang, J. *Langmuir* **2008**, *24*, 5233−5237.

(54) Tan, C.-Y.; Huang, Y.-X. *J. Chem. Eng. Data* **2015**, *60*, 2827−2833.

(55) Piliarik, M.; Homola, J. *Opt. Express* **2009**, *17*, 16505−16517.

(56) Sherry, L. J.; Jin, R.; Mirkin, C. A.; Schatz, G. C.; Van Duyne, R. P. *Nano Lett.* **2006**, *6*, 2060−2065.

(57) López-Tejeira, F.; Paniagua-Domínguez, R.; Sánchez-Gil, J. A. *ACS Nano* **2012**, *6*, 8989−8996.

(58) Ma, C.; Liu, Y.; Zhao, F.; Xu, F.; Yan, J.; Li, X.; Guan, B.-O.; Yang, G.; Chen, K. *J. Mater. Chem. C* **2020**, *8*, 6350−6357.

(59) Bukasov, R.; Shumaker-Parry, J. S. *Nano Lett.* **2007**, *7*, 1113−1118.

(60) Michieli, N.; Balasa, I. G.; Kalinic, B.; Cesca, T.; Mattei, G. *Nanoscale Adv.* **2020**, *2*, 3304−3315.

(61) Litti, L.; Reguera, J.; García de Abajo, F. J.; Meneghetti, M.; Liz-Marzán, L. M. *Nanoscale Horiz.* **2019**, *5*, 102−108.

(62) Brilmayer, R.; Kübelbeck, S.; Khalil, A.; Brodrecht, M.; Kunz, U.; Kleebe, H. J.; Buntkowsky, G.; Baier, G.; Andrieu-Brunsen, A. *Adv. Mater. Interfaces* **2020**, *7*, 1901914.

(63) Tom, J. C.; Appel, C.; Andrieu-Brunsen, A. *Soft Matter* **2019**, *15*, 8077−8083.

(64) Silies, L.; Gonzalez Solveyra, E.; Szleifer, I.; Andrieu-Brunsen, A. *Langmuir* **2018**, *34*, 5943−5953.

(65) Andrieu-Brunsen, A.; Micoureau, S.; Tagliazucchi, M.; Szleifer, I.; Azzaroni, O.; Soler-Illia, G. J. A. A. *Chem. Mater.* **2015**, *27*, 808−821.

(66) Bodelón, G.; Montes-García, V.; López-Puente, V.; Hill, E. H.; Hamon, C.; Sanz-Ortiz, M. N.; Rodal-Cedeira, S.; Costas, C.; Celiksoy, S.; Pérez-Juste, I.; Scarabelli, L.; La Porta, A.; Pérez-Juste, J.; Pastoriza-Santos, I.; Liz-Marzán, L. M. *Nat. Mater.* **2016**, *15*, 1203−1211.

Surface Plasmons and Visible Light Iniferter Initiated Polymerization for Nanolocal Functionalization of Mesoporous Separation Layers

Daniel John, Mathias Stanzel, and Annette Andrieu-Brunsen*

Although the technological relevance of mesoporous ceramic polymer hybrid materials is well accepted, missing functionalization concepts enabling 3D nanoscale local control of polymer placement into mesoporous materials, including thin films, and ideally using controlled polymerization techniques limit the application potential. Here, nanolocal functionalization of mesoporous separation layers using controlled, visible light iniferter initiated polymerization allowing responsive polymer functionalization locally limited to the irradiated spot is introduced. Thereby, two visible light sensitive iniferters, s-p-trimethoxysilylbenzyl-S´-dodecyltrithiocarbonate and 4-cyano-4-((dodecylsulfanylthiocarbonyl)sulfanyl)pentanoic acid, are developed for polymer functionalization of mesoporous films in a grafting from and a grafting through approach. 3D nanolocal polymer placement close to the proximity of the plasmonic field source is demonstrated by combining these visible light iniferter initiated polymerizations with optical near field modes, such as localized surface plasmon resonance (LSPR). As the location of the LSPR in mesoporous films can be controlled by placing metal alloy nanoparticles into these films and film thicknesses can be adjusted, this strategy is applied for precise positioning of polymers into mesoporous films with nanolocal control in three dimensions and thus reduces the gap in precision of functional group positioning between technological and biological nanopores.

1. Introduction

Mesoporous oxide films are materials with technological relevance in sensing,[1] molecular sieving,[2] catalysis, and energy conversion.[3] All these technologies depend on molecular transport in nanoscale pores. Often inspired by the structural precision and performance of biological pores, transport through mesopores has been strongly investigated within the last two decades and especially polymers have been used to implement new functions

D. John, M. Stanzel, Prof. A. Andrieu-Brunsen
Ernst-Berl-Institut für Technische und Makromolekulare Chemie
Technische Universität Darmstadt
Alarich-Weiss-Straße 8, Darmstadt 64287, Germany
E-mail: andrieu-brunsen@smartmem.tu-darmstadt.de

The ORCID identification number(s) for the author(s) of this article can be found under https://doi.org/10.1002/adfm.202009732.

and specific transport characteristics into such nanoscale pores. In this context, polymer functionalization of mesopores advanced significantly within the last years. The majority of polymer functionalized mesopores focuses on responsive polymer grafting resulting, for example, in tuneable gating of ionic permselectivity. Within the last decade, gating of mesopore transport has been demonstrated by applying different stimuli such as pH,[4] temperature,[5] presence of ions,[6] light,[7] or voltage.[8] Contemporary studies related to polymer functionalized mesopores demonstrated control of polymer amount and thus controllable functional density in mesoporous silica.[4,9] In addition, our research group recently demonstrated re-initiation of iniferter initiated polymerization resulting in block-*co*-oligomer functionalized silica mesopores.[10] This allows investigation of the influence of chain architecture on mesopore transport and demonstrates the utility of living polymerizations in mesoporous materials to generate multifunctional and multiresponsive pores.[10b,11]

Being inspired by biological pores and their transport performance, their precise local arrangement of functional units within a pore is of interest for transport design. Strategies to locally control the polymer grafting at the nanoscale and especially within mesoporous films are still very limited and have rarely been combined with living polymerization techniques. To date, (nano)local resolution in pore functionalization has been demonstrated by stepwise and thus layer-wise material deposition which could be followed by locally limited polymerization.[12] Very recently, we demonstrated precise placement of three different functional units of molecular and polymeric nature into inverse opal monolayers as model system using orthogonal surface chemistry and wetting control.[13] These approaches result in local functionalization along the porous film thickness, but no simultaneous nanoscale local resolution within x- and y-direction was achieved. In this context, near field mode induced polymerization is a promising approach as the electromagnetic field is localized into nanoscale dimensions. As demonstrated by Soppera and coworkers and by Kreiter and coworkers, near field mode induced chemistry allows nanolocally limited (polymer) functionalization of plasmonic metal nanostructures.[14] Although, tunable by particle size

**ADVANCED
SCIENCE NEWS**
www.advancedsciencenews.com

**ADVANCED
FUNCTIONAL
MATERIALS**
www.afm-journal.de

and composition of colloidal metal, near field modes, such as surface plasmons, usually emit light in the visible wavelength range larger than 400 nm. Thus, near field mode compatible photopolymerizations have to be selected or developed.

The combination of metal nanoparticles and mesoporous oxide thin films has been demonstrated in several studies in the last 15 years, and such composite materials are proposed for applications in catalysis,[3a,15] optics,[16] and sensing.[17] The bases for this application potential are new properties, which arise due to the synergy of the individual components. Several approaches for incorporation of the metallic nanoparticles into the mesoporous oxide thin films are known and the position inside the porous matrix can be precisely adjusted.[18] Nonetheless, incorporated in the mesoporous matrix, metallic nanoparticles remain accessible for chemical reactions. For example, Angelomé et al. demonstrated the growing and branching of gold nanoparticles that had been immobilized on a glass surface and covered with a mesoporous silica thin film.[19] Furthermore, these systems can be very diverse, as the properties of metallic nanoparticles can be tuned beforehand by following well known synthesis protocols,[20] and mesoporous oxide films are tunable in pore size, film thickness, as well as surface functionalization.[21]

Within the last years, visible light induction has been demonstrated for many polymerization mechanisms such as atom radical transfer polymerization (ATRP),[22] ring opening metathesis polymerization,[23] dye sensitized polymerizations,[14a,24] and iniferter initiated polymerizations.[25] The majority of these visible light induced polymerizations is using wavelengths around 400 nm, which is mostly not suitable for surface plasmon generation. Nevertheless, the number of photopolymerizations induced by larger wavelengths increases. For example, the induction wavelength of ATRP has been shifted to 464 nm by Zhu and coworkers[26] using [Ir(ppy)₃] as photoredox catalyst and to 400–500 nm by Yagci and coworkers[27] performing a metal-free ATRP by using perylene. Only a few examples for polymerizations at higher wavelengths are known and limited to photoinduced electron transfer reversible addition fragmentation termination (PET-RAFT)[28] or dye sensitized polymerizations.[29] Surface plasmon induced polymerizations at wavelength higher than 400 nm have been mainly combined with dye sensitized polymerizations[14a,24] and reversible addition fragmentation termination (RAFT) polymerization using azobisisobutyronitrile (AIBN) as an initiator.[30] Very recently, a first example of so-called plasmon catalyzed PET-RAFT polymerization on gold gratings has been reported.[31] In terms of RAFT polymerizations, a tolerance versus oxygen has been achieved in combination with photoredox catalysts[32] or dyes, for example, Eosin Y, and ascorbic acid.[33] The combination with dyes is even more beneficial, as light above 516 nm becomes suitable for polymerization induction. Furthermore, the catalytic presence of Eosin Y leads to faster reaction kinetics compared to polymerizations in absence of the dye.[34] Furthermore, a PET-RAFT approach, which utilizes zinc tetraphenylporphyrin enabling visible light induction, was very recently applied on planar surfaces by the group of Boyer.[35]

Although, the number of visible light induced controlled or living polymerizations is increasing rapidly at the moment, almost all present studies related to near field induced polymerizations use free-radical polymerization approaches mostly using commercial components which strongly limits their diversity. Thereby, controlled polymerization techniques are of special interest as these would not only allow a certain control on polymer amount, but further provide access to chain composition control in addition to nanolocal placement. However, as the LSPR is usually generated upon visible light irradiation, suitable polymerization techniques are required.

In this context, the first example of nanoscale polymer functionalization using a controlled polymerization reaction has very recently been reported by Soppera and coworkers demonstrating re-initiation using near-field mode induced ATRP, and by this, showing preparation of multifunctional metal/polymer nanostructures.[36] Compared to ATRP, iniferter initiated polymerization is versatile as it offers polymerization control without requiring additional radical sources such as AIBN.[25b,37] This is especially useful for functionalization of nanoscale pores with restricted pore accessibility. The development of such visible light sensitive iniferter molecules attained constantly increasing attraction since 2015,[38] and iniferter polymerization induced by visible light was demonstrated for the first time by the group of Qiao in 2015.[25a]

Here, we demonstrate visible light induced and nanolocal polymer functionalization of mesoporous separation layers using visible light and plasmon induced iniferter initiated polymerization. Therefore, gold-silver alloy nanoparticles (Au/Ag-NPs) were integrated into mesoporous silica films as surface plasmon and thus nanoscale light source. S-p-trimethoxysilylbenzyl-S'-dodecyltrithiocarbonate (SBDTTC) which possesses an absorption maximum at 434 nm in DMSO (Figure S8, Supporting Information) is used to functionalize mesoporous films in a grafting from approach. The iniferter 4-cyano-4-((dodecylsulfanylthiocarbonyl)sulfanyl)pentanoic acid (CDTPA) possessing an absorption maximum at 448 nm in ethanol (Figure S8, Supporting Information) is used to functionalize mesoporous silica films with grafted allyl triethoxysilane (allyl functionalized silica) in a grafting through approach applying visible light irradiation and surface plasmon near field modes of the embedded nanoparticles. Nanolocally limited polymer functionalization is demonstrated for CDTPA by electron microscopy.

2. Results and Discussion

Polymer functionalization of mesoporous thin films is achieved by applying visible light and iniferter initiated polymerization. The iniferter CDTPA is used in a grafting through approach, whereas SBDTTC (synthesis described in the supporting information and characterization shown in Figures S1–S3, Supporting Information) is used in a grafting from approach (**Figure 1**). The polymer placement in mesoporous films is investigated. Dimethylaminoethyl methacrylate (DMAEMA) was used as monomer due to its responsivity to pH and reported transport regulation.[11]

Polymerizations were conducted under visible light irradiation without additional radical sources or catalysts in 600–800 nm thick mesoporous silica films with pore sizes of 12 nm (neck) and 16 nm (Figure S4, Supporting Information).

2009732 (2 of 9)

ADVANCED
SCIENCE NEWS
www.advancedsciencenews.com

ADVANCED
FUNCTIONAL
MATERIALS
www.afm-journal.de
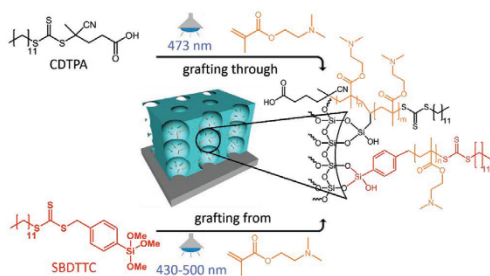
Figure 1. Chemical structures of CDTPA (black) and SBDTTC (red). Polymer functionalization of mesoporous silica films using CDTPA follows a grafting through approach after covalent grafting of allyltriethoxysilane to the mesopore wall, whereas polymer functionalization using SBDTTC is achieved by grafting from after binding SBDTTC to the mesopore wall.

The mesoporous films show a porosity of 55 vol% as calculated by the Bruggeman effective medium theory (BEMT) applying the refractive index determined by ellipsometry at a relative humidity of 20% as further described in literature (see also Table S1, Supporting Information).[10a,39] In order to achieve polymer functionalization in a grafting from approach, SBDTTC is covalently grafted to the mesoporous silica surface. Prior to polymerization under visible light irradiation, the SBDTTC functionalized mesoporous silica films are CO_2-plasma treated for removal of SBDTTC at the outer planar mesoporous film surface according to a protocol from Babu et al.[40] Consequently, polymerization can only proceed within the mesoporous film, but not on the planar outer surface.

The SBDTTC functionalization becomes evident by the mass loss of 20% in TGA-measurements (**Figure 2c**, black and red). The SBDTTC functionalized mesoporous films are then used for visible light induced polymerization. As SBDTTC did not initiate polymerizations under thermal treatment up to 70 °C under the applied experimental conditions (Figures S10–S12, Supporting Information), the increasing C=O stretching vibrational band at 1728 cm^{-1} is attributed to poly(2-(dimethylamino) ethyl methacrylate) (PDMAEMA). Increasing PDMAEMA amount with increasing polymerization time is observed (Figure 2b,c). After 5 h of polymerization, a relative C=O vibrational band intensity of 0.05 at 1728 cm^{-1} (Figure 2b, blue) is observed. By increasing the polymerization time to 17 h, this relative C=O stretching vibrational band intensity at 1728 cm^{-1} increases to 0.08 (Figure 2b, dark yellow). Characterization by TGA shows an initial mass loss of 3% between 100 and 200 °C which is attributed to adsorbed water (Figure 2c, black). The observed mass loss of 7% between 400 and 600 °C is ascribed to chemisorbed water (Figure 2c, black).[41] A total mass loss of 20% at 600 °C is observed for SBDTTC functionalized mesoporous silica films (Figure 2c, red) indicating successful functionalization with SBDTTC. Considering a specific surface area range of 170–610 m^2 g^{-1}, as determined by two different approaches, a grafting density of SBDTTC of 0.44 – 1.59 molecules nm^{-2} is calculated. The upper value is very probably higher than the actual iniferter density, because the specific surface area is rather underestimated due to the sample preparation of scratching off 600–800 nm thick films from a substrate. This is supported by nitrogen sorption of additionally prepared bulk mesoporous silica using the sol in a petri dish under otherwise identical evaporation and calcination conditions resulting in a
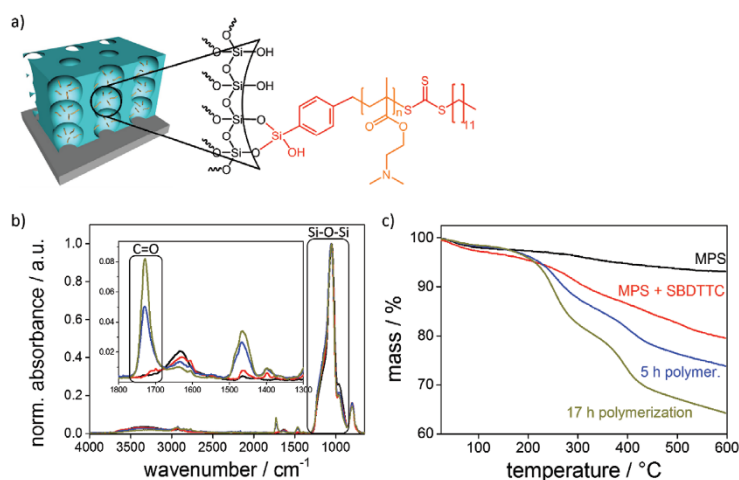
Figure 2. a) PDMAEMA functionalization of CO_2-plasma treated mesoporous silica films in a grafting from approach with surface bound SBDTTC. b) ATR-IR spectra of mesoporous silica (black), mesoporous silica functionalized with SBDTTC (red), after 5 h of polymerization (blue), and after 17 h of polymerization (dark yellow) of DMAEMA on CO_2-plasma treated mesoporous films. For measuring ATR-IR, the films were scratched off the substrate. c) TGA measurements of mesoporous silica (black), mesoporous silica functionalized with SBDTTC (red), and after 5 h (blue) as well as after 17 h (dark yellow) polymerization time of DMAEMA on CO_2-plasma treated mesoporous silica films. Spectra were recorded in air.

**ADVANCED
SCIENCE NEWS**
www.advancedsciencenews.com

**ADVANCED
FUNCTIONAL
MATERIALS**
www.afm-journal.de
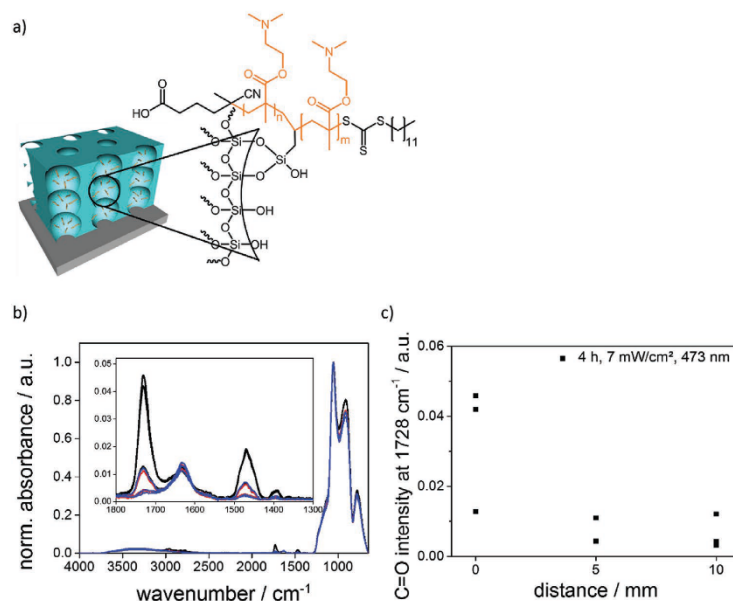
Figure 3. a) Schematic representation of PDMAEMA functionalization of allyltriethoxysilane functionalized mesoporous silica films using CDTPA in a grafting through approach. b) ATR-IR spectra recorded after CDTPA induced polymerization of DMAEMA in allyltriethoxysilane functionalized mesoporous silica films under irradiation with a blue laser (473 nm) for 4 h at the laser spot (black spectra), 5 mm distance (red spectra), and 10 mm distance to the laser spot (blue spectra). The ATR-IR spectra of the functionalized mesoporous silica film were recorded directly on the substrate. c) C=O vibrational stretching absorbance at 1728 cm^{-1} normalized to the Si-O-Si vibrational band at 1050 cm^{-1} versus the distance from the laser focused spot recorded at allyl functionalized mesoporous silica films. The polymerizations are carried out in ethanolic solution of DMAEMA (1.7 M) and CDTPA, induced by laser light (473 nm, 7 mW) for 4 h. The irradiation is conducted on 3 individual substrates and the substrates are characterized by ATR-IR spectroscopy at the laser spot, in 5 mm distance, and in 10 mm distance to the laser spot.

surface area of 610 $m^2\ g^{-1}$ (Figure S5, Supporting Information). In addition, the anchor group containing three methoxy groups is expected to form multilayers as well reducing the real grafting density as compared to the value of 1.59 molecules nm^{-2}. After an irradiation time of 5 h, a total mass loss of 26% (Figure 2c, blue) is observed, which is correlated to 1 to 2 repeating units of PDMAEMA assuming all iniferter molecules reacted and exhibit identical chain length. In accordance with attenuated total reflexion-infrared (ATR-IR) results, this total mass loss increases to 35% correlating to 4 to 5 repeating units after 17 h irradiation (Figure 2c, dark yellow). As discussed above, the real polymer chain length is expected to be higher as the density of reactive iniferters is expected to be overestimated. Nevertheless, this estimation gives a good idea on the minimum polymer chain length and the maximum chain density within the mesopores. Furthermore, polymer functionalized mesoporous silica films show a typical two step degradation in TGA measurements between 200 and 450 °C which is a clear indication for successful PDMAEMA functionalization of the mesoporous films.[42]

To achieve polymer functionalization in a grafting through approach applying CDTPA, the polymerizable group allyl triethoxysilane is covalently attached to the mesoporous silica surface. As CDTPA shows sufficient absorption at 473 nm (Figure S8,

Supporting Information), irradiation using a 473 nm laser (Figure S13, Supporting Information) results in PDMAEMA grafting as indicated by the C=O stretching vibrational band intensity at 1728 cm^{-1} within the normalized ATR-IR spectra (**Figure 3**).

In addition, the PDMAEMA functionalization can be limited to the laser spot region (Figure 3b black and Figure 3c at 0 mm). In that case, no significant PDMAEMA formation is observed in 5 or 10 mm distance from the laser irradiated spot (Figure 3c) indicating the potential of the applied functionalization concept for locally limited functionalization.

To demonstrate nanolocally limited functionalization of mesoporous silica films applying visible light induced iniferter initiated polymerizations, mesoporous silica films were equipped with Au/Ag-NPs as plasmonic near field source with a suitable wavelength for iniferter initiated polymerization. For this, mesoporous architectures, particularly mesoporous silica double layer and mesoporous allyl silica double layer films with precisely positioned Au/Ag-NPs (**Figure 4**) between the two layers are constructed. In the first step, mesostructured films, silica or allyl silica (co-condensed), were deposited on substrates via dip coating using the well-established EISA process.[43] By amine modification of the outer silica surface via 3-(ethoxydimethylsilyl)propylamine grafting, immobilization
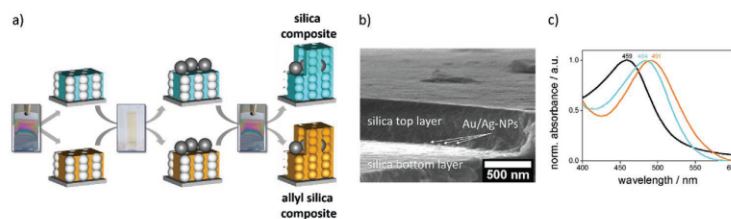
**ADVANCED
SCIENCE NEWS**

www.advancedsciencenews.com

**ADVANCED
FUNCTIONAL
MATERIALS**

www.afm-journal.de

Figure 4. a) Schematic representation of the mesoporous silica and allyl silica composite material fabrication procedure: After deposition of the first mesostructured silica thin film, Au/Ag NPs are immobilized on the outer film surface followed by deposition of the second layer and template removal to the final architectures. b) SEM micrograph of a mesoporous silica composite's cross section depicting mainly the top mesoporous layer located on top of the bottom layer and alloy Au/Ag-NPs. c) Absorption spectra of aqueous alloy Au/Ag NP's suspension (black), mesoporous silica composite (cyan), and mesoporous allyl silica composite (orange). Measurements of composite materials were performed in air.

of Au/Ag-NPs becomes accessible due to electrostatic interaction between the positively charged amine groups with the stabilizing citrate groups of the Au/Ag-NPs. Finally, the desired mesoporous architecture is completed, after deposition of the second silica layer followed by template extraction (Figure 4). Besides these architectures, a reference film comprised of a mesoporous silica double layer without Au/Ag-NPs is prepared and used to validate near field induced polymerization. Single mesoporous silica thin films have a thickness of 564 ± 34 nm and 60 vol% porosity, whereas mesoporous allyl silica thin films have a thickness of 585 ± 12 nm and 59 vol% porosity as obtained by ellipsometry measurements and the BEMT (Table S2, Supporting Information). The permselective filter function of the mesoporous double layered films, without and with the incorporation of Au/Ag-NPs, has been investigated via cyclic voltammetry and can be found in Figure S7, Supporting Information. Au/Ag-NPs show a particle size of 23 ± 2 nm as derived from TEM micrographs (Figure S6, Supporting Information) and an absorption maximum at 459 nm. Immobilization of the Au/Ag-NPs has been investigated by UV–vis spectroscopy. Due to the localized plasmons of the Au/Ag-NPs, the final materials show coloration visible by eye (yellow). By comparison of the UV–vis spectrum of the NPs suspension with the spectra observed from mesoporous composites (Figure 4), a controlled and homogeneous immobilization of the NPs can be stated, since no change in shape of the LSPR absorption is observed, thus aggregate formation is not very probable. However, a redshift of the LSPR absorption maximum is observed upon incorporation into mesoporous silica and even a higher shift is observed when incorporated in mesoporous allyl silica with its lower porosity and higher refractive index. This sensitivity of the plasmon resonance conditions on the refractive index of the nanoparticles vicinity makes them not only interesting for light induced reactions, but also attractive for sensing refractive index changes on the nanoscale, for example, induced by polymer functionalization.

Visible light induced iniferter initiated polymerization of DMAEMA in mesoporous composite materials was carried out by using CDTPA within the above described grafting through approach and by applying an energy dosage of 41.4 J cm^{-2}, which corresponds to an irradiation time of 1 h at a power density of 11.5 mW cm^{-2}. Successful polymer functionalization of the composite materials is again indicated by the C=O

vibrational band of DMAEMA at 1728 cm^{-1} in the ATR-IR spectra which appears for both composite materials as shown in **Figure 5**. As the C=O vibrational band can also be observed in the ATR-IR spectra of the reference material, a far field polymerization is assumed. Reducing the energy dose of the irradiation source to 6.9 J cm^{-2}, similar observations can be made for all three materials, whereas the intensity of the C=O band is reduced in all cases compared to the signal intensity after irradiating with 41.4 J cm^{-2}.

Since the energy of the electromagnetic field of surface plasmons is enhanced as compared to the irradiation beam, plasmon induced iniferter initiated polymerization is expected to be locally limited to the plasmon field when using even lower energy dosage below the threshold energy for polymerization. Therefore, polymerization of DMAEMA in mesoporous composites was performed by applying 0.6 J cm^{-2} which corresponds to an irradiation with 1 mW cm^{-2} for 10 min. Comparing the ATR-IR spectra after polymerization, signals at 1728 cm^{-1} corresponding to the C=O vibrational band can only be detected for composite materials bearing Au/Ag-NPs and do not appear in the spectrum of the reference material indicating a successful near field induced iniferter initiated polymerization of DMAEMA in mesoporous films.

As the plasmonic resonance of metal NPs is highly sensitive to the refractive index of their vicinity, as mentioned above, and can be monitored by investigation of the absorption properties of the composite materials before and after polymerization, polymerization can be directly monitored. In **Figure 6**, absorption spectra of the silica composite and the allyl silica composite before and after polymerization with 41.4 J cm^{-2} (far field) as well as the spectra of the allyl silica composite before and after polymerization with 0.6 J cm^{-2} are shown. After polymer functionalization, a redshift of the LSPR band due to an increase of the refractive index of the nanoparticles vicinity are observed additionally supporting the assumption of local near field induced functionalization with respect to the absorption spectra of the allyl silica composite that has been irradiated with the lowest energy dose of 0.6 J cm^{-2}.

Furthermore, TEM micrographs of the composites that have been irradiated with 41.4 J cm^{-2} depicted in Figure 6 do not indicate nanolocal placement of polymer, whereas the micrograph of the allyl silica composite that has been irradiated with 0.6 J cm^{-2} clearly shows the formation of polymer halos with

**ADVANCED
SCIENCE NEWS**
www.advancedsciencenews.com

**ADVANCED
FUNCTIONAL
MATERIALS**
www.afm-journal.de
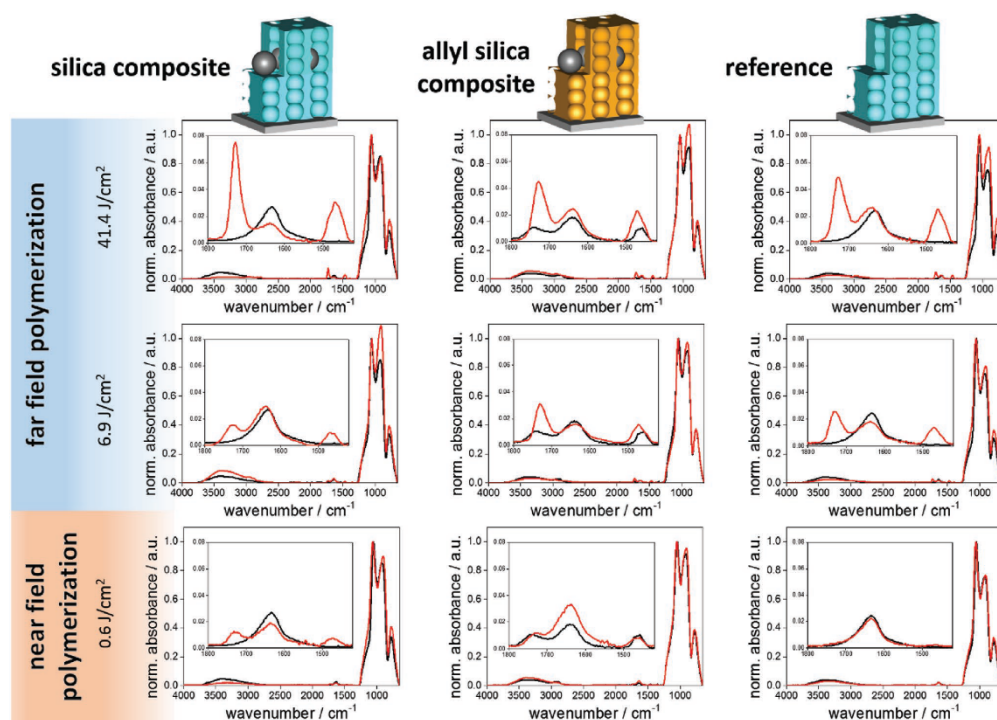
Figure 5. ATR-IR spectra of mesoporous silica and allyl silica composites as well as of the reference mesoporous silica double layer (from left to right) before (black curves) and after light induced polymerization of DMAEMA (red curves) by applying an energy dosage of 41.4 J cm^{-2} (top row), 6.9 J cm^{-2} (mid row) and 0.6 J cm^{-2} (bottom row) respectively. For comparison, all spectra are normalized to the Si-O-Si vibrational band at 1050 cm^{-1}.

a thickness of ≈10 nm around the Au/Ag-NPs demonstrating the successful near field induced iniferter initiated polymer functionalization in complex mesoporous architectures on the nanoscale. Further data on near field induced polymerization can be found in Figures S16 and S17, Supporting Information.

3. Conclusion

In summary, two approaches using visible light sensitive iniferter molecules are presented for visible light and surface plasmon induced polymer functionalization of mesoporous silica films in absence of external radical sources or catalysts. Applying SBDTTC, mesoporous silica films were successfully functionalized with PDMAEMA at 430–500 nm in a grafting from approach. Applying CDTPA, mesoporous films were successfully functionalized with PDMAEMA at 473 nm in a grafting through approach. Thereby, PDMAEMA functionalization could be locally limited to the laser spot region. Based on these promising results, PDMAEMA functionalization using iniferter initiated polymerization in a grafting through approach was achieved by surface plasmon irradiation after integrating

plasmonic alloy Ag/Au nanoparticles into mesoporous silica films. We expect this combination of potentially controlled polymerization and nanolocal polymer deposition by using surface plasmons as nanoscale light source for mesoporous film functionalization to open up new pathways for porous hybrid materials and device design.

4. Experimental Section

Materials: Tetraethylorthosilicate (98%, reagent grade) (TEOS), sodium hydride (dry, 95%), carbondisulfide (99.9%),CDTPA (97%), allyltriethoxysilane (AITES) (96%) and Pluronic F127 were purchased from Sigma Aldrich. (p-Chloromethylphenyl)trimethoxysilane (95%) was received by abcr, Karlsruhe, Germany. Dodecanethiol (98%) was purchased by Alfa Aesar. DMAEMA was purchased from Sigma Aldrich and destabilized over a γ-alumina column prior to use. Anhydrous toluene (0.5 ppm residual water content) and anhydrous tetrahydrofurane (max 0.0075% residual water) were received from AppliChem. All chemicals were used as received unless noted otherwise.

Preparation of Dip Coating Solution for Mesoporous Silica Films: According to reported protocols,[11,44] Pluronic F127 (5.2 g; 0.38 mmol, BioReagent, Sigma Aldrich, 13 800 g mol^{-1}) was suspended in ethanol (48 mL; 820 mmol) under stirring. An aqueous hydrochloric acid solution
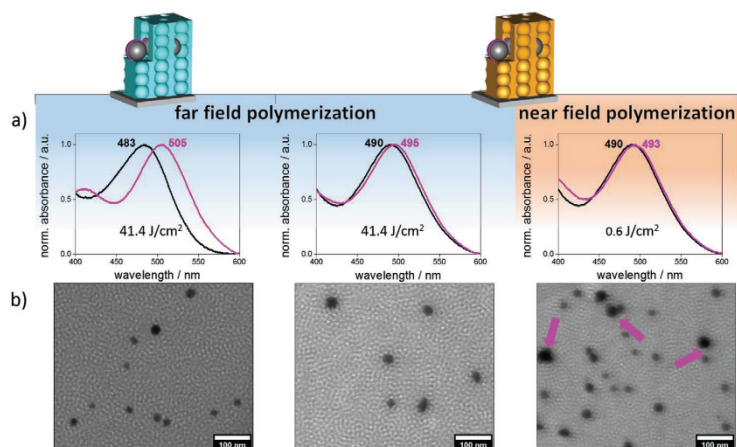
Figure 6. a) Normalized absorption spectra of mesoporous silica composite (left) and mesoporous allyl silica composite (mid) before (black curves) and after far field polymerization of DMAEMA (magenta curves) and of mesoporous allyl silica composite after near field polymerization (right) showing redshifts due to an increase of the refractive index in the vicinity of the NPs. b) TEM micrographs of mesoporous silica composite (left) and mesoporous allyl silica composite (mid) after far field polymerization of DMAEMA and of mesoporous allyl silica composite after near field polymerization (right).

(0.05 mol L^{-1}; 11 mL) was freshly prepared from water (10.44 mL) and hydrochloric acid (37 wt%; 0.66 mL). The acidic solution was added and the template dissolved immediately. TEOS (9.76 mL; 44 mmol) was added and the solution was stirred overnight at room temperature. The molar ratios of the solution were 1 TEOS: 0.009 F127: 19 EtOH: 14 H$_2$O: 0.015 HCl. The solution was stored at −18 °C until being used for mesoporous silica film preparation.

Silica Film Deposition: Glass slides and silicon wafers were cleaned with ethanol and used as substrates for dip coating with a withdrawal speed of 2 mm s^{-1} under controlled environmental conditions (50% rel. humidity, 22–25 °C). Subsequently, the films were stored under these conditions for 60 min followed by a temperature treatment at 60 °C for 60 min, which was followed by a temperature increase to 130 °C within 10 min keeping 130 °C for 60 min. A final heating to 350 °C for 2 h using a heating rate of 1 °C min^{-1} resulted in template calcination.

Synthesis of Alloy Au/Ag-1:1-NPs: Au/Ag-NPs were synthesized based on a reported procedure.[45] A solution of 7.1 mg of HAuCl$_4$·3 H$_2$O (0.018 mmol, 1 eq) in 150 mL of Milli-Q water was refluxed for 10 min. Under vigorous stirring, a solution of 3.1 mg AgNO$_3$ (0.018 mmol, 1 eq) in 170 μL water and a solution of 78.15 mg sodium citrate (0.219 mmol, 24 eq) in 742 μL water were added quickly and the solution was stirred for another 3 h while reducing the temperature to 80 °C. Then, the mixture was cooled to 0 °C and filtered (0.4 μm). The mixture was stored at 4 °C protected from light.

Synthesis of Mesoporous Silica Alloy NP Composite Films: Mesoporous silica thin films were prepared as previously described[46] in accordance via sol-gel chemistry using TEOS and AITES as inorganic precursors and an amphiphilic triblock copolymer, Pluronic F127, as structure directing template that undergoes micellization upon solvent evaporation resulting in formation of a porous inorganic network. The molar ratios of these compounds in the precursor solution used for dip coating of mesoporous silica thin films were 1 TEOS: 0.009 F127: 19 EtOH: 14 H$_2$O: 0.015 HCl and for dip coating of allyl silica thin films 0.9 TEOS: 0.1 AITES: 0.01 F127: 19 EtOH: 16.4 H$_2$O: 0.015 HCl resulting in 16 nm mesopores (12 nm pore neck). The precursor solutions were prepared at room temperature and stirred for 20 min before deposition on glass and silicon wafer. The films were dip coated at a withdrawal speed of 2 mm s^{-1} at 23 °C and 50% relative humidity. After deposition, the films were kept at 23 °C and 50% relative humidity for 1 h. The first

film was stabilized by a temperature treatment at 60 and 130 °C for 1 h respectively. For immobilization of Au/Ag-NPs, the mesostructured silica film was functionalized with 3-aminopropyldimethylmethoxysilane using a 0.01 wt% solution in toluene. The reaction mixture as well as the functionalization itself had to be prepared under inert conditions. The reaction mixture was added to the mesostructured film and heated at 80 °C for 1 h. Then, the film was rinsed with toluene and ethanol to remove unbound silane. After drying, the amine functionalized mesostructured film was incubated in the Au/Ag-NP dispersion overnight. The Au/Ag-NP functionalized mesostructured films were then covered with a second silica film via dip coating using the above mentioned conditions and stored at 23 °C and 50% relative humidity for 1 h. Finally, the mesoporous composite material was obtained, after template removal. For silica composites, a consecutive temperature treatment at 60 and 130 °C for 1 h, followed by calcination step up to 350 °C with a heating rate of 1 °C min^{-1} and holding the temperature for 2 h was conducted. In case of co-condensed allyl silica composites, template removal was performed by extracting the mesoporous composite in acidic ethanol (0.01 M HCl) for 3 days after consecutive temperature treatments at 60, 130 °C for 1 h respectively and at 200 °C for 2 h.

Surface Grafting of SBDTTC: Mesoporous silica films deposited on glass substrates or silicon wafers were immersed into a solution of SBDTTC (0.1 M) in toluene. The functionalization was conducted at 70 °C for 4 h. Hereafter, the films were extensively extracted in ethanol for 1 h to remove unbound silane. Prepared films were kept under protection from light until further use.

Surface Initiated Polymerizations with SBDTTC: SBDTTC functionalized mesoporous silica films were placed into a solution of DMAEMA (1.3 mol L^{-1}) in DMSO. The solution was degassed by purging with nitrogen and the sample was irradiated with a lamp (LUMATEC, Superlite S400, Deisenhofen, Germany, Filter 6, 430–500 nm, 12 mW cm^{-2}) for indicated reaction times. Afterward, the substrates were extracted in water for 1 h.

Surface Grafting of Allyl Silane: AITES (45 μL; 41 mg; 0.2 mmol) was dissolved in toluene (200 mL). Silica films were placed into the silane solution in flame dried flattened schlenk flasks. The samples were heated up to 80 °C for 1 h. The silica films were extensively extracted in ethanol for 1 h to remove unbound silane.

473 nm Laser Induced Polymerizations: Monochromatic and linear, transverse-magnetic polarized (Glan–Thompson polarizer, B. Halle) laser light (Diode pumped solid state laser, Laser 2000, λ = 473 nm, 50 mW) was directed onto the sample placed in the polymerization solution after degassing the solution by purging with nitrogen for 1 min. The polymerization solution was prepared by dissolving CDTPA (46 mg; 0.11 mmol) and DMAEMA (4 mL; 3.7 g; 24 mmol; 1.7 mol L^{-1}) in ethanol (14 mL) with a molar CDTPA to DMAEMA ratio of 1:200. Polymerization was performed at the indicated time and laser beam power. The laser power of the polymerization was controlled by adjusting the angle of the first passed polarizer, according to a two polarizer system described by Malus' law. The laser power versus polarizer angle dependence was determined with a THORLABS PM100A Optical Power Meter after passing two polarizers.

LSPR Induced Polymerization: Polymer functionalization of mesoporous composite materials was performed by mixing 2.9 g (18 mmol) destabilized DMAEMA and 40 mg CDTPA (99 µmol) in 10 mL absolute ethanol. The solution was purged with nitrogen for 10 min and then transferred to cuvettes in which the mesoporous composite material was placed. The cuvettes were irradiated with a lamp (LUMATEC, Superlite S400, Deisenhofen, Germany, Filter 6, 430–500 nm) using a power density of 1 mW cm^{-2} for 10 min and 11.5 mW cm^{-2} for 1 h at a distance of 10 cm to the irradiation source. Subsequently, the substrates were extracted with ethanol for 30 min before drying and storing under ambient conditions.

Infrared Spectroscopy: IR spectra were recorded in ATR mode using a Spectrum One FT-IR spectrometer from Perkin–Elmer. Corresponding spectra were recorded directly from the substrate or from films, which were scratched off the substrate. Each spectrum was recorded from 4000 to 650 cm^{-1}. The spectra were background corrected and normalized to the Si-O-Si asymmetric stretching vibrational band at 1050 cm^{-1}.

CO_2-Plasma Treatment: CO_2-plasma treatment was performed according to a literature protocol[7b,40] using a Femto SRS plasma generator (Diener electronics, model Femto, 13.56 MHz, maximum RF power: 200 W). The samples were degassed and CO_2 gas was introduced. The RF generator was switched on for 12 s after a stable pressure of 0.3 mbar was achieved.

Thermogravimetric Analysis: TGA was recorded in a Mettler–Toledo instrument (TGA 1) recorded in air atmosphere. The samples obtained by scratching off the mesoporous silica films from its glass supports were heated from room temperature to a final temperature of 600 °C with a heating rate of 10 K min^{-1}.

UV–Vis Spectroscopy: UV–vis spectra were recorded with an Agilent Cary 60 UV–vis spectrometer. All spectra were background corrected to the respective solvent.

Supporting Information

Supporting Information is available from the Wiley Online Library or from the author.

Acknowledgements

Conflict of Interest

The authors declare no conflict of interest.

Data Availability Statement

Research data are not shared.

Keywords

[1] a) C. Ghazaly, M. Hébrant, E. Langlois, B. Castel, M. Guillemot, M. Etienne, *Sensors* **2019**, *19*, 3508; b) A. Mutschler, V. Stock, L. Ebert, E. M. Björk, K. Leopold, M. Lindén, *Nanomaterials* **2019**, *9*, 35; c) M. Saadaoui, I. Fernández, G. Luna, P. Diez, S. Campuzano, N. Raouafi, A. Sánchez, J. M. Pingarrón, R. Villalonga, *Anal. Bioanal. Chem.* **2016**, *408*, 7321.

[2] N. Vilà, E. André, R. Ciganda, J. Ruiz, D. Astruc, A. Walcarius, *Chem. Mater.* **2016**, *28*, 2511.

[3] a) M. Rafti, A. Brunsen, M. C. Fuertes, O. Azzaroni, G. J. Soler-Illia, *ACS Appl. Mater. Interfaces* **2013**, *5*, 8833; b) P.-H. Wu, P. Mäkie, M. Odén, E. M. Björk, *Nanomaterials* **2019**, *9*, 562.

[4] A. Calvo, B. Yameen, F. J. Williams, G. J. A. A. Soler-Illia, O. Azzaroni, *J. Am. Chem. Soc.* **2009**, *131*, 10866.

[5] S. Schmidt, S. Alberti, P. Vana, G. J. A. A. Soler-Illia, O. Azzaroni, *Chem. - Eur. J.* **2017**, *23*, 14500.

[6] L. Silies, A. Andrieu-Brunsen, *Langmuir* **2017**, *34*, 807.

[7] a) A. K. Bohaty, M. R. Newton, I. Zharov, *J. Porous Mater.* **2010**, *17*, 465; b) F. Krohm, J. Kind, R. Savka, M. A. Janßen, D. Herold, H. Plenio, C. M. Thiele, A. Andrieu-Brunsen, *J. Mater. Chem. C* **2016**, *4*, 4067.

[8] a) Z. S. Siwy, S. Howorka, *Chem. Soc. Rev.* **2010**, *39*, 1115; b) S. F. Buchsbaum, G. Nguyen, S. Howorka, Z. S. Siwy, *J. Am. Chem. Soc.* **2014**, *136*, 9902; c) J. Elbert, F. Krohm, C. Rüttiger, S. Kienle, H. Didzoleit, B. N. Balzer, T. Hugel, B. Stühn, M. Gallei, A. Brunsen, *Adv. Funct. Mater.* **2014**, *24*, 1591.

[9] a) M. Kruk, *Isr. J. Chem.* **2012**, *52*, 246; b) A. Gamero-Quijano, C. Karman, N. Vilà, G. g. Herzog, A. Walcarius, *Langmuir* **2017**, *33*, 4224; c) A. Andrieu-Brunsen, S. Micoureau, M. Tagliazucchi, I. Szleifer, O. Azzaroni, G. J. A. A. Soler-Illia, *Chem. Mater.* **2015**, *27*, 808; d) L. Silies, H. Didzoleit, C. Hess, B. Stühn, A. Andrieu-Brunsen, *Chem. Mater.* **2015**, *27*, 1971.

[10] a) J. C. Tom, R. Brilmayer, J. Schmidt, A. Andrieu-Brunsen, *Polymers* **2017**, *9*, 539; b) R. Brilmayer, C. Hess, A. Andrieu-Brunsen, *Small* **2019**, *15*, 1902710.

[11] R. Brilmayer, S. Kübelbeck, A. Khalil, M. Brodrecht, U. Kunz, H. J. Kleebe, G. Buntkowsky, G. Baier, A. Andrieu-Brunsen, *Adv. Mater. Interfaces* **2020**, *7*, 1901914.

[12] A. M. M. Jani, I. M. Kempson, D. Losic, N. H. Voelcker, *Angew. Chem., Int. Ed.* **2010**, *49*, 7933.

[13] M. Ochs, R. Mohammadi, N. Vogel, A. Andrieu-Brunsen, *Small* **2020**, *16*, 1906463.

[14] a) C. Deeb, C. Ecoffet, R. Bachelot, J. Plain, A. Bouhelier, O. Soppera, *J. Am. Chem. Soc.* **2011**, *133*, 10535; b) T. Ding, J. Mertens, A. Lombardi, O. A. Scherman, J. J. Baumberg, *ACS Photonics* **2017**, *4*, 1453; c) H. Minamimoto, T. Toda, R. Futashima, X. Li, K. Suzuki, S. Yasuda, K. Murakoshi, *J. Phys. Chem. C* **2016**, *120*, 16051; d) Y. Takahashi, Y. Furukawa, T. Ishida, S. Yamada, *Nanoscale* **2016**, *8*, 8520; e) Y. Wang, S. Wang, S. Zhang, O. A. Scherman, J. J. Baumberg, T. Ding, H. Xu, *Nano Res.* **2018**, *11*, 6384; f) K.-H. Dostert, M. Álvarez, K. Koynov, A. n. del Campo, H.-J. r. Butt, M. Kreiter, *Langmuir* **2012**, *28*, 3699.

[15] G. Cortial, M. Siutkowski, F. Goettmann, A. Moores, C. Boissière, D. Grosso, P. Le Floch, C. Sanchez, *Small* **2006**, *2*, 1042.

[16] a) L. Bois, F. Chassagneux, Y. Battie, F. Bessueille, L. Mollet, S. Parola, N. Destouches, N. Toulhoat, N. Moncoffre, *Langmuir* **2010**, *26*, 1199; b) C. M. Leroy, T. Cardinal, V. Jubera, C. Aymonier, M. Treguer-Delapierre, C. Boissière, D. Grosso, C. Sanchez, B. Viana, F. Pellé, *Microporous Mesoporous Mater.* **2013**, *170*, 123.

[17] a) P. C. Angelomé, L. M. Liz-Marzán, *J. Phys. Chem. C* **2010**, *114*, 18379; b) M. M. Zalduendo, V. Oestreicher, J. Langer, L. M. Liz-Marzán, P. C. Angelomé, *Anal. Chem.* **2020**, *92*, 13656.

[18] P. C. Angelomé, L. M. Liz-Marzán, *J. Sol-Gel Sci. Technol.* **2014**, *70*, 180.

[19] P. C. Angelomé, I. Pastoriza-Santos, J. Pérez-Juste, B. Rodríguez-González, A. Zelcer, G. J. A. A. Soler-Illia, L. M. Liz-Marzán, *Nanoscale* **2012**, *4*, 931.

[20] a) K. L. Kelly, E. Coronado, L. L. Zhao, G. C. Schatz, *J. Phys. Chem. B* **2003**, *107*, 668; b) K.-S. Lee, M. A. El-Sayed, *J. Phys. Chem. B* **2006**, *110*, 19220; c) M. A. Garcia, *J. Phys. D: Appl. Phys.* **2012**, *45*, 389501.

[21] a) G. J. A. A. Soler-Illia, O. Azzaroni, *Chem. Soc. Rev.* **2011**, *40*, 1107; b) P. Innocenzi, L. Malfatti, *Chem. Soc. Rev.* **2013**, *42*, 4198; c) S. Alberti, G. J. A. A. Soler-Illia, O. Azzaroni, *Chem. Commun.* **2015**, *51*, 6050; d) Z. Zhang, L. Wen, L. Jiang, *Chem. Soc. Rev.* **2018**, *47*, 322; e) M. Tiemann, C. Weinberger, *Adv. Mater. Interfaces* **2020**, *8*, 2001153.

[22] a) B. P. Fors, C. J. Hawker, *Angew. Chem., Int. Ed.* **2012**, *51*, 8850; b) N. J. Treat, B. P. Fors, J. W. Kramer, M. Christianson, C.-Y. Chiu, J. Read de Alaniz, C. J. Hawker, *ACS Macro Lett.* **2014**, *3*, 580.

[23] a) A. J. Boydston, K. A. Ogawa, A. E. Goetz, *Synlett* **2015**, *27*, 203; b) P. Lu, N. M. Alrashdi, A. J. Boydston, *J. Polym. Sci., Part A: Polym. Chem.* **2017**, *55*, 2977.

[24] N. Herzog, J. Kind, C. Hess, A. Andrieu-Brunsen, *Chem. Commun.* **2015**, *51*, 11697.

[25] a) T. G. McKenzie, Q. Fu, E. H. H. Wong, D. E. Dunstan, G. G. Qiao, *Macromolecules* **2015**, *48*, 3864; b) J. Yeow, O. R. Sugita, C. Boyer, *ACS Macro Lett.* **2016**, *5*, 558.

[26] X. Liu, Y. Ni, J. Wu, H. Jiang, Z. Zhang, L. Zhang, Z. Cheng, X. Zhu, *Polym. Chem.* **2018**, *9*, 584.

[27] C. Aydogan, G. Yilmaz, Y. Yagci, *Macromolecules* **2017**, *50*, 9115.

[28] A. Bagheri, J. Yeow, H. Arandiyan, J. Xu, C. Boyer, M. Lim, *Macromol. Rapid Commun.* **2016**, *37*, 905.

[29] J.-P. Fouassier, F. Morlet-Savary, J. Lalevée, X. Allonas, C. Ley, *Materials* **2010**, *3*, 5130.

[30] M. Erzina, O. Guselnikova, P. Postnikov, R. Elashnikov, Z. Kolska, E. Miliutina, V. Švorčík, O. Lyutakov, *Adv. Mater. Interfaces* **2018**, *5*, 1801042.

[31] J. Jiang, G. Ye, F. Lorandi, Z. Liu, Y. Liu, T. Hu, J. Chen, Y. Lu, K. Matyjaszewski, *Angew. Chem.* **2019**, *131*, 12224.

[32] N. Corrigan, D. Rosli, J. W. J. Jones, J. Xu, C. Boyer, *Macromolecules* **2016**, *49*, 6779.

[33] J. Yeow, R. Chapman, J. Xu, C. Boyer, *Polym. Chem.* **2017**, *8*, 5012.

[34] C. A. Figg, J. D. Hickman, G. M. Scheutz, S. Shanmugam, R. N. Carmean, B. S. Tucker, C. Boyer, B. S. Sumerlin, *Macromolecules* **2018**, *51*, 1370.

[35] M. Li, M. Fromel, D. Ranaweera, S. Rocha, C. Boyer, C. W. Pester, *ACS Macro Lett.* **2019**, *8*, 374.

[36] F. Kameche, W. Heni, S. Telitel, D. Ge, L. Vidal, F. Dumur, D. Gigmes, J. Lalevée, S. Marguet, L. Douillard, C. Fiorini-Debuisschert, R. Bachelot, O. Soppera, *Mater. Today* **2020**, *40*, 38.

[37] T. Otsu, M. Yoshida, T. Tazaki, *Makromol. Chem., Rapid Commun.* **1982**, *3*, 133.

[38] a) M. J. Garcia-Soto, K. Haupt, C. Gonzato, *Polym. Chem.* **2017**, *8*, 4830; b) Z. Huang, T. Qiu, H. Xu, H. Shi, J. Rui, X. Li, L. Guo, *Macromolecules* **2018**, *51*, 7329; c) M. Rubens, P. Latsrisaeng, T. Junkers, *Polym. Chem.* **2017**, *8*, 6496; d) S. Shanmugam, J. Cuthbert, J. Flum, M. Fantin, C. Boyer, T. Kowalewski, K. Matyjaszewski, *Polym. Chem.* **2019**, *10*, 2477.

[39] a) C. Boissiere, D. Grosso, S. Lepoutre, L. Nicole, A. B. Bruneau, C. Sanchez, *Langmuir* **2005**, *21*, 12362; b) J. E. Spanier, I. P. Herman, *Phys. Rev. B: Condens. Matter Mater. Phys.* **2000**, *61*, 10437.

[40] D. J. Babu, S. Yadav, T. Heinlein, G. Cherkashinin, J. J. Schneider, *J. Phys. Chem. C* **2014**, *118*, 12028.

[41] a) M. Save, G. Granvorka, J. Bernard, B. Charleux, C. Boissière, D. Grosso, C. Sanchez, *Macromol. Rapid Commun.* **2006**, *27*, 393; b) H. Naono, R. Fujiwara, M. Yagi, *J. Colloid Interface Sci.* **1980**, *76*, 74.

[42] a) H. Hemmatpour, V. Haddadi-Asl, H. Roghani-Mamaqani, *Polymer* **2015**, *65*, 143; b) J. M. Cervantes-Uc, J. V. Cauich-Rodríguez, W. A. Herrera-Kao, H. Vázquez-Torres, A. Marcos-Fernández, *Polym. Degrad. Stab.* **2008**, *93*, 1891.

[43] C. J. Brinker, Y. Lu, A. Sellinger, H. Fan, *Adv. Mater.* **1999**, *11*, 579.

[44] D. R. Dunphy, P. H. Sheth, F. L. Garcia, C. J. Brinker, *Chem. Mater.* **2015**, *27*, 75.

[45] M. Roskamp, *Oberflächenfunktionalisierung von Nanopartikeln zur gezielten Wechselwirkung mit Biomolekülen*, Freie Universität Berlin **2010**.

[46] N. Herzog, R. Brilmayer, M. Stanzel, A. Kalyta, D. Spiehl, E. Dörsam, C. Hess, A. Andrieu-Brunsen, *RSC Adv.* **2019**, *9*, 23570.

6. Conclusion

The aim of this work was to investigate the possibility of creating mesoporous step gradient architectures with respect to pore size, surface wettability, and surface charge, by combining different MSTFs. Furthermore, new strategies for the precise function placement, e.g. by polymer placement, in such mesoporous film architectures with nanoscale precision should be developed in order to increase the complexity analogue to biological paragons. Such step gradient architectures are especially interesting in the context of separation and energy harvesting, for instance, as concluded in **Chapter 2: State of research**.

In order to address the formation of mesoporous film step gradients as well as new strategies of function placement, this work was divided into three main sections: material library, mesoporous architectures, and (nano-)local polymer placement, as depicted in **Figure 28**.
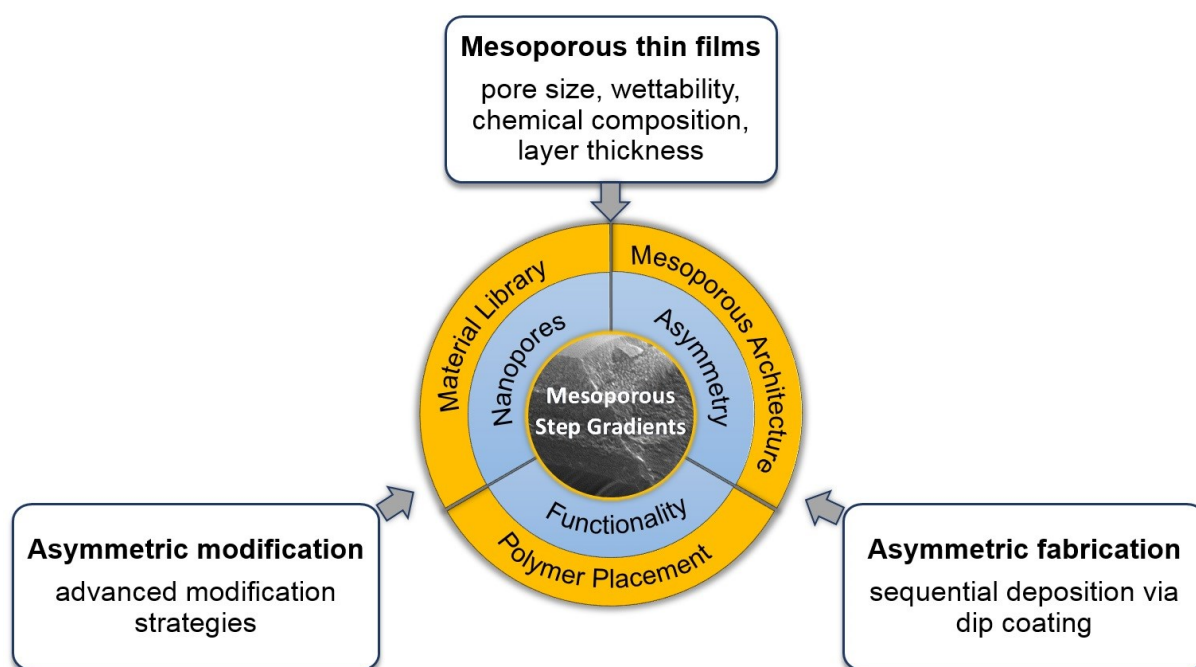
Figure 28: Representation of the strategic outline of this work.

A fundamental understanding of physical and chemical properties of MSTFs are required with respect to the preparation of hierarchical mesoporous architectures. Therefore, hydrophilic MSTFs templated with Pluronic® F127 were systematically investigated regarding their ionic pore accessibility in dependence of preparation parameters, i.e. the template removal performed either by calcination up to 350 °C or extraction in acidic ethanol (stabilizing heat treatment up to 200 °C). A much more pronounced permselective behavior in case of template removal via extraction was observed via CV measurements due to the higher amount of surface silanol groups in consequence of lower stabilization treatment up to 200 °C. This observation is

consistent with a higher silanol vibration in the ATR-IR spectrum further indicating a lower degree of silica condensation at lower temperatures.

For the preparation of mesoporous surface wettability step gradients, hydrophobic MSTFs were developed applying the methylated precursors MTMS and DMDMS together with TEOS in a co-condensation approach. By variation of the mole fractions of MTMS and DMDMS with respect to TEOS, MSTFs with gradual tunable surface wettability with apparent water contact angles from 10° up to 113° were successfully prepared. Investigating the structural properties of these MSTFs, revealed thinner film thicknesses as well as lower porosities with increasing amount of MTMS and DMDMS in consequence of an increased amount of organic groups in the resulting MSTFs.

MSTFs prepared by using the precursors MTMS, DMDMS together with TEOS not only showed the opportunity to prepare MSTFs with tunable surface wettability, but also showed higher chemical stability in harsh basic environment. There, higher chemical stability at pH 10 was observed with higher amount of MTMS and DMDMS. MSTFS with low molar ratios of TEOS, i.e. 0.5 and lower, resulted in chemically stable MSTFs with respect to a total investigation time of 240 minutes. Similarly, MOSTFs that were developed using the bridged precursor BTESE also showed a chemical stability at pH 10 for the time of investigation of 240 minutes. Comparable film thickness and a lower porosity were determined for the MOSTFs prepared using BTESE templated with Pluronic® F127 as compared to MSTFs prepared by using TEOS as silica source. The lower porosity can be explained due to the incorporation of organic bridging groups applying BTESE.

As a bio-based alternative to petro-based structure directing templates, HPC was successfully applied for the preparation of hydrophilic MSTFs with a possible chiral pore structure. Thereby, MSTFs with a mean pore size of 2.9 nm and a relatively high porosity of 61% were prepared, which showed typical ionic pore accessibility of MSTFs in dependence of environmental pH.

In order to prepare MSTF architectures, double layer thin films represent the simplest construction for the preparation of multilayer step gradients. MSTFs with pore size step gradients were successfully prepared by asymmetric fabrication, i.e. sequential deposition of Pluronic® F127 templated MSTFs resulting in films with 6-8 nm pore size and CTAB templated MSTFs resulting in films with 1-3 nm pore size via dip coating. Investigation of the ionic pore accessibility indicated a successful pore connection between the two different MSTFs double layer arrangements of both possible sequences guaranteeing transport of charge through MSTFs with pore size step gradients. Interestingly, structural investigation through ellipsometry revealed thinner MSTFs, if deposited on a mesostructured silica bottom layer, most likely due to different adhesive forces compared to single MSTFs deposited on glass, silicon, or ITO covered glass substrates.

Successful preparation of MSTFs with surface wettability step gradients was performed applying asymmetric fabrication of hydrophilic and hydrophobic MSTFs templated with Pluronic® F127. Therefore, hydrophilic MSTFs and hydrophobic MSTFs prepared by co-condensation of MTMS, DMDMS together with TEOS (x_{TEOS}=0.2) were sequentially deposited via dip coating. Different film thicknesses of the hydrophobic top layer were achieved by variation of the withdrawal speed in the dip coating process. Investigation of the ionic pore accessibility of the positively charged probe molecule $[Ru(NH_3)_6]^{2+/3+}$ at acidic and basic environmental pH resulted in peak current densities at basic conditions for the double layer MSTF with surface wettability step gradient and the thinnest hydrophobic top layer of 60 nm. No peak current densities were obtained with thicker layers of the hydrophobic top layer. There, no quantitative statement on a limiting film thickness of the hydrophobic top layer with respect to the observed effect was made due to the necessity of further investigations, which are part of ongoing research in the group of *Annette Andrieu-Brunsen*. However, the observed effect can be explained by an overcoming of the hydrophobic barrier of the top layer through electrostatic attraction of the negatively charged hydrophilic bottom layer and the positively charged probe molecule, which has an impact on data interpretation as well as on the design of complex nanoporous architectures.

In order to prepare MSTFs with charge step gradients and by that to increase the function density in a single layer of a double layer MSTF, a concept for the layer-selective polymer placement in double layer arrangements was developed. Therefore, hydrophilic double layer MSTFs were prepared via dip coating. Amine predisposition of one layer using APTES as co-condensate allowed further selective modification of one layer with an iniferter. Due to a low unspecific adsorption, the carboxylic acid bearing iniferter was successfully bound selectively on the amine predisposed mesoporous layer by utilizing the amide forming coupling agent HATU. After careful extraction of unbound iniferter, a photopolymerization of METAC was successfully performed in only one mesoporous layer of the double layer thin film by applying UV light at a wavelength of 365 nm. The layer-selective polymer functionalization was concluded by the collective results obtained from IR spectroscopy, ellipsometry, charged dye immobilization experiments, and EDX spectroscopy. Investigation of the ionic pore accessibility of mesoporous double layer thin films before and after polymer functionalization revealed a dominant role of the bottom layer on the pore accessibility overcoming local electrostatic repulsion of the top layer.

Although this concept allows to generate charge step gradients at the nanoscale, since the film thickness of the individual layers can be adjusted by variation of the deposition technique's process parameters, a new strategy to further investigate the limits of polymer placement in

mesoporous architectures was pursued. Therefore, plasmonic metal NPs were incorporated in hydrophilic MSTFs with high spatial control and used as nanoscopic light source in combination with photopolymerizations. To construct the mesoporous composite materials, a mesostructured silica thin film as bottom layer was deposited initially via dip coating. Selective functionalization of the outer silica surface with amine groups allowed the immobilization of citrate stabilized plasmonic metal NPs, which were then covered by another MSTF as top layer. Investigation of the composite material via UV/Vis spectroscopy demonstrated a tunable NP density by varying the immobilization time of the NPs. As the thickness of each individual silica layer can be regulated by variation of process parameters of dip coating, the position of the plasmonic metal NPs can be precisely adjusted on the nanoscale. The optical properties of a composite material bearing Au-NPs were systematically investigated in dependence of the surrounding medium refractive index by applying UV/Vis spectroscopy. Thereby, a sensing sensitivity of 51 nm/RIU was determined, which is in very good agreement to FEM simulations as well as with reported sensing sensitivity for spherical Au-NPs in dispersion solutions. In addition, local sensing inside the mesoporous material was proven by covering the composite material with a hydrophobic polysiloxane layer and observing no change of the absorption maximum (LSPR) in the UV/Vis upon variation of the surrounding refractive index, as no liquid was able to enter the mesoporous thin film.

For the application of the Au-NPs as nanoscopic light source to induce a photopolymerization at the nanoscale, a dye-sensitized polymerization formulation was developed and optimized in solution to determine the threshold energy considering the detection limit of the applied characterization methods (ATR-IR). A covalent grafting of polymer in the nanoscopic surrounding of the Au-NPs was then achieved by applying the dye-sensitized photopolymerization below the threshold energy, hence inducing the polymerization via LSPR. In consequence, a red-shift of the LSPR of the Au-NPs was observed due to an increase of the refractive index of the NP's surrounding, indicating successful nanolocal polymer placement around the NPs. Investigating of the optical properties in dependence of the composite material's surrounding media revealed a reduced sensing sensitivity of 44 nm/RIU, which can be explained due to the polymer shell of the Au-NPs. As a consequence, plasmonic metal NPs in MSTFs do not only allow nanolocal near-field induced polymer placement, but as well allow to monitor refractive index changes of the NP's surrounding in situ.

The concept of applying plasmonic metal NPs as nanoscopic light source for the precise positioning of polymers into mesoporous thin films with nanolocal control was then transferred to an iniferter-based controlled-radical polymerization approach. Therefore, a suitable polymerization formulation was developed and optimized by *Daniel John*, which was then

applied to composite materials bearing plasmonic alloy Ag/Au-NPs. By systematically reducing the irradiation energy dosage, a near-field induced iniferter initiated polymerization was successfully carried out applying the composite material bearing the plasmonic alloy Ag/Au-NPs. The combination of plasmonic metal NPs as nanoscale light source to initiate potentially controlled photopolymerizations for the accurate and spatially resolved polymer placement in MSTFs is envisioned to open new pathways for the generation of hybrid porous materials and device design. Furthermore, the incorporated sensing ability of the plasmonic NPs is expected to generate nanoscopic local information in the confinement of mesoporous materials along with insights into the functionalization and transport properties of such materials.

Concluding, it was demonstrated that different MSTFs can be combined by asymmetric fabrication for the preparation of complex mesoporous architectures with pore size along with surface wettability step gradients. Thereby, hydrophobic MSTFs can be prepared by co-condensation of methylated precursors, such as MTMS and DMDMS, together with TEOS. Incorporation of organic groups via co-condensation, or by applying bridged precursors leads to MSTFs with improved chemical stability at basic environment. As an alternative to petro-based templating agents, HPC was successfully applied as sustainable and bio-based template for the preparation of MSTFs with possible chiral structure. New strategies for the precise (nano-)local polymer placement in double layer MSTFs were demonstrated by a layer-selective polymerization approach, and by nanoscopic polymer placement using plasmonic metal NPs as nanoscale light sources to induce photopolymerizations.

7. Experimental Section

In this chapter, the applied characterization methods and respective data acquisition are illustrated. Moreover, the used chemicals and synthetic protocols with respect to the preparation of single and double layered MSTFs are described.

7.1. Equipment

7.1.1. ATR-IR spectroscopy

ATR-IR spectra of prepared MSTFs deposited on glass substrates were recorded on the supporting substrate using a Perkin Elmer Instrument Spectrum One FT-IR Spectrometer equipped with an Universal ATR Polarization Accessory (Waltham, MA, USA). All spectra were recorded between 4000 and 650 cm^{-1} with a resolution of 4 cm^{-1} using the Spectrum Software (Version 10.5.4.738, PerkinElmer, Inc., Waltham, MA, USA, 2016), and automatic background and baseline corrections were performed. Signals from MSTFs are partially superimposed by signals originating from the glass substrate in the range of 830-1250 cm^{-1} in dependence of the penetration depth of the ATR-IR evanescent wave. Nevertheless, IR-spectra of different films can be compared due to the comparable film thicknesses. Further data processing was performed in OriginPro9 (ADDITIVE Soft- und Hardware für Technik und Wissenschaft GmbH, Friedrichsdorf, Germany, 2012). IR spectra of MSTFs are either normalized to the stretching vibration of free silanol groups at ~ 905 cm^{-1} or to the asymmetric stretching vibration of Si-O-Si at ~ 1050 cm^{-1} depending on the strongest band obtained. However, only MSTFs that have been prepared identically are directly compared.

7.1.2. Ellipsometry

Thickness and refractive indices of MSTFs deposited on silicon wafer substrates were determined applying a Nanofilm EP3-SE imaging ellipsometer from Accurion with the measurement software EP3-View. One-zone AOI measurements were performed between AOIs of 36-68° in 2° steps with a laser wavelength of 658 nm and one region of interest (ROI) of approximately 700 x 700 μm, while keeping the relative humidity constant at 15% relative humidity (humidity control: ACE-flow, Solgelway). Refractive indices and film thicknesses were determined using the measured ellipsometric angles Δ and Ψ with the software EP4 Model (version 1.2.0) supplied with the instrument. The thickness of the natural silicon oxide layer of

the silicon substrate was fitted allowing an iteration between 0 and 10 nm. With respect to the determination of layer thicknesses of MSTFs and MOSTFs, iteration limits were individually applied. Refractive indices of MSTFs and MOSTFs were simultaneously fitted by iteration between the values 1.0 and 1.5. All films were measured on three spots along the direction of dip coating unless stated otherwise. Porosities were calculated using the determined values for refractive indices and applying the BEMA.

7.1.3. Profilometer

Profilometer measurements were performed as complementary method to ellipsometry to determine film thicknesses with a profiler device Dektak XT from Bruker with a vertical resolution of 1, and a horizontal resolution of 120 000 points. Measurements were performed using a tip size of 25 μm, a scan length of 5 mm, and an applied force of 1 mg. All measurements were recorded in Hills & Valley mode.

7.1.4. SEM

SEM micrographs were recorded using a Philips XL30 FEG scanning electron microscope equipped with a tungsten cathode and a back scattered electron yttrium aluminum garnet (BSE YAG) detector. An accelerating voltage of 20-30 kV, a 30 μm aperture, and a spot size of 2-4 were applied. Samples were coated with 7 nm Pd/Pt prior to measurements. Digital micrographs were recorded over a range of magnifications at a working distance of 6-12 using a SE2 detector.

7.1.5. TEM

TEM micrographs were recorded using a Philips FEI CM-20 transmission electron microscope (Philips, Netherlands) supplied with a LaB$_6$ cathode and an Olympus CCD camera with a maximum resolution of 2.3 Å operating at an accelerating voltage of 200 kV. MSTF samples were prepared by scratching off the films from the substrate and dispersing in filtered absolute ethanol. The dispersion was drop casted onto 3.05 mm Cu grids (mesh size 200) with a Lacey carbon film (Plano GmbH, article number S166-2), after sonication for 5 min. The prepared samples were dried under ambient conditions. Measurements were performed by Ulrike Kunz (Department of Materials and Earth Sciences, Physical Metallurgy Group, Technical University of Darmstadt).

7.1.6. Determination of Water Contact Angles

Apparent water contact angles were determined using a OCA35 device from DataPhysics Instruments GmbH with the software SCA 4.5.2 Build 1052 (DataPhysics Instruments GmbH, Germany). All films were measured at least on three positions along the direction of dip coating with a water drop volume of 2-4 μL and a dosing rate of 0.5 μL/s.

7.1.7. CV

The ionic pore accessibility of MSTFs was investigated via CV using the charged and redox-active probe molecules $[Ru(NH_3)_6]^{2+/3+}$ and $[Fe(CN)_6]^{3-/4-}$. Measurements were performed using a Metrohm Autolab PGSTAT302N potentiostat with the software Nova 2.1.2 Build 633 (Metrohm Autolab B.V., Netherlands). MSTFs prepared on ITO coated glass substrates were immersed in 100 mM KCl electrolyte solution for at least 30 min prior to measurements. The ionic pore accessibility of MSTFs was investigated using a 1 mM solution of either positively or negatively charged probe molecule in 100 mM KCl electrolyte solution. The pH-dependent ionic pore accessibility was performed by adjusting the probe molecule solution pH between 2 and 11.5 by addition of either concentrated aqueous NaOH or HCl, and determined using pH paper (Carl Roth/VWR) or a pH-meter (pH110, VWR). An Ag/AgCl reference electrode (BASi RE-6) and a graphite counter electrode was used in the sample cell. The measured working electrode (ITO) area was 0.21 cm^2. Ionic pore accessibility was measured for each pH using a scan rate sequence of 200, 100, 25, 300, 500/1000, and 200 mV s^{-1}, with each scan rate cycled for three times. Quality control of the cyclic voltammograms was conducted by ensuring comparability of the first and last scan rate of 200 mV s^{-1}. Furthermore, cyclic voltammograms were only discussed based on the third cycle of a scan rate obtained, if at least the cyclic voltammograms of the second and third cycle were comparable ensuring an equilibrium state. Additionally, the first applied pH was re-measured for all scan rates ensuring reversibility of charge and thus ionic pore accessibility unless stated otherwise.

7.2. Synthesis

7.2.1. Chemicals and Materials

All chemicals and solvents were purchased from Sigma-Aldrich, Acros Organics, Carl Roth, and VWR and used as received unless stated otherwise. Microscope slides (Carl Roth/VWR, glass, cut edges) were cleaned with technical grade ethanol and dried under ambient conditions prior

to dip coating. Silicon wafer substrates (Si-Mat, Kaufering, Germany, 100 mm diameter, 525 ± 25 μm thickness, tupe P/Bor, <001> orientation, CZ growth method, 2-5 Ω resistivity, polished on one side) and indium tin oxide coated glass substrates (ITO, Delta Technologies, Ltd., Loveland, CO, USA, polished float glass, 150 x 150 x 1.1 mm, SiO_2 passivated/indium tin oxide coated one surface, RS=4-8 Ω, cut edges) were cut to desired size with a diamond cutter, cleaned using technical grade ethanol, and dried under ambient conditions prior to dip coating.

7.2.2. Preparation of MSTFs templated with Pluronic® F127

MSTFs were prepared via sol-gel chemistry using TEOS as inorganic precursor and an amphiphilic triblock copolymer Pluronic® F127 as structure-directing template. The molar ratios of the compounds used in the precursor solution applied for dip coating were 1 TEOS / 40 EtOH / 0.0075 F127 / 10 H_2O / 0.28 HCl resulting in MSTFs with 6-8 nm mesopores. The precursor solution was prepared at room temperature and stirred overnight prior to deposition on glass, silicon wafer, and ITO coated glass substrates applying the EISA. At 23-25 °C and 50% relative humidity, the films were dip coated with a withdrawal speed of 2 mm s^{-1}. Subsequently, the films were stored at 23-25 °C and 50% relative humidity for 1 h. Mesostructured films were stabilized by a temperature treatment at 60 °C and 130 °C for 1 h respectively. MSTFs were obtained, after template removal that was either performed by calcination up to 350 °C for 2 h or by extraction in acidic ethanol (0.01 M HCl) for three days.

7.2.3. Preparation of MSTFs templated with CTAB

Based on a modified procedure of reference [232], MSTFs were prepared via sol-gel chemistry using TEOS as inorganic precursor and the surfactant CTAB as structure-directing template. The molar ratios of the compounds used in the precursor solution applied for dip coating were 1 TEOS / 20 EtOH / 0.14 CTAB / 5 H_2O / 0.004 HCl resulting in MSTFs with 1-3 nm mesopores. The precursor solution was prepared at room temperature and stirred overnight prior to deposition on glass, silicon wafer, and ITO coated glass substrates applying the EISA. At 23-25 °C and 50% relative humidity, the films were dip coated with a withdrawal speed of 2 mm s^{-1}. Subsequently, the films were stored at 23-25 °C and 50% relative humidity for 24 h. Mesostructured films were stabilized by a temperature treatment at 60 °C and 130 °C for 24 h respectively. MSTFs were obtained, after template removal that was performed by calcination up to 350 °C for 2 h.

7.2.4. MSTFs with tunable surface wettability

MSTFs were prepared via sol-gel chemistry using TEOS, MTMS, and DMDMS as inorganic precursors and an amphiphilic triblock copolymer Pluronic® F127 as structure-directing template. The molar ratios of the compounds used in the precursor solution applied for dip coating were

x TEOS / (1-x)·0.6 MTMS / (1-x)·0.4 DMDMS / 40 EtOH / 0.0075 F127 / 10 H_2O / 0.028 HCl.

The precursor solution was prepared at room temperature and stirred for 10 min prior to deposition on glass, silicon wafer, and ITO coated glass substrates applying the EISA. At 23-25 °C and 50% relative humidity, the films were dip coated with a withdrawal speed of 2 mm s^{-1}. Subsequently, the films were stored at 23-25 °C and 50% relative humidity for 1 h. The films were stabilized by a temperature treatment at 60 °C and 130 °C for 1 h respectively. MSTFs were obtained, after template removal that was either performed by calcination up to 350 °C for 2 h or by extraction in acidic ethanol (0.01 M HCl) for three days.

7.2.5. MOSTFs prepared from bridged silica precursor

MOSTFs were prepared via sol-gel chemistry using BTESE as inorganic precursor and an amphiphilic triblock copolymer Pluronic® F127 as structure-directing template. The molar ratios of the compounds used in the precursor solution applied for dip coating were 1 BTESE / 80 EtOH / 0.015 F127 / 20 H_2O / 0.56 HCl resulting in MSTFs with an average pore size of 8.6 nm. The precursor solution was prepared at room temperature and stirred overnight prior to deposition on glass, silicon wafer, and ITO coated glass substrates applying the EISA. At 23-25 °C and 50% relative humidity, the films were dip coated with a withdrawal speed of 2 mm s^{-1}. Subsequently, the films were stored at 23-25 °C and 50% relative humidity for 1 h. Mesostructured films were stabilized by a temperature treatment at 60 °C and 130 °C for 1 h respectively. MSTFs were obtained, after template removal that was performed by extraction in acidic ethanol (0.01 M HCl) for 3 days.

7.2.6. MSTFs templated with HPC

MSTFs were prepared via sol-gel chemistry using TEOS as inorganic precursor and HPC (MW 100 000) as template. The molar ratios of the compounds used in the precursor solution applied for dip coating were 1 TEOS / 40 EtOH / 0.001 HPC / 10 H_2O / 0.28 HCl resulting in MSTFs with an average pore size of 2.9 nm. The precursor solution was prepared at room temperature and stirred overnight prior to deposition on glass, silicon wafer, and ITO coated glass substrates

applying the EISA. At 23-25 °C and 50% relative humidity, the films were dip coated with a withdrawal speed of 2 mm s^{-1}. Subsequently, the films were stored at 23-25 °C and 50% relative humidity for 24 h. Mesostructured films were stabilized by a temperature treatment at 60 °C and 130 °C for 1 h respectively. MSTFs were obtained, after template removal via calcination at 350 °C and 540 °C for 2 h respectively.

7.2.7. Preparation of double layered MSTFs

Double layered MSTFs were prepared via sol-gel chemistry applying EISA. The first layer was deposited on glass, silicon wafer, and ITO coated glass substrates at 23-25 °C and 50% relative humidity with a withdrawal speed of 2 mm s^{-1}. Subsequently, the films were stored at 23-25 °C and 50% relative humidity for 1 h in case of Pluronic® F127 templated films, and 24 h in case of CTAB templated films. The films were stabilized by a temperature treatment at 60 °C and 130 °C for 1 h respectively, before deposition of the second layer. The second layer was deposited on the first layer at 23-25 °C and 50% relative humidity with a withdrawal speed of 2 mm s^{-1} unless stated otherwise. Subsequently, the films were stored at 23-25 °C and 50% relative humidity for 1 h in case of Pluronic® F127 templated films, and 24 h in case of CTAB templated films. Finally, double layered MSTFs were obtained, after template removal that was performed by calcination up to 350 °C for 2 h.

7.2.8. Investigation of chemical stability of MSTFs and MOSTFs

Investigation of chemical stability at pH 10 of prepared MSTFs and MOSTFs deposited on silicon wafer substrates was conducted using ellipsometry. First, the initial thicknesses of the films were determined by ellipsometry applying 3 ROIs of approximately 100 x 100 μm on one spot of a film, and the measurement procedure described above. After incubation in pH 10 buffer solution (HI 7010, HANNA Instruments) for 30, 60, 90, 120, 150, 180, 210, and 240 min, the MSTFs and MOSTFs were rinsed with water and technical ethanol, respectively, and dried with pressured air, before determining the film thicknesses using ellipsometry. Samples were prepared for each incubation time.

Abbreviations

A	Analyzer
AAO	Anodized aluminum oxide
Ag-NP	Silver nanoparticle
AIBN	Azobisisobutyronitrile
ALD	Atomic layer deposition
AOI	Angle of incidence
APTES	(3-Aminopropyl)triethoxysilane
ATR-IR	Attenuated total reflection - infrared
ATRP	Atom transfer radical polymerization
Au-NP	Gold nanoparticle
BCP	Block copolymer
BDC	4-(N,N-Diethyldithiocarbamoylmethyl)benzoic acid
BEMA	Bruggemann effective medium approximation
BTESE	1,2-Bis(triethoxysilyl)ethane
C	Compensator
CCD	Charge-coupled device
CDTPA	4-Cyano-4-((dodecylsulfanylthiocarbonyl)sulfanyl)pentanoic acid
CNT	Carbon nanotube
CTA	Chain transfer agent
CTAB	Cetyltrimethylammonium bromide
CV	Cyclic voltammetry
CVD	Chemical vapor deposition
DE	Diarylethene
DLP	Diffusion limited patterning
DMDMS	Dimethyldimethoxysilane
DMSO	Dimethyl sulfoxide
DNA	Deoxyribonucleic acid
DNP	Dynamic nuclear polarization
E	Electric field
EDC	1-Ethyl-3-(3-dimethylaminopropyl)carbodiimide hydrochloride
EDX	Energy-dispersive X-ray spectroscopy
EISA	Evaporation-induced self-assembly
FEM	Finite element method

HATU	1-[Bis(dimethylamino)methylene]-1H-1,2,3-triazolo[4,5-b]pyridinium-3-oxide hexafluorophosphate
HF	Hydrophobic force
HMM	Hybrid mesoporous materials
HMSTF	Hybrid mesoporous silica thin films
HP	Hydrostatic pressure
HPC	Hydroxypropyl cellulose
ICR	Ion current rectification
iCVD	Initiated chemical vapor deposition
ITO	Indium-tin oxide
IUPAC	International Union of Pure and Applied Chemistry
LSPR	Localized surface plasmon resonance
METAC	[2-(Methacryloyloxy)ethyl]trimethylammonium chloride
MOSTF	Mesoporous (organo)silica thin films
MSM	Mesoporous silica materials
MSTF	Mesoporous silica thin film
MTMS	Methyltrimethoxysilane
NIR	Near-infrared
NP	Nanoparticle
OTS	Octadecyltrimethoxysilane
P	Polarizer
PAA	Polyacrylic acid
PAN	Polyacrylonitrile
PDA	Polydopamine
PDMS	Polydimethylsiloxane
PEI	Polyethyleneimine
PET	Polyethylene terephthalate
PIMP	Photoiniferter-mediated polymerization
PMETAC	Poly(2-(methacryloyloxy)ethyltrimethylammonium chloride
PMEP	Poly(2-methacryloyloxy)ethyl phosphate
PNiPAM	Poly(N-isopropylacrylamide)
PP	Polypropylene
PU	Polyurethane
PVP	Polyvinylpyridine
RAFT	Reversible addition-fragmentation chain-transfer polymerization

RIU	Refractive index unit
RMSE	Root mean square error
ROMP	Ring opening metathesis polymerization
S	Sample
SBDTTC	s-p-Trimethoxysilylbenzyl-S'-dodecyltrithiocarbonate
SEM	Scanning electron microscopy
SERS	Surface enhanced Raman scattering
SI-	Surface-initiated
SIGP	Photopolymerization and photografting
SP	Surface plasmon
SPR	Surface plasmon resonance
SSNMR	Solid-state nuclear magnetic resonance
TEM	Transmission electron microscopy
TEOS	Tetraethylorthosilicate
UV	Ultraviolet

References

1.   Chu, Z.; Seeger, S., Superamphiphobic surfaces. *Chemical Society reviews* **2014,** *43* (8), 2784-98.
2.   Pathak, S., Biomimicry: (Innovation Inspired by Nature). *International Journal of New Technology and Research* **2019,** *5* (6), 34-38.
3.   Nasrollahzadeh, M.; Sajadi, S. M.; Sajjadi, M.; Issaabadi, Z., Applications of Nanotechnology in Daily Life. *Interface Science and Technology* **2019,** *28,* 113-143.
4.   Giwa, A.; Hasan, S. W.; Yousuf, A.; Chakraborty, S.; Johnson, D. J.; Hilal, N., Biomimetic membranes: A critical review of recent progress. *Desalination* **2017,** *420,* 403-424.
5.   Dong, B.; Pei, Y.; Zhao, F.; Goh, T. W.; Qi, Z.; Xiao, C.; Chen, K.; Huang, W.; Fang, N., In situ quantitative single-molecule study of dynamic catalytic processes in nanoconfinement. *Nature Catalysis* **2018,** *1* (2), 135-140.
6.   Agrawal, K. V.; Shimizu, S.; Drahushuk, L. W.; Kilcoyne, D.; Strano, M. S., Observation of extreme phase transition temperatures of water confined inside isolated carbon nanotubes. *Nature Nanotechnology* **2017,** *12* (3), 267-273.
7.   Pugliese, P.; Conde, M. M.; Rovere, M.; Gallo, P., Freezing Temperatures, Ice Nanotubes Structures, and Proton Ordering of TIP4P/ICE Water inside Single Wall Carbon Nanotubes. The *Journal of Physical Chemistry B* **2017,** *121* (45), 10371-10381.
8.   Raju, M.; van Duin, A.; Ihme, M., Phase transitions of ordered ice in graphene nanocapillaries and carbon nanotubes. *Scientific Reports* **2018,** *8* (1), 3851.
9.   Bottenus, D.; Oh, Y. J.; Han, S. M.; Ivory, C. F., Experimentally and theoretically observed native pH shifts in a nanochannel array. *Lab on a Chip* **2009,** *9* (2), 219-231.
10.   Brilmayer, R.; Kübelbeck, S.; Khalil, A.; Brodrecht, M.; Kunz, U.; Kleebe, H. J.; Buntkowsky, G.; Baier, G.; Andrieu-Brunsen, A., Influence of Nanoconfinement on the pKa of Polyelectrolyte Functionalized Silica Mesopores. *Advanced Materials Interfaces* **2020,** *7* (7), 1901914.
11.   Kowalczyk, S. W.; Blosser, T. R.; Dekker, C., Biomimetic nanopores: learning from and about nature. *Trends in Biotechnology* **2011,** *29* (12), 607-14.
12.   Grzybowski, B. A.; Huck, W. T., The nanotechnology of life-inspired systems. *Nature Nanotechnology* **2016,** *11* (7), 585-92.
13.   Merindol, R.; Walther, A., Materials learning from life: concepts for active, adaptive and autonomous molecular systems. *Chemical Society reviews* **2017,** *46* (18), 5588-5619.
14.   Sholl, D. S.; Lively, R. P., Seven chemical separations to change the world. *Nature* **2016,** *532* (7600), 435-7.
15.   Haywood, D. G.; Saha-Shah, A.; Baker, L. A.; Jacobson, S. C., Fundamental studies of nanofluidics: nanopores, nanochannels, and nanopipets. *Analytical Chemistry* **2015,** *87* (1), 172-87.
16.   Zhang, H.; Tian, Y.; Jiang, L., Fundamental studies and practical applications of bio-inspired smart solid-state nanopores and nanochannels. *Nano Today* **2016,** *11* (1), 61-81.
17.   Buchsbaum, S. F.; Nguyen, G.; Howorka, S.; Siwy, Z. S., DNA-modified polymer pores allow pH- and voltage-gated control of channel flux. *Journal of the American Chemical Society* **2014,** *136* (28), 9902-5.
18.   Zhang, Z.; Wen, L.; Jiang, L., Bioinspired smart asymmetric nanochannel membranes. *Chemical Society reviews* **2018,** *47* (2), 322-356.
19.   Perez Sirkin, Y. A.; Tagliazucchi, M.; Szleifer, I., Transport in nanopores and nanochannels: some fundamental challenges and nature-inspired solutions. *Materials Today Advances* **2020,** *5,* 100047.
20.   Zhou, H.; Wang, H.; Niu, H.; Lin, T., Superphobicity/philicity Janus fabrics with switchable, spontaneous, directional transport ability to water and oil fluids. *Scientific Reports* **2013,** *3,* 2964.

21.	Wang, Z.; Yang, X.; Cheng, Z.; Liu, Y.; Shao, L.; Jiang, L., Simply realizing "water diode" Janus membranes for multifunctional smart applications. *Materials Horizons* **2017,** *4* (4), 701-708.

22.	Nau, M.; Herzog, N.; Schmidt, J.; Meckel, T.; Andrieu-Brunsen, A.; Biesalski, M., Janus-Type Hybrid Paper Membranes. *Advanced Materials Interfaces* **2019,** *6* (18), 1900892.

23.	Söz, Ç. K.; Trosien, S.; Biesalski, M., Janus Interface Materials: A Critical Review and Comparative Study. *ACS Materials Letters* **2020,** *2* (4), 336-357.

24.	Siwy, Z.; Fulinski, A., Fabrication of a synthetic nanopore ion pump. *Physical Review Letters* **2002,** *89* (19), 198103.

25.	Siwy, Z. S., Ion-Current Rectification in Nanopores and Nanotubes with Broken Symmetry. *Advanced Functional Materials* **2006,** *16* (6), 735-746.

26.	Siwy, Z.; Gu, Y.; Spohr, H. A.; Baur, D.; Wolf-Reber, A.; Spohr, R.; Apel, P.; Korchev, Y. E., Rectification and voltage gating of ion currents in a nanofabricated pore. *Europhysics Letters* **2002,** *60* (3), 349-355.

27.	Daiguji, H.; Oka, Y.; Shirono, K., Nanofluidic diode and bipolar transistor. *Nano Letters* **2005,** *5* (11), 2274-80.

28.	Cheng, L. J.; Guo, L. J., Ionic current rectification, breakdown, and switching in heterogeneous oxide nanofluidic devices. *ACS Nano* **2009,** *3* (3), 575-84.

29.	Yan, R.; Liang, W.; Fan, R.; Yang, P., Nanofluidic diodes based on nanotube heterojunctions. *Nano Letters* **2009,** *9* (11), 3820-5.

30.	Siwy, Z. S.; Howorka, S., Engineered voltage-responsive nanopores. *Chemical Society reviews* **2010,** *39* (3), 1115-32.

31.	Li, C.-Y.; Ma, F.-X.; Wu, Z.-Q.; Gao, H.-L.; Shao, W.-T.; Wang, K.; Xia, X.-H., Solution-pH-Modulated Rectification of Ionic Current in Highly Ordered Nanochannel Arrays Patterned with Chemical Functional Groups at Designed Positions. *Advanced Functional Materials* **2013,** *23* (31), 3836-3844.

32.	Lin, C.-Y.; Hsu, J.-P.; Yeh, L.-H., Rectification of ionic current in nanopores functionalized with bipolar polyelectrolyte brushes. *Sensors and Actuators B: Chemical* **2018,** *258*, 1223-1229.

33.	Madai, E.; Valisko, M.; Boda, D., Application of a bipolar nanopore as a sensor: rectification as an additional device function. *Physical Chemistry Chemical Physics* **2019,** *21* (36), 19772-19784.

34.	Wu, Z. Q.; Li, Z. Q.; Wang, Y.; Xia, X. H., Regulating Ion Transport in a Nanochannel with Tandem and Parallel Structures via Concentration Polarization. *Journal of Physical Chemistry Letters* **2020,** *11* (2), 524-529.

35.	Zhang, H.; Hou, X.; Zeng, L.; Yang, F.; Li, L.; Yan, D.; Tian, Y.; Jiang, L., Bioinspired artificial single ion pump. *Journal of the American Chemical Society* **2013,** *135* (43), 16102-10.

36.	Zhang, Z.; Li, P.; Kong, X. Y.; Xie, G.; Qian, Y.; Wang, Z.; Tian, Y.; Wen, L.; Jiang, L., Bioinspired Heterogeneous Ion Pump Membranes: Unidirectional Selective Pumping and Controllable Gating Properties Stemming from Asymmetric Ionic Group Distribution. *Journal of the American Chemical Society* **2018,** *140* (3), 1083-1090.

37.	Xiao, K.; Chen, L.; Chen, R.; Heil, T.; Lemus, S. D. C.; Fan, F.; Wen, L.; Jiang, L.; Antonietti, M., Artificial light-driven ion pump for photoelectric energy conversion. *Nature Communications* **2019,** *10* (1), 74.

38.	Bernardos, A.; Aznar, E.; Marcos, M. D.; Martinez-Manez, R.; Sancenon, F.; Soto, J.; Barat, J. M.; Amoros, P., Enzyme-responsive controlled release using mesoporous silica supports capped with lactose. *Angewandte Chemie International Edition in English* **2009,** *48* (32), 5884-7.

39.	Coll, C.; Mondragon, L.; Martinez-Manez, R.; Sancenon, F.; Marcos, M. D.; Soto, J.; Amoros, P.; Perez-Paya, E., Enzyme-mediated controlled release systems by anchoring peptide sequences on mesoporous silica supports. *Angewandte Chemie International Edition in English* **2011,** *50* (9), 2138-40.

40.   Zhang, D. X.; Yoshikawa, C.; Welch, N. G.; Pasic, P.; Thissen, H.; Voelcker, N. H., Spatially Controlled Surface Modification of Porous Silicon for Sustained Drug Delivery Applications. *Scientific Reports* **2019,** *9* (1), 1367.

41.   Guo, W.; Tian, Y.; Jiang, L., Asymmetric ion transport through ion-channel-mimetic solid-state nanopores. *Accounts of chemical research* **2013,** *46* (12), 2834-46.

42.   Szczesniak, B.; Choma, J.; Jaroniec, M., Major advances in the development of ordered mesoporous materials. *Chemical Communications* **2020,** *56* (57), 7836-7848.

43.   Lei, Q.; Guo, J.; Noureddine, A.; Wang, A.; Wuttke, S.; Brinker, C. J.; Zhu, W., Sol–Gel-Based Advanced Porous Silica Materials for Biomedical Applications. *Advanced Functional Materials* **2020,** *30* (41), 1909539.

44.   Soler-Illia, G. J.; Azzaroni, O., Multifunctional hybrids by combining ordered mesoporous materials and macromolecular building blocks. *Chemical Society reviews* **2011,** *40* (2), 1107-50.

45.   Alberti, S.; Soler-Illia, G. J.; Azzaroni, O., Gated supramolecular chemistry in hybrid mesoporous silica nanoarchitectures: controlled delivery and molecular transport in response to chemical, physical and biological stimuli. *Chemical Communications* **2015,** *51* (28), 6050-75.

46.   Sanchez, C.; Boissiere, C.; Grosso, D.; Laberty, C.; Nicole, L., Design, synthesis, and properties of inorganic and hybrid thin films having periodically organized nanoporosity. *Chemistry of Materials* **2008,** *20* (3), 682-737.

47.   Brunsen, A.; Cui, J.; Ceolin, M.; del Campo, A.; Soler-Illia, G. J.; Azzaroni, O., Light-activated gating and permselectivity in interfacial architectures combining "caged" polymer brushes and mesoporous thin films. *Chemical Communications* **2012,** *48* (10), 1422-4.

48.   Silies, L.; Didzoleit, H.; Hess, C.; Stühn, B.; Andrieu-Brunsen, A., Mesoporous Thin Films, Zwitterionic Monomers, and Iniferter-Initiated Polymerization: Polymerization in a Confined Space. *Chemistry of Materials* **2015,** *27* (6), 1971-1981.

49.   Herzog, N.; Kind, J.; Hess, C.; Andrieu-Brunsen, A., Surface plasmon & visible light for polymer functionalization of mesopores and manipulation of ionic permselectivity. *Chemical Communications* **2015,** *51* (58), 11697-700.

50.   Krohm, F.; Kind, J.; Savka, R.; Alcaraz Janßen, M.; Herold, D.; Plenio, H.; Thiele, C. M.; Andrieu-Brunsen, A., Photochromic spiropyran- and spirooxazine-homopolymers in mesoporous thin films by surface initiated ROMP. *Journal of Materials Chemistry* **2016,** *4* (18), 4067-4076.

51.   Elbert, J.; Krohm, F.; Rüttiger, C.; Kienle, S.; Didzoleit, H.; Balzer, B. N.; Hugel, T.; Stühn, B.; Gallei, M.; Brunsen, A., Polymer-Modified Mesoporous Silica Thin Films for Redox-Mediated Selective Membrane Gating. *Advanced Functional Materials* **2014,** *24* (11), 1591-1601.

52.   Kruk, M.; Dufour, B.; Celer, E. B.; Kowalewski, T.; Jaroniec, M.; Matyjaszewski, K., Synthesis of mesoporous carbons using ordered and disordered mesoporous silica templates and polyacrylonitrile as carbon precursor. *The Journal of Physical Chemistry B* **2005,** *109* (19), 9216-25.

53.   Pasetto, P.; Blas, H.; Audouin, F.; Boissière, C.; Sanchez, C.; Save, M.; Charleux, B., Mechanistic Insight into Surface-Initiated Polymerization of Methyl Methacrylate and Styrene via ATRP from Ordered Mesoporous Silica Particles. *Macromolecules* **2009,** *42* (16), 5983-5995.

54.   Kruk, M., Surface-Initiated Controlled Radical Polymerization in Ordered Mesoporous Silicas. *Israel Journal of Chemistry* **2012,** *52* (3-4), 246-255.

55.   Andrieu-Brunsen, A.; Micoureau, S.; Tagliazucchi, M.; Szleifer, I.; Azzaroni, O.; Soler-Illia, G. J. A. A., Mesoporous Hybrid Thin Film Membranes with PMETAC@Silica Architectures: Controlling Ionic Gating through the Tuning of Polyelectrolyte Density. *Chemistry of Materials* **2015,** *27* (3), 808-821.

56.   Tom, J.; Brilmayer, R.; Schmidt, J.; Andrieu-Brunsen, A., Optimisation of Surface-Initiated Photoiniferter-Mediated Polymerisation under Confinement, and the Formation of Block Copolymers in Mesoporous Films. *Polymers* **2017,** *9* (10), 539.

57.   Tiemann, M.; Weinberger, C., Selective Modification of Hierarchical Pores and Surfaces in Nanoporous Materials. *Advanced Materials Interfaces* **2020**, 2001153.

58.   Villaescusa, L. A.; Mihi, A.; Rodriguez, I.; Garcia-Bennett, A. E.; Miguez, H., Growth of mesoporous materials within colloidal crystal films by spin-coating. *The Journal of Physical Chemistry B* **2005,** *109* (42), 19643-9.

59.   Angelomé, P. C.; Fuertes, M. C.; Soler-Illia, G. J. A. A., Multifunctional, Multilayer, Multiscale: Integrative Synthesis of Complex Macroporous and Mesoporous Thin Films with Spatial Separation of Porosity and Function. *Advanced Materials* **2006,** *18* (18), 2397-2402.

60.   Brezesinski, T.; Antonietti, M.; Smarsly, B. M., Self-Assembled Metal Oxide Bilayer Films with "Single-Crystalline" Overlayer Mesopore Structure. *Advanced Materials* **2007,** *19* (8), 1074-1078.

61.   Faustini, M.; Nicole, L.; Boissière, C.; Innocenzi, P.; Sanchez, C.; Grosso, D., Hydrophobic, Antireflective, Self-Cleaning, and Antifogging Sol−Gel Coatings: An Example of Multifunctional Nanostructured Materials for Photovoltaic Cells. *Chemistry of Materials* **2010,** *22* (15), 4406-4413.

62.   Faustini, M.; Ceratti, D. R.; Louis, B.; Boudot, M.; Albouy, P. A.; Boissiere, C.; Grosso, D., Engineering functionality gradients by dip coating process in acceleration mode. *ACS Applied Materials & Interfaces* **2014,** *6* (19), 17102-10.

63.   Grosso, D., How to exploit the full potential of the dip-coating process to better control film formation. *Journal of Materials Chemistry* **2011,** *21* (43), 17033-17038.

64.   El Ahrach, H. I.; Bachelot, R.; Vial, A.; Lerondel, G.; Plain, J.; Royer, P.; Soppera, O., Spectral degeneracy breaking of the plasmon resonance of single metal nanoparticles by nanoscale near-field photopolymerization. *Physical Review Letters* **2007,** *98* (10), 107402.

65.   Deeb, C.; Bachelot, R.; Plain, J.; Baudrion, A. L.; Jradi, S.; Bouhelier, A.; Soppera, O.; Jain, P. K.; Huang, L.; Ecoffet, C.; Balan, L.; Royer, P., Quantitative analysis of localized surface plasmons based on molecular probing. *ACS Nano* **2010,** *4* (8), 4579-86.

66.   Deeb, C.; Ecoffet, C.; Bachelot, R.; Plain, J.; Bouhelier, A.; Soppera, O., Plasmon-based free-radical photopolymerization: effect of diffusion on nanolithography processes. *Journal of the American Chemical Society* **2011,** *133* (27), 10535-42.

67.   López-Puente, V.; Abalde-Cela, S.; Angelomé, P. C.; Alvarez-Puebla, R. A.; Liz-Marzán, L. M., Plasmonic Mesoporous Composites as Molecular Sieves for SERS Detection. *The Journal of Physical Chemistry Letters* **2013,** *4* (16), 2715-2720.

68.   Martínez, E. D.; Boissière, C.; Grosso, D.; Sanchez, C.; Troiani, H.; Soler-Illia, G. J. A. A., Confinement-Induced Growth of Au Nanoparticles Entrapped in Mesoporous TiO2 Thin Films Evidenced by in Situ Thermo-Ellipsometry. *The Journal of Physical Chemistry C* **2014,** *118* (24), 13137-13151.

69.   Innocenzi, P.; Malfatti, L., Nanoparticles in mesoporous films, a happy marriage for materials science. *Journal of Nanoparticle Research* **2018,** *20* (6).

70.   Angelome, P. C.; Pastoriza-Santos, I.; Perez-Juste, J.; Rodriguez-Gonzalez, B.; Zelcer, A.; Soler-Illia, G. J.; Liz-Marzan, L. M., Growth and branching of gold nanoparticles through mesoporous silica thin films. *Nanoscale* **2012,** *4* (3), 931-9.

71.   Tagliazucchi, M.; Szleifer, I., Transport mechanisms in nanopores and nanochannels: can we mimic nature? *Materials Today* **2015,** *18* (3), 131-142.

72.   Hänggi, P.; Bartussek, R., Brownian rectifiers: How to convert brownian motion into directed transport. *Lecture Notes in Physics* **1996,** *476*, 294-308.

73.   Hänggi, P.; Marchesoni, F., Artificial Brownian motors: Controlling transport on the nanoscale. *Reviews of Modern Physics* **2009,** *81* (1), 387-442.

74.   Hou, X.; Yang, F.; Li, L.; Song, Y.; Jiang, L.; Zhu, D., A biomimetic asymmetric responsive single nanochannel. *Journal of the American Chemical Society* **2010,** *132* (33), 11736-42.

75.   Rothman, J. E.; Lenard, J., Membrane asymmetry. *Science* **1977,** *195* (4280), 743-53.

76.   Shaw, R. S.; Packard, N.; Schroter, M.; Swinney, H. L., Geometry-induced asymmetric diffusion. *Proceedings of the National Academy of Sciences of the U S A* **2007,** *104* (23), 9580-4.

77.   Wei, C.; Bard, A. J.; Feldberg, S. W., Current Rectification at Quartz Nanopipet Electrodes. *Analytical Chemistry* **1997,** *69* (22), 4627-4633.

78.   Umehara, S.; Pourmand, N.; Webb, C. D.; Davis, R. W.; Yasuda, K.; Karhanek, M., Current rectification with poly-l-lysine-coated quartz nanopipettes. *Nano Letters* **2006,** *6* (11), 2486-92.

79.   White, H. S.; Bund, A., Ion current rectification at nanopores in glass membranes. *Langmuir : the ACS journal of surfaces and colloids* **2008,** *24* (5), 2212-8.

80.   Schiedt, B.; Healy, K.; Morrison, A. P.; Neumann, R.; Siwy, Z., Transport of ions and biomolecules through single asymmetric nanopores in polymer films. *Nuclear Instruments and Methods in Physics Research Section B: Beam Interactions with Materials and Atoms* **2005,** *236* (1-4), 109-116.

81.   He, Y.; Gillespie, D.; Boda, D.; Vlassiouk, I.; Eisenberg, R. S.; Siwy, Z. S., Tuning transport properties of nanofluidic devices with local charge inversion. *Journal of the American Chemical Society* **2009,** *131* (14), 5194-202.

82.   Ma, T.; Janot, J. M.; Balme, S., Track-Etched Nanopore/Membrane: From Fundamental to Applications. *Small Methods* **2020,** *4* (9), 2000366.

83.   Apel, P. Y.; Korchev, Y. E.; Siwy, Z.; Spohr, R.; Yoshida, M., Diode-like single-ion track membrane prepared by electro-stopping. *Nuclear Instruments and Methods in Physics Research Section B: Beam Interactions with Materials and Atoms* **2001,** *184* (3), 337-346.

84.   Siwy, Z.; Apel, P.; Baur, D.; Dobrev, D. D.; Korchev, Y. E.; Neumann, R.; Spohr, R.; Trautmann, C.; Voss, K.-O., Preparation of synthetic nanopores with transport properties analogous to biological channels. *Surface Science* **2003,** *532-535*, 1061-1066.

85.   Harrell, C. C.; Siwy, Z. S.; Martin, C. R., Conical nanopore membranes: controlling the nanopore shape. *Small* **2006,** *2* (2), 194-8.

86.   Chen, P.; Mitsui, T.; Farmer, D. B.; Golovchenko, J.; Gordon, R. G.; Branton, D., Atomic Layer Deposition to Fine-Tune the Surface Properties and Diameters of Fabricated Nanopores. *Nano Letters* **2004,** *4* (7), 1333-1337.

87.   Siwy, Z.; Gu, Y.; Spohr, H. A.; Baur, D.; Wolf-Reber, A.; Spohr, R.; Apel, P.; Korchev, Y. E., Rectification and voltage gating of ion currents in a nanofabricated pore. *Europhysics Letters* **2002,** *60* (3), 349-355.

88.   Siwy, Z.; Heins, E.; Harrell, C. C.; Kohli, P.; Martin, C. R., Conical-nanotube ion-current rectifiers: the role of surface charge. *Journal of the American Chemical Society* **2004,** *126* (35), 10850-1.

89.   Nishizawa, M.; Menon, V. P.; Martin, C. R., Metal nanotubule membranes with electrochemically switchable ion-transport selectivity. *Science* **1995,** *268* (5211), 700-2.

90.   Coster, H. G. L., A Quantitative Analysis of the Voltage-Current Relationships of Fixed Charge Membranes and the Associated Property of "Punch-Through". *Biophysical Journal* **1965,** *5* (5), 669-686.

91.   Bassignana, I. C.; Reiss, H., Ion transport and water dissociation in bipolar ion exchange membranes. *Journal of Membrane Science* **1983,** *15* (1), 27-41.

92.   Mafé, S.; Ramírez, P., Electrochemical characterization of polymer ion-exchange bipolar membranes. *Acta Polymerica* **1997,** *48* (7), 234-250.

93.   Vlassiouk, I.; Siwy, Z. S., Nanofluidic diode. *Nano Letters* **2007,** *7* (3), 552-6.

94.   Karnik, R.; Duan, C.; Castelino, K.; Daiguji, H.; Majumdar, A., Rectification of ionic current in a nanofluidic diode. *Nano Letters* **2007,** *7* (3), 547-51.

95.   Karnik, R.; Castelino, K.; Duan, C.; Majumdar, A., Diffusion-limited patterning of molecules in nanofluidic channels. *Nano Letters* **2006,** *6* (8), 1735-40.

96.   Vlassiouk, I.; Kozel, T. R.; Siwy, Z. S., Biosensing with nanofluidic diodes. *Journal of the American Chemical Society* **2009,** *131* (23), 8211-20.

97.   Ali, M.; Nasir, S.; Ensinger, W., Bioconjugation-induced ionic current rectification in aptamer-modified single cylindrical nanopores. *Chemical Communications* **2015,** *51* (16), 3454-7.

98.   Nguyen, G.; Howorka, S.; Siwy, Z. S., DNA strands attached inside single conical nanopores: ionic pore characteristics and insight into DNA biophysics. *The Journal of Membrane Biology* **2011,** *239* (1-2), 105-13.

99.   Kalman, E. B.; Vlassiouk, I.; Siwy, Z. S., Nanofluidic Bipolar Transistors. *Advanced Materials* **2008,** *20* (2), 293-297.

100.   Huang, X.; Kong, X.-Y.; Wen, L.; Jiang, L., Bioinspired Ionic Diodes: From Unipolar to Bipolar. *Advanced Functional Materials* **2018,** *28* (49), 1801079.

101.   de la Escosura-Muniz, A.; Merkoci, A., Nanochannels preparation and application in biosensing. *ACS Nano* **2012,** *6* (9), 7556-83.

102.   Yang, H. C.; Hou, J.; Chen, V.; Xu, Z. K., Janus Membranes: Exploring Duality for Advanced Separation. *Angewandte Chemie International Edition in English* **2016,** *55* (43), 13398-13407.

103.   Yang, H. C.; Xie, Y.; Hou, J.; Cheetham, A. K.; Chen, V.; Darling, S. B., Janus Membranes: Creating Asymmetry for Energy Efficiency. *Advanced Materials* **2018,** *30* (43), e1801495.

104.   Li, H. N.; Yang, J.; Xu, Z. K., Asymmetric Surface Engineering for Janus Membranes. *Advanced Materials Interfaces* **2020,** *7* (7), 1902064.

105.   Parker, A. R.; Lawrence, C. R., Water capture by a desert beetle. *Nature* **2001,** *414* (6859), 33-4.

106.   Casagrande, C.; Fabre, P.; Raphaël, E.; Veyssié, M., "Janus Beads": Realization and Behaviour at Water/Oil Interfaces. *Europhysics Letters (EPL)* **1989,** *9* (3), 251-255.

107.   Wang, H.; Ding, J.; Dai, L.; Wang, X.; Lin, T., Directional water-transfer through fabrics induced by asymmetric wettability. *Journal of Materials Chemistry* **2010,** *20* (37), 7938.

108.   Lim, H. S.; Park, S. H.; Koo, S. H.; Kwark, Y. J.; Thomas, E. L.; Jeong, Y.; Cho, J. H., Superamphiphilic Janus fabric. *Langmuir : the ACS journal of surfaces and colloids* **2010,** *26* (24), 19159-62.

109.   Chen, Q.; Meng, L.; Li, Q.; Wang, D.; Guo, W.; Shuai, Z.; Jiang, L., Water transport and purification in nanochannels controlled by asymmetric wettability. *Small* **2011,** *7* (15), 2225-31.

110.   Tian, X.; Li, J.; Wang, X., Anisotropic liquid penetration arising from a cross-sectional wettability gradient. *Soft Matter* **2012,** *8* (9), 2633.

111.   Wu, J.; Wang, N.; Wang, L.; Dong, H.; Zhao, Y.; Jiang, L., Unidirectional water-penetration composite fibrous film via electrospinning. *Soft Matter* **2012,** *8* (22), 5996.

112.   Wu, S.; Wildhaber, F.; Vazquez-Mena, O.; Bertsch, A.; Brugger, J.; Renaud, P., Facile fabrication of nanofluidic diode membranes using anodic aluminium oxide. *Nanoscale* **2012,** *4* (18), 5718-23.

113.   Dong, Y.; Kong, J.; Phua, S. L.; Zhao, C.; Thomas, N. L.; Lu, X., Tailoring surface hydrophilicity of porous electrospun nanofibers to enhance capillary and push-pull effects for moisture wicking. *ACS Applied Materials & Interfaces* **2014,** *6* (16), 14087-95.

114.   Wang, H.; Zhou, H.; Niu, H.; Zhang, J.; Du, Y.; Lin, T., Dual-Layer Superamphiphobic/Superhydrophobic-Oleophilic Nanofibrous Membranes with Unidirectional Oil-Transport Ability and Strengthened Oil-Water Separation Performance. *Advanced Materials Interfaces* **2015,** *2* (4), 1400506.

115.   Hou, L.; Wang, N.; Man, X.; Cui, Z.; Wu, J.; Liu, J.; Li, S.; Gao, Y.; Li, D.; Jiang, L.; Zhao, Y., Interpenetrating Janus Membrane for High Rectification Ratio Liquid Unidirectional Penetration. *ACS Nano* **2019,** *13* (4), 4124-4132.

116.   Wang, X.; Huang, Z.; Miao, D.; Zhao, J.; Yu, J.; Ding, B., Biomimetic Fibrous Murray Membranes with Ultrafast Water Transport and Evaporation for Smart Moisture-Wicking Fabrics. *ACS Nano* **2019,** *13* (2), 1060-1070.

117.   Shi, L.; Liu, X.; Wang, W.; Jiang, L.; Wang, S., A Self-Pumping Dressing for Draining Excessive Biofluid around Wounds. *Advanced Materials* **2019,** *31* (5), e1804187.

118.   Zhou, S.; Liu, F.; Wang, J.; Lin, H.; Han, Q.; Zhao, S.; Tang, C. Y., Janus Membrane with Unparalleled Forward Osmosis Performance. *Environmental Science & Technology Letters* **2019**, *6* (2), 79-85.

119.   Hu, L.; Gao, S.; Zhu, Y.; Zhang, F.; Jiang, L.; Jin, J., An ultrathin bilayer membrane with asymmetric wettability for pressure responsive oil/water emulsion separation. *Journal of Materials Chemistry A* **2015**, *3* (46), 23477-23482.

120.   Yang, J.; Wen, G.; Gou, X.; Song, H.; Guo, Z., A study on the manufacture of Kevlar membrane modified by inorganic nanoparticles with universal applicability in separating diffident types of emulsions. *Journal of Membrane Science* **2018**, *563*, 326-335.

121.   Zhang, J.; Yang, Y.; Zhang, Z.; Wang, P.; Wang, X., Biomimetic multifunctional nanochannels based on the asymmetric wettability of heterogeneous nanowire membranes. *Advanced Materials* **2014**, *26* (7), 1071-5.

122.   Lei, J.; Wang, L.; Zhang, J., Ratiometric pH sensor based on mesoporous silica nanoparticles and Forster resonance energy transfer. *Chemical Communications (Camb)* **2010**, *46* (44), 8445-8447.

123.   Rao, S.; Si, K. J.; Yap, L. W.; Xiang, Y.; Cheng, W., Free-Standing Bilayered Nanoparticle Superlattice Nanosheets with Asymmetric Ionic Transport Behaviors. *ACS Nano* **2015**, *9* (11), 11218-24.

124.   Cao, M.; Xiao, J.; Yu, C.; Li, K.; Jiang, L., Hydrophobic/Hydrophilic Cooperative Janus System for Enhancement of Fog Collection. *Small* **2015**, *11* (34), 4379-84.

125.   Meng, Z.; Chen, Y.; Li, X.; Xu, Y.; Zhai, J., Cooperative effect of pH-dependent ion transport within two symmetric-structured nanochannels. *ACS Applied Materials & Interfaces* **2015**, *7* (14), 7709-16.

126.   Zhang, Z.; Kong, X. Y.; Xiao, K.; Liu, Q.; Xie, G.; Li, P.; Ma, J.; Tian, Y.; Wen, L.; Jiang, L., Engineered Asymmetric Heterogeneous Membrane: A Concentration-Gradient-Driven Energy Harvesting Device. *Journal of the American Chemical Society* **2015**, *137* (46), 14765-72.

127.   Zhang, Z.; Sui, X.; Li, P.; Xie, G.; Kong, X. Y.; Xiao, K.; Gao, L.; Wen, L.; Jiang, L., Ultrathin and Ion-Selective Janus Membranes for High-Performance Osmotic Energy Conversion. *Journal of the American Chemical Society* **2017**, *139* (26), 8905-8914.

128.   Sui, X.; Zhang, Z.; Zhang, Z.; Wang, Z.; Li, C.; Yuan, H.; Gao, L.; Wen, L.; Fan, X.; Yang, L.; Zhang, X.; Jiang, L., Biomimetic Nanofluidic Diode Composed of Dual Amphoteric Channels Maintains Rectification Direction over a Wide pH Range. *Angewandte Chemie International Edition in English* **2016**, *55* (42), 13056-13060.

129.   Chang, Y.; Wang, Z.; Shi, Y.-e.; Ma, X.; Ma, L.; Zhang, Y.; Zhan, J., Hydrophobic W18O49 mesocrystal on hydrophilic PTFE membrane as an efficient solar steam generation device under one sun. *Journal of Materials Chemistry A* **2018**, *6* (23), 10939-10946.

130.   Li, T.; Liu, F.; Zhang, S.; Lin, H.; Wang, J.; Tang, C. Y., Janus Polyvinylidene Fluoride Membrane with Extremely Opposite Wetting Surfaces via One Single-Step Unidirectional Segregation Strategy. *ACS Applied Materials & Interfaces* **2018**, *10* (29), 24947-24954.

131.   Liu, Y.; Xiao, T.; Bao, C.; Fu, Y.; Yang, X., Fabrication of novel Janus membrane by nonsolvent thermally induced phase separation (NTIPS) for enhanced performance in membrane distillation. *Journal of Membrane Science* **2018**, *563*, 298-308.

132.   Song, H.-M.; Chen, C.; Shui, X.-X.; Yang, H.; Zhu, L.-J.; Zeng, Z.-X.; Xue, Q.-J., Asymmetric Janus membranes based on in situ mussel-inspired chemistry for efficient oil/water separation. *Journal of Membrane Science* **2019**, *573*, 126-134.

133.   Zhang, Y.; Barboiu, M., Dynameric asymmetric membranes for directional water transport. *Chemical Communications* **2015**, *51* (88), 15925-7.

134.   Zhang, Q.; Hu, Z.; Liu, Z.; Zhai, J.; Jiang, L., Light-Gating Titania/Alumina Heterogeneous Nanochannels with Regulable Ion Rectification Characteristic. *Advanced Functional Materials* **2014**, *24* (4), 424-431.

135.   Gao, J.; Guo, W.; Feng, D.; Wang, H.; Zhao, D.; Jiang, L., High-performance ionic diode membrane for salinity gradient power generation. *Journal of the American Chemical Society* **2014**, *136* (35), 12265-72.

136. Ma, S.; Liu, J.; Ye, Q.; Wang, D.; Liang, Y.; Zhou, F., A general approach for construction of asymmetric modification membranes for gated flow nanochannels. *Journal of Materials Chemistry A* **2014,** *2* (23), 8804-8814.

137. He, A.; Zhang, C.; Lv, Y.; Zhong, Q. Z.; Yang, X.; Xu, Z. K., Mussel-Inspired Coatings Directed and Accelerated by an Electric Field. *Macromolecular Rapid Communications* **2016,** *37* (17), 1460-5.

138. Sasaki, K.; Tenjimbayashi, M.; Manabe, K.; Shiratori, S., Asymmetric Superhydrophobic/Superhydrophilic Cotton Fabrics Designed by Spraying Polymer and Nanoparticles. *ACS Applied Materials & Interfaces* **2016,** *8* (1), 651-9.

139. Zhou, H.; Wang, H.; Niu, H.; Zeng, C.; Zhao, Y.; Xu, Z.; Fu, S.; Lin, T., One-Way Water-Transport Cotton Fabrics with Enhanced Cooling Effect. *Advanced Materials Interfaces* **2016,** *3* (17), 1600283.

140. Alf, M. E.; Asatekin, A.; Barr, M. C.; Baxamusa, S. H.; Chelawat, H.; Ozaydin-Ince, G.; Petruczok, C. D.; Sreenivasan, R.; Tenhaeff, W. E.; Trujillo, N. J.; Vaddiraju, S.; Xu, J.; Gleason, K. K., Chemical vapor deposition of conformal, functional, and responsive polymer films. *Advanced Materials* **2010,** *22* (18), 1993-2027.

141. Tian, X.; Jin, H.; Sainio, J.; Ras, R. H. A.; Ikkala, O., Droplet and Fluid Gating by Biomimetic Janus Membranes. *Advanced Functional Materials* **2014,** *24* (38), 6023-6028.

142. Yang, Q.; Lin, X.; Wang, Y.; Su, B., Nanochannels as molecular check valves. *Nanoscale* **2017,** *9* (46), 18523-18528.

143. Kalman, E. B.; Sudre, O.; Vlassiouk, I.; Siwy, Z. S., Control of ionic transport through gated single conical nanopores. *Analytical and Bioanalytical Chemistry* **2009,** *394* (2), 413-9.

144. Sheng, Q.; Wang, L.; Wang, C.; Wang, X.; Xue, J., Fabrication of nanofluidic diodes with polymer nanopores modified by atomic layer deposition. *Biomicrofluidics* **2014,** *8* (5), 052111.

145. Tufani, A.; Ozaydin Ince, G., Protein gating by vapor deposited Janus membranes. *Journal of Membrane Science* **2019,** *575*, 126-134.

146. Chen, J.; Liu, Y.; Guo, D.; Cao, M.; Jiang, L., Under-water unidirectional air penetration via a Janus mesh. *Chemical Communications* **2015,** *51* (59), 11872-5.

147. Wang, H.; Zhou, H.; Yang, W.; Zhao, Y.; Fang, J.; Lin, T., Selective, Spontaneous One-Way Oil-Transport Fabrics and Their Novel Use for Gauging Liquid Surface Tension. *ACS Applied Materials & Interfaces* **2015,** *7* (41), 22874-80.

148. Abraham, S.; Ma, G.; Montemagno, C. D., Janus Carbon Nanotube Membranes by Selective Surface Plasmoxidation. *Advanced Materials Interfaces* **2016,** *3* (18), 1600445.

149. Fu, Y.; Jiang, Y. B.; Dunphy, D.; Xiong, H.; Coker, E.; Chou, S. S.; Zhang, H.; Vanegas, J. M.; Croissant, J. G.; Cecchi, J. L.; Rempe, S. B.; Brinker, C. J., Ultra-thin enzymatic liquid membrane for CO2 separation and capture. *Nature Communications* **2018,** *9* (1), 990.

150. Ding, D.; Mao, H.; Chen, X.; Qiu, M.; Fan, Y., Underwater superoleophobic-underoil superhydrophobic Janus ceramic membrane with its switchable separation in oil/water emulsions. *Journal of Membrane Science* **2018,** *565*, 303-310.

151. Li, C.; Li, X.; Du, X.; Tong, T.; Cath, T. Y.; Lee, J., Antiwetting and Antifouling Janus Membrane for Desalination of Saline Oily Wastewater by Membrane Distillation. *ACS Applied Materials & Interfaces* **2019,** *11* (20), 18456-18465.

152. Yong, J.; Chen, F.; Huo, J.; Fang, Y.; Yang, Q.; Zhang, J.; Hou, X., Femtosecond laser induced underwater superaerophilic and superaerophobic PDMS sheets with through microholes for selective passage of air bubbles and further collection of underwater gas. *Nanoscale* **2018,** *10* (8), 3688-3696.

153. Gu, J.; Xiao, P.; Chen, J.; Zhang, J.; Huang, Y.; Chen, T., Janus polymer/carbon nanotube hybrid membranes for oil/water separation. *ACS Applied Materials & Interfaces* **2014,** *6* (18), 16204-9.

154. Wang, Z.; Wang, Y.; Liu, G., Rapid and Efficient Separation of Oil from Oil-in-Water Emulsions Using a Janus Cotton Fabric. *Angewandte Chemie International Edition in Englsih* **2016,** *55* (4), 1291-4.

155.   Yang, H. C.; Hou, J.; Wan, L. S.; Chen, V.; Xu, Z. K., Janus Membranes with Asymmetric Wettability for Fine Bubble Aeration. *Advanced Materials Interfaces* **2016,** *3* (9), 1500774.

156.   Yang, H.-C.; Zhong, W.; Hou, J.; Chen, V.; Xu, Z.-K., Janus hollow fiber membrane with a mussel-inspired coating on the lumen surface for direct contact membrane distillation. *Journal of Membrane Science* **2017,** *523,* 1-7.

157.   Lee, W.; Park, S. J., Porous anodic aluminum oxide: anodization and templated synthesis of functional nanostructures. *Chemical reviews* **2014,** *114* (15), 7487-556.

158.   Brilmayer, R.; Forster, C.; Zhao, L.; Andrieu-Brunsen, A., Recent trends in nanopore polymer functionalization. *Current Opinion in Biotechnology* **2020,** *63,* 200-209.

159.   Mutalib Md Jani, A.; Kempson, I. M.; Losic, D.; Voelcker, N. H., Dressing in layers: layering surface functionalities in nanoporous aluminum oxide membranes. *Angewandte Chemie International Edition in English* **2010,** *49* (43), 7933-7.

160.   Tagliazucchi, M.; Azzaroni, O.; Szleifer, I., Responsive Polymers End-Tethered in Solid-State Nanochannels: When Nanoconfinement Really Matters. *Journal of the American Chemical Society* **2010,** *132,* 12404–12411.

161.   Huang, K.; Szleifer, I., Design of Multifunctional Nanogate in Response to Multiple External Stimuli Using Amphiphilic Diblock Copolymer. *Journal of the American Chemical Society* **2017,** *139* (18), 6422-6430.

162.   Qin, S.; Huang, K.; Szleifer, I., Design of Multifunctional Nanopore Using Polyampholyte Brush with Composition Gradient. *ACS Nano* **2021**.

163.   Daniel, M. C.; Astruc, D., Gold nanoparticles: assembly, supramolecular chemistry, quantum-size-related properties, and applications toward biology, catalysis, and nanotechnology. *Chemical reviews* **2004,** *104* (1), 293-346.

164.   Zayats, M.; Baron, R.; Popov, I.; Willner, I., Biocatalytic growth of Au nanoparticles: from mechanistic aspects to biosensors design. *Nano Letters* **2005,** *5* (1), 21-5.

165.   Haick, H., Chemical sensors based on molecularly modified metallic nanoparticles. *Journal of Physics D: Applied Physics* **2007,** *40* (23), 7173-7186.

166.   Zhao, W.; Brook, M. A.; Li, Y., Design of gold nanoparticle-based colorimetric biosensing assays. *ChemBioChem* **2008,** *9* (15), 2363-71.

167.   Sperling, R. A.; Rivera Gil, P.; Zhang, F.; Zanella, M.; Parak, W. J., Biological applications of gold nanoparticles. *Chemical Society reviews* **2008,** *37* (9), 1896-908.

168.   Wilson, R., The use of gold nanoparticles in diagnostics and detection. *Chemical Society reviews* **2008,** *37* (9), 2028-45.

169.   Bunz, U. H.; Rotello, V. M., Gold nanoparticle-fluorophore complexes: sensitive and discerning "noses" for biosystems sensing. *Angewandte Chemie International Edition in English* **2010,** *49* (19), 3268-79.

170.   Zeng, S.; Yong, K.-T.; Roy, I.; Dinh, X.-Q.; Yu, X.; Luan, F., A Review on Functionalized Gold Nanoparticles for Biosensing Applications. *Plasmonics* **2011,** *6* (3), 491-506.

171.   Garcia, M. A., Surface plasmons in metallic nanoparticles: fundamentals and applications. *Journal of Physics D: Applied Physics* **2012,** *45* (38), 389501.

172.   Barnes, W. L.; Dereux, A.; Ebbesen, T. W., Surface plasmon subwavelength optics. *Nature* **2003,** *424* (6950), 824-30.

173.   Fritzsche, W.; Taton, T. A., Metal nanoparticles as labels for heterogeneous, chip-based DNA detection. *Nanotechnology* **2003,** *14* (12), R63-73.

174.   Hu, M.; Chen, J.; Li, Z. Y.; Au, L.; Hartland, G. V.; Li, X.; Marquez, M.; Xia, Y., Gold nanostructures: engineering their plasmonic properties for biomedical applications. *Chemical Society reviews* **2006,** *35* (11), 1084-94.

175.   Eustis, S.; el-Sayed, M. A., Why gold nanoparticles are more precious than pretty gold: noble metal surface plasmon resonance and its enhancement of the radiative and nonradiative properties of nanocrystals of different shapes. *Chemical Society reviews* **2006,** *35* (3), 209-17.

176.   Pillai, S.; Catchpole, K. R.; Trupke, T.; Green, M. A., Surface plasmon enhanced silicon solar cells. *Journal of Applied Physics* **2007,** *101* (9), 093105.

177.   Matheu, P.; Lim, S. H.; Derkacs, D.; McPheeters, C.; Yu, E. T., Metal and dielectric nanoparticle scattering for improved optical absorption in photovoltaic devices. *Applied Physics Letters* **2008,** *93* (11), 113108.

178.   Atwater, H. A.; Polman, A., Plasmonics for improved photovoltaic devices. *Nature Materials* **2010,** *9* (3), 205-13.

179.   Narayanan, R.; El-Sayed, M. A., Catalysis with transition metal nanoparticles in colloidal solution: nanoparticle shape dependence and stability. *The Journal of Physical Chemistry B* **2005,** *109* (26), 12663-76.

180.   Awazu, K.; Fujimaki, M.; Rockstuhl, C.; Tominaga, J.; Murakami, H.; Ohki, Y.; Yoshida, N.; Watanabe, T., A plasmonic photocatalyst consisting of silver nanoparticles embedded in titanium dioxide. *Journal of the American Chemical Society* **2008,** *130* (5), 1676-80.

181.   Larsson, E. M.; Langhammer, C.; Zoric, I.; Kasemo, B., Nanoplasmonic probes of catalytic reactions. *Science* **2009,** *326* (5956), 1091-4.

182.   Ozbay, E., Plasmonics: merging photonics and electronics at nanoscale dimensions. *Science* **2006,** *311* (5758), 189-93.

183.   Fleischmann, M.; Hendra, P. J.; McQuillan, A. J., Raman spectra of pyridine adsorbed at a silver electrode. *Chemical Physics Letters* **1974,** *26* (2), 163-166.

184.   Jeanmaire, D. L.; Van Duyne, R. P., Surface raman spectroelectrochemistry. *Journal of Electroanalytical Chemistry and Interfacial Electrochemistry* **1977,** *84* (1), 1-20.

185.   Albrecht, M. G.; Creighton, J. A., Anomalously intense Raman spectra of pyridine at a silver electrode. *Journal of the American Chemical Society* **1977,** *99* (15), 5215-5217.

186.   Sun, M.; Zhang, Z.; Zheng, H.; Xu, H., In-situ plasmon-driven chemical reactions revealed by high vacuum tip-enhanced Raman spectroscopy. *Scientific Reports* **2012,** *2,* 647.

187.   Baffou, G.; Quidant, R., Nanoplasmonics for chemistry. *Chemical Society reviews* **2014,** *43* (11), 3898-907.

188.   Henglein, A., Small-particle research: physicochemical properties of extremely small colloidal metal and semiconductor particles. *Chemical reviews* **2002,** *89* (8), 1861-1873.

189.   Nabika, H.; Takase, M.; Nagasawa, F.; Murakoshi, K., Toward Plasmon-Induced Photoexcitation of Molecules. *The Journal of Physical Chemistry Letters* **2010,** *1* (16), 2470-2487.

190.   Oubre, C.; Nordlander, P., Optical Properties of Metallodielectric Nanostructures Calculated Using the Finite Difference Time Domain Method. *The Journal of Physical Chemistry B* **2004,** *108* (46), 17740-17747.

191.   Atay, T.; Song, J.-H.; Nurmikko, A. V., Strongly Interacting Plasmon Nanoparticle Pairs: From Dipole−Dipole Interaction to Conductively Coupled Regime. *Nano Letters* **2004,** *4* (9), 1627-1631.

192.   Xu, H.; Aizpurua, J.; Kall, M.; Apell, P., Electromagnetic contributions to single-molecule sensitivity in surface-enhanced raman scattering. *Physical Review. E Statistical Physics, Plasmas, Fluids, and Related Interdisciplinary Topics* **2000,** *62* (3 Pt B), 4318-24.

193.   Hao, E.; Schatz, G. C., Electromagnetic fields around silver nanoparticles and dimers. *Journal of Chemical Physics* **2004,** *120* (1), 357-66.

194.   Hubert, C.; Rumyantseva, A.; Lerondel, G.; Grand, J.; Kostcheev, S.; Billot, L.; Vial, A.; Bachelot, R.; Royer, P.; Chang, S. H.; Gray, S. K.; Wiederrecht, G. P.; Schatz, G. C., Near-field photochemical imaging of noble metal nanostructures. *Nano Letters* **2005,** *5* (4), 615-9.

195.   Ueno, K.; Juodkazis, S.; Shibuya, T.; Yokota, Y.; Mizeikis, V.; Sasaki, K.; Misawa, H., Nanoparticle plasmon-assisted two-photon polymerization induced by incoherent excitation source. *Journal of the American Chemical Society* **2008,** *130* (22), 6928-9.

196.   Juan, M. L.; Plain, J.; Bachelot, R.; Vial, A.; Royer, P.; Gray, S. K.; Montgomery, J. M.; Wiederrecht, G. P., Plasmonic electromagnetic hot spots temporally addressed by photoinduced molecular displacement. *The Journal of Physical Chemistry A* **2009,** *113* (16), 4647-51.

197.   Galarreta, B. C.; Rupar, I.; Young, A.; Lagugné-Labarthet, F., Mapping Hot-Spots in Hexagonal Arrays of Metallic Nanotriangles with Azobenzene Polymer Thin Films. *The Journal of Physical Chemistry C* **2011,** *115* (31), 15318-15323.

198.	König, T.; Nataraja Sekhar, Y.; Santer, S., Surface plasmon nanolithography: impact of dynamically varying near-field boundary conditions at the air–polymer interface. *Journal of Materials Chemistry* **2012,** *22* (13), 5945.

199.	Sundaramurthy, A.; Schuck, P. J.; Conley, N. R.; Fromm, D. P.; Kino, G. S.; Moerner, W. E., Toward nanometer-scale optical photolithography: utilizing the near-field of bowtie optical nanoantennas. *Nano Letters* **2006,** *6* (3), 355-60.

200.	Ueno, K.; Misawa, H., Surface plasmon-enhanced photochemical reactions. *Journal of Photochemistry and Photobiology C: Photochemistry Reviews* **2013,** *15*, 31-52.

201.	Yokoyama, T.; Masuhara, A.; Onodera, T.; Kasai, H.; Oikawa, H., Plasmon-Enhanced Photopolymerization of SU-8 on Rough Gold Surfaces. *The Journal of Physical Chemistry C* **2010,** *114* (46), 19596-19599.

202.	Tsuboi, Y.; Shimizu, R.; Shoji, T.; Kitamura, N., Near-infrared continuous-wave light driving a two-photon photochromic reaction with the assistance of localized surface plasmon. *Journal of the American Chemical Society* **2009,** *131* (35), 12623-7.

203.	Nishi, H.; Asahi, T.; Kobatake, S., Enhanced One-Photon Cycloreversion Reaction of Diarylethenes near Individual Gold Nanoparticles. *The Journal of Physical Chemistry C* **2011,** *115* (11), 4564-4570.

204.	Cumpston, B. H.; Ananthavel, S. P.; Barlow, S.; Dyer, D. L.; Ehrlich, J. E.; Erskine, L. L.; Heikal, A. A.; Kuebler, S. M.; Lee, I. Y. S.; McCord-Maughon, D.; Qin, J.; Röckel, H.; Rumi, M.; Wu, X.-L.; Marder, S. R.; Perry, J. W., Two-photon polymerization initiators for three-dimensional optical data storage and microfabrication. *Nature* **1999,** *398* (6722), 51-54.

205.	Sun, H.-B.; Matsuo, S.; Misawa, H., Three-dimensional photonic crystal structures achieved with two-photon-absorption photopolymerization of resin. *Applied Physics Letters* **1999,** *74* (6), 786-788.

206.	Kawata, S.; Sun, H. B.; Tanaka, T.; Takada, K., Finer features for functional microdevices. *Nature* **2001,** *412* (6848), 697-8.

207.	Srituravanich, W.; Fang, N.; Sun, C.; Luo, Q.; Zhang, X., Plasmonic Nanolithography. *Nano Letters* **2004,** *4* (6), 1085-1088.

208.	Ueno, K.; Takabatake, S.; Nishijima, Y.; Mizeikis, V.; Yokota, Y.; Misawa, H., Nanogap-Assisted Surface Plasmon Nanolithography. *The Journal of Physical Chemistry Letters* **2010,** *1* (3), 657-662.

209.	Dostert, K. H.; Alvarez, M.; Koynov, K.; del Campo, A.; Butt, H. J.; Kreiter, M., Near field guided chemical nanopatterning. *Langmuir : the ACS journal of surfaces and colloids* **2012,** *28* (8), 3699-703.

210.	Galloway, C. M.; Kreuzer, M. P.; Acimovic, S. S.; Volpe, G.; Correia, M.; Petersen, S. B.; Neves-Petersen, M. T.; Quidant, R., Plasmon-assisted delivery of single nano-objects in an optical hot spot. *Nano Letters* **2013,** *13* (9), 4299-304.

211.	Goerlitzer, E. S. A.; Speichermann, L. E.; Mirza, T. A.; Mohammadi, R.; Vogel, N., Addressing the plasmonic hotspot region by site-specific functionalization of nanostructures. *Nanoscale Advances* **2020,** *2* (1), 394-400.

212.	Nguyen, M.; Lamouri, A.; Salameh, C.; Levi, G.; Grand, J.; Boubekeur-Lecaque, L.; Mangeney, C.; Felidj, N., Plasmon-mediated chemical surface functionalization at the nanoscale. *Nanoscale* **2016,** *8* (16), 8633-40.

213.	Nguyen, M.; Kherbouche, I.; Gam-Derouich, S.; Ragheb, I.; Lau-Truong, S.; Lamouri, A.; Levi, G.; Aubard, J.; Decorse, P.; Felidj, N.; Mangeney, C., Regioselective surface functionalization of lithographically designed gold nanorods by plasmon-mediated reduction of aryl diazonium salts. *Chemical Communications* **2017,** *53* (82), 11364-11367.

214.	Tijunelyte, I.; Kherbouche, I.; Gam-Derouich, S.; Nguyen, M.; Lidgi-Guigui, N.; de la Chapelle, M. L.; Lamouri, A.; Levi, G.; Aubard, J.; Chevillot-Biraud, A.; Mangeney, C.; Felidj, N., Multi-functionalization of lithographically designed gold nanodisks by plasmon-mediated reduction of aryl diazonium salts. *Nanoscale Horizons* **2018,** *3* (1), 53-57.

215.	Kameche, F.; Heni, W.; Telitel, S.; Vidal, L.; Marguet, S.; Douillard, L.; Fiorini-Debuisschert, C.; Bachelot, R.; Soppera, O., Probing Plasmon-Induced Chemical Mechanisms by

Free-Radical Nanophotopolymerization. *The Journal of Physical Chemistry C* **2021,** *125* (16), 8719-8731.

216. Kameche, F.; Heni, W.; Telitel, S.; Ge, D.; Vidal, L.; Dumur, F.; Gigmes, D.; Lalevée, J.; Marguet, S.; Douillard, L.; Fiorini-Debuisschert, C.; Bachelot, R.; Soppera, O., Plasmon-triggered living photopolymerization for elaboration of hybrid polymer/metal nanoparticles. *Materials Today* **2020,** *40*, 38.

217. Bellino, M. G.; Regazzoni, A. E.; Soler-Illia, G. J., Amylase-functionalized mesoporous silica thin films as robust biocatalyst platforms. *ACS Appl Mater Interfaces* **2010,** *2* (2), 360-5.

218. Dunphy, D. R.; Sheth, P. H.; Garcia, F. L.; Brinker, C. J., Enlarged Pore Size in Mesoporous Silica Films Templated by Pluronic F127: Use of Poloxamer Mixtures and Increased Template/SiO2 Ratios in Materials Synthesized by Evaporation-Induced Self-Assembly. *Chemistry of Materials* **2014,** *27* (1), 75-84.

219. Sing, K. S. W., Reporting physisorption data for gas/solid systems with special reference to the determination of surface area and porosity (Recommendations 1984). *Pure and Applied Chemistry* **1985,** *57* (4), 603-619.

220. Hoffmann, F.; Cornelius, M.; Morell, J.; Froba, M., Silica-based mesoporous organic-inorganic hybrid materials. *Angewandte Chemie International Edition in English* **2006,** *45* (20), 3216-51.

221. Lin, C. C. H.; Dambrowitz, K. A.; Kuznicki, S. M., Evolving applications of zeolite molecular sieves. *The Canadian Journal of Chemical Engineering* **2012,** *90* (2), 207-216.

222. Chen, L. H.; Sun, M. H.; Wang, Z.; Yang, W.; Xie, Z.; Su, B. L., Hierarchically Structured Zeolites: From Design to Application. *Chemical reviews* **2020,** *120* (20), 11194-11294.

223. Beck, J. S., A New Family of Mesoporous Molecular Sieves Prepared with Liquid Crystal Templates. *Journal of the American Chemical Society* **1992,** *114*, 10834-10843.

224. Kresge, C. T.; Leonowicz, M. E.; Roth, W. J.; Vartuli, J. C.; Beck, J. S., Ordered Mesoporous Molecular-Sieves Synthesized by a Liquid-Crystal Template Mechanism. *Nature* **1992,** *359* (6397), 710-712.

225. Zhao, D.; Huo, Q.; Feng, J.; Chmelka, B. F.; Stucky, G. D., *Journal of The American Chemical Society* **1998,** *120*, 6024-6036.

226. Innocenzi, P.; Malfatti, L., Mesoporous thin films: properties and applications. *Chemical Society reviews* **2013,** *42* (9), 4198-216.

227. Walcarius, A.; Sibottier, E.; Etienne, M.; Ghanbaja, J., Electrochemically assisted self-assembly of mesoporous silica thin films. *Nature Materials* **2007,** *6* (8), 602-8.

228. Brinker, C. J.; Lu, Y. F.; Sellinger, A.; Fan, H. Y., Evaporation-induced self-assembly: Nanostructures made easy. *Advanced Materials* **1999,** *11* (7), 579-585.

229. Boissière, C.; Larbot, A.; Bourgaux, C.; Prouzet, E.; Bunton, C. A., A Study of the Assembly Mechanism of the Mesoporous MSU-X Silica Two-Step Synthesis. *Chemistry of Materials* **2001,** *13* (10), 3580-3586.

230. Schubert, U., Sol-Gel-Chemie. *Chemie in unserer Zeit* **2018,** *52* (1), 18-25.

231. Soler-Illia, G. J. d. A. A.; Crepaldi, E. L.; Grosso, D.; Sanchez, C., Block copolymer-templated mesoporous oxides. *Current Opinion in Colloid & Interface Science* **2003,** *8* (1), 109-126.

232. Grosso, D.; Cagnol, F.; Soler-Illia, G. J. D. A.; Crepaldi, E. L.; Amenitsch, H.; Brunet-Bruneau, A.; Bourgeois, A.; Sanchez, C., Fundamentals of mesostructuring through evaporation-induced self-assembly. *Advanced Functional Materials* **2004,** *14* (4), 309-322.

233. Grosso, D.; Babonneau, F.; Sanchez, C.; Soler-Illia, G. J. D. A.; Crepaldi, E. L.; Albouy, P. A.; Amenitsch, H.; Balkenende, A. R.; Brunet-Bruneau, A., A first insight in the mechanisms involved in the self-assembly of 2D-hexagonal templated SiO2 and TiO2 mesostructured films during dip-coating. *Journal of Sol-Gel Science and Technology* **2003,** *26* (1-3), 561-565.

234. Choi, S. Y.; Mamak, M.; von Freymann, G.; Chopra, N.; Ozin, G. A., Mesoporous bragg stack color tunable sensors. *Nano Letters* **2006,** *6* (11), 2456-61.

235.   Yang, P.; Zhao, D.; Margolese, D. I.; Chmelka, B. F.; Stucky, G. D., Generalized syntheses of large-pore mesoporous metal oxides with semicrystalline frameworks. *Nature* **1998,** *396* (6707), 152-155.

236.   Bruhwiler, D., Postsynthetic functionalization of mesoporous silica. *Nanoscale* **2010,** *2* (6), 887-92.

237.   Ritter, H.; Nieminen, M.; Karppinen, M.; Brühwiler, D., A comparative study of the functionalization of mesoporous silica MCM-41 by deposition of 3-aminopropyltrimethoxysilane from toluene and from the vapor phase. *Microporous and Mesoporous Materials* **2009,** *121* (1-3), 79-83.

238.   Khalil, A.; Zimmermann, M.; Bell, A. K.; Kunz, U.; Hardt, S.; Kleebe, H. J.; Stark, R. W.; Stephan, P.; Andrieu-Brunsen, A., Insights into the interplay of wetting and transport in mesoporous silica films. *Journal of Colloid and Interface Science* **2020,** *560*, 369-378.

239.   Baccile, N.; Reboul, J.; Blanc, B.; Coq, B.; Lacroix-Desmazes, P.; In, M.; Gerardin, C., Ecodesign of ordered mesoporous materials obtained with switchable micellar assemblies. *Angewandte Chemie International Edition in English* **2008,** *47* (44), 8433-7.

240.   Molina, E.; Warnant, J.; Mathonnat, M.; Bathfield, M.; In, M.; Laurencin, D.; Jerome, C.; Lacroix-Desmazes, P.; Marcotte, N.; Gerardin, C., Drug-Polymer Electrostatic Complexes as New Structuring Agents for the Formation of Drug-Loaded Ordered Mesoporous Silica. *Langmuir : the ACS journal of surfaces and colloids* **2015,** *31* (47), 12839-44.

241.   Bathfield, M.; Warnant, J.; Gérardin, C.; Lacroix-Desmazes, P., Asymmetric neutral, cationic and anionic PEO-based double-hydrophilic block copolymers (DHBCs): synthesis and reversible micellization triggered by temperature or pH. *Polymer Chemistry* **2015,** *6* (8), 1339-1349.

242.   Bathfield, M.; Reboul, J.; Cacciaguerra, T.; Lacroix-Desmazes, P.; Gérardin, C., Thermosensitive and Drug-Loaded Ordered Mesoporous Silica: A Direct and Effective Synthesis Using PEO-b-PNIPAM Block Copolymers. *Chemistry of Materials* **2016,** *28* (10), 3374-3384.

243.   Houssein, D.; Warnant, J.; Molina, E.; Cacciaguerra, T.; Gérardin, C.; Marcotte, N., Mesoporous silica templated by polyion complex micelles: A versatile approach for controlling the mesostructure. *Microporous and Mesoporous Materials* **2017,** *239*, 244-252.

244.   Molina, E.; Mathonnat, M.; Richard, J.; Lacroix-Desmazes, P.; In, M.; Dieudonne, P.; Cacciaguerra, T.; Gerardin, C.; Marcotte, N., pH-mediated control over the mesostructure of ordered mesoporous materials templated by polyion complex micelles. *Beilstein Journal of Nanotechnology* **2019,** *10*, 144-156.

245.   Tom, J. C.; Appel, C.; Andrieu-Brunsen, A., Fabrication and in situ functionalisation of mesoporous silica films by the physical entrapment of functional and responsive block copolymer structuring agents. *Soft Matter* **2019,** *15* (40), 8077-8083.

246.   Herzog, N.; Hubner, H.; Ruttiger, C.; Gallei, M.; Andrieu-Brunsen, A., Functional Metalloblock Copolymers for the Preparation and In Situ Functionalization of Porous Silica Films. *Langmuir : the ACS journal of surfaces and colloids* **2020,** *36* (15), 4015-4024.

247.   Schüth, F., Engineered Porous Catalytic Materials. *Annual Review of Materials Research* **2005,** *35* (1), 209-238.

248.   Widenmeyer, M.; Anwander, R., Pore Size Control of Highly Ordered Mesoporous Silica MCM-48. *Chemistry of Materials* **2002,** *14* (4), 1827-1831.

249.   Nicole, L.; Boissiere, C.; Grosso, D.; Quach, A.; Sanchez, C., Mesostructured hybrid organic-inorganic thin films. *Journal of Materials Chemistry* **2005,** *15* (35-36), 3598-3627.

250.   Lim, M. H.; Stein, A., Comparative studies of grafting and direct syntheses of inorganic-organic hybrid mesoporous materials. *Chemistry of Materials* **1999,** *11* (11), 3285-3295.

251.   Franceschini, E. A.; Llave, E. d. l.; Williams, F. J.; Soler-Illia, G. J. A. A., A simple three step method for selective placement of organic groups in mesoporous silica thin films. *Materials Chemistry and Physics* **2016,** *169*, 82-88.

252.   Babu, D. J.; Yadav, S.; Heinlein, T.; Cherkashinin, G.; Schneider, J. J., Carbon Dioxide Plasma as a Versatile Medium for Purification and Functionalization of Vertically Aligned Carbon Nanotubes. *The Journal of Physical Chemistry C* **2014,** *118* (22), 12028-12034.

253.	Walcarius, A.; Delacôte, C., Rate of Access to the Binding Sites in Organically Modified Silicates. 3. Effect of Structure and Density of Functional Groups in Mesoporous Solids Obtained by the Co-Condensation Route. *Chemistry of Materials* **2003,** *15* (22), 4181-4192.

254.	Wang, X.; Lin, K. S.; Chan, J. C.; Cheng, S., Direct synthesis and catalytic applications of ordered large pore aminopropyl-functionalized SBA-15 mesoporous materials. *The Journal of Physical Chemistry B* **2005,** *109* (5), 1763-9.

255.	Gaslain, F. O. M.; Delacôte, C.; Walcarius, A.; Lebeau, B., One-step preparation of thiol-modified mesoporous silica spheres with various functionalization levels and different pore structures. *Journal of Sol-Gel Science and Technology* **2008,** *49* (1), 112-124.

256.	Calvo, A.; Joselevich, M.; Soler-Illia, G. J. A. A.; Williams, F. J., Chemical reactivity of amino-functionalized mesoporous silica thin films obtained by co-condensation and post-grafting routes. *Microporous Mesoporous Mater.* **2009,** *121* (1-3), 67-72.

257.	Kobayashi, T.; Singappuli-Arachchige, D.; Wang, Z.; Slowing, II; Pruski, M., Spatial distribution of organic functional groups supported on mesoporous silica nanoparticles: a study by conventional and DNP-enhanced (29)Si solid-state NMR. *Physical Chemistry Chemical Physics* **2017,** *19* (3), 1781-1789.

258.	Yang, Q.; Liu, J.; Zhang, L.; Li, C., Functionalized periodic mesoporous organosilicas for catalysis. *Journal of Materials Chemistry* **2009,** *19* (14), 1945.

259.	Ghaedi, H.; Zhao, M., Review on Template Removal Techniques for Synthesis of Mesoporous Silica Materials. *Energy & Fuels* **2022**.

260.	Zoppe, J. O.; Ataman, N. C.; Mocny, P.; Wang, J.; Moraes, J.; Klok, H. A., Surface-Initiated Controlled Radical Polymerization: State-of-the-Art, Opportunities, and Challenges in Surface and Interface Engineering with Polymer Brushes. *Chemical reviews* **2017,** *117* (3), 1105-1318.

261.	Chen, Q.; Salami-Kalajahi, M., Surface-Initiated Ring-Opening Metathesis Polymerization (SI-ROMP): History, General Features, and Applications in Surface Engineering with Polymer Brushes. *International Journal of Polymer Science* **2021,** *2021*, 1-15.

262.	Lejars, M.; Margaillan, A.; Bressy, C., Fouling release coatings: a nontoxic alternative to biocidal antifouling coatings. *Chemical reviews* **2012,** *112* (8), 4347-90.

263.	Moad, G.; Rizzardo, E.; Thang, S. H., Living Radical Polymerization by the RAFT Process - A Third Update. *Australian Journal of Chemistry* **2012,** *65* (8), 985.

264.	Henze, M.; Mädge, D.; Prucker, O.; Rühe, J., "Grafting Through": Mechanistic Aspects of Radical Polymerization Reactions with Surface-Attached Monomers. *Macromolecules* **2014,** *47* (9), 2929-2937.

265.	Barbey, R.; Lavanant, L.; Paripovic, D.; Schuwer, N.; Sugnaux, C.; Tugulu, S.; Klok, H. A., Polymer brushes via surface-initiated controlled radical polymerization: synthesis, characterization, properties, and applications. *Chemical reviews* **2009,** *109* (11), 5437-527.

266.	Fristrup, C. J.; Jankova, K.; Hvilsted, S., Surface-initiated atom transfer radical polymerization—a technique to develop biofunctional coatings. *Soft Matter* **2009,** *5* (23), 4623.

267.	Xu, F. J.; Neoh, K. G.; Kang, E. T., Bioactive surfaces and biomaterials via atom transfer radical polymerization. *Progress in Polymer Science* **2009,** *34* (8), 719-761.

268.	Hui, C. M.; Pietrasik, J.; Schmitt, M.; Mahoney, C.; Choi, J.; Bockstaller, M. R.; Matyjaszewski, K., Surface-Initiated Polymerization as an Enabling Tool for Multifunctional (Nano-)Engineered Hybrid Materials. *Chemistry of Materials* **2013,** *26* (1), 745-762.

269.	Banerjee, S.; Paira, T. K.; Mandal, T. K., Surface confined atom transfer radical polymerization: access to custom library of polymer-based hybrid materials for speciality applications. *Polymer Chemistry* **2014,** *5* (14), 4153.

270.	Matyjaszewski, K.; Dong, H.; Jakubowski, W.; Pietrasik, J.; Kusumo, A., Grafting from surfaces for "everyone": ARGET ATRP in the presence of air. *Langmuir : the ACS journal of surfaces and colloids* **2007,** *23* (8), 4528-31.

271.	Barner-Kowollik, C.; Davis, T. P.; Heuts, J. P. A.; Stenzel, M. H.; Vana, P.; Whittaker, M., RAFTing down under: Tales of missing radicals, fancy architectures, and mysterious holes. *Journal of Polymer Science Part A: Polymer Chemistry* **2003,** *41* (3), 365-375.

272.   Matyjaszewski, K.; Gnanou, Y.; Leibler, L. In *Macromolecular Engineering: From Precise Macromolecular Synthesis to Macroscopic Materials Properties and Applications aims to provide a broad overview of recent developments in precision macromolecular synthesis and in the design and ap- plications of complex polymeric assemblies of controlled size,* **2007**.

273.   Oster, G., Dye-Sensitized Photopolymerization. *Nature* **1954,** *173* (4398), 300-301.

274.   Rubens, M.; Latsrisaeng, P.; Junkers, T., Visible light-induced iniferter polymerization of methacrylates enhanced by continuous flow. *Polymer Chemistry* **2017,** *8* (42), 6496-6505.

275.   Gruber, H. F., Photoinitiators for free radical polymerization. *Progress in Polymer Science* **1992,** *17* (6), 953-1044.

276.   Carlini, C.; Angiolini, L.; Caretti, D.; Corelli, E., Recent Advances on Photosensitive Polymers: Polymeric Photoinitiators. *Polymers for Advanced Technologies* **1996,** *7* (5-6), 379-384.

277.   Pan, X.; Tasdelen, M. A.; Laun, J.; Junkers, T.; Yagci, Y.; Matyjaszewski, K., Photomediated controlled radical polymerization. *Progress in Polymer Science* **2016,** *62,* 73-125.

278.   Fouassier, J. P.; Lalevee, J., *Photoinitiators for Polymer Synthesis*. WILEY-VCH: 2012.

279.   Otsu, T.; Yoshida, M.; Tazaki, T., A model for living radical polymerization. *Die Makromolekulare Chemie, Rapid Communications* **1982,** *3* (2), 133-140.

280.   Otsu, T.; Matsunaga, T.; Doi, T.; Matsumoto, A., Features of living radical polymerization of vinyl monomers in homogeneous system using N,N-diethyldithiocarbamate derivatives as photoiniferters. *European Polymer Journal* **1995,** *31* (1), 67-78.

281.   Xiao, P.; Zhang, J.; Dumur, F.; Tehfe, M. A.; Morlet-Savary, F.; Graff, B.; Gigmes, D.; Fouassier, J. P.; Lalevée, J., Visible light sensitive photoinitiating systems: Recent progress in cationic and radical photopolymerization reactions under soft conditions. *Progress in Polymer Science* **2015,** *41,* 32-66.

282.   Dietlin, C.; Schweizer, S.; Xiao, P.; Zhang, J.; Morlet-Savary, F.; Graff, B.; Fouassier, J.-P.; Lalevée, J., Photopolymerization upon LEDs: new photoinitiating systems and strategies. *Polymer Chemistry* **2015,** *6* (21), 3895-3912.

283.   Tasdelen, M. A.; Yagci, Y., Photochemical Methods for the Preparation of Complex Linear and Cross-linked Macromolecular Structures. *Australien Journal of Chemistry* **2011,** *64* (8), 982.

284.   Moad, G.; Rizzardo, E.; Thang, S. H., Living radical polymerization by the RAFT process - A first update. *Australian Journal of Chemistry* **2006,** *59* (10), 669-692.

285.   de Boer, B.; Simon, H. K.; Werts, M. P. L.; van der Vegte, E. W.; Hadziioannou, G., "Living" Free Radical Photopolymerization Initiated from Surface-Grafted Iniferter Monolayers. *Macromolecules* **2000,** *33* (2), 349-356.

286.   John, D.; Mohammadi, R.; Vogel, N.; Andrieu-Brunsen, A., Surface-Plasmon- and Green-Light-Induced Polymerization in Mesoporous Thin Silica Films. *Langmuir : the ACS journal of surfaces and colloids* **2020,** *36* (7), 1671-1679.

287.   Kim, D.; Scranton, A. B.; Stansbury, J. W., Effect of the electron donor structure on the shelf-lifetime of visible-light activated three-component initiator systems. *Journal of Applied Polymer Science* **2009,** *114* (3), 1535-1542.

288.   Avens, H. J.; Bowman, C. N., Mechanism of Cyclic Dye Regeneration During Eosin-Sensitized Photoinitiation in the Presence of Polymerization Inhibitors. *Journal of Polymer Science Part A: Polymer Chemistry* **2009,** *47* (22), 6083-6094.

289.   Angelini, I.; Artioli, G.; Bellintani, P.; Diella, V.; Gemmi, M.; Polla, A.; Rossi, A., Chemical analyses of Bronze Age glasses from Frattesina di Rovigo, Northern Italy. *Journal of Archaeological Science* **2004,** *31* (8), 1175-1184.

290.   Barber, D. J.; Freestone, I. C., An Investigation of the Origin of the Colour of the Lycurgus Cup by Analytical Transmission Electron Microscopy. *Archaeometry* **1990,** *32* (1), 33-45.

291.   Freestone, I.; Meeks, N.; Sax, M.; Higgitt, C., The Lycurgus Cup — A Roman nanotechnology. *Gold Bulletin* **2007,** *40* (4), 270-277.

292. Jose-Yacaman, M.; Rendon, L.; Arenas, J.; Serra Puche, M. C., Maya Blue Paint: An Ancient Nanostructured Material. *Science* **1996**, *273* (5272), 223-5.

293. Colomban, P.; Truong, C., Non-destructive Raman study of the glazing technique in lustre potteries and faience(9–14th centuries): silver ions, nanoclusters, microstructure and processing. *Journal of Raman Spectroscopy* **2004**, *35* (3), 195-207.

294. Brun, N.; Mazerolles, L.; Pernot, M., Microstructure of opaque red glass containing copper. *Journal of Materials Science Letters* **1991**, *10* (23), 1418-1420.

295. Nakai, I.; Numako, C.; Hosono, H.; Yamasaki, K., Origin of the Red Color of Satsuma Copper-Ruby Glass as Determined by EXAFS and Optical Absorption Spectroscopy. *Journal of the American Ceramic Society* **2004**, *82* (3), 689-695.

296. Wood, N., *Chinese Glazes*. University of Pennsylvania Press: Philadelphia, 1999.

297. Saha, K.; Agasti, S. S.; Kim, C.; Li, X.; Rotello, V. M., Gold nanoparticles in chemical and biological sensing. *Chemical reviews* **2012**, *112* (5), 2739-79.

298. Capek, I., Polymer decorated gold nanoparticles in nanomedicine conjugates. *Adv Colloid Interface Sci* **2017**, *249*, 386-399.

299. Huang, X.; El-Sayed, M. A., Gold nanoparticles: Optical properties and implementations in cancer diagnosis and photothermal therapy. *Journal of Advanced Research* **2010**, *1* (1), 13-28.

300. Mie, G., Beiträge zur Optik trüber Medien, speziell kolloidaler Metallösungen. *Annalen der Physik* **1908**, *25*, 377.

301. Link, S.; El-Sayed, M. A., Optical properties and ultrafast dynamics of metallic nanocrystals. *Annual Review of Physical Chemistry* **2003**, *54*, 331-66.

302. Jain, P. K.; Huang, X.; El-Sayed, I. H.; El-Sayed, M. A., Noble metals on the nanoscale: optical and photothermal properties and some applications in imaging, sensing, biology, and medicine. *Accounts of chemical research* **2008**, *41* (12), 1578-86.

303. Halas, N. J.; Lal, S.; Chang, W. S.; Link, S.; Nordlander, P., Plasmons in strongly coupled metallic nanostructures. *Chemical reviews* **2011**, *111* (6), 3913-61.

304. Kelly, K. L.; Coronado, E.; Zhao, L. L.; Schatz, G. C., The Optical Properties of Metal Nanoparticles: The Influence of Size, Shape, and Dielectric Environment. *The Journal of Physical Chemistry B* **2002**, *107* (3), 668-677.

305. Nishi, H.; Torimoto, T.; Tatsuma, T., Wavelength- and efficiency-tunable plasmon-induced charge separation by the use of Au-Ag alloy nanoparticles. *Physical Chemistry Chemical Physics* **2015**, *17* (6), 4042-6.

306. Amendola, V.; Meneghetti, M., Size Evaluation of Gold Nanoparticles by UV−vis Spectroscopy. *The Journal of Physical Chemistry C* **2009**, *113* (11), 4277-4285.

307. Amendola, V.; Saija, R.; Marago, O. M.; Iati, M. A., Superior plasmon absorption in iron-doped gold nanoparticles. *Nanoscale* **2015**, *7* (19), 8782-92.

308. Sonnichsen, C.; Franzl, T.; Wilk, T.; von Plessen, G.; Feldmann, J.; Wilson, O.; Mulvaney, P., Drastic reduction of plasmon damping in gold nanorods. *Physical Review Letters* **2002**, *88* (7), 077402.

309. Olson, J.; Dominguez-Medina, S.; Hoggard, A.; Wang, L. Y.; Chang, W. S.; Link, S., Optical characterization of single plasmonic nanoparticles. *Chemical Society reviews* **2015**, *44* (1), 40-57.

310. Scholl, J. A.; Garcia-Etxarri, A.; Koh, A. L.; Dionne, J. A., Observation of quantum tunneling between two plasmonic nanoparticles. *Nano Letters* **2013**, *13* (2), 564-9.

311. Nicoletti, O.; de la Pena, F.; Leary, R. K.; Holland, D. J.; Ducati, C.; Midgley, P. A., Three-dimensional imaging of localized surface plasmon resonances of metal nanoparticles. *Nature* **2013**, *502* (7469), 80-4.

312. Atre, A. C.; Brenny, B. J.; Coenen, T.; Garcia-Etxarri, A.; Polman, A.; Dionne, J. A., Nanoscale optical tomography with cathodoluminescence spectroscopy. *Nature Nanotechnology* **2015**, *10* (5), 429-36.

313. Losquin, A.; Zagonel, L. F.; Myroshnychenko, V.; Rodriguez-Gonzalez, B.; Tence, M.; Scarabelli, L.; Forstner, J.; Liz-Marzan, L. M.; Garcia de Abajo, F. J.; Stephan, O.; Kociak, M.,

Unveiling nanometer scale extinction and scattering phenomena through combined electron energy loss spectroscopy and cathodoluminescence measurements. *Nano Letters* **2015,** *15* (2), 1229-37.

314.   Faraday, M., Preparation of colloidal gold. *Philos. Trans. R. Soc. London* **1857,** *147,* 145.

315.   Turkevich, J.; Stevenson, P. C.; Hillier, J., A study of the nucleation and growth processes in the synthesis of colloidal gold. *Discussions of the Faraday Society* **1951,** *11,* 55.

316.   Frens, G., Controlled Nucleation for the Regulation of the Particle Size in Monodisperse Gold Suspensions. *Nature Physical Science* **1973,** *241* (105), 20-22.

317.   Chow, M. K.; Zukoski, C. F., Gold Sol Formation Mechanisms: Role of Colloidal Stability. *Journal of Colloid and Interface Science* **1994,** *165* (1), 97-109.

318.   Xia, Y. N.; Yang, P. D.; Sun, Y. G.; Wu, Y. Y.; Mayers, B.; Gates, B.; Yin, Y. D.; Kim, F.; Yan, Y. Q., One-dimensional nanostructures: Synthesis, characterization, and applications. *Advanced Materials* **2003,** *15* (5), 353-389.

319.   Hao, E.; Schatz, G. C.; Hupp, J. T., Synthesis and Optical Properties of Anisotropic Metal Nanoparticles. *Journal of Fluorescence* **2004,** *14* (4), 331-341.

320.   Murphy, C. J.; Sau, T. K.; Gole, A. M.; Orendorff, C. J.; Gao, J.; Gou, L.; Hunyadi, S. E.; Li, T., Anisotropic metal nanoparticles: Synthesis, assembly, and optical applications. *The Journal of Physical Chemistry B* **2005,** *109* (29), 13857-70.

321.   Cushing, B. L.; Kolesnichenko, V. L.; O'Connor, C. J., Recent advances in the liquid-phase syntheses of inorganic nanoparticles. *Chemical reviews* **2004,** *104* (9), 3893-946.

322.   Serrano-Montes, A. B.; Jimenez de Aberasturi, D.; Langer, J.; Giner-Casares, J. J.; Scarabelli, L.; Herrero, A.; Liz-Marzan, L. M., A General Method for Solvent Exchange of Plasmonic Nanoparticles and Self-Assembly into SERS-Active Monolayers. *Langmuir : the ACS journal of surfaces and colloids* **2015,** *31* (33), 9205-13.

323.   Kang, H.; Buchman, J. T.; Rodriguez, R. S.; Ring, H. L.; He, J.; Bantz, K. C.; Haynes, C. L., Stabilization of Silver and Gold Nanoparticles: Preservation and Improvement of Plasmonic Functionalities. *Chemical reviews* **2019,** *119* (1), 664-699.

324.   Roskamp, M. Oberflächenfunktionalisierung von Nanopartikeln zur gezielten Wechselwirkung mit Biomolekülen. Freie Universität Berlin, Berlin, 2010.

325.   Mabbott, G. A., An introduction to cyclic voltammetry. *Journal of Chemical Education* **1983,** *60* (9), 697.

326.   Elgrishi, N.; Rountree, K. J.; McCarthy, B. D.; Rountree, E. S.; Eisenhart, T. T.; Dempsey, J. L., A Practical Beginner's Guide to Cyclic Voltammetry. *Journal of Chemical Education* **2017,** *95* (2), 197-206.

327.   Walcarius, A., Mesoporous materials and electrochemistry. *Chemical Society Reviews* **2013,** *42* (9), 4098-140.

328.   Steinberg, P. Y.; Zanotto, F. M.; Soler-Illia, G. J. A. A.; Dassie, S. A.; Angelomé, P. C., Molecular Transport through TiO2 Mesoporous Thin Films: Correlation with the Partially Blocked Electrode Model. *The Journal of Physical Chemistry C* **2021,** *125* (42), 23521-23532.

329.   Gueshi, T.; Tokuda, K.; Matsuda, H., Voltammetry at partially covered electrodes. *Journal of Electroanalytical Chemistry and Interfacial Electrochemistry* **1979,** *101* (1), 29-38.

330.   Wei, T. C.; Hillhouse, H. W., Mass transport and electrode accessibility through periodic self-assembled nanoporous silica thin films. *Langmuir : the ACS journal of surfaces and colloids* **2007,** *23* (10), 5689-99.

331.   Etienne, M.; Walcarius, A., Evaporation induced self-assembly of templated silica and organosilica thin films on various electrode surfaces. *Electrochemistry Communications* **2005,** *7* (12), 1449-1456.

332.   Etienne, M.; Quach, A.; Grosso, D.; Nicole, L.; Sanchez, C.; Walcarius, A., Molecular Transport into Mesostructured Silica Thin Films: Electrochemical Monitoring and Comparison between p6m,P63/mmc, and Pm3n Structures. *Chemistry of Materials* **2007,** *19* (4), 844-856.

333.   Sel, O.; Sallard, S.; Brezesinski, T.; Rathouský, J.; Dunphy, D. R.; Collord, A.; Smarsly, B. M., Periodically Ordered Meso- and Macroporous SiO2 Thin Films and Their Induced

Electrochemical Activity as a Function of Pore Hierarchy. *Advanced Functional Materials* **2007,** *17* (16), 3241-3250.

334.   Etienne, M.; Sallard, S.; Schröder, M.; Guillemin, Y.; Mascotto, S.; Smarsly, B. M.; Walcarius, A., Electrochemical Generation of Thin Silica Films with Hierarchical Porosity. *Chemistry of Materials* **2010,** *22* (11), 3426-3432.

335.   Tompkins, H. G.; Irene, E. A., *Handbook of Ellipsometry*. William Andrew, Inc.: 2005.

336.   Bruggeman, D. A. G. v., Berechnung verschiedener physikalischer Konstanten von heterogenen Substanzen. *Annalen der Physik* **1935,** *416* (7), 636-664.

337.   Malitson, I. H., Interspecimen Comparison of the Refractive Index of Fused Silica*,†. *Journal of the Optical Society of America* **1965,** *55* (10), 1205.

338.   Spanier, J. E.; Herman, I. P., Use of hybrid phenomenological and statistical effective-medium theories of dielectric functions to model the infrared reflectance of porous SiC films. *Physical Review B* **2000,** *61* (15), 10437-10450.

339.   Brunsen, A.; Calvo, A.; Williams, F. J.; Soler-Illia, G. J.; Azzaroni, O., Manipulation of molecular transport into mesoporous silica thin films by the infiltration of polyelectrolytes. *Langmuir : the ACS journal of surfaces and colloids* **2011,** *27* (8), 4328-4333.

340.   Hayase, G.; Kanamori, K.; Nakanishi, K., New flexible aerogels and xerogels derived from methyltrimethoxysilane/dimethyldimethoxysilane co-precursors. *Journal of Materials Chemistry* **2011,** *21* (43), 17077.

341.   Hayase, G.; Kanamori, K.; Fukuchi, M.; Kaji, H.; Nakanishi, K., Facile synthesis of marshmallow-like macroporous gels usable under harsh conditions for the separation of oil and water. *Angewandte Chemie International Edition in English* **2013,** *52* (7), 1986-9.

342.   Pham, A. L.; Sedlak, D. L.; Doyle, F. M., Dissolution of Mesoporous Silica Supports in Aqueous Solutions: Implications for Mesoporous Silica-based Water Treatment Processes. *Applied Catalysis B* **2012,** *126*, 258-264.

343.   El Mourabit, S.; Guillot, M.; Toquer, G.; Cambedouzou, J.; Goettmann, F.; Grandjean, A., Stability of mesoporous silica under acidic conditions. *RSC Advances* **2012,** *2* (29), 10916.

344.   Alberti, S.; Steinberg, P. Y.; Gimenez, G.; Amenitsch, H.; Ybarra, G.; Azzaroni, O.; Angelome, P. C.; Soler-Illia, G., Chemical Stability of Mesoporous Oxide Thin Film Electrodes under Electrochemical Cycling: from Dissolution to Stabilization. *Langmuir : the ACS journal of surfaces and colloids* **2019,** *35* (19), 6279-6287.

345.   Dral, A. P.; Lievens, C.; Ten Elshof, J. E., Influence of Monomer Connectivity, Network Flexibility, and Hydrophobicity on the Hydrothermal Stability of Organosilicas. *Langmuir : the ACS journal of surfaces and colloids* **2017,** *33* (22), 5527-5536.

346.   Inagaki, S.; Guan, S.; Fukushima, Y.; Ohsuna, T.; Terasaki, O., Novel Mesoporous Materials with a Uniform Distribution of Organic Groups and Inorganic Oxide in Their Frameworks. *Journal of the American Chemical Society* **1999,** *121* (41), 9611-9614.

347.   Melde, B. J.; Holland, B. T.; Blanford, C. F.; Stein, A., Mesoporous Sieves with Unified Hybrid Inorganic/Organic Frameworks. *Chemistry of Materials* **1999,** *11* (11), 3302-3308.

348.   Wahab, M. A.; Kim, I.; Ha, C.-S., Bridged amine-functionalized mesoporous organosilica materials from 1,2-bis(triethoxysilyl)ethane and bis[(3-trimethoxysilyl)propyl]amine. *Journal of Solid State Chemistry* **2004,** *177* (10), 3439-3447.

349.   Wahab, M., Hybrid periodic mesoporous organosilica materials prepared from 1,2-bis(triethoxysilyl)ethane and (3-cyanopropyl)triethoxysilane. *Microporous and Mesoporous Materials* **2004,** *69* (1-2), 19-27.

350.   Masse, S.; Laurent, G.; Babonneau, F., High temperature behavior of periodic mesoporous ethanesilica glasses prepared from a bridged silsesquioxane and a non-ionic triblock copolymer. *Journal of Non-Crystalline Solids* **2007,** *353* (11-12), 1109-1119.

351.   Thomas, A.; Antonietti, M., Silica Nanocasting of Simple Cellulose Derivatives: Towards Chiral Pore Systems with Long-Range Order and Chiral Optical Coatings. *Advanced Functional Materials* **2003,** *13* (10), 763-766.

352.   Giese, M.; Blusch, L. K.; Khan, M. K.; MacLachlan, M. J., Functional materials from cellulose-derived liquid-crystal templates. *Angewandte Chemie International Edition in English* **2015,** *54* (10), 2888-910.

353.   Kelly, J. A.; Giese, M.; Shopsowitz, K. E.; Hamad, W. Y.; MacLachlan, M. J., The development of chiral nematic mesoporous materials. *Accounts of chemical research* **2014,** *47* (4), 1088-96.

354.   Shopsowitz, K. E.; Qi, H.; Hamad, W. Y.; Maclachlan, M. J., Free-standing mesoporous silica films with tunable chiral nematic structures. *Nature* **2010,** *468* (7322), 422-5.

355.   Hiromitsu Naono, R. F., and Masahide Yagi, Determination of Physisorbed and Chemisorbed Waters on Silica Gel and Porous Silica Glass by Means of Desorption Isotherms of Water Vapor. **1980.**

356.   Pliskin, W. A.; Esch, R. P., Refractive Index of SiO2 Films Grown on Silicon. *Journal of Applied Physics* **1965,** *36* (6), 2011-2013.

357.   Herzog, N.; Brilmayer, R.; Stanzel, M.; Kalyta, A.; Spiehl, D.; Dörsam, E.; Hess, C.; Andrieu-Brunsen, A., Gravure printing for mesoporous film preparation. *RSC Advances* **2019,** *9* (41), 23570-23578.

358.   Rafti, M.; Brunsen, A.; Fuertes, M. C.; Azzaroni, O.; Soler-Illia, G. J., Heterogeneous catalytic activity of platinum nanoparticles hosted in mesoporous silica thin films modified with polyelectrolyte brushes. *ACS Applied Materials & Interfaces* **2013,** *5* (18), 8833-40.

359.   Zalduendo, M. M.; Langer, J.; Giner-Casares, J. J.; Halac, E. B.; Soler-Illia, G. J. A. A.; Liz-Marzán, L. M.; Angelomé, P. C., Au Nanoparticles–Mesoporous TiO2 Thin Films Composites as SERS Sensors: A Systematic Performance Analysis. *The Journal of Physical Chemistry C* **2018,** *122* (24), 13095-13105.

360.   Cortial, G.; Siutkowski, M.; Goettmann, F.; Moores, A.; Boissiere, C.; Grosso, D.; Le Floch, P.; Sanchez, C., Metallic nanoparticles hosted in mesoporous oxide thin films for catalytic applications. *Small* **2006,** *2* (8-9), 1042-5.

361.   Bois, L.; Chassagneux, F.; Battie, Y.; Bessueille, F.; Mollet, L.; Parola, S.; Destouches, N.; Toulhoat, N.; Moncoffre, N., Chemical growth and photochromism of silver nanoparticles into a mesoporous titania template. *Langmuir : the ACS journal of surfaces and colloids* **2010,** *26* (2), 1199-206.

362.   Leroy, C. M.; Cardinal, T.; Jubera, V.; Aymonier, C.; Treguer-Delapierre, M.; Boissière, C.; Grosso, D.; Sanchez, C.; Viana, B.; Pellé, F., Luminescence properties of ZrO2 mesoporous thin films doped with Eu3+ and Agn. *Microporous and Mesoporous Materials* **2013,** *170*, 123-130.

363.   Angelomé, P. C.; Liz-Marzán, L. M., Monitoring Solvent Evaporation from Thin Films by Localized Surface Plasmon Resonance Shifts. *The Journal of Physical Chemistry C* **2010,** *114* (43), 18379-18383.

364.   Zalduendo, M. M.; Oestreicher, V.; Langer, J.; Liz-Marzan, L. M.; Angelome, P. C., Monitoring Chemical Reactions with SERS-Active Ag-Loaded Mesoporous TiO2 Films. *Analytical Chemistry* **2020,** *92* (20), 13656-13660.

365.   Xu, Y.; Bai, P.; Zhou, X.; Akimov, Y.; Png, C. E.; Ang, L. K.; Knoll, W.; Wu, L., Optical Refractive Index Sensors with Plasmonic and Photonic Structures: Promising and Inconvenient Truth. *Advanced Optical Materials* **2019,** *7* (9), 1801433.

366.   Chen, H.; Kou, X.; Yang, Z.; Ni, W.; Wang, J., Shape- and size-dependent refractive index sensitivity of gold nanoparticles. *Langmuir : the ACS journal of surfaces and colloids* **2008,** *24* (10), 5233-7.

Appendix

Appendix related to **Chapter 5.1.2**:

Table A1: Film thicknesses d and refractive indices n, as well as the respective root mean square error (RMSE) of the fit for MSTFs with tunable surface wettability in dependence of the mole fraction of TEOS in the dip coating solution. Values obtained by ellipsometry at 23 °C and 15 rH%.

sample	spot	d / nm	n / a.u.	RMSE
x=0 TEOS	1	93.7 ± 0.1	1.332 ± 0	0.094
	2	96.7 ± 0.1	1.347 ± 0	0.081
	3	99.1 ± 0.2	1.336 ± 0.001	0.31
x=0.2 TEOS	1	115.8 ± 0.1	1.311 ± 0	0.176
	2	111.9 ± 0	1.313 ± 0	0.081
	3	112 ± 0.1	1.318 ± 0	0.12
x=0.5 TEOS	1	162.1 ± 0.2	1.268 ± 0.001	0.377
	2	153.4 ± 0.1	1.271 ± 0	0.211
	3	165.1 ± 0.1	1.272 ± 0	0.229
x=0.8 TEOS	1	170.5 ± 0.1	1.222 ± 0	0.245
	2	168.3 ± 0.2	1.223 ± 0.001	0.277
	3	174.5 ± 0.1	1.223 ± 0	0.206
x=1 TEOS	1	152.8 ± 0.1	1.205 ± 0	0.132
	2	155.5 ± 0.1	1.205 ± 0	0.166
	3	164.8 ± 0.1	1.211 ± 0	0.183

Table A2: Apparent water contact angles for MSTFs with tunable surface wettability in dependence of the mole fraction of TEOS in the dip coating solution. Values obtained with a water drop of 2 μL at 23 °C and 50 rH%.

sample	spot	CA / °
x=0 TEOS	1	113.31
	2	116.82
	3	109.69
x=0.2 TEOS	1	108.52
	2	105.54
	3	106.39
x=0.5 TEOS	1	72.82
	2	78.41
	3	76.98
x=0.8 TEOS	1	44.63
	2	44.98
	3	46.65
x=1 TEOS	1	11.35
	2	9.37
	3	9.48

Appendix related to **Chapter 5.1.3**.

Table A3: Film thicknesses d and refractive indices n, as well as the respective root mean square error (RMSE) of the fit for MOSTFs prepared with the bridged precursor BTESE. Values obtained by ellipsometry at 23 °C and 15 rH%.

sample	spot	d / nm	n / a.u.	RMSE
MOSTF	1	215.2 ± 0.6	1.309 ± 0.002	0.619
	2	218.8 ± 0.6	1.311 ± 0.002	0.55
	3	212.8 ± 0.6	1.308 ± 0.002	0.706
	4	220.4 ± 0.6	1.311 ± 0.002	0.541
	5	217.9 ± 0.5	1.311 ± 0.001	0.487
	6	217.2 ± 0.7	1.312 ± 0.002	0.752
	7	219.5 ± 0.6	1.313 ± 0.002	0.602
	8	230.5 ± 0.8	1.327 ± 0.003	0.669

Table A4: Apparent water contact angles for MOSTF prepared with the bridged precursor BTESE. Values obtained with a water drop of 4 µL at 23 °C and 50 rH%.

sample	spot	CA / °
MOSTF	1	38.52
	2	41.15
	3	39.03

Appendix related to **Chapter 5.1.4**.

Table A5: Film thicknesses d and refractive indices n, as well as the respective root mean square error (RMSE) of the fit for MSTFs prepared by using HPC as template. Values obtained by ellipsometry at 23 °C and 15 rH%.

sample	spot	d / nm	n / a.u.	RMSE
HPC-MSTF	1	368 ± 42.5	1.179 ± 0.074	5.915
	2	382.5 ± 56.8	1.168 ± 0.09	6.476
	3	395.2 ± 61.6	1.161 ± 0.089	5.856

Table A6: Apparent water contact angles for MSTF prepared by using HPC as template. Values obtained with a water drop of 2 µL at 23 °C and 50 rH%.

sample	spot	CA / °
HPC-MSTF	1	23.18
	2	26.65
	3	24.84

Appendix related to **Chapter 5.2.1**.

Table A7: Film thicknesses d and refractive indices n, as well as the respective root mean square error (RMSE) of the fit for single layer MSTFs prepared by using Pluronic® F127 and CTAB as template, respectively. Values obtained by ellipsometry at 23 °C and 15 rH%.

sample	spot	d / nm	n / a.u.	RMSE
F127 single MSTF	1	169.8 ± 0.2	1.211 ± 0.001	0.307
	2	177.2 ± 0.2	1.212 ± 0.001	0.336
	3	180 ± 0.3	1.213 ± 0.001	0.493
CTAB single MSTF	1	222 ± 0.2	1.201 ± 0	0.279
	2	222.7 ± 0.1	1.203 ± 0	0.152
	3	227.9 ± 0.1	1.206 ± 0	0.139

Table A8: Film thicknesses d and refractive indices n, as well as the respective root mean square error (RMSE) of the fit for double layered MSTFs prepared by using Pluronic® F127 and CTAB as template, respectively. Values obtained by ellipsometry at 23 °C and 15 rH%.

sample	d / nm	n / a.u.	RMSE
CTAB bottom	207.8 ± 0.6	1.22 ± 0.001	0.809
double layered MSTF	282.3 ± 3	1.357 ± 0.009	0.644
F127 bottom MSTF	161 ± 0.3	1.237 ± 0.001	0.498
double layered MSTF	238.6 ± 0.5	1.374 ± 0.002	0.21

Table A9: Film thicknesses of double layered MSTFs with pore size step gradients determined by profilometer measurements.

sample	spot	thickness / nm
F127 bottom	1	113.7679
	2	205.1988
	3	185.7452
CTAB top	1	80.0392
	2	74.1124
	3	77.9264
CTAB bottom	1	176.8441
	2	175.0473
	3	175.6143
F127 top	1	63.1843
	2	62.7305
	3	64.8954

Appendix related to **Chapter 5.2.2**.

Table A10: Film thicknesses d and refractive indices n, as well as the respective root mean square error (RMSE) of the fit for double layered MSTFs with wettability step gradients. Values obtained by ellipsometry at 23 °C and 15 rH%.

sample	spot	d / nm	n / a.u.	RMSE
hydrophilic bottom layer	1	170.1 ± 0.1	1.293 ± 0	0.222
	2	169.9 ± 0.2	1.289 ± 0.001	0.346
	3	171.7 ± 0.2	1.286 ± 0.001	0.459
hydrophobic top layer withdrawn with 1 mm s^{-1}	1	63.1 ± 0.3	1.311 ± 0.001	0.282
	2	63.5 ± 0.2	1.306 ± 0.001	0.166
	3	60 ± 0.1	1.302 ± 0	0.108
hydrophobic top layer withdrawn with 2 mm s^{-1}	1	82.6 ± 0.4	1.314 ± 0.001	0.248
	2	88.6 ± 0.4	1.317 ± 0.001	0.189
	3	87.5 ± 0.5	1.319 ± 0.002	0.209
hydrophobic top layer withdrawn with 3 mm s^{-1}	1	103.8 ± 3.1	1.325 ± 0.01	103.8
	2	118.8 ± 3.9	1.307 ± 0.011	118.8
	3	119.8 ± 4.4	1.303 ± 0.012	119.8

Table A11: Apparent water contact angles of the hydrophilic bottom layer MSTF prepared by using Pluronic® F127 as template, and hydrophobic top layers deposited using different withdrawing speeds. Values obtained with a water drop of 2 µL at 23 °C and 50 rH%.

sample	spot	CA / °
F127 single MSTF	1	27.56
	2	28.74
	3	27.9
hydrophobic top layer withdrawn with 1 mm s^{-1}	1	108.2
	2	108.66
	3	107.99
hydrophobic top layer withdrawn with 2 mm s^{-1}	1	107.89
	2	108.04
	3	107.95
hydrophobic top layer withdrawn with 3 mm s^{-1}	1	106.23
	2	106.88
	3	107.03

Erklärung laut Promotionsordnung

§8 Abs. 1 lit. c PromO

Ich versichere hiermit, dass die elektronische Version meiner Dissertation mit der schriftlichen Version übereinstimmt und für die Durchführung des Promotionsverfahrens vorliegt.

§8 Abs. 1 lit. d PromO

Ich versichere hiermit, dass zu einem vorherigen Zeitpunkt noch keine Promotion versucht wurde und zu keinem früheren Zeitpunkt an einer in- oder ausländischen Hochschule eingereicht wurde. In diesem Fall sind nähere Angaben über Zeitpunkt, Hochschule, Dissertationsthema und Ergebnis dieses Versuchs mitzuteilen.

§9 Abs. 1 PromO

Ich versichere hiermit, dass die vorliegende Dissertation selbstständig und nur unter Verwendung der angegebenen Quellen verfasst wurde.

§9 Abs. 2 PromO

Diese Arbeit hat bisher noch nicht zu Prüfungszwecken gedient.

Darmstadt, den

………………………………

Mathias Stanzel

Erklärung zur Begutachtung der Publikationen

Referentin: Prof. Dr. Annette Andrieu-Brunsen

Koreferent: Prof. Dr. Markus Biesalski

23.05.2022

Weder Frau Prof. Dr. Annette Andrieu-Brunsen noch Herr Prof. Dr. Markus Biesalski der vorliegenden kumulativen Doktorarbeit waren an der Begutachtung nachstehender Publikationen beteiligt:

[1] Stanzel, M. Kunz, U., Andrieu-Brunsen, A., „Layer-selective functionalisation in mesoporous double layer via iniferter initiated polymerization for nanoscale step gradient formation", *Eur. Polym. J.*, **2021**, 156, 110604.

[2] Stanzel, M., Zhao, L., Mohammadi, R., Pardehkhorram, R., Kunz, U., Vogel, N., Andrieu-Brunsen, A., „Simultaneous Nanolocal Polymer and In Situ Readout Unit Placement in Mesoporous Separation Layers", *Anal. Chem.*, **2021**, 93, 13, 5394-5402.

[3] John, D.*, Stanzel, M.*, Andrieu-Brunsen, A., „Surface Plasmons and Visible Light Iniferter Initiated Polymerization for Nanolocal Functionalization of Mesoporous Separation Layers", *Adv. Funct. Mater.*, **2021**, 2009732.

*D.J. and M.S. contributed equally to this work/D.J. und M.S. haben gleichermaßen zur Arbeit beigetragen (Geteilte Erstautorenschaft).

[4] Khalil, A., Schäfer, F., Postulka, N., Stanzel, M., Biesalski, M., Andrieu-Brunsen, A., "Wettability-defined droplet imbibition in ceramic mesopores", *Nanoscale*, **2020**, 12, 24228-24236.

[5] Herzog, N., Brilmayer, R., Stanzel, M., Kalyta, A., Spiehl, D., Dörsam, E., Hess, C., Andrieu-Brunsen, A., „Gravure printing for mesoporous film preparation", *RSC Adv.*, **2019**, 9, 23570-23578.

Datum 26.5.2022

Referentin
(Prof. Dr. Annette Andrieu-Brunsen)

Koreferent
(Prof. Dr. Markus Biesalski)

Erklärung zum Eigenanteil an den Publikationen

Im Folgenden ist aufgelistet, mit welchem Anteil ich an den Publikationen beteiligt war.

Mein Anteil an der folgenden Publikation beträgt 90%.

[1]   **Stanzel, M.**, Kunz, U., Andrieu-Brunsen, A., „Layer-selective functionalisation in mesoporous double layer via iniferter initiated polymerization for nanoscale step gradient formation", *Eur. Polym. J.*, **2021**, 156, 110604.

Mein Anteil an der folgenden Publikation beträgt 70%.

[2]   **Stanzel, M.**, Zhao, L., Mohammadi, R., Pardehkhorram, R., Kunz, U., Vogel, N., Andrieu-Brunsen, A., „Simultaneous Nanolocal Polymer and In Situ Readout Unit Placement in Mesoporous Separation Layers", *Anal. Chem.*, **2021**, 93, 13, 5394-5402.

Mein Anteil an der folgenden Publikation beträgt 45%.

[3]   John, D.*, **Stanzel, M.***, Andrieu-Brunsen, A., „Surface Plasmons and Visible Light Iniferter Initiated Polymerization for Nanolocal Functionalization of Mesoporous Separation Layers", *Adv. Funct. Mater.*, **2021**, 2009732.

*D.J. and M.S. contributed equally to this work/D.J. und M.S. haben gleichermaßen zu dieser Arbeit beigetragen.

Mein Anteil an der folgenden Publikation beträgt 5%.

[4]   Khalil, A., Schäfer, F., Postulka, N., **Stanzel, M.**, Biesalski, M., Andrieu-Brunsen, A., "Wettability-defined droplet imbibition in ceramic mesopores", *Nanoscale*, **2020**, 12, 24228-24236.

Mein Anteil an der folgenden Publikation beträgt 10%.

[5]   Herzog, N., Brilmayer, R., **Stanzel, M.**, Kalyta, A., Spiehl, D., Dörsam, E., Hess, C., Andrieu-Brunsen, A., „Gravure printing for mesoporous film preparation", *RSC Adv.*, **2019**, 9, 23570-23578.

Erklärung zum Eigenanteil an den Publikationen